MICROSTRUCTURAL CHARACTERISTICS AND MECHANICAL PERFORMANCE OF Bi-Sb-Ni ADDED Sn-3.0Ag-0.5Cu MULTICOMPONENT LEAD-FREE SOLDER ALLOY

ZHOU DING

FACULTY OF ENGINEERING
UNIVERSITI MALAYA
KUALA LUMPUR

2024

MICROSTRUCTURAL CHARACTERISTICS AND MECHANICAL PERFORMANCE OF Bi-Sb-Ni ADDED Sn-3.0Ag-0.5Cu MULTICOMPONENT LEAD-FREE SOLDER ALLOY

ZHOU DING

THESIS SUBMITTED IN FULFILMENT OF THE REQUIREMENTS FOR THE DEGREE OF DOCTOR OF PHILOSOPHY

FACULTY OF ENGINEERING
UNIVERSITI MALAYA
KUALA LUMPUR

2024

UNIVERSITI MALAYA

ORIGINAL LITERARY WORK DECLARATION

Name of Candidate: ZHOU DING

Matric No: 17012502/3 (KVA180003)

Name of Degree: Doctor of Philosophy

Title of Project Paper/Research Report/Dissertation/Thesis ("this Work"):

Microstructural Characteristics and Mechanical Performance of Bi-Sb-Ni Added Sn-3.0Ag-0.5Cu Multicomponent Lead-Free Solder Alloy

Field of Study: Engineering Materials

I do solemnly and sincerely declare that:

(1) I am the sole author/writer of this Work;
(2) This Work is original;
(3) Any use of any work in which copyright exists was done by way of fair dealing and for permitted purposes and any excerpt or extract from, or reference to or reproduction of any copyright work has been disclosed expressly and sufficiently and the title of the Work and its authorship have been acknowledged in this Work;
(4) I do not have any actual knowledge nor do I ought reasonably to know that the making of this work constitutes an infringement of any copyright work;
(5) I hereby assign all and every rights in the copyright to this Work to the Universiti Malaya ("UM"), who henceforth shall be owner of the copyright in this Work and that any reproduction or use in any form or by any means whatsoever is prohibited without the written consent of UM having been first had and obtained;
(6) I am fully aware that if in the course of making this Work I have infringed any copyright whether intentionally or otherwise, I may be subject to legal action or any other action as may be determined by UM.

Candidate's Signature Date: 27/02/2024

Subscribed and solemnly declared before,

Witness's Signature Date: 27/02/2024

Name:

Designation:

ABSTRACT

Sn-Ag-Cu (SAC) alloys have been identified as promising replacements for standard 63Sn-37Pb eutectic solder after the restriction in legislation of lead (Pb) in electronics has been actively pursued. However, the reliability of Pb-free solders, used in harsh conditions such as in automotive, is still a serious concern. Simultaneous additions of multiple alloying elements to conventional SAC based solders have recently been investigated to improve their reliability.

The present study contains two parts. In the first part of the study, the effects of isothermal aging on the microstructure and mechanical properties were investigated for Sn-3.0Ag-0.5Cu (SAC305) and a SAC305 based alloy with simultaneously addition Bi, Sb and Ni added (noted as solder M with composition of Sn-3.0Ag-0.5Cu-3.2Bi-2.95Sb-0.037Ni). The solder alloys were thermally aged at 125℃ for up to 1008 hours. Subsequently, tensile tests under different strain rates and creep tests at various applied tensile stresses for up to $5x10^4$ s were conducted. In addition, microhardness tests of thermally aged solder alloys after creep tests were studied, the changes of hardness from fracture tips to clamping side were discussed. The findings showed that aging time led to the global increase of grain size significantly. The average grain diameter of as-received solder M was 2.5 times smaller than SAC305. After 1008h aging at 125℃, the increase of grain diameter of solder M was also lesser than SAC305. Overall, the addition of Bi, Sb, and Ni improved microstructural refinement, suppressed the grain growth of solder M, and reduced the grain growth rate in comparison with SAC305. Tensile tests showed that the ultimate tensile strength (UTS) of the solder M was higher than SAC305 during 125℃ aging. In addition, thermal aging resulted in a decreased creep rate for solder M, but the opposite performance of SAC305 was found. Different performances of two aged solder alloys revealed that Sb and Ni increased the mechanical strength of SAC305 by forming

intermetallic phases, while Bi provided both solid solution and precipitation strengthening.

In the second part of this work, simulations of SAC305 in a novel hybrid quad flat package (QFP) under thermal cyclic loading were conducted by using finite element method (FEM). Due to the variation of temperature during service, solder alloy applied in the novel QFP undergoes high thermal stress, which can lead to large deformation and failure. Thus, the prediction of thermal stress and strain distributions of solder is a prerequisite for reliability analysis of electronic package. Simulations of SAC305 in a novel hybrid QFP under thermal cyclic loading were conducted by using ANSYS. The stress distribution and accumulated creep strain were found in the critical location of solder in package, and lifetime was predicted. Furthermore, the simulation results were compared with experimental results from industry.

Keywords: Multicomponent solder, Mechanical strength, Sn-3.0Ag-0.5Cu, Thermal aging, Microstructure.

ABSTRAK

Aloi Sn-Ag-Cu (SAC) telah dikenal pasti sebagai pengganti yang menjanjikan untuk pateri eutektik standard 63Sn-37Pb selepas sekatan dalam perundangan plumbum (Pb) dalam elektronik telah dilaksanakan secara aktif. Walau bagaimanapun, kebolehpercayaan pateri bebas Pb, yang digunakan dalam keadaan yang teruk seperti dalam automotif, masih menjadi kebimbangan serius. Penambahan serentak berbilang unsur pengaloian kepada pemateri berasaskan SAC konvensional baru-baru ini telah disiasat untuk meningkatkan kebolehpercayaan mereka.

Kajian ini mengandungi dua bahagian. Dalam bahagian pertama kajian, kesan penuaan isoterma pada struktur mikro dan sifat mekanikal telah disiasat untuk Sn-3.0Ag-0.5Cu (SAC305) dan aloi berasaskan SAC305 dengan penambahan Bi, Sb dan Ni serentak (dikenali sebagai pateri M dengan komposisi Sn-3.0Ag- 0.5Cu-3.2Bi-2.95Sb-0.037Ni). Aloi pateri telah berumur secara terma pada 125 °C sehingga 1008 jam. Selepas itu, ujian tegangan di bawah kadar terikan yang berbeza dan ujian rayapan pada pelbagai tegasan tegangan yang dikenakan sehingga $5x10^4$ s telah dijalankan. Di samping itu, ujian mikrokekerasan aloi pateri berumur terma selepas ujian rayapan dikaji, perubahan kekerasan daripada hujung patah kepada bahagian pengapit telah dibincangkan. Penemuan menunjukkan bahawa masa penuaan membawa kepada peningkatan global saiz bijirin dengan ketara. Purata diameter butiran bagi pateri M yang diterima adalah 2.5 kali lebih kecil daripada SAC305. Selepas penuaan 1008j pada 125 °C, peningkatan diameter butiran pateri M juga lebih rendah daripada SAC305. Secara keseluruhannya, penambahan Bi, Sb, dan Ni meningkatkan penghalusan mikrostruktur, menekan pertumbuhan bijian pateri M, dan mengurangkan kadar pertumbuhan bijian berbanding dengan SAC305. Ujian tegangan menunjukkan bahawa kekuatan tegangan muktamad (UTS) pateri M adalah lebih tinggi daripada SAC305 semasa penuaan 125°C. Di samping itu, penuaan haba menyebabkan kadar rayapan menurun untuk pateri M, tetapi prestasi

bertentangan SAC305 ditemui. Prestasi berbeza bagi dua aloi pateri berumur mendedahkan bahawa Sb dan Ni meningkatkan kekuatan mekanikal SAC305 dengan membentuk fasa antara logam, manakala Bi menyediakan kedua-dua larutan pepejal dan pengukuhan kerpasan.

Dalam bahagian kedua kerja ini, simulasi SAC305 dalam pakej flat quad hibrid baru (QFP) di bawah beban kitaran haba telah dijalankan dengan menggunakan kaedah unsur terhingga (FEM). Disebabkan oleh variasi suhu semasa perkhidmatan, aloi pateri yang digunakan dalam novel QFP mengalami tekanan haba yang tinggi, yang boleh menyebabkan ubah bentuk dan kegagalan yang besar. Oleh itu, ramalan tegasan haba dan taburan terikan pateri adalah prasyarat untuk analisis kebolehpercayaan pakej elektronik. Simulasi SAC305 dalam QFP hibrid novel di bawah pemuatan kitaran haba telah dijalankan dengan menggunakan ANSYS. Taburan tegasan dan terikan rayapan terkumpul ditemui di lokasi kritikal pateri dalam bungkusan, dan jangka hayat telah diramalkan. Tambahan pula, keputusan simulasi telah dibandingkan dengan keputusan eksperimen daripada industri.

Kata kunci: Pateri berbilang komponen, Kekuatan mekanikal, Sn-3.0Ag-0.5Cu, Penuaan terma, Mikrostruktur.

I dedicate this work to the love and care given by my Grandmother

致丁丁最亲最爱的奶奶

ACKNOWLEDGEMENTS

I would like to express my immense indebtedness and gratitude to my respected supervisors Prof. Dr. A. S. M. A. Haseeb and Prof. Ir. Dr. Andri Andriyana, as well as Associate Prof. Ir. Dr. Nik Nazri Bin Nik Ghazali for their support, guidance, valuable comments, ideas, and motivation that helped me in conducting my research and in completion of this research. I would express special gratitude to Mrs. Zhou Shanshan for the help and advice during the completion of this study. Sincere thanks to lab technicians and my colleagues in Faculty of Engineering, Universiti Malaya and engineers in NXP semiconductor for their cooperation and support throughout this study.

I gratefully acknowledge the research funding (P12: Hybrid-High Density Lead-frame Package), (P09C3–14: Packaging and Process Development of Low Cost Universal Substrate), (P10C3-14: Development and Characterization of Embedded Ball Grid Array Package) from Malaysia Collaborative Research in Engineering, Science & Technology and (RK003-2016A: Hybrid-High Density Lead-frame Package), (RK006-2018: Development and Characterization of Embedded Ball Grid Array Package), (RK007–2018: Development and Characterization of Low Cost Universal Substrate) from Universiti Malaya Partnership Grant.

Finally, it would be understated to say thanks to my mother, my grandparents, my family in China and my friends in Malaysia, as I consider it beyond myself to express such feelings for them in always being there as a source of encouragement and inspiration.

Zhou Ding

February 2024

TABLE OF CONTENTS

LIST OF FIGURES

LIST OF TABLES

LIST OF SYMBOLS AND ABBREVIATIONS

Bi	:	Bismuth
Sb	:	Antimony
Ni	:	Nickel
SAC	:	Sn-Ag-Cu
QFP	:	Quad flat packages
PLCC	:	Plastic leaded chip carrier
EU	:	European Union
U.S.	:	United States
EPA	:	Environmental Protection Agency
RoHS	:	Restriction of Hazardous Substances Directive
SAC305	:	96.5Sn-3.0Ag-0.5Cu
SAC387	:	95.5Sn-3.8Ag-0.7Cu
SAC396	:	95.5Sn-3.9Ag-0.6Cu
SMT	:	Surface-mount technology
Sn-Pb	:	Tin-lead
T_m	:	melting temperature
NEMI	:	National Electronics Manufacturing Initiatives
JEITA	:	Japan Electronics and Information Technology Industries Association
α		Alpha
β	:	Beta
γ	:	Gamma
ζ	:	Zeta
δ	:	Delta
IMC	:	Intermetallic compound

SEM	:	Scanning electron microscope
UBM	:	Under bump metallization
ECM	:	Electrochemical migration
QFN	:	Quad flat no-leads package
CTE	:	Coefficient of thermal expansion
ΔT	:	Difference in temperature
PCB	:	Printed circuit board
YS	:	Yield strength
FEM	:	Finite element method
WD	:	Water drop
THB	:	Temperature and humidity bias
JEDEC	:	Joint Electron Device Engineering Council
Mn	:	Manganese
Fe	:	Iron
Zn	:	Zinc
In	:	Indium
Te	:	Tellurium
Ge	:	Germanium
Co	:	Cobalt
EDX	:	Energy dispersive X-ray
RT	:	Room temperature
USS	:	Ultimate shear strength
HV	:	Vickers hardness
σ	:	Stress
ε	:	Strain
E	:	Modulus of elasticity

n	:	Strain hardening exponent
$\dot{\varepsilon}_s$	:	Steady-state creep-rate
γ_T	:	Primary creep Amplitude of strain
B	:	Material constants for creep response under deformation mechanism
σ_y	:	Yield strength
σ_i	:	Constant of overall resistance of the lattice to dislocation movement
D	:	Grain size
$\dot{\varepsilon}$	:	Strain rate
T	:	Test temperature
A_0	:	Function of the weight percentage of Sn in the alloy
T_r	:	Real temperature
n_0	:	Strain hardening exponent
σ_0	:	Stress coefficient
t	:	Time
C	:	Constant depends on the material and creep mechanism
h	:	Constant which depends on creep mechanism
Q	:	Activation energy of the material
k	:	Boltzmann constant
m	:	Creep stress exponent
Ω	:	Activation volume
ASTM	:	American Society for Testing and Materials
XRF	:	X-ray fluorescence
XRD	:	X-ray diffraction
ICDD	:	International Center for Diffraction Data
DSC	:	Differential scanning calorimetry
F	:	Indentation force

p	:	Average length of the diagonal left by the indenter
RM	:	Repeated measures
EMC	:	Epoxy mold compound
DNP	:	Distance to neutral point
A	:	Material constant
R	:	Gas constant
N_f	:	Number of cycles to failure
$\Delta\varepsilon_{cr}$	:	Creep strain per cycle
Θ	:	Corresponding coefficients of SAC305
σ_t	:	True flow stress
K	:	Strength coefficient
ε_t	:	True plastic strain

CHAPTER 1

INTRODUCTION

1.1 Background

Soldering is a metallurgical joining technique that involves utilizing solder with a melting temperature of less than 425°C as a filler (Abtew & Selvaduray, 2000). Throughout the history of electronics packaging, 63Sn-37Pb and 60Sn-40Pb have been the most widely used soldering alloys. The Sn-Pb binary system features a melting eutectic temperature as low as 183 °C and provides material compatibility with most substrate materials and devices. Moreover, 63Sn-37Pb alloy was extensively employed in the electronics sector prior to the development of lead-free (Pb-free) solder because of its good mechanical and thermal qualities (El-Daly &Hammad, 2010).

However, the European Union (EU) has officially prohibited the use of Pb-based goods since 2006 (El-Daly & Hammad, 2010). Lead (Pb), on the other hand, is toxic to the environment and human health. Pb usage is being controlled, and regulations such as notice of new Pb-containing items to the Environmental Protection Agency (EPA) were enacted. The Restriction of Hazardous Substances Directive (RoHS) directive has recently prompted substantial study into Pb-free solders (Kroupa et al., 2012).

The microelectronic packaging industry's tendency has prompted the development of high-performance Pb-free solders. Alternative solders with the appropriate reliability are required. However, the shift to Pb-free manufacturing is a difficult task. Sn-Ag-Cu (SAC) series, a ternary system that derives from Sn-Ag and Sn-Cu binary systems, has become the most promising replacement and many SAC alloys have been adopted by major electronics manufacturers.

The alloy Sn-3.0Ag-0.5Cu (SAC305) has been widely accepted in Japan, 95.5Sn-3.8Ag-0.7Cu (SAC387) is now the leading Pb-free choice in the EU, and 95.5Sn-3.9Ag-0.6Cu (SAC396) has gained its popularity with the U.S. (Ma et al., 2006). companies. However, the reliability of Pb-free solders, used in harsh conditions such as in automotive, is still a serious concern (Puttlitz & Kathleen, 2004). Moreover, only a few studies address stress distribution and creep strain analysis during temperature cycling test of SAC305 alloy applied in newly developed Pb-free packages (Ganesan et al., 2006; Puttlitz & Kathleen, 2004; Tao et al., 2016).

Furthermore, the properties of the solder are likely to degrade over long usage due to aging effects, especially in harsh conditions under high temperature and stress (Ma et al., 2006; Lopez et al., 2010). For example, automotive electronics manufacturers are facing significant challenges in respect to the thermo-mechanical reliability of solder joints. Solder joints display complex mechanical structure in electronic packaging. Up to date, several methods have been applied in improving the solder mechanical strength to ensure that the material properties remain after long-term services. One of the strategies that researchers used in their study is by adding multiple additional elements mentioned above to enhance the properties of the SAC solder alloys (Hammad, 2018; Mahdavifard et al., 2015). These supplemented elements were added to fabricate a multicomponent solder so that the improved overall properties could be obtained, such as higher strength and reliability under harsh operation conditions (Alam et al., 2019). Simultaneous additions of Fe and Bi to SAC105 refined the microstructure and improved tensile properties, while decreased the melting temperature of the SAC105 alloy (Ali et al., 2016). Adding In and Ce into SAC solder was effective in improving the shear strength, ductility, and fracture toughness (Fallahi et al., 2012). SAC solder with Bi and Sb, or Ni and Sb provided higher reliability under high operating temperature and high stress conditions (Tao et al., 2016; Lopez et al., 2010).

Along this line, multi additional elements were chosen and added into SAC solder to improve the performance under both thermal and mechanical challenges (Gyenes et al., 2017). The effect on the mechanical performance for simultaneous additions of alloying elements added into SAC solders has been studied, and comparisons between multicomponent solders and SAC solders have also been made. Among these studies, a commercial alloy known as Innolot was reported (Tao et al., 2016; Kang et al., 2021; Gyenes et al., 2017). It contains 3 wt.% Bi, 1.5 wt.% Sb and 0.15 wt.% Ni in SAC387 based composition. The evaluations of the mechanical properties for Innolot alloy showed improved tensile, shear strength, and creep resistance. The ultimate tensile strength (UTS) of Innolot increased by 16.25% and 121.4% respectively as compared with SAC405 and SAC105, while the shear strength of this alloy increased by 16.8% in compared to SAC-Bi alloy (Tao et al., 2016; Chowdhury et al., 2016). Furthermore, a 5.12% reduction of UTS for Innolot as compared to 14.99% of SAC105 and 9.7% of SAC305 was reported as after undergoing 60 days aging under 50 ℃ (Lall et al., 2013). As for creep behavior, Innolot possessed more resistance to creep at high temperatures with only 33% of creep rate than SAC405 (Fahim et al., 2016). In addition, the thermal aging effect was also reported on the creep resistance.

However, there is not much data available for the mechanical performance of the multicomponent solder under high temperature aging condition. Furthermore, microstructure change of the multicomponent solder under thermal aging condition was also not correlated with its mechanical properties. One concern is the decline in mechanical strength due to the change in microstructural stability during thermal aging (Long et al., 2018; Zhang et al., 2012).

Thus, it is important to understand how the mechanical behavior of solder alloys varies with changes in thermal aging condition. The other concern is that there is not much work reported on the observation of intermetallic compounds (IMCs) of this multicomponent solder during harsh operating conditions. In addition, the fracture behavior of the thermally aged multicomponent solder in tensile testing lacks in-depth study. Therefore, it is imperative to study the mechanical performance of the multicomponent solder and its microstructural change to give insight into its thermo-mechanical properties and reliability.

In comparison to SAC387 alloy, which is used in Innolot as the base solder, SAC305 is an alternative option for base solder offering a lower cost. There has not been much work done on SAC305 as a base solder with different weight percentages of multielement additions.

In the first part of this study, the effects of simultaneous additions of Bi, Sb, and Ni to SAC305 solder on the microstructural and mechanical properties under thermal aging at 125 ℃ for up to 1008 hours were investigated. This multicomponent alloy is noted as solder M in this work with composition of Sn-3.0Ag-0.5Cu-3.2Bi-2.95Sb-0.037Ni. Superior microstructural stability and improved mechanical strength of solder M at longer aging time and its fracture behavior were discussed. Furthermore, the characterizations of each element weight percentage and chemical compounds were reported. Microstructural observation of grain growth and IMCs for SAC305 and solder M with different thermal aging time were compared and analyzed.

In the second part, as SAC305 is still widely used in electronic packages in most industries, the analysis of its reliability in the real application is important to contribute to electronic production and technical report. Thus, simulations of the stress distribution and creep strain of SAC305 alloy during temperature cycling in an application of a novel

quad flat package (QFP) are reported. Furthermore, the simulation results were compared with experimental results from industry.

1.2 Objectives of this research

1. To investigate the effect of thermal aging on mechanical properties and creep characteristics of SAC305 and Solder M at room temperature.

2. To evaluate the effect of thermal aging on the microstructure and fracture surface of SAC305 and solder M.

3. To analyze the effect of additional elements Bi, Sb and Ni on the mechanical properties of SAC305 alloy.

4. To assess the reliability of SAC305 used in a novel QFP under thermal cyclic loading.

1.3 Scope of this research

In the present study, the effects of simultaneous additions of Bi, Sb, and Ni to SAC305 solder on the microstructural and mechanical properties under thermal aging at 125 °C for up to 1008 h were investigated. Superior microstructural stability and improved mechanical strength of solder M at longer aging time and its fracture behavior were discussed. Furthermore, the characterizations of each element weight percentage and chemical compounds were reported.

Microstructural observation of grain growth and IMCs for SAC305 and solder M with different thermal aging time were compared and analyzed. Furthermore, Vickers microhardness tests are conducted on the samples to measure the hardness of the materials from the fractured tip of the material towards the edge of material after creep tests during thermal aging. The hardness values are then compared with other alloys which were

subjected to the same stress to get better understanding of creep behaviors of two Pb-free solders.

Following this, a displacement creep model is fitted for solder M to compare with SAC305 during thermal aging. Finally, the simulation of application of SAC305 in a novel quad flat package are conducted and the stress distribution and creep strain analysis during temperature cycling test are reported.

1.4 Organization of the thesis

This thesis is divided into five chapters. Chapter one briefly states the background, objectives, and the scope of the present research work. Chapter two gives a comprehensive survey of the existing literature and background on various topics related to this study. These topics include electronic packaging technology, Pb-free solder alloys development, microstructural observation of Pb-free solders, and reliability of solder alloy in electronic package. The methodology of the research work is presented in chapter three which describes raw materials and their characterization, tensile testing procedure, creep testing procedure, microstructural observations, and modelling of thermal fatigue failure. Chapter four of this thesis explains the results obtained from the experimental work. In-depth analysis and explanations of the results are presented and compared with the other published works. Chapter five summarizes the findings of the present work and recommends future research work.

CHAPTER 2

LITERATURE REVIEW

2.1 Solder alloy and its usage

Solder is a metallic material that is used to connect metal workpieces. The choice of specific solder alloys depends on their melting point, chemical reactivity, mechanical properties, toxicity, and other properties. Soldering is the joining of two metal surfaces mechanically and electrically, with the use of metal called solder. Solder secures the connection, so it does not break loose due to vibration or other mechanical forces. It also provides electrical continuity, so that the electronic signal can travel through the connection without interruption. The solder is normally melted by using a soldering iron, and flux is used to clean and prepare the surfaces, which allows the melted solder to flow and bond with the metal surfaces (Brand et al., 2017).

Hand soldering is the process of soldering one connection which is also known as solder joint at a time, as opposed to more automated soldering processes such as wave soldering for thru-hole components or reflow soldering for surface-mount technology (SMT) components. The electronics industry has depended heavily on tin-lead (Sn-Pb) type solders to build computer chips, circuits, and many other electronic components for the past 50 years. In the electrical industry, there are various types of potential Pb-free solders. A choice must be made as to which is the most appropriate. Low melting temperature (T_m), good wettability, strong creep resistance, low shear strength, low electrical resistivity, high thermal conductivity, and increased coefficient of thermal expansion are all needed qualities (Clech et al., 2019). Sn-Pb has a T_m of 183°C, but certain Pb-free solder alloys have a much higher T_m. Increased T_m can deteriorate components, soldering flux or paste chemistry, and materials that are attached to them.

As a result, the melting temperature of potential Pb-free solder alloys must be the most significant element to consider. It must be close to or lower than the melting point of Sn-37Pb solder (183°C). This is due to most electronic assembly equipment and technologies utilizing 183°C as a reference temperature. A much higher or lower melting point of the replacement Pb-free solder will need the purchase of new equipment, increasing capital investment and product cost. Another significant reason to keep the melting point at 183°C is to avoid degradation of common applications such as epoxy resins, soldering flux or paste, and die attach material (Manikam & Cheong, 2011).

The range of Pb-free alloys to displace Sn-Pb looks to be narrowing to keep the melting point close to 183°C. Wettability, tensile strength, electrical resistivity, thermal, conductivity, density, and other criteria are used to evaluate the performance of Pb-free solder alloys in addition to the melting point. SAC, Sn-Bi, Sn-Ag, Sn-Zn, Sn-Cu, Sn-Sb, and Sn-In alloys are among the most promising Pb-free solders to be used on the most frequent substrates Ag, Au, Cu, and Ni.

2.2 Development of lead-free solders

2.2.1 History of lead solder alloys

In the electronics packaging business, Sn-Pb solders have been widely employed in chip connection and surface-mount techniques (El-Daly and Hammad, 2010). In terms of mechanical dependability, eutectic Sn-Pb solder has been extensively used for a long period of time with satisfactory mechanical qualities (Kotadia, et al., 2014). Eutectic Sn–Pb solder is soft, melts quickly, and wets copper with a small angle (Glazer, 1995). Sn-Pb has a low eutectic temperature of 183°C. The solder used in board level packaging is mostly 63Sn-37Pb, a eutectic composition, or 60Sn-40Pb, a near eutectic composition (Abtew and Selvaduray, 2000).

Low cost, good soldering qualities, acceptable melting temperature range, good wettability, and relatively good mechanical, metallurgical, physical, and fatigue resistant properties and longer lifespans are all reasons why Pb-containing solders are frequently utilized (ahir Rizvi, 2007). On the other hand, Pb is a poisonous substance that may harm both humans and the environment (Ara & Usmani, 2015). As a result of the environmental and health risks linked with Pb consumption, legislation in the EU and elsewhere has pushed to ban its use (Damalas & Eleftherohorinos, 2011).

2.2.2 Legislation restricting use lead solder

Since 1990, the elimination of Pb from electronics manufacturing has been addressed. The initial impetus was a planned legislative prohibition in the United States. However, there was no solder alloy alternative for Sn-Pb at the time, and the law was abandoned due to significant industry lobbying (Bath, 2007).

Pb usage was being controlled, and regulations such as notice of new Pb-containing items to the EPA were enacted. Under the Toxic Substance Control Act, the EPA has issued an Advanced Notice of Proposal Rule which has substantial regulatory consequences of Pb using for nations such as the United States, Japan, and Korea (Body, et al., 1991). There has been significant controversy in the United States about mandating the electronics sector to eradicate Pb in solder alloys, and the similar movement has gained traction and support in Europe. European countries were forced to stop using Pb, mercury (Hg), cadmium (Cd), hexavalent chromium, as well as certain brominated flame retardants in a variety of items as of July 1, 2006 (Ladou & Lovegrove, 2008). The shift to Pb-free manufacturing is a difficult task. The choice of a substitute solder alloy is one of the initial problems in industry. After a four-year study, the National Center for Manufacturing Sciences found in 1997 that there were no drop-in substitutes for eutectic Sn-Pb (Artaki et al., 1999; Sattiraju et al., 2002).

2.2.3 Choice of Lead-free solders

The RoHS directive has recently prompted substantial study into Pb-free solders (Ma & Suhling, 2009). The microelectronic packaging industry tended to prompt the development of high-performance Pb-free solders with the appropriate reliability (Li & Wong, 2006). Eradication of Pb-containing components was a major goal. Sn-Sb, Sn-In, Sn-Zn, Sn-Au, Sn-Bi, Sn-Pd, and Sn-Ag are some of the Pb-free solder alloys that have been studied as potential Pb-free replacements to the conventional Sn-Pb alloy. When compared to typical Sn-Pb alloys, these alloys exhibit lower melting temperatures and better wettability (Evans, 2007). Any novel solder alloys will be compared to classic eutectic or near-eutectic Sn-Pb systems, according to Evans (2007), and will be expected to perform similarly well or better in most aspects. As a result, any component changes to Sn based systems must meet the following fundamental criteria:

- Lower the surface tension of pure Sn to increase wettability.
- Assist in faster formation of intermetallic compounds between the substrate and solder via diffusion.
- Helps in avoiding transformation of β-Sn to α-Sn, which results in in undesirable volume changes and compromises the structural integrity and dependability of the solder.
- Maintains the melting temperature roughly around 183 °C with eutectic or near eutectic composition where the liquid phase might transit into two or more solid phases.
- Helps to enhance mechanical properties like mechanical shock, thermomechanical fatigue, creep, vibration, and thermal ageing.
- Avoid excessive growth of tin whisker.
- Enhance the ductile property of Sn.

2.3 Sn-Ag-Cu (SAC) series alloys

JEIDA and NEMI both suggested near-eutectic and eutectic SAC alloys in National Electronics Manufacturing Initiatives (NEMI) in 1999, "Roadmap 2002 for Commercialization of lead-free Solder" organized by Pb-Free Soldering Roadmap Committee (Fukuda et al., 2003)., and ''Lead-free Assembly Projects'' in Japan Electronics and Information Technology industries Association (JEITA) (Handwerker et al., 2003). Sn-0.7 wt.% Cu and Sn-3.5 wt.% Ag solders were considered as potential Pb-free alternatives. The Sn-rich corner of the Sn-Ag-Cu ternary system, which includes the binary Sn-Ag eutectic, binary Sn-Cu eutectic, and ternary Sn-Ag-Cu eutectic is where the most significant Pb-free solders were found as shown in Figures 2.1 to 2.3.

There are two intermetallic compounds, ζ-Ag4Sn and ϵ-Ag_3Sn, two peritectic reactions, and one eutectic reaction, liquid = Ag_3Sn + Sn as illustrated in Figure 2.1 (Karakaya & Thompson, 1987). Sn-3.5wt% Ag is the eutectic composition, and the melting temperature is 221°C. This system has been thermodynamically studied by Kattner and Boettinger (Kattner & Boettinger, 1994). They employed Ag, Sn, liquid, and ζ phase solution models, and they assumed the ε-Ag_3Sn was a line compound. The computed phase diagrams correlate well with experimental results, with the eutectic temperature and liquid composition being 220.9°C and Sn-3.87 at Ag percent respectively.

As for Sn–Cu binary system shown in Figure 2.2, seven intermetallic compounds (β, γ, ζ, δ, ε-Cu_3Sn, η-Cu_6Sn_5 and η'-Cu_6Sn_5) and 13 invariant reactions are found (Saunders & Miodownik, 1990). Phase equilibria in the Sn-rich corner are more relevant for soldering purposes, and there are three intermetallic compounds, ε-Cu_3Sn, η-Cu_6Sn_5 and η'-Cu_6Sn_5, one eutectic, liquid = Sn + η-Cu_6Sn_5, and one probable eutectoid, η-Cu_6Sn_5 = Sn + η'-Cu_6Sn_5. The liquid composition of eutectic is Sn-0.7wt% Cu and the temperature is at 227°C. The binary Sn-Cu system has been thermodynamically modeled by Shim

et al. (1996) and Boettinger et al. (1993). ζ, δ, ε-Cu_3Sn, η-Cu_6Sn_5 and η'-Cu_6Sn_5 are investigated as the line compounds. For the β and γ phases, the solution model and the two-sublattices model are utilized. Furthermore, the experimental results and the model calculated phase diagrams are in good agreement.

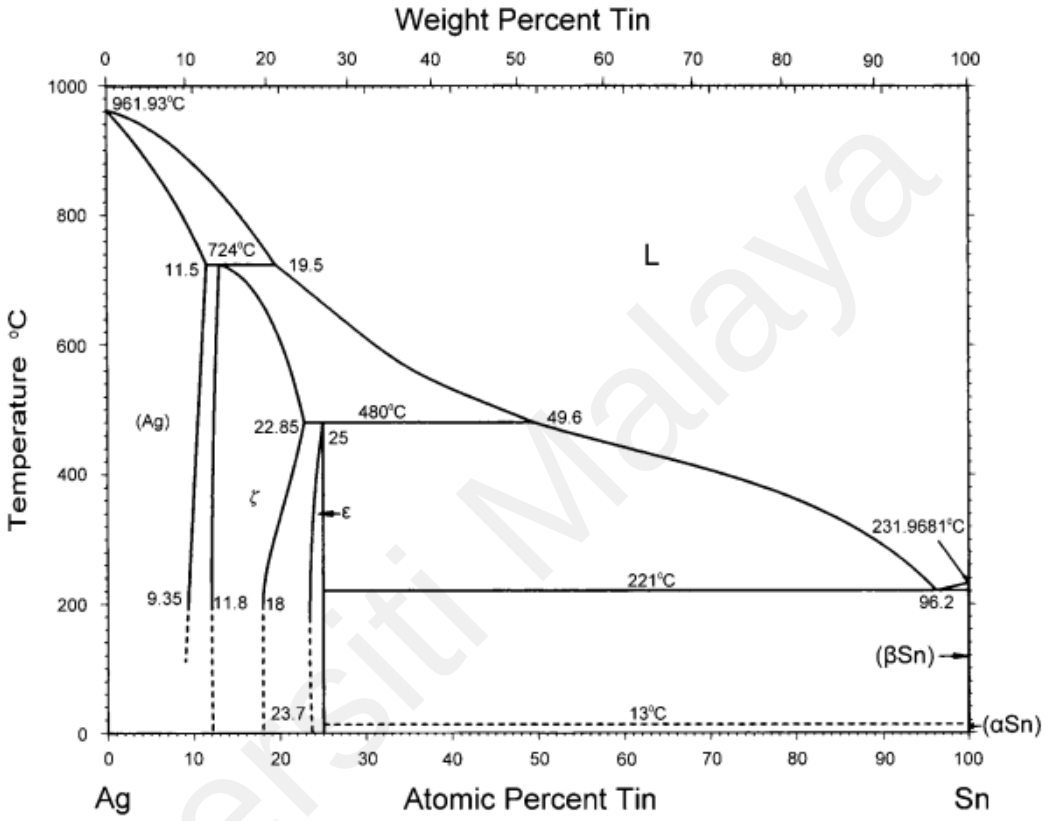

Figure 2.1: The Sn-Ag binary phase diagram (Karakaya & Thompson, 1987).

The isothermal sections of the ternary SnAgCu system phase equilibria were experimentally determined by Gebhardt and Petzow (1959) and Yen and Chen (2004). There have been no ternary compounds discovered. The ε -Cu_3Sn phase exhibits tie-lines with all the solid phases, as seen in Figure 2.3(a) of the 240°C isothermal section and ternary solubilities of the binary compounds are restricted. In 225°C, Gebhardt and Petzow (1959) hypothesized a class II reaction at the Sn-rich corner, L + η-Cu_6Sn_5 = ε-

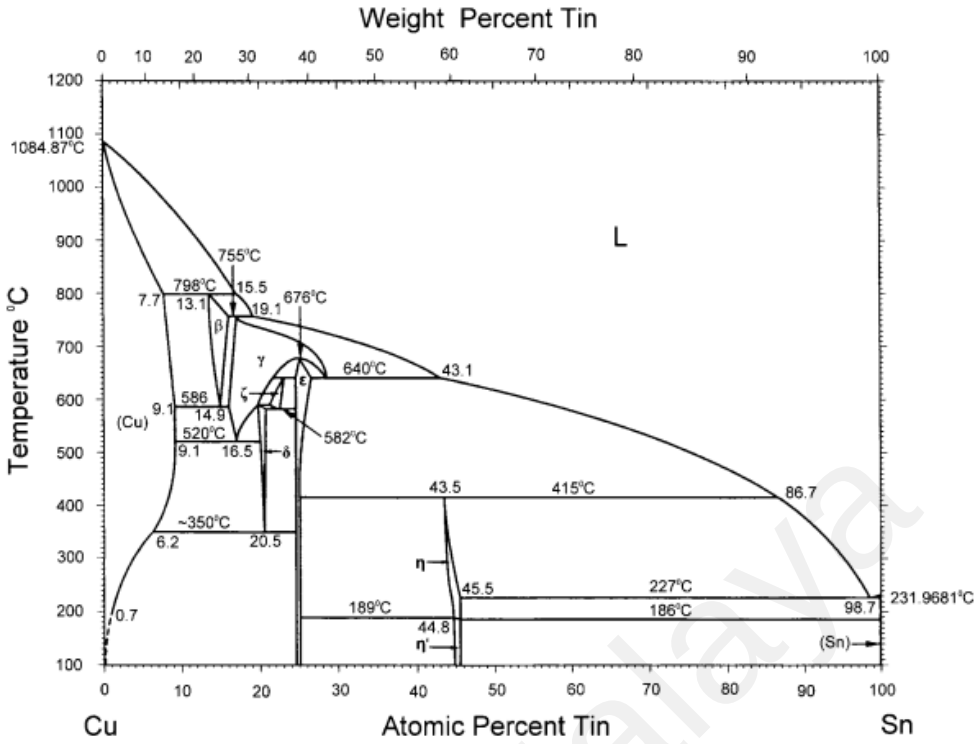

Figure 2.2: The Sn-Cu binary phase diagram (Saunders & Miodownik, 1990).

Ag_3Sn + Sn. Miller et al. (1994) found a different result, indicating that the invariant reaction must be a class I reaction L= η-Cu_6Sn_5 + ε-Ag_3Sn + Sn at 216.8°C. Figure 2.3(b) depicts the Sn-Ag-Cu liquidus projection. In the Sn-rich corner, the invariant reaction is a class I reaction according to more recent phase equilibria studies (Moon et al., 2000; Ohnuma et al., 2000; Yen & Chen, 2004).

The eutectic composition was reported to be Sn-3.5wt.% Ag-0.9wt.% Cu by Loomans and Fine (2000). Moon et al. (2000) measured the temperature and liquid composition of the ternary eutectic to be Sn-3.5wt.% Ag-0.9wt.% Cu and 217.2°C respectively and calculated Sn-3.66wt.% Ag-0.91wt.% Cu and 216.3°C. According to Ohnuma et al. (2000) the ternary eutectic is Sn-3.24wt.% Ag-0.57wt.% Cu and 217.7°C.

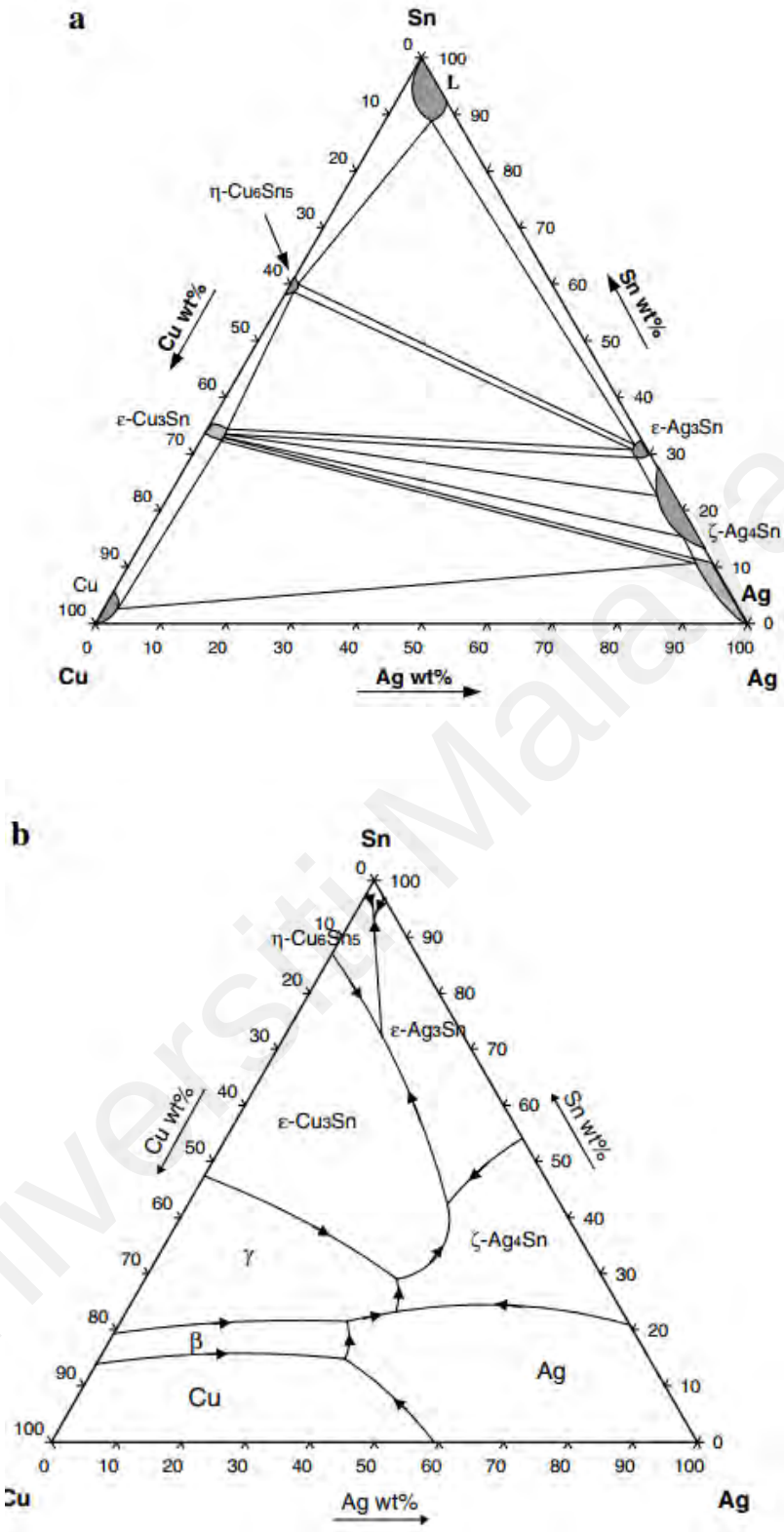

Figure 2.3: (a) The Sn-Ag-Cu ternary system isothermal section at 240 °C; (b) Liquidus projection of the ternary system Sn-Ag-Cu (Yen & Chen, 2004).

Pb-free solders for electronic applications are made from Sn-rich compounds with melting temperatures of 40 °C or more than eutectic Pb-Sn alloys at 183 °C. They include eutectic Sn-3.5Ag alloys with Bi, Cu, Sb, In, or Zn as alloying elements. There have also been proposals for alloys based on the Sn-Cu, Sn-In, Sn-Sb, Sn-Bi, and Sn-Zn systems. A tiny two-phase zone with difference in temperature between liquidus and solidus prevents the joint from moving and being disrupted while solidification. Simpler alloys, such as binary or ternary near-eutectic alloys, are also preferred because they limit the risk of compositional differences affecting solder joint performance.

As for the thermal behavior, Figure 2.4 shows a graph of possible solder alloy melting temperatures. Based on the requirements listed above, the Pb-free solder alloys Sn-0.7Cu, Sn-3.5Ag, and SAC387 are the most prospective, with the greatest level of acceptability in the electronics sector. Pb-free alloys vary from eutectic Sn-Pb in soldering quality, intermetallic formation, and mechanical behavior. These discrepancies Pb to multiple critical obstacles that should be overcome for Pb-free solders to be effectively used in consumer electronics (Glazer, 1994). The Pb-free solder melting temperature is higher than the eutectic Sn-Pb 183°C, and the packages should reach the melting temperature requiring at least 20°C higher to reflow. The reflow temperature for Sn-Pb is generally 220°C. The reflow temperature for Pb-free solders is normally between 240°C and 260°C. Pb-free reflow requires a higher temperature since the solders do not wet as well performance as Sn-Pb, and the higher temperature is utilized to compensate. This increased reflow temperature might have a significant influence on commercial devices (Frear, 2001).

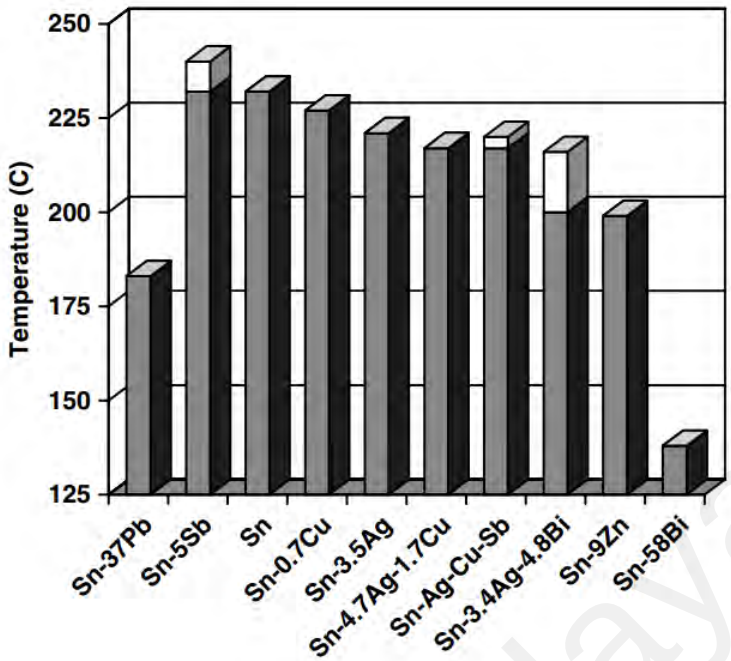

Figure 2.4: Chart of Pb-free solder temperatures (dark represents solidus, light represents liquidus) (Frear, 2001).

Manufacturers have been pursuing a new generation of Pb-free solders to replace Sb-Pb solders. Tin-silver (Sn-Ag) and SAC alloys have been identified as promising replacements for standard 63Sn-37Pb eutectic solder (Ganesan, 2006). SAC solders consist of SAC305 in Japan, SAC387 in the EU, and SAC 396 in the USA (Ma et al., 2006). The main benefits of the various SAC alloy systems are their relatively low melting temperatures in compare with the 96.5Sn-3.5Ag binary eutectic alloy, as well as their superior mechanical and solderability properties in contrast to other Pb-free solders (Karl et al., 2004). However, reliability of Pb-free solders, used in harsh conditions such as under high temperature in automotive, is still a serious concern (Karl et al., 2004; Tao et al., 2016). There are many challenges existing in both process and reliability of application in service.

2.4 Lead-free solder challenges in electronic packaging

2.4.1 Lead-free solder process challenges

The higher reflow temperatures of Pb-free solders normally exacerbate the reliability issue during soldering process. A scanning acoustic microscope image with light areas indicates delamination in a module package as shown in Figure 2.5. Since the materials designed under the lower temperature reflow conditions were optimized for Sn-Pb solders, there was not much problem found in soldering process for Sn-Pb eutectic applications. However, challenges have arisen due to the increased reflow temperature of 20-40 °C higher for Pb-free solder. Reflowing at a higher temperature would cause reliability issue due to thermal stress and thermal mismatch occurred. The issue must be solved by improving the strength of the components in the packages and lowering the thermal mismatches of different materials (Subramanian & Frear, 2007).

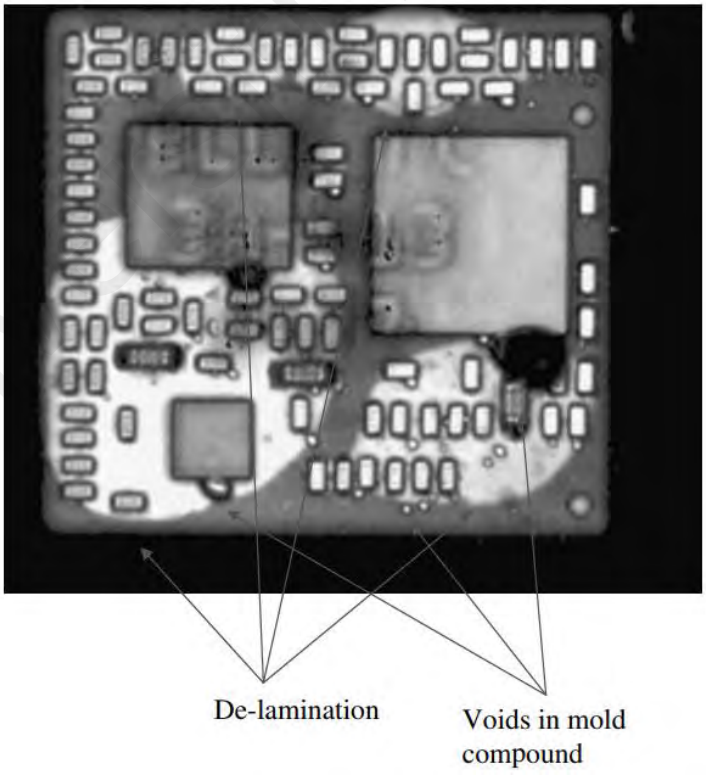

Figure 2.5: Scanning Acoustic image of a molecule package showing evidence of delamination caused by water uptake then reflow (Subramanian & Frear, 2007).

Mechanical properties are deteriorated by the solid-state processes that turn solder-wettable coatings into intermetallic compounds (IMCs). Complex crystal structures with limited crystallographic planes to accommodate stress make interfacial intermetallic brittle, particularly when the strain is in tensile mode. There would be fracture of IMCs within brittle structure when strain is increased. Pb-free solders with high Sn concentration increase the possibility of intermetallic growth. It is considered as a serious challenge during soldering process which has effect on the reliability issue of commercial electronic packages (Jiang et al., 2019).

For Pb-free solders, interfacial IMCs are formed when molten solders contact nickel (Ni) or copper substrate, and gradually form rod-like or scallop shape structures in the solder while it is solid. They would continue to expand as the solder cools down and hardens. There were differences in morphology and reaction kinetics among Pb-free alloys although Sn was present in all the investigated solders.

IMCs play an important role in solder reliability and mechanical behavior. The underlying metallization may be consumed by IMCs if they become too thick, which may lead to fall off finally. Moreover, further IMC growth can be a problem as fracture paths in joints under shock or cyclic loading condition (Mattila et al., 2006).

As compared to Pb-free solder, when Sn-37Pb alloy is used, Cu_6Sn_5 and Cu_3Sn formed in a two-phase intermetallic on Cu substrate. One side is close to the solder and the other to the substrate. The Cu_3Sn has a planar shape within columnar grain structure, while the Cu_6Sn_5 has nodule shape and are elongated. Eutectic Sn-Pb forms Ni_3Sn_4 with an uneven shape on Ni substrate. These IMCs between Cu, Ni, and eutectic Sn-Pb solder have been reported, and they do not cause a serious solder spall due to the parabolic growth kinetics mechanism (W. Boettinger et al., 1993; Frear & Vianco, 1994).

Figure 2.6 shows the intermetallic formation of Pb-free solder on Ni substrate in scanning electron microscope (SEM). The interface structure on electroless Ni-P, but the same observation is made for electrolytic Ni under bump metallization (UBM). The IMC formed is Ni_3Sn_4, and this IMC between Sn-0.7Cu and Ni is thin and regular which is the most uniform among Pb-free alloys. Sn-3.5Ag solder on Ni has a different intermetallic morphology that consists of nodules and chunks scattered into the solder. This morphology is attributed to the lack of Cu in the solder. It is speculated that the role of Cu is to saturate the solder with respect to Ni and to inhibit the dissolution and exfoliation of intermetallic compounds in the solder (Kim et al., 1996). Interfacial intermetallic growth is a concern when Pb-free solder is in the solid state.

IMC can consume the solderable metallization and cause the decrease of wettability of joint at layers below the UBM if the IMC layer thickens fast. In addition, since IMC is brittle, it becomes a vulnerable part of the solder joint and can become a site for crack initiation and propagation when the solder joint is deformed. These observations proved that the IMC growth is always a challenge to be controlled in Pb-free solder application in soldering process (Lee et al., 2014).

Figure 2.7 shows the Ni layer consumed by the formation of Ni_3Sn_4 IMC during solid-state aging for different Pb-free solder alloy when aged at 150 ℃ and 170 ℃ for 1000 hours. Lesser than 2 μm was converted to Ni_3Sn_4 on electroless Ni-P/Au in UBM. Ni is often preferred as the metallization layer for Sn-rich solders since it reacts slowly with Sn-based solders. Pb-free solders consume more Ni and form more IMCs than Sn-Pb series solders (Dariavach et al., 2006; Subramanian, 2007).

The interaction between SAC solder and a Ni substrate during soldering is a complex process that results in the formation of IMCs. The types of IMCs formed at the interface are critical for the mechanical integrity and reliability of the solder joint (Yang et al.,

2016). The reaction products, primarily Ni_3Sn_4 or Cu_6Sn_5, depend significantly on the Cu concentration in the solder, among other factors (Zeng et al., 2010).

First, the Ni and Sn Reaction happens when SAC solder is used on a Ni substrate, the Sn component in the solder reacts with Ni to form the IMC Ni_3Sn_4. This reaction is a direct result of the affinity between Sn and Ni and occurs relatively early during the soldering process (Yoon et al., 2004). However, the concentration of Cu plays an important role. At lower Cu concentrations in the SAC solder, the formation of Ni_3Sn_4 is favored because there is less Cu available to react with Sn. Consequently, Sn is more likely to react with Ni from the substrate, promoting the formation of Ni_3Sn_4 (Hammad, 2013; Satyanarayan & Prabhu, 2013).

However, Cu_6Sn_5 is another IMC that forms when the Cu in the SAC solder reacts with Sn. This compound is commonly seen in solder joints and is crucial for the integrity of bond. As the Cu concentration in the SAC solder increases, the likelihood of Cu_6Sn_5 formation increases (Coyle et al., 2014; Xiong & Zhang, 2019). This is because higher levels of Cu in the solder provide more opportunities for Cu to react with Sn, forming Cu_6Sn_5 instead of allowing Sn to react with the Ni substrate. Higher concentrations of Cu in the solder can suppress the formation of Ni_3Sn_4 by consuming the Sn available for reaction with Ni. This shifts the balance towards the formation of Cu_6Sn_5 (Aisha et al., 2011; Yen et al., 2010).

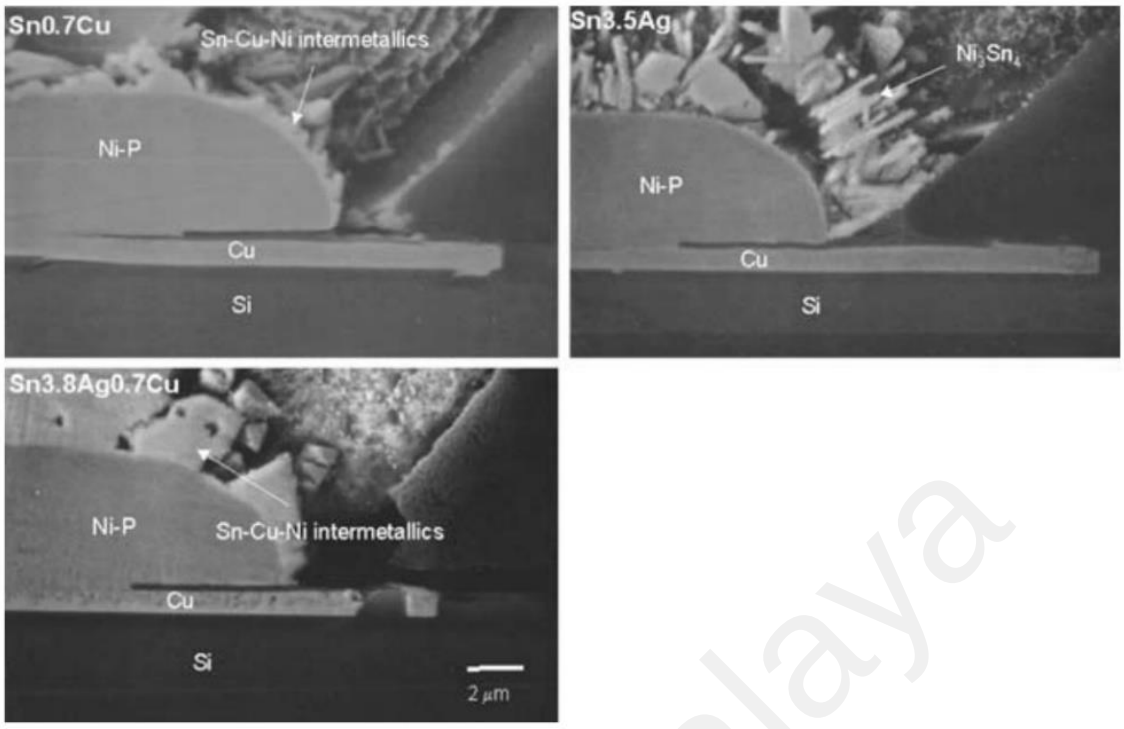

Figure 2.6: SEM micrographs of the Pb-free solders on an electroless Ni UBM showing the morphology of the interfacial intermetallic (Mattila et al., 2006).

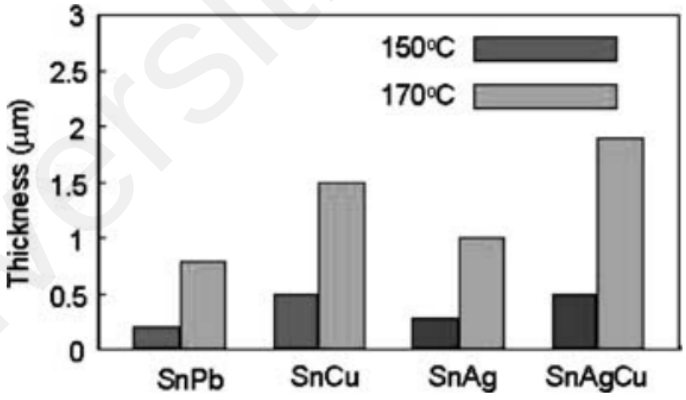

Figure 2.7: Thickness of consumed Cu for the solders on electroless Ni–P/Au UBM after 1000 h aging at 150 °C and 170 °C (Subramanian, 2007).

Figure 2.8 shows the SEM image of the Pb-free solder on Cu substrate. The IMC formed is Cu_6Sn_5, but Cu_3Sn was not found. However, it might be too thin to be observed. The interfacial IMCs of all Pb-free alloys have the same morphology as the Sn-Pb eutectic. The IMC consists of regularly distributed Cu_6Sn_5 particles. Both silver-containing solders

have a large amount of Ag_3Sn IMC attached to the Cu_6Sn_5 interface. All three Pb-free alloys contain discrete small particles of Cu_6Sn_5 in most solders.

For Sn-0.7Cu, Cu is present in the solder before attaching to the UBM. For Sn-3.5Ag solder, Cu_6Sn_5 is present due to some UBM dissolved into the solder. No spalling behavior of IMC was observed in the molten solder, which is believed to be due to the presence of Cu in each solder during reflow. Cu inhibits the growth and spalling behavior of IMC since it saturates the solder (Frear, 1988). Among the three Pb-free alloys on Cu, the Sn-0.7Cu solder structure is the most uniform and the IMC structure is the thinnest (Subramanian, 2007).

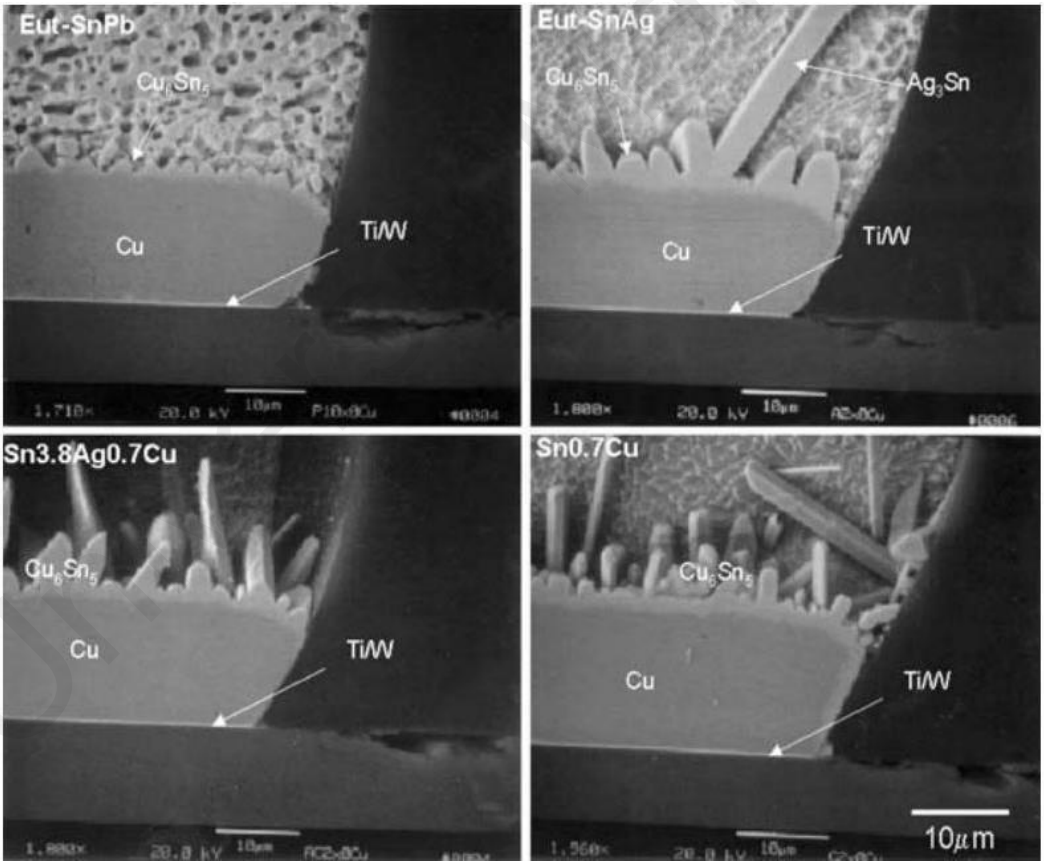

Figure 2.8: SEM micrographs of the Pb-free solders on Cu UBM (Subramanian, 2007).

However, using Sn-rich Pb-free solders leads copper to react with the solder faster, and makes the UBM dissolve during reflow. Figure 2.9 shows the Cu consumption value for Sn-Pb and Pb-free solders after 2 times reflows. Pb-free solder consumes 10-20% more Cu than Sn-Pb after reflow process. Pb appears to play a role in enhancing IMC growth, possibly by enhancing the diffusion of Sn to the interface in between intermetallic and solder. All these observations reported in literature show the process challenge of Pb-free solder in real application of electronic industry (Frear et al., 2001).

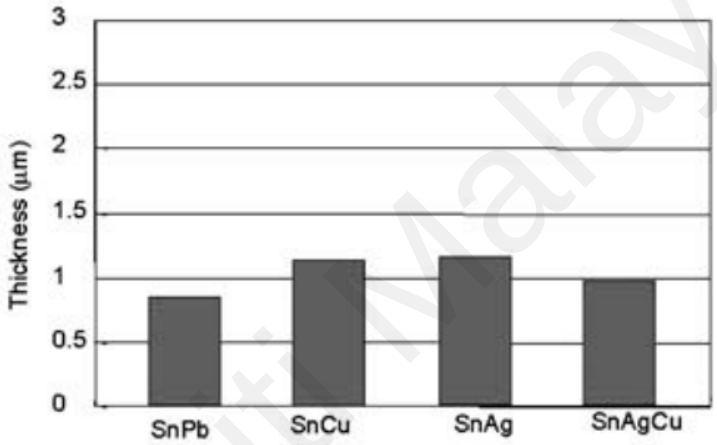

Figure 2.9: Consumed Cu thickness after 2 reflows for the solders on a Cu UBM (Frear et al., 2001).

2.4.2 Lead-free solder reliability challenges

The reliability of commercial electronic systems includes everything that can happen after the package is manufactured. There are many effects that drive package degradation, such as temperature, thermal cycling, humidity, and electrochemical migration (ECM). These environmental conditions are usually applied externally and cannot be controlled in electronic applications for either cost or manufacturing limitations (Li & Wong, 2006; Pecht et al., 2016). The following sections are issues related to thermal cycling and ECM that can affect the reliability of consumer products.

2.4.2.1 Thermal Cycling

The solder junction is a mechanical connector that must be strong enough to keep the connected components in accurate places, but also flexible enough so that the applied strain is not transferred to the attached components. The solder joint is a mechanical interconnect that must have sufficient strength to hold connected components in fixed locations. Furthermore, it must also be deformed sufficiently so that the applied strains are not transferred to connected components.

In commercial applications, there are many different types of packages, such as quad flat package (QFP), quad flat no-leads package (QFN) and plastic leaded chip carrier (PLCC) which have been used for decades. In these surface mount assemblies, a lot of work focused on the evaluation of their reliability (Vandevelde et al., 2004). Due to differences in coefficient of thermal expansion (CTE) between the assembly materials and solder joint, stresses and strains are generated from thermal mismatch (Zhang et al., 2014; Vasudevan, 2008). During service, thermal loading generated inside of package will expand the leads in the package so that stress analysis is imperative to be studied to evaluate the reliability of the product (Erinc et al., 2008; Shah, 1990). A more challenging thermal issue is the thermal cyclic stress in components of packages during its operational life.

When chips are running hotter, the difference in temperature (ΔT) increases between itself and the leads as well as a solder material. Plastic deformation or fatigue failure in leads and solder joint frequently occur despite several new designs attempting to avoid it (Lau et al., 1990a; Lau, et al., 1990b; Enke et al., 1989). Leads connect die and solder joint. Heat generated from die would transfer to the solder joint. As package size shrinks, thermal stress on leads would be increased since the distance between die and solder joint

becomes smaller. This reduced the heat transfer process and made the thermal mismatch more serious.

Hence, the optimization for the geometry of lead design is required (Vaynman, 1989; Frear 1989). Recently, many semiconductor companies have made innovative designs of electronic packages to increase the I/O number with miniature size. Solder joints are the electrical and mechanical connections of the package and are soldered to the surface of a printed circuit board (PCB). Thus, displacement and stress distribution play important roles in the lead frames during service. Thus, reliability tests are necessary to assess the performance of solders subjected to thermal stress (Hall, 1987). When the local stress exceeds the yield strength (YS), plastic deformation occurs.

Furthermore, there would be an undesirable consequence for the whole system when the stress in any part of the lead reaches its critical value. For instance, the stress in the critical locations on the solder must be evaluated to avoid any potential hazardous deformation or fracture. In previous works, Pang & Chong (2000) used the simulation method to evaluate flip-chip reliability. Michaelides and Sitaraman (1998) and Pang et al. (1998) found out stress status of different packages with underfill epoxy at 140 ◦C.

Lau et al. (1987 & 1988) and Lau (1990) studied thermal stresses and strains of PLCC subjected to thermal cyclic loading by using the finite-element method (FEM) and experimental analysis. They pointed out that the analysis of relevant research would be expected for the smaller packages. Meanwhile, Lau et al. (1988, 1989, 1990a and 1990b) also did parametric study on thermal stress and reliability of QFP by using FEM, and comparisons were made with PLCC. Emphasis was placed on the effects of solder joint geometry on the package. However, seldom works have been done to find out the optimal geometry design of leads of QFP or PLCC, and stress analysis for it by using parametric

study was found even few in recent works (Zienkiewicz & Morice, 1977; Lau, 1987; Lau, 1973).

In summary, solder joint strength and creep behavior are directly related to fatigue performance in temperature cycling test. Pb-free solder with higher strength, more compliance, and faster steady-state creep rate has a longer fatigue life. Eutectic Sn-Pb has the lower shear strength as compared to Pb-free solder but has a shorter thermal fatigue life due to inhomogeneous coarsening. Pb-free alloy undergoes substantial deformation during thermal cycling, and this deformation protects the semiconductor device from damage due to the applied strain. Interestingly, even with significant surface deformation, the crack formation time of Pb-free solder was longer than other solders without surface deformation. It accommodates thermal strain through grain boundary sliding and rotation. Self-diffusion of Sn to accommodate sliding and rotation is sufficient to retard crack formation. Another positive aspect of the Pb-free solder is that failures were only observed in solder joints away from the brittle interface between IMC and solder.

2.4.2.2 Solder creep performance during QFP development

The development of QFP and the creep performance of solder alloys applied to them during service, particularly with novel designs, involves a series of advancements in packaging technology and materials science (Tummala, 2001). The QFP is a type of integrated circuit package designed for surface mounting on PCBs. The development of QFP began in the early 1980s as a response to the growing need for more compact electronic components with a higher density of interconnections. The design allowed for a large number of leads or pins to be spaced closely around the four edges of a square or rectangular package (Lau & Pao, 1997; Depiver et al., 2021).

Over the years, the QFP has evolved to accommodate the increasing complexity of electronic devices (Jiang et al., 2019). This evolution included the development of finer

lead pitches of which the distance between adjacent leads has been reduced many times. This is the way to increase the lead count without significantly increasing the package size (KS et al., 2004; Shangguan, 2005). The introduction of thin QFPs (TQFP) and low-profile quad flat packages (LQFP) are examples of such advancements, aimed at reducing the package thickness and footprint (Cheng et al., 2017).

The manufacturing process of QFPs has also seen improvements, including the use of better materials for the package body, such as advanced plastics and ceramics, to enhance thermal performance and mechanical strength. The lead frames have been made from high-conductivity alloys for improved electrical performance. The solder alloy used for attaching QFPs to PCBs plays a crucial role in the reliability of electronic assemblies. Traditional Sn-Pb solders have been largely replaced by Pb-free alternatives due to environmental and health concerns. Common Pb-free solder alloys include SAC solder and Sn-Cu solder, etc (Noble, 2013).

Creep, the time-dependent deformation under constant stress, is a critical factor affecting the long-term reliability of solder joints, especially in high-temperature operating conditions. The miniaturization of packages and the increase in power density have raised the operational temperatures, making creep performance a key concern. To address these challenges, novel solder alloys and composite solders have been developed with improved creep resistance. These include adding elements like bismuth (Bi), antimony (Sb), and Ni to modify the microstructure and strengthen the solder matrix. Additionally, the development of IMCs within the solder can enhance its creep resistance but must be carefully controlled to avoid brittleness (Suganuma, 2003).

Novel QFP designs, including those with heat sinks or enhanced lead frame materials, aim to distribute thermal and mechanical stress more evenly, reducing the creep strain on solder joints. The layout of leads and the use of underfill materials can also help mitigate

the effects of creep by providing additional mechanical support to the solder joints (Plumbridge et al., 2007).

In summary, the development of QFPs with novel designs and the improvement of solder alloy creep performance during service involve a multifaceted approach. It includes advancements in package design, materials science, and assembly techniques to meet the demands of modern electronic devices for reliability and performance under increasingly challenging conditions.

2.4.2.3 Electrochemical migration

ECM is the dissolution and movement of metal ions in the presence of an electric potential, resulting in the growth of a dendritic structure between the anode and cathode. This process is most observed in solders on printed circuit boards, where it can significantly reduce the insulation between conductors (Minzari, 2010). The main factor that promotes ECM is material, distance between the conductors, bias voltage, contamination and underfill process under water drop (WD), temperature and humidity bias (THB) (Nor & Jung, 2008). The growth of the dendrites in ECM takes only a fraction of a second, and the resistance between the anode and cathode drops to almost zero (Zhou et al., 2013).

Tin solder material, as a main factor that affects ECM in electronic packages, was initially created as a recommendation to replace Pb solders for the electronics industry, and gradually became a widespread use in electronic packages such as QFP and PLCC. However, one of the main issues of shifting the Pb solder to Pb-free solder is the formation of tin whiskers or dendrites. The tin whiskers or dendrites can cause short circuits when a bridge is formed between the leads of the package and this will cause failure of the electronic devices and eventually, to the whole system (Kadesch & Brusse, 2001). Hence,

tin whisker studies are especially directed towards the usage of Pb-free solders in electronic devices.

The mechanism of tin whisker was not widely known until recently, but a lot of research had concluded that it is formed due to the stress relief resulting from the reflow of the solder material, which is related to the existence of intermetallic compounds inside the solder matrix. The stress relief in the solder matrix pushes the surrounding Sn particles out from the matrix and tin whiskers form as the result of the process (Chuang, 2006). Tin whiskers in electronic components can be formed with different shapes.

Some of the commonly observed whiskers, as proposed by Joint Electron Device Engineering Council (JEDEC) are kinked shape, branched shape, etc. Some other important investigations on tin whiskers are the whisker length and the whisker population, which are the important criteria that determine the reliability of QFPs. Whisker length of more than 10 micron is considered important for research (JESD22A121, J. S., 2005).

One of the factors that affects the length of the whiskers formed is the grain size of the Sn material, Chen et al. discovered that Sn films with smaller grain sizes formed longer whiskers while larger Sn films with larger grains formed shorter whiskers (Chen et al., 2015). Whisker length was a minor issue when Pb materials were used as surface finishes and in the solder materials since there would be minimum or no whisker formation when lead is applied into the materials.

Other than tin whisker, reliability issues also arise from the formation of dendrites from the solder joint materials, which is also the result of ECM. Dendrites form in fern-like or snowflake-like patterns growing along a surface rather than outward from it. The growth mechanism for dendrites is well-understood and requires some type of moisture capable

of dissolving tin into a solution of metal ions which are then redistributed by electromigration in the presence of an electromagnetic field. Like tin whiskers, the bridging between two adjacent leads or solders can cause short circuit. However, the mechanism of ECM is different from that of tin whisker formation. ECM occurs due to the migration of ionic particles, mainly metal ions between cathode and anode when there is a presence of moisture. The type of flux is one of the major factors in the migration behaviours of the solders. Yu et al. described that the same solder alloy composition can lead to different migration behaviours due to different types of fluxes used, this is because fluxes affect the wettability of the solder (Yu et al., 2006).

Other factors that enhance electrochemical migration are the solubility of the ion, the mobility of the ion, the effect of pH on solubility, the reactivity of the ion, temperature, and relative humidity (Shangguan, 2005). As for the distance between the conductors, Pb-free solder applied in minimized electronic package is also critical to be studied. Since electronics package use has steadily increased, the package as key component has been designed more delicate. QFP is a surface mount integrated circuit package with "gull wing" leads extending from each of the four sides (Greig, 2007). Versions ranging from 32 to 304 pins with a pitch ranging from 0.4 to 1.0 mm are common. QFP was manufactured in the beginning with the size of 1.27 mm and within decades, advancements had been undergoing which led to a reduced size at 0.4 mm within a few decades (Tummala & Rymaszewski, 1997). Besides, a PLCC which is similar with QFP but has pins with larger pitch, 1.27 mm, curved up underneath a thicker body to simplify socketing or soldering. It is commonly used for NOR flash memories and other programmable components (Cohn & Harper, 2004). In this advancement, smaller lead pitch is difficult to be achieved due to the factors related to lead co-planarity, solder bridging, tin whisker formation, etc. Attempts had been made before in the literature to shrink the fine pitch in electronic packages down to 0.25 mm (Totani et al., 1995).

Nevertheless, up until now, based on our knowledge, none of these smaller pitch sizes have been implemented in the industry and the smallest pitch size that is currently used in the industry for QFP is 0.4 mm. A fine pitch package means high numbers of interconnections accommodated around the device to satisfy the growing complexity of many integrated circuits nowadays. Pan et al. has investigated that the smaller pitch and size of the package saves more solder material on the surface the mounting process (Pan et al., 2004).

As the die sizes of integrated circuits get smaller the lead tips on the lead frames need to get finer and finer in pitch to approach the ever-shrinking integrated circuit. Current size of die pads is limited by pitch size, cannot approach a smaller die pad (Chroneos et al., 1993). Thus, the finer pitch package is desirable to be designed to satisfy the need of nowadays package in electronic industry. In the meantime, reliability challenge such as solder bridging, tin whisker/dendrite formation are crucial to be addressed. Therefore, it is imperative to study the reliability of Pb-free solders applied in the minimized electronic packages.

2.5 Improvement brought by additional elements

2.5.1 Single element addition to SAC alloys

To improve the properties of these Pb-free solders, some alloying elements have been added to the Pb-free solders. The most popular choices among the alloying elements are Bi, Sb, Ni, manganese (Mn), iron (Fe), zinc (Zn), indium (In), tellurium (Te), germanium (Ge), cobalt (Co), etc. (Gao et al., 2010; Tang et al., 2017). The effects of the elements on Pb-free solders with references are listed in Table 2.1.

Table 2.1: The effects of additional element on Pb -free solders.

Element	Effects	References
Bi	Increases the wettability of the solder, reduces the melting temperature, and improves mechanical properties. However, in high concentrations, Bi can lead to brittleness and phase separation issues in certain alloys.	(Wang et al., 2019; Erer et al., 2018; Sayyadi & Naffakh-Moosavy, 2019; Zhang et al., 2024)
Sb	Acts as a strengthening agent and improves the mechanical strength of the solder. It helps in preventing tin pest in colder climates. However, excessive Sb makes the solder more brittle.	(Das, 2014; Sanders, 2016; Chudnovsky, 2012)
Ni	Enhances the mechanical properties of the solder and improves its wetting characteristics on copper and Ni surfaces. Ni is often used in small quantities to stabilize the microstructure of the solder and prevent the growth of intermetallic compounds.	(Tay et al., 2013; Lee & Lee, 2005; Li et al., 2014)
Mn	improves the resistance to thermal fatigue of solder and increase its strength. Mn is also known for improving the wettability of certain substrates.	(Boesenberg, 2011; Crandall, 2011)
Fe	Similar to Ni, Fe improves mechanical properties of solders and stabilizes microstructure. It helps in reducing the growth rate of intermetallic compounds at the solder-substrate interface.	(Ramli et al., 2022; Yiteng, 2014; Mohammad Hossein, 2017)

Table 2.1: Continued.

Element	Effects	References
Zn	Used in small quantities to improve corrosion resistance and prevent oxidation. Zn can also reduce the melting point of the solder alloy.	(Mohd Nazeri et al., 2019; Zhang et al., 2010; Liyana et al., 2019)
In	Lowers the melting point of the solder and improves its wettability. In-containing solders are particularly useful for low-temperature applications and for joining heat-sensitive components.	(Ahn, 2021; Fallahi et al., 2012a, 2012b)
Te	Acts as a grain refiner and can improve the creep resistance of the solder. However, Te must be used in very small amounts to avoid embrittlement.	(Sukhontapatipak & Sungkhaphaitoon, 2023; El-Daly et al., 2022; El-Daly et al., 2021)
Ge	Acts as a deoxidizer and can improve the wettability of the solder. Ge is used in very small amounts to prevent oxidation during solder reflow.	(Tan et al., 2020; Hua et al., 2010; Cheng et al., 2017)
Co	Similar to Ni and Fe, Co can enhance the mechanical strength of the solder and stabilize its microstructure. Co also helps in controlling the growth of intermetallic compounds.	(Shen et al., 2021; Ali, 2015)

Many studies have demonstrated that the behaviors of the Pb-free solders are indeed improved by adding these elements to generate new solders which are used in some demanded services. The following sections would demonstrate the improvement of performance brought by Bi, Sb and Ni as single additional element in SAC alloys.

2.5.1.1 Bismuth

The microstructure, melt properties and mechanical properties of Pb-free solder would be improved by adding Bi as reported in literature (El-Daly et al., 2015). The addition of Bi less than 2 wt.% could dissolve in the β-Sn matrix and form a solid solution strengthening mechanism. Bi addition greater than 2 wt.% resulted in Bi precipitation in the β-Sn matrix and the formation of a precipitation strengthening mechanism as shown in Figure 2.10 (Okamoto, 2010; Shen et al., 2015; Tateyama et al., 2000).

From microstructures evaluation, Figure 2.11 shows the microstructure images of three SAC solder alloys. With an average diameter of 15 μm, the β-Sn grains in the plain SAC157 alloy have a pretty number of tiny primary β-Sn grains that are distributed around each eutectic area as shown in Figure 2.11(a). The microstructure of the SAC157-1.0Bi specimen has significant difference in comparison to the SAC157 shown in Figure 2.11(b).

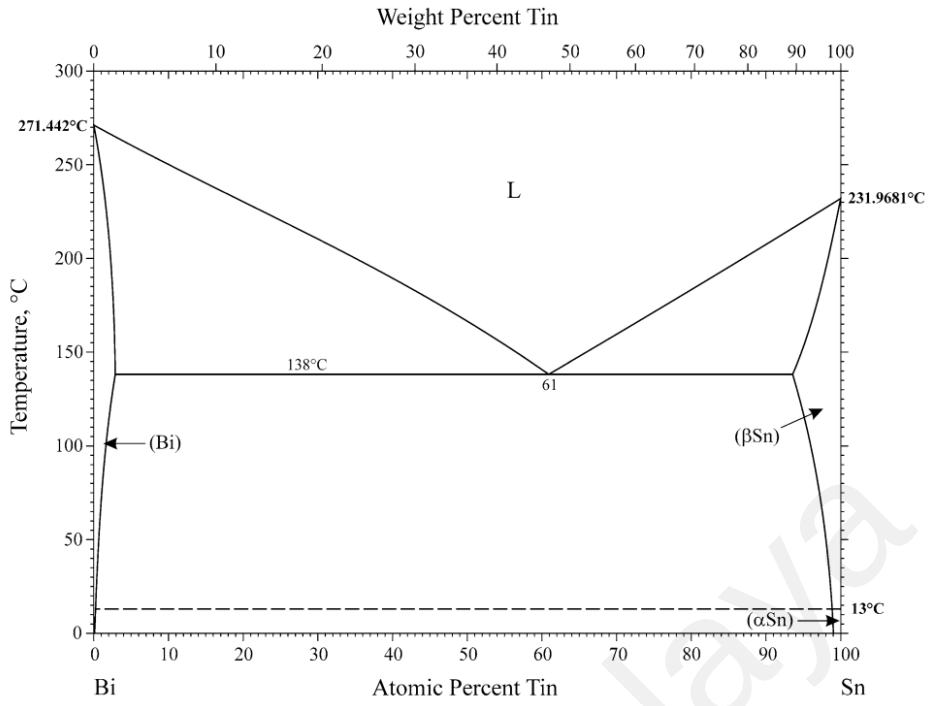

Figure 2.10: Binary phase diagram of Bi-Sn. (Okamoto, 2010).

Adding Bi to a SAC solder specimen changes the microstructure dramatically from a high number of β-Sn grain enclosed in eutectic areas to an abundance of fine needle-like Ag_3Sn and dark grey Cu_6Sn_5 particles evenly dispersed throughout the alloy matrix. 3 wt.% Bi concentration resulted in 2 μm-sized clusters of Bi particles. IMC Ag_3Sn in light grey and Cu_6Sn_5 in dark grey in mostly needle-like shape distributed in the Sn matrix evenly. There are no visible main β-Sn grains in the microstructure; instead, the alloy matrix of Sn-rich phase can be recognized. The size of Ag_3Sn and Cu_6Sn_5 particles are both in the range of between 0.5 and 5.0 μm (El-Daly et al., 2015).

SAC157-1Bi solder has no precipitated Bi particles because of the high solubility of Bi in Sn with 1.0 to 1.8 wt. % at ambient temperature (Braga et al., 2007; Witkin, 2012a). The microstructures of SAC-Bi solders have shown both solid solution strengthening and precipitation strengthening in previous findings (He et al., 2008).

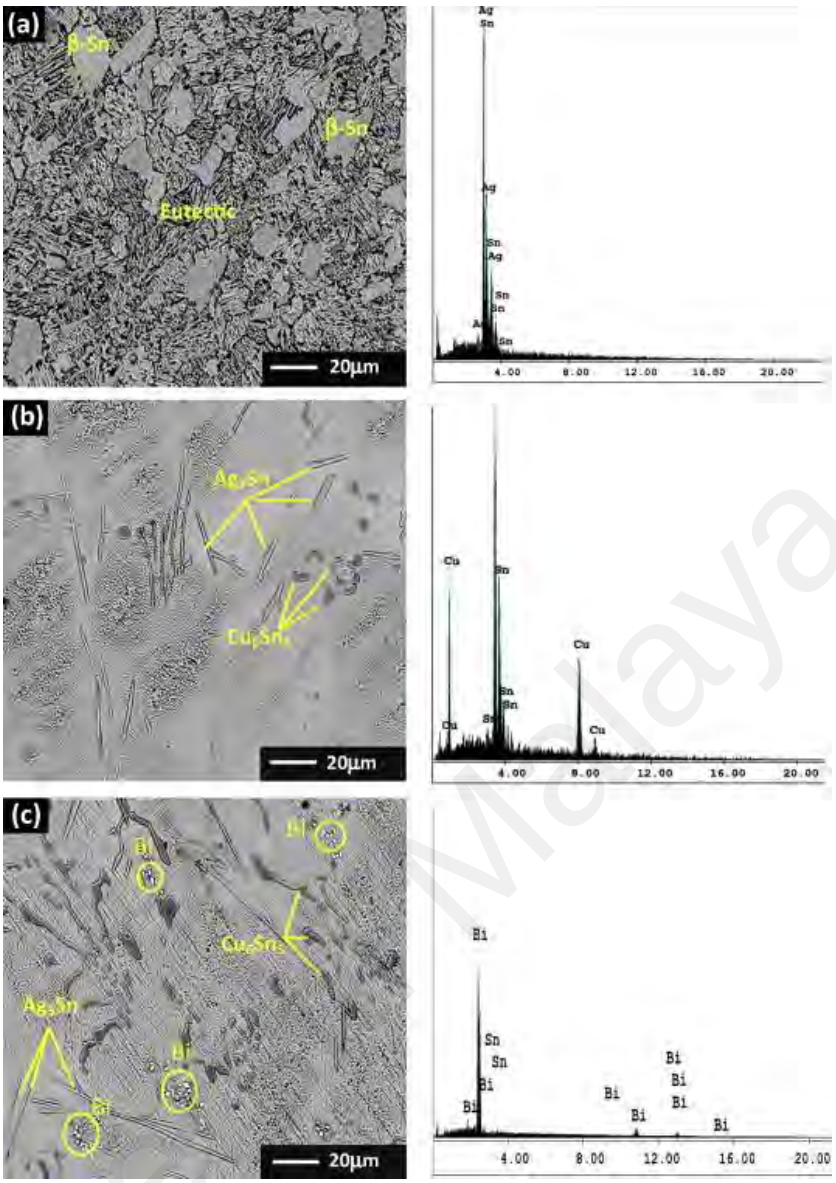

Figure 2.11: SEM microstructures of (a) SAC157, (b) SAC157-1Bi and (c) SAC157-3Bi solder alloys and corresponding EDX analysis of Cu_6Sn_5, Ag_3Sn IMCs and Bi (El-Daly et al., 2015).

However, when the weight percentage of Bi increased in SAC solder, the precipitate particles in white in Figure 2.11(c) formed clusters of smaller particles with diameters of 0.5 to 2.0 μm within 3.0 wt.% percent Bi added to SAC157 solder. The net-like microstructure of these dispersed-particles of Bi is found in the Sn matrix which is supported by the energy dispersive X-ray (EDX) data. When Bi was added at 3.0 wt.%, the Ag_3Sn and η-Cu_6Sn_5 IMC particles were also found in the alloy matrix.

Huang & Wang (2005) also discovered that Bi tended to prevent the production of massive Ag_3Sn precipitates from the solder matrix. Increasing addition of Bi resulted in finer phases of Ag_3Sn and Cu_6Sn_5 in SAC387-4Bi when compared to SAC387-2Bi. Figure 2.12(b) shows the microstructure of SAC387-2Bi solder. The IMC Ag_3Sn phase was mostly in the form of a spherical with a diameter of less than 1 µm distributed throughout the Sn matrix (Anderson et al., 2002). In comparison to SAC387-2Bi, SAC387-4Bi exhibited a finer microstructure, as illustrated in Figure 2.12(c). The Ag_3Sn and Cu_6Sn_5 phases in the IMC solder were noticeably finer than those in the SAC387-2Bi solder.

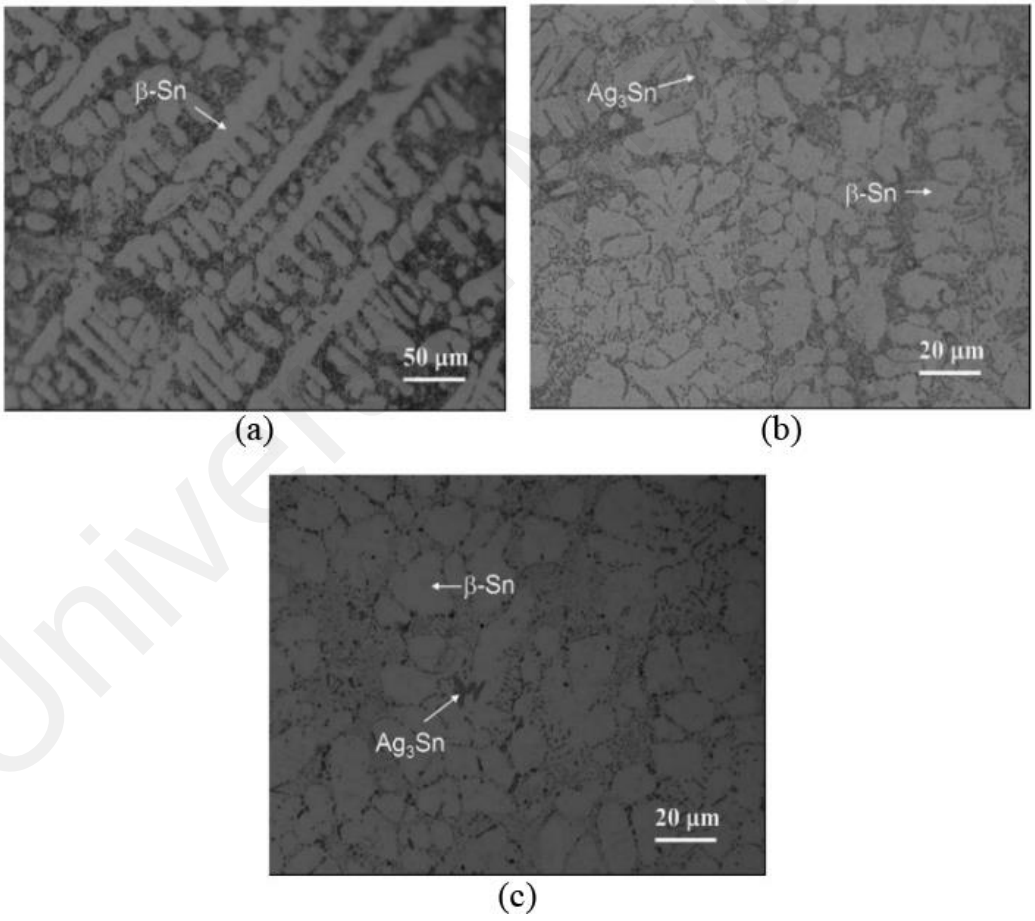

Figure 2.12: Optical micrographs of Pb-free solders: (a) SAC387, (b) SAC387-2Bi, (c) SAC387-4Bi (Huang & Wang, 2005).

The SEM micrograph of the investigated further of Pb-free solders is shown in Figure 2.13. In SAC387 solder, dendritic β-Sn and eutectic areas were typically visible. In the eutectic area, Ag_3Sn particles with a diameter of 0.5 m are finely distributed (Anderson et al., 2002). There were no Bi particles in the SAC387-2Bi solder, but there was a small amount of precipitated Bi particles in the SAC387-4Bi solder. The solid solubility limit of Bi in Sn- matrix at room temperature (RT) is estimated to be around 4 wt.%. Bi will dissolve in the Sn matrix if the Bi addition in the solder is less than 4 wt.%. Figure 2.13(b) shows that the SAC387-2Bi solder contained some large Ag_3Sn particles along with Cu_6Sn_5, whereas the SAC387-4Bi solder contained smaller Ag_3Sn and Cu_6Sn_5 precipitates in Figure 2.13(c). The addition of Bi to the Sn-Ag-Cu matrix clearly inhibited the formation of large Ag_3Sn.

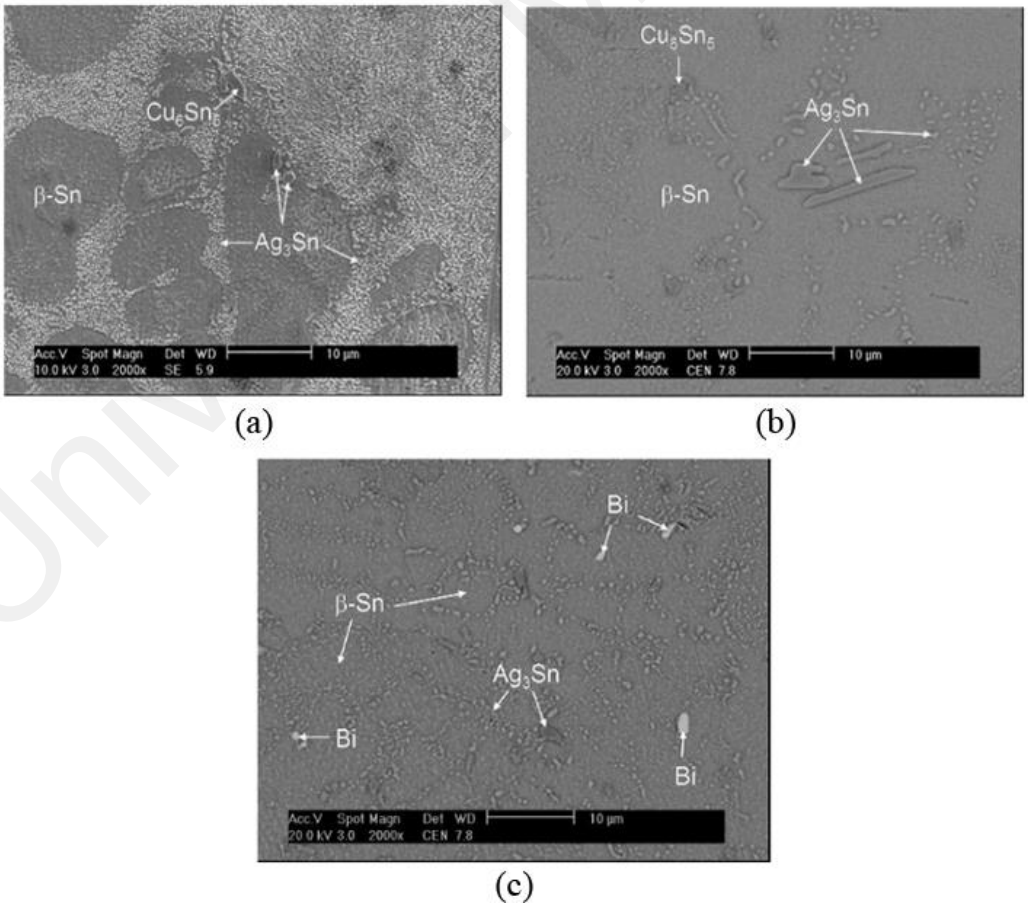

Figure 2.13: SEM micrographs of Pb-frees solders: (a) SAC387, (b) SAC387-2Bi, (c) SAC387-4Bi (Huang & Wang, 2005).

Furthermore, at the same stress level and testing temperature, Bi-containing SAC157 solders had a creep resistance 126.1 times more than SAC157 solder. The solid solution or precipitation strengthening actions of Bi led to the increased creep resistance. As a result of the addition of 3 wt.% Bi, the creep fracture time of SAC157 alloy was greatly increased by 23.7 times.

Creep curves for SAC157, SAC157-1.0Bi, and a SAC157-3.0Bi solder alloy are shown in Figure 2.14 at 25 °C and with different loading stresses. Stress and Bi addition weight percentage had significant effects on the creep strain rate and the rupture time. Increasing the Bi addition to the same stress level reduces the creep rate while increases the creep rupture time. Solid solution of Bi atoms and precipitated Bi particles are primarily responsible for SAC157-1Bi and SAC157-3Bi superior creep resistance of Pb-free alloys because of Bi precipitation strengthening effect. Bi particles have modified both the gliding of dislocations distance between these particles as well as their climbing force during creep (Chen et al., 2014).

Meanwhile, Ali et al. (2021) also reported that the addition of Bi resulted in an increase of mechanical properties such as YS and UTS. The improvement of mechanical properties was linearly proportional to the percent of Bi doped in SAC305 as shown in Figure 2.15. The UTS for SAC305was 46 MPa, but for SAC305-1Bi, SAC305-2Bi, and SAC305-3Bi, it was raised to 58.5,77.6, and 96.7 MPa respectively.

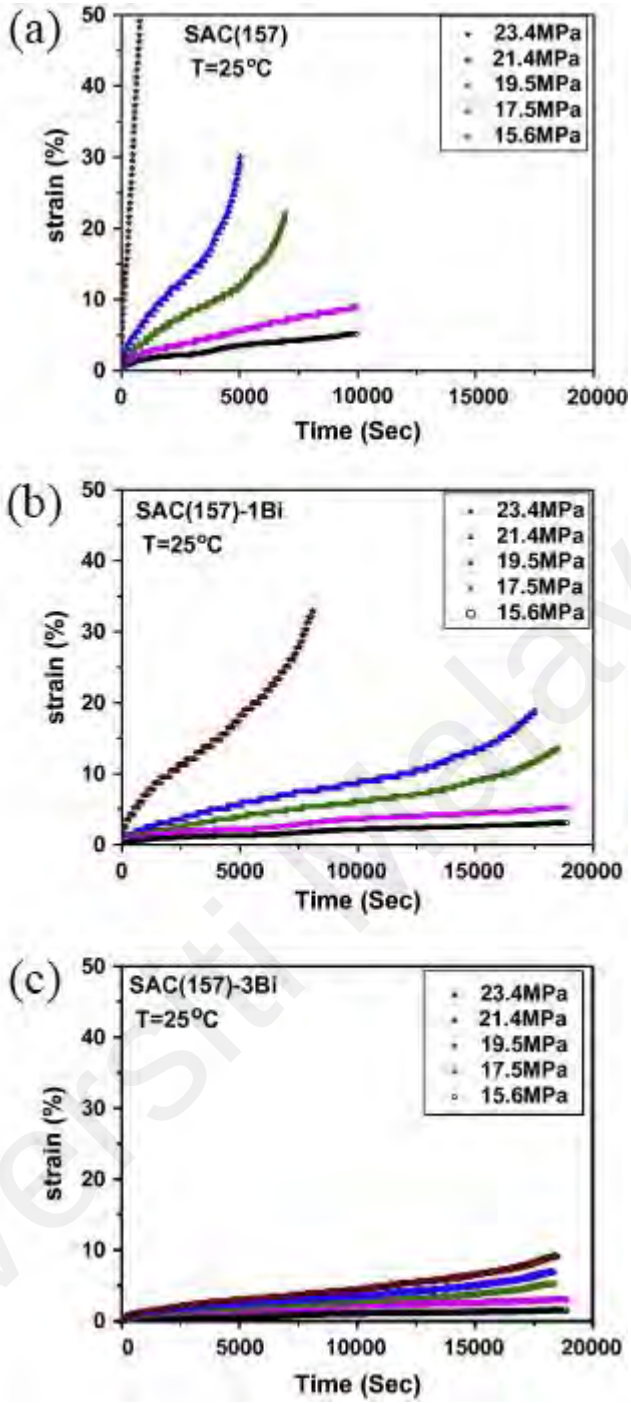

Figure 2.14: Creep curves for (a) SAC157, (b) SAC157-1Bi and (c) SAC157-3Bi under different stresses at T= 25°C (El- Daly et al., 2015).

Moreover, Sayyadi & Naffakh-Moosavy (2019) investigated the physical and mechanical properties of SAC257-xBi (x=0, 1, 2.5, 5) solder and their joint. Microstructure and mechanical properties of SAC257-Bi, x=0, 1, 2.5, 5 were studied. It was reported that the tensile strength was enhanced by adding Bi to the base solder due to a solid solution strengthening mechanism and the development of fine Bi precipitates in the matrix. However, owing to the production of coarse Bi-rich precipitates at high Bi levels of 5 wt.%, tensile strength and elongation percentage reduced. The tensile test results for SAC257 base solder and SAC257-xBi alloy solders are shown in Figure 2.16.

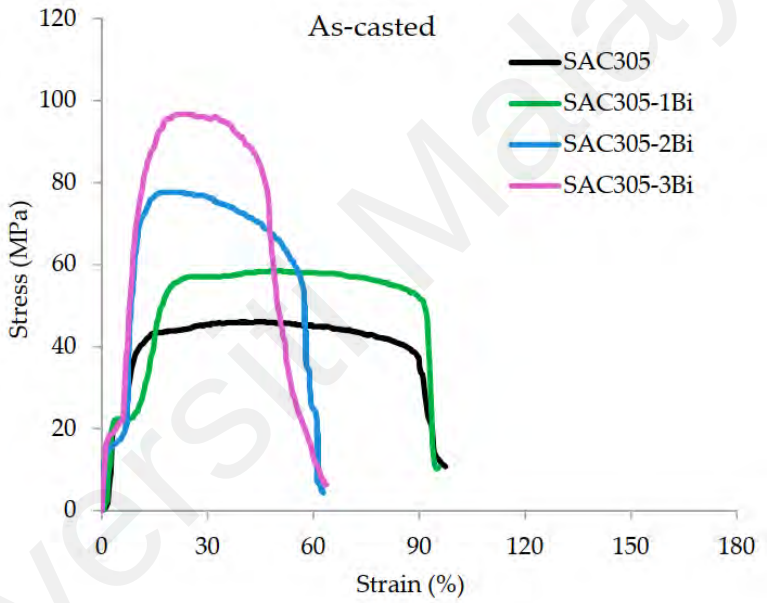

Figure 2.15: Stress-strain curves of SAC305 alloys with different weight percentage of Bi (Ali et al., 2021).

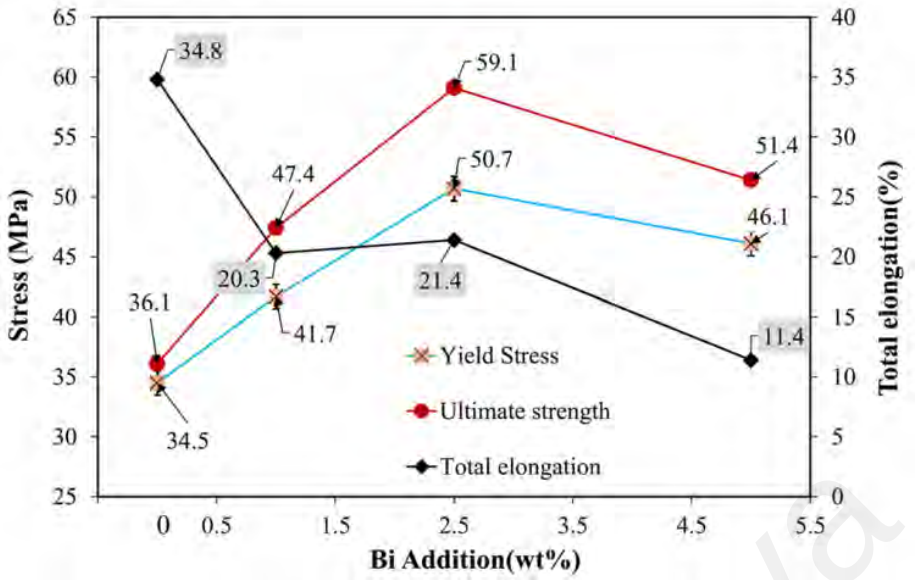

Figure 2.16: The tensile test results of the SAC257 base solder and SAC257-xBi alloy solders (Sayyadi & Naffakh-Moosavy, 2019).

As per the findings, the yield stress and tensile strength of alloy solders increased with Bi containing up to 2.5 wt.%, while the percentage of elongation decreases gradually. The yield and tensile strengths of the SAC257-5Bi alloy solder, on the other hand, are much lower, as is the percentage of elongation. Bi is naturally brittle, dissolves in little quantities in the Sn matrix (approximately 1%), and the high concentration of Bi in the Sn alloy causes massive solid-state precipitates in the matrix. As a result, the large level of Bi has a negative impact on mechanical qualities. The maximum strength and elongation of the SAC257-1Bi alloy solder junction are 30% and 38% greater than the SAC257 base solder joint respectively.

As for fractography, the rapture surfaces following a tensile-shear test are also critical to be analyzed and the findings are important to study the fracture mechanisms. When the fracture surfaces of base SAC solder and solder SAC257-Bi were compared, it was discovered that the fracture mechanism in the base solder junction shifts from IMC control with poor reliability to solder control under a ductile fracture condition in the

SAC257-1Bi connection, which is more durable (An & Qin, 2011; Bashir et al., 2016; Kim et al., 2003). The fractured surfaces of the SAC257/Cu in Figure 2.17 show that a part of the surface is ductile, with stretched dimples evident under shear stress, while the remainder is brittle which lacks dimples. Failure behavior may be justified by considering the thickness of the IMCs at the interface as well as the shear strength.

In summary, the addition of Bi less than 2 wt.% could dissolve in the β-Sn matrix and form a solid solution strengthening mechanism. Bi addition greater than 2 wt.% resulted in Bi precipitation in the β-Sn matrix and the formation of a precipitation strengthening mechanism as shown in Figure 2.10 (Okamoto, 2010; Shen et al., 2015; Tateyama et al., 2000). Both mechanisms improved the strength of the SAC solder.

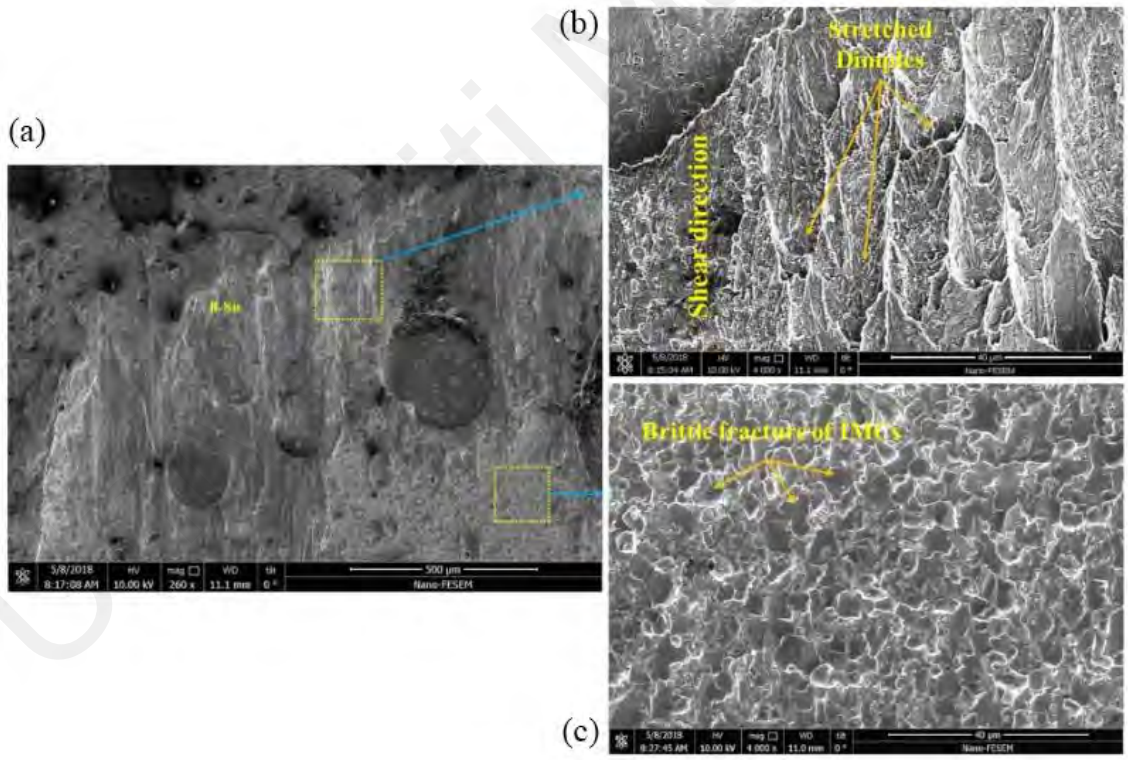

Figure 2.17: The fractured surfaces of the SAC257/Cu (Sayyadi & Naffakh-Moosavy, 2019).

The stress-strain curves of SAC305-xBi (x= 0, 1, 2, 3), Bi is inherently brittle, dissolves in lesser than 2 wt.% in the Sn matrix and the high percentage of Bi in the Sn alloy forms large precipitates in the matrix by solid state precipitation of Bi (Ali et al., 2021). To validate the explanation of mechanical performance of SAC solder added with high weight percentage (larger than 3.2 wt.%) of Bi addition, the tensile test results of the SAC257-xBi alloy solder is given in Figure 2.16 (Sayyadi & Naffakh-Moosavy, 2019). According to the results, for the alloy solders with Bi up to 2.5 wt.%, the UTS increased. However, the UTS reduced when the weight percentage of Bi increased from 2.5 wt.% to 5 wt.%. Therefore, within low percentages of Bi (lower than 5 wt.%), the strength of SAC solder can be benefited through both the formation of a solid solution with Sn matrix and formation of fine precipitates of Bi addition.

2.5.1.2 Antimony

The addition of Sb could not dissolve in the β-Sn matrix or form a solid solution strengthening mechanism. Due to the low solubility of Sb in Sn, Sb addition could form SbSn precipitation strengthening as shown in Figure 2.18(a). However, finer strengthening IMC precipitates SbSn could effectively obstruct the dislocation movement initiated in Sn matrix which led to an increase to the effective properties of the alloy and contributes to suppress the coarsening of Ag_3Sn phase (Hammad, 2018). In addition, Ag_3(Sn, Sb) particles precipitate on Cu_6Sn_5 layer after adding Sb, which generated the hardening effect and increased the strength of SAC solder as shown in Figure 2.18(b) (Borzone et al., 2021; Okamoto, 2007).

Li et al. (2006) explored the effects of Sb on the tensile properties of the Pb-free solder alloy SAC357 and its joints. Solder paste with different compositions was used in this research with the design as SAC357-xSb (x = 0, 1, 2). They also researched the effect of different temperatures and strain rates on the mechanical properties of the solder joints.

The tensile behavior of bulk solder materials is heavily influenced by temperature. Strength decreased at high temperatures. Figure 2.19 shows that for all strain rates tested, the SAC357-2Sb alloy has the maximum tensile strength at 25 °C and the SAC357-1Sb alloy has the least temperature sensitivity than the other two alloys at lower strain rates.

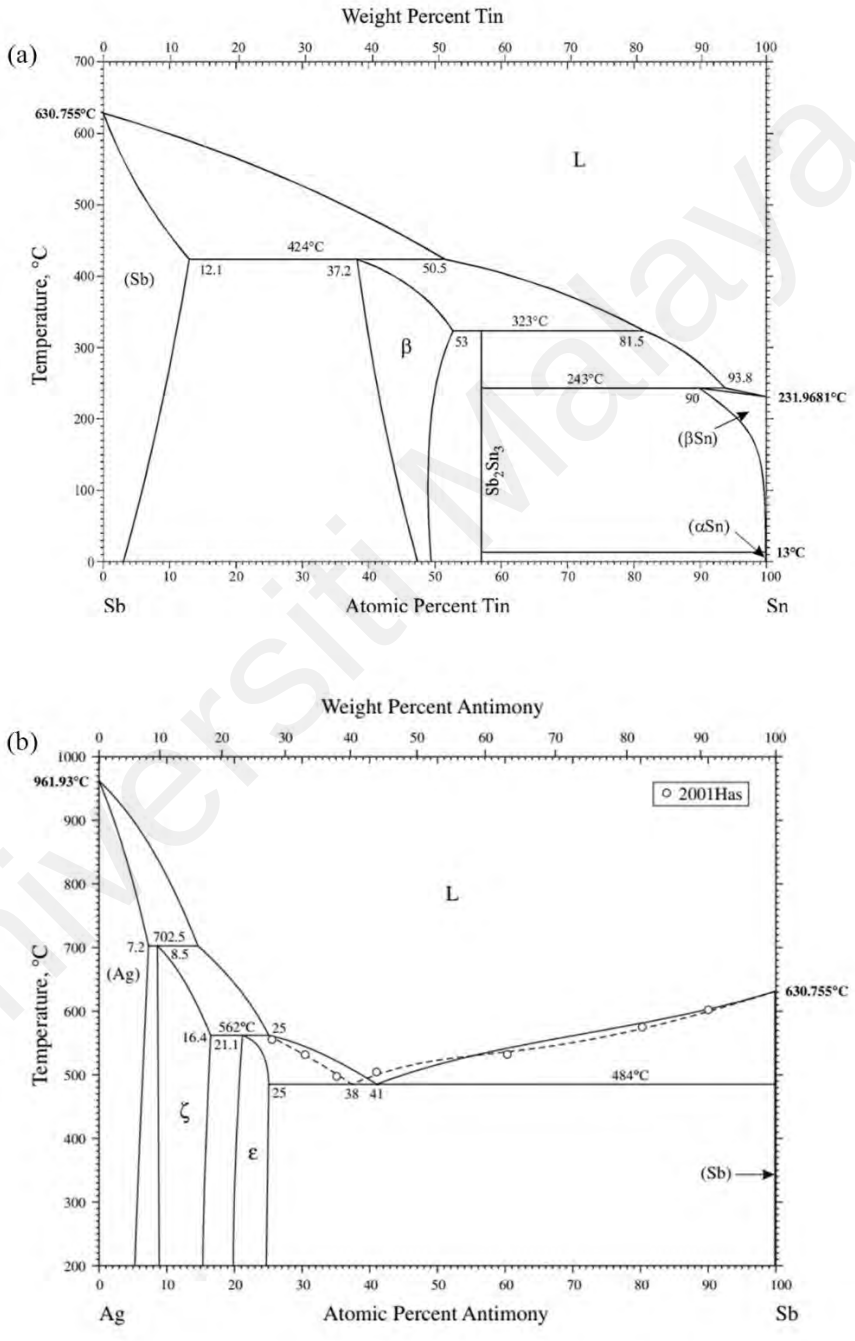

Figure 2.18: (a) Binary phase diagram of Sb-Sn (Okamoto, 2012); (b) Binary phase diagram of Ag-Sb (Okamoto, 2007).

Temperature has the least effect on the strength of the SAC357-1Sb alloy, which is reduced by roughly 20% at the lowest strain rate of 10^{-2} s^{-1} when the temperature is increased from 25 °C to 125 °C. In terms of strength, the SAC357 is the weakest. It is reasonable to conclude that the UTS lowers as temperature increases based on the experimental evidence.

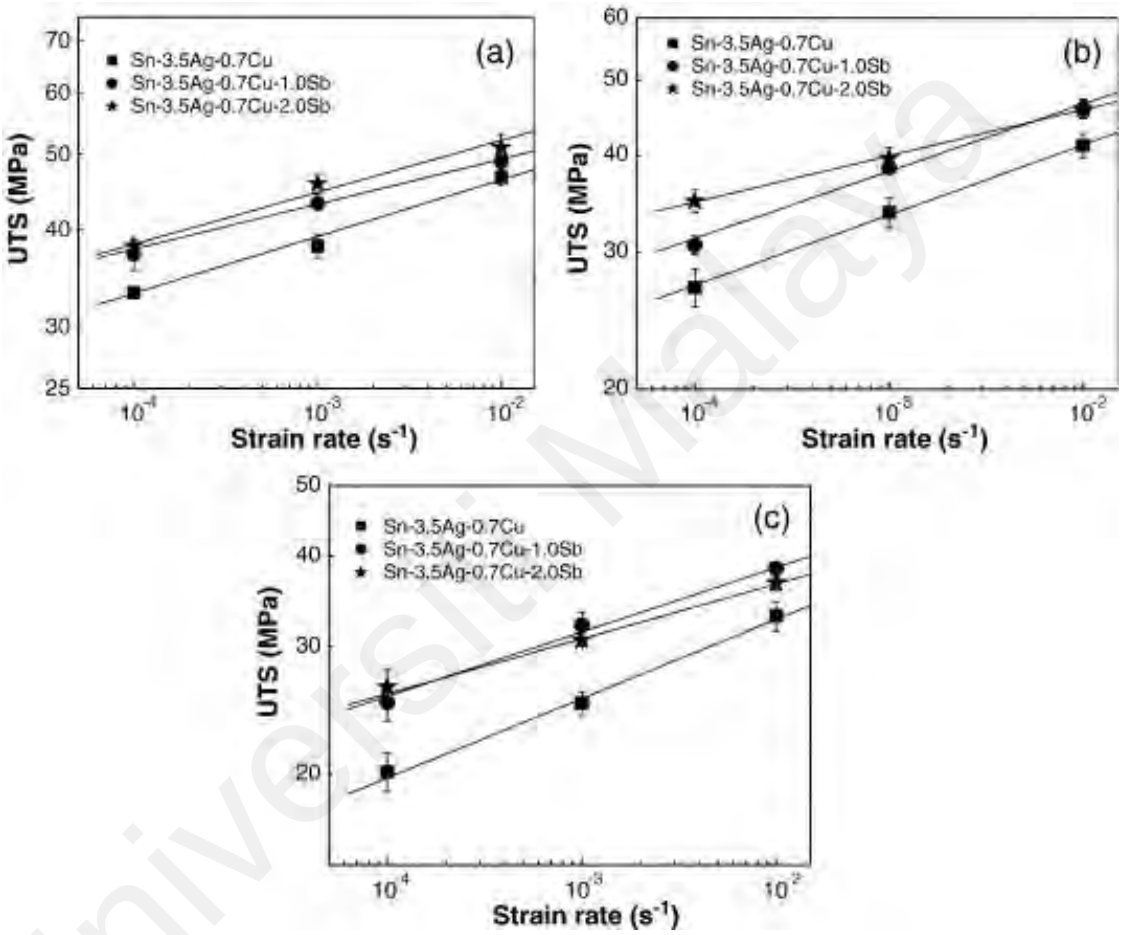

Figure 2.19: Effect of strain rate on UTS at different testing temperatures: (a) 25 °C, (b) 75 °C, and (c) 125 °C (Li et al., 2006).

Figure 2.20 summarizes the UTS and YS of both SAC305 and SAC-Sb solders. The UTS of SAC-Sb was 10 to 72 MPa, with YS ranging from 8 to 69.2 MPa under temperature 25°C to 125°C and loading rates 10^{-4} s^{-1} to 10^{-2} s^{-1}, whereas those of SAC305 were 4.54 to 75.5 MPa and 2.99 to 74.44 MPa (Chen et al., 2014). With increasing temperature, the UTS and YS of SAC305 declined linearly, whereas those of SAC-Sb decreased

logarithmically. Under the same temperatures and loading rates, the UTS and YS of SAC-Sb were often greater than that of SAC305.

When the temperature was raised from 25 °C to 125 °C, the UTS for SAC-Sb declined from 0.96 to 0.88, while the UTS for SAC305 was between 0.98 and 0.81. Adding Sb to solder increased mechanical stability at high temperatures at 125°C, but the strengthening effect is not as noticeable at RT.

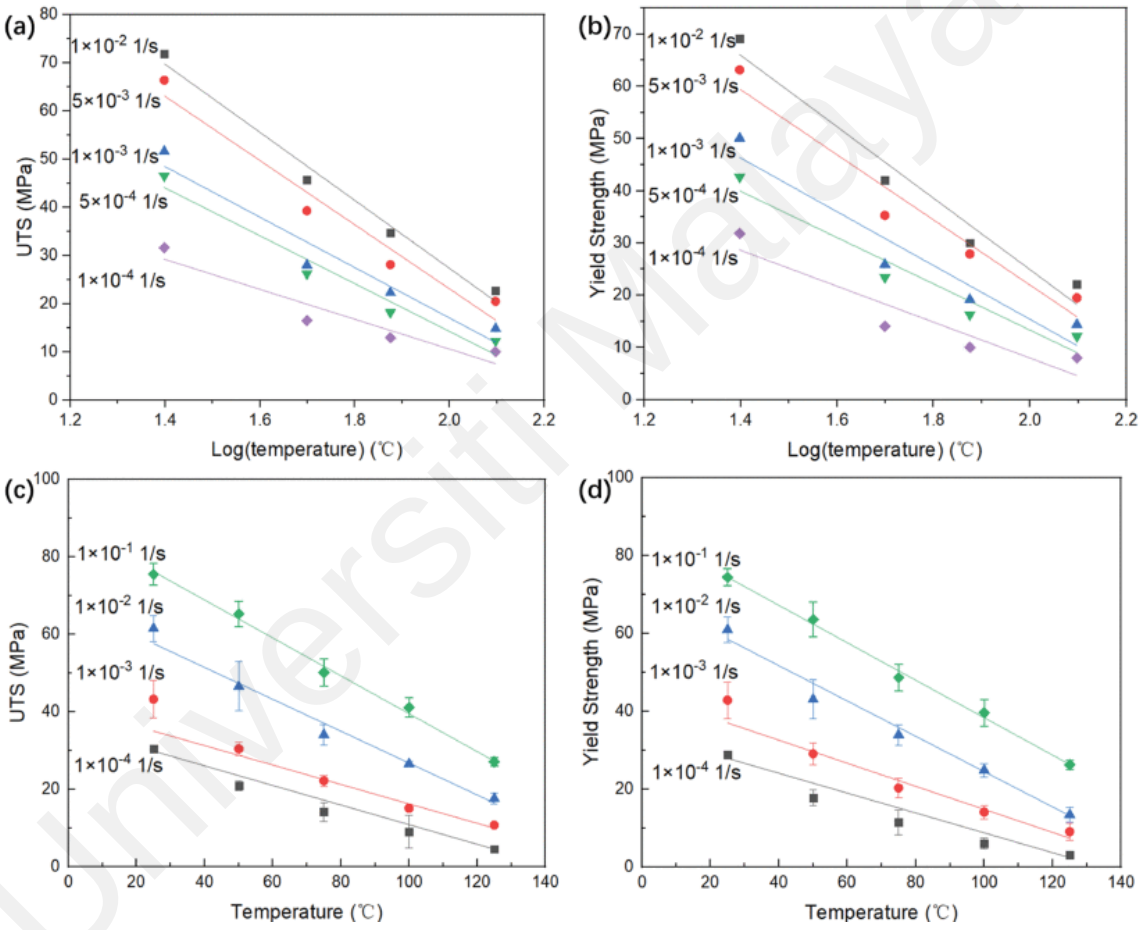

Figure 2.20: Comparison of UTS and YS between SAC305 and SAC-Sb. (a) UTS of SAC-Sb; (b) YS of SAC-Sb; (c) UTS of SAC305; (d) YS of SAC305 (Chen et al., 2021).

In fractographies of both SAC305 and SAC-Sb solders, large dimples can be seen in the samples, indicating ductile fracture (Chen et al., 2021). However, it should be noted that dimples in SAC-Sb are substantially more obvious than those in SAC305. At 25°C under strain rate 0.011 s^{-1}, the average size of dimple in SAC305 is 17 μm^2, which is much less than those in SAC-Sb of 100 μm^2 as shown in Figure 2.21.

The dimple size is related to the size of the voids at the coalescences in the fracture, and the strain required for void growth increases with the final size of the void. Therefore, dimple size is positively correlated with ductility. This indicates that the ductility of SAC-Sb solder is much better than SAC305. Thus, doping of Sb in the SAC305 alloy helps to significantly enhance the ductility of SAC-Sb solder. (Kawabata & Izumi, 1976; Qin et al., 2019).

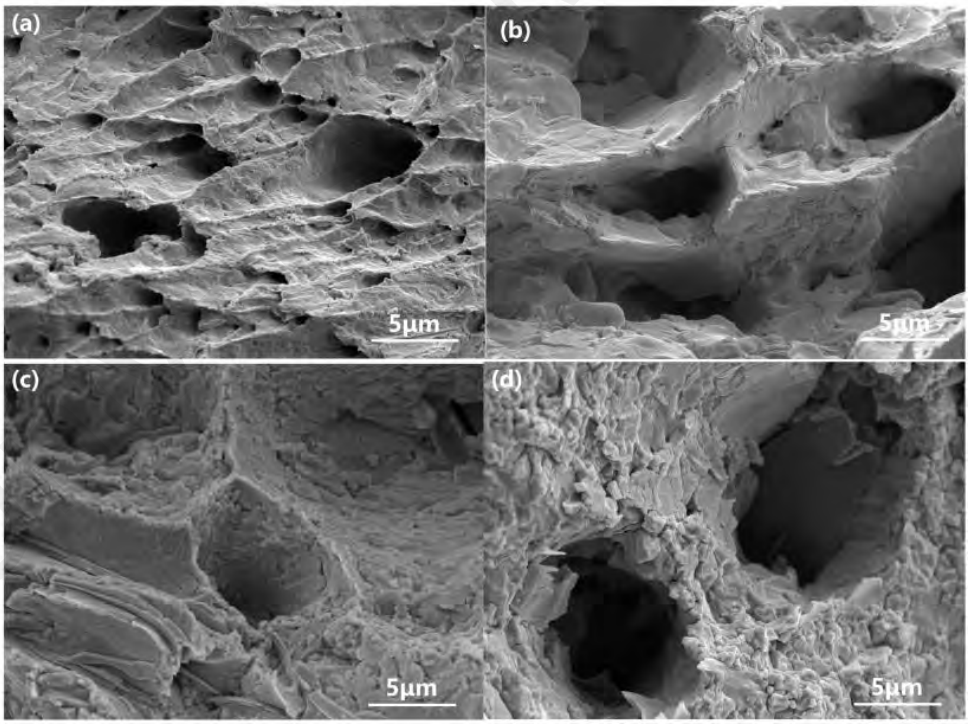

Figure 2.21: Fracture surfaces of SAC305 at (a) 25°C and (b) 125°C with a strain rate of 0.01 s^{-1} and SAC-Sb at (c) 25°C and (d) 125°C at the same strain rate (Chen et al., 2021).

2.5.1.3 Nickel

Ni is hard to be dissolved in Sn matrix according to the binary Sn-Ni phase diagram shown in Figure 2.22 (Okamoto, 2008). The addition of Ni added into SAC solder alloy leads to the formation of $(Cu, Ni)_6Sn_5$ IMC. Ni with 0.05 wt.% addition produced smaller Sn-rich phase and the more uniform distribution of IMCs. Ni with 0.1 wt.% into SAC solder has high fraction of the primary β-Sn phase due to the low solubility of Ni in Sn (Hammad, 2018). The solid solution strengthening of SAC alloy would not be benefited much by adding 0.037 wt.% Ni addition, thus the UTS would not be increased (Hammad, 2013).

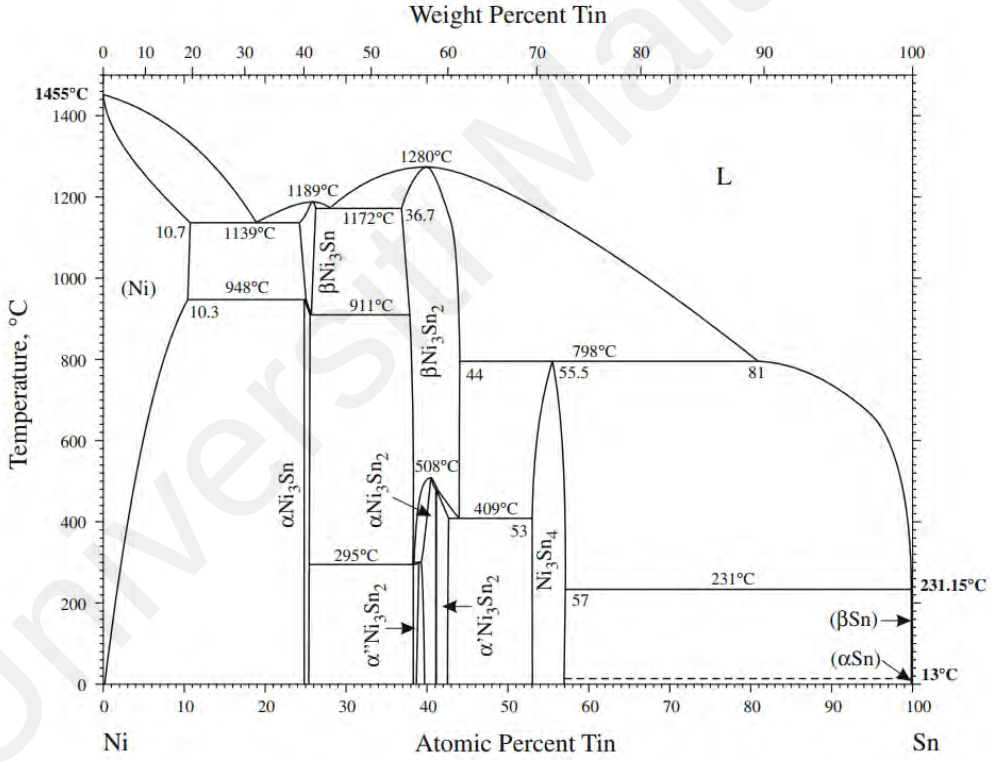

Figure 2.22: Binary phase diagram of Ni-Sn (Okamoto, 2008).

El-Daly et al. (2014) investigated a series of SAC305 solders with minor Ni addition. The effects of Ni addition on the microstructure, thermal behavior, and creep resistance of SAC305 solder were investigated under temperatures ranging from 25 °C to 120 °C and different loads. After 0.5 wt.% Ni added, microstructure observation indicated that Ni

could replace the Cu atoms in the Cu_6Sn_5 phase, resulting in a new η-(Cu, Ni)$_6Sn_5$ IMC phase containing a large amount of Ni, which presented additional obstacle for dislocation pile up in connected grains. Figure 2.23 shows the microstructures of as-solidified samples with different weight percentages of Ni addition. The microstructure of near-eutectic SAC305 solder under equilibrium solidification conditions consists of a large volume proportion of β-Sn matrix surrounded by a eutectic including needle-like and dot-shaped Ag_3Sn particles and polyhedron-shape Cu_6Sn_5 IMCs.

The high-volume percentage of β-Sn matrix dramatically decreased with the addition of 0.5 wt.% Ni to SAC305. The fundamental issue is that the needle-like Ag_3Sn particles are changed into fiber-like Ag_3Sn particles with smaller spacing. This sort of mechanism may provide a more efficient pinning action, decreasing dislocation motion in the solder matrix and making the solder tougher (Chen et al., 2012; Chinnam et al., 2011).

A few long fiber shape Ag_3Sn precipitates with significant spacing are created mostly within the β-Sn phase because of the addition of 1 wt.% Ni. At the surface of the β-Sn matrix, the formation of scallop-like and plate-like η-(Cu, Ni)$_6Sn_5$ morphology has also been observed. The η-(Cu, Ni)$_6Sn_5$ phase is larger in size. However, the large η-(Cu, Ni)$_6Sn_5$ IMCs are more difficult for the joints to relieve the internal tension through plastic deformation of the bulk solder, it may perform worse in drop impact and mechanical testing (Cheng et al., 2008). The high magnification cross-sectional SEM images acquired for the component phases generated at the surface of the β-Sn matrix, as well as the related EDX analysis, are shown in Figure 2.24. Both the Ag_3Sn and Cu_6Sn_5 IMCs can be seen in the eutectic region of SAC305 solder in the SEM picture of Figure 2.24(a). The needle-like features of Ag_3Sn with an average particle size of 20 μm are visible. Cu_6Sn_5 IMC is around 5 μm in size. SAC305-0.5Ni alloy has been discovered to have a higher eutectic region and less primary β-Sn phase as shown in Figure 2.24(b).

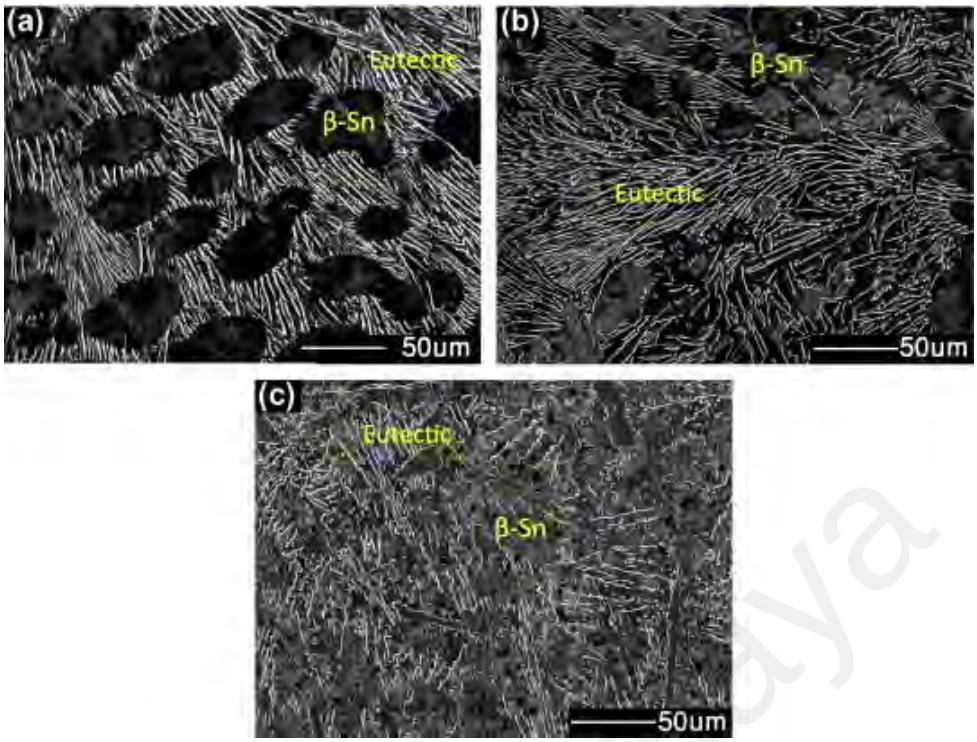

Figure 2.23: SEM of as-solidified: (a) SAC305, (b) SAC305-0.5Ni, (c) SAC305-1Ni solders (El-Daly et al., 2014).

The existence of scallop-like or hexagonal-like (Cu, Ni)$_6$Sn$_5$ IMCs indicated that all the particles tested contain a high quantity of Ni, with an average value of 35.4 wt.% Ni. It meant that during cooling, the Cu$_6$Sn$_5$ phase was changed to the η-(Cu, Ni)$_6$Sn$_5$ phase. Anisotropy of surface energies and compositions linked to the existence of Ni, which increased the growth of Cu$_6$Sn$_5$ that may result in the production of scallop-like η-(Cu, Ni)$_6$Sn$_5$ morphology (Dong et al., 2009). In contrast, adding 1.0 wt.% Ni to SAC305 alloy increased the average size of η-(Cu, Ni)$_6$Sn$_5$ IMC particles while lowering the distribution of fiber-like Ag$_3$Sn precipitates as shown in Figure 2.24(c). It has been discovered that coarsening (Cu, Ni)$_6$Sn$_5$ IMCs strengthens the solder matrix and reduces fiber-like Ag$_3$Sn precipitates. Increased Ni addition can also speed up the formation of cracks within (Cu, Ni)$_6$Sn$_5$ IMCs during cooling. The creep characteristics and lifetimes of SAC305-1Ni solder joints will be significantly reduced. According to microstructure analysis in literature, the fiber-like Ag$_3$Sn particles and fine (Cu, Ni)$_6$Sn$_5$ IMCs had a crucial impact

on the creep properties in the SAC305-0.5Ni solder brought by their precipitation strengthening. In alloys containing less than 1.0 wt.% Ni, $(Cu, Ni)_6Sn_5$ IMC increased in both number and size. Within the inter-dendritic zones, dislocation interaction with tiny Ag_3Sn and $(Cu, Ni)_6Sn_5$ particles performs the most important function in solder strengthening. These fine precipitates greatly improved the creep resistance of SAC alloy.

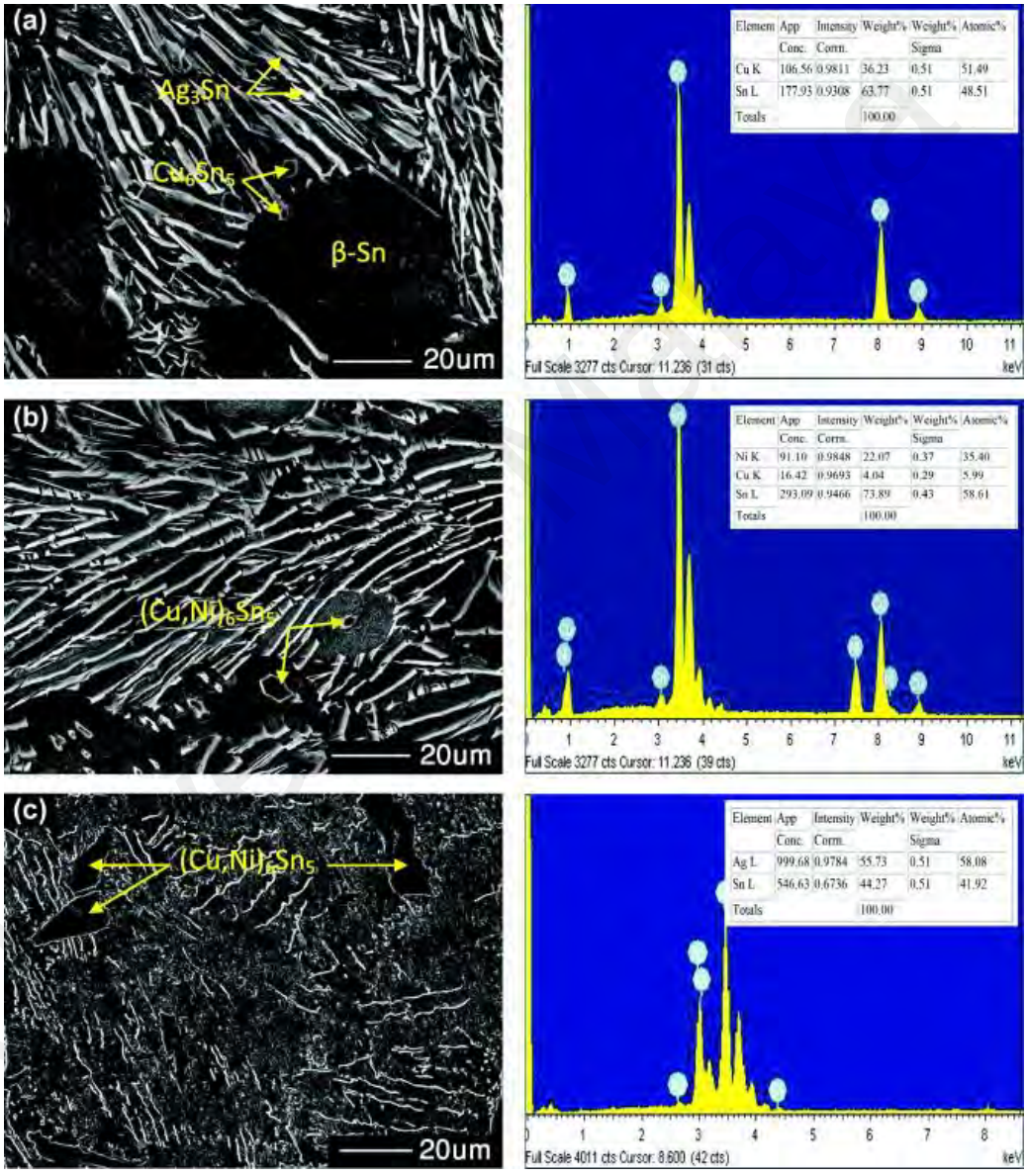

Figure 2.24: SEM microstructure of (a) SAC305, (b) SAC305-0.5Ni, (c) SAC305-1Ni solders and corresponding EDX analyses (El-Daly et al., 2014).

As for the mechanical properties, the addition of 0.5Ni add into SAC305 alloy increased the creep resistance as well as total fracture duration, whereas the advantages of creep behavior and fracture time were shortened in SAC305-1.0Ni solder due to the formation of small amounts of coarsen Ag_3Sn and coarsening of $(Cu, Ni)_6Sn_5$ IMCs.

At RT and a constant stress of 16.7 MPa, Figure 2.25 illustrates typical creep curves up to the rupture times for the three solders. At 25°C, the SAC305-0.5Ni solder is substantially stronger creep resistant than the SAC305 solder, although the SAC305-1Ni solder has less creep resistance than SAC305.

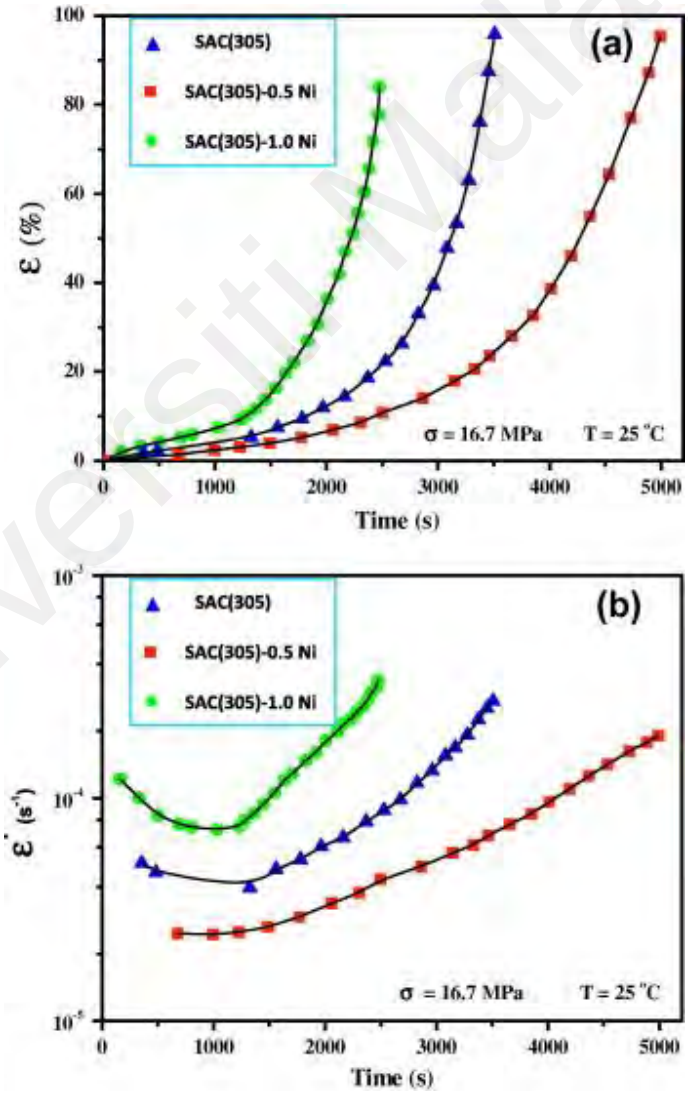

Figure 2.25: (a) Comparison of creep curves at T=25 °C and σ= 16.7 MPa (b) creep behavior of SAC305-0.5Ni and SAC305-1 Ni solder alloys (El-Daly et al., 2014).

Minimum creep strain rates were measured and shown as a function of time to compare the precise creep resistance of the three alloy samples. With increasing Ni weight percentage, the creep rate increased, and the rupture life reduced as shown in Figure 2.25(b). The average creep rates for SAC305, SAC305-0.5Ni, and SAC305-1.0Ni alloys were $4.2x10^{-5}$ s^{-1}, $2.3x10^{-5}$ s^{-1}, and $7.0x10^{-5}$ s^{-1}, respectively.

2.5.2 Double element additions to SAC alloys

Up to date, several methods have been applied in improving the solder mechanical strength to ensure that the material properties remain after long-term services. One of the strategies that researchers used in their study is by adding multiple additional elements mentioned above to enhance the properties of the SAC solder alloys (Hammad, 2018; Mahdavifard et al., 2015). These supplemented elements were added to fabricate a multicomponent solder so that the improved overall properties could be obtained, such as higher strength and reliability under harsh operation conditions (Alam et al., 2019). Simultaneous additions of Fe and Bi to SAC105 refined the microstructure and improved tensile properties, while decreased the melting temperature of the SAC105 alloy (Ali, et al., 2016). Adding In and Ce into SAC solder was effective in improving the shear strength, ductility, and fracture toughness (Fallahi et al., 2012).

Ali et al. (2016) investigated the effect of adding Fe and Bi into SAC105, and they found that Fe doping does not help much to improve the mechanical properties of the SAC105. However, Bi helps to strengthen the alloy by solid solution strengthening as smaller grain sizes were observed for SAC105-Fe-2Bi when compared to SAC105. Large β-Sn grains with dendrites consist of the microstructure of the SAC105, whereas eutectic Ag_3Sn and Cu_6Sn_5 IMC particles distribute the inter-dendritic area. SAC105-Fe-1Bi and SAC105-Fe-2Bi have microstructures with smaller primary β-Sn grains surrounded by three different kinds of eutectic IMC particles: Ag_3Sn, Cu_6Sn_5, and $FeSn_2$. Some Fe is

converted to $FeSn_2$, while the rest is distributed as insoluble particles in the bulk alloy. $FeSn_2$ IMCs are very rare in the microstructure of Fe/Bi alloys since very low Fe content can solute into Sn matrix. Hence, they have no influence on the mechanical characteristics. Bi is clearly found in the solder bulk, and its solid solution strengthening mechanism enhances the alloy. Bi also inhibits the production of IMCs, particularly Cu_6Sn_5 IMCs (Cai et al., 2012; Hodúlová et al., 2011). The diameters of Ag_3Sn and Cu_6Sn_5 IMCs in Fe/Bi found in SAC105 are smaller than the base alloy SAC105 as shown in Figure 2.26. This is due to the presence of Bi in the alloy, which inhibits the development of IMCs, and therefore the size of IMCs reduces as Bi concentration in the alloy increases (Wu et al., 2004; Armstrong et al., 2014).

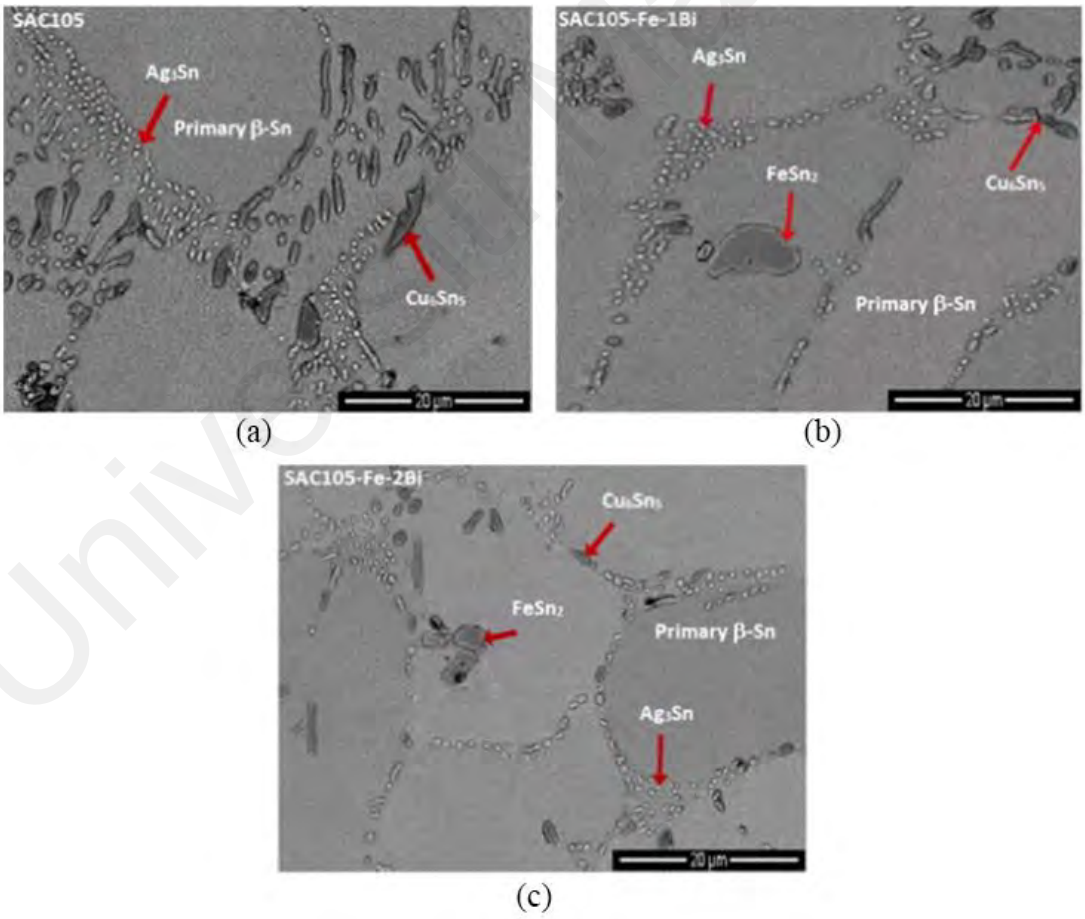

Figure 2.26: FESEM micrographs of the basic alloy (a) SAC105 and Fe/Bi enhanced (b) SAC105-Fe-1Bi and (c) SAC105-Fe-2Bi (Ali et al., 2016).

In contrast to the Sn matrix in SAC105, the IMCs are rich in Ag and Cu which are hard and brittle in nature and impact the mechanical characteristics of Pb-free solder. The smaller IMCs particles provide more obstacles to dislocation slippage, resulting in a substantial solder strengthening effect (Vianco & Rejent, 1999).

Meanwhile, the grains were studied in Figure 2.27. The bulk of grains in SAC105 were 60 to100 µm in size, however with the addition of Fe/Bi to the alloy, grain sizes shrank to 20 to 40µm. This drop in average grain size is due to the addition of Fe/Bi in the alloy, which provides extra nucleation sites for grain formation and hence reduces grain size.

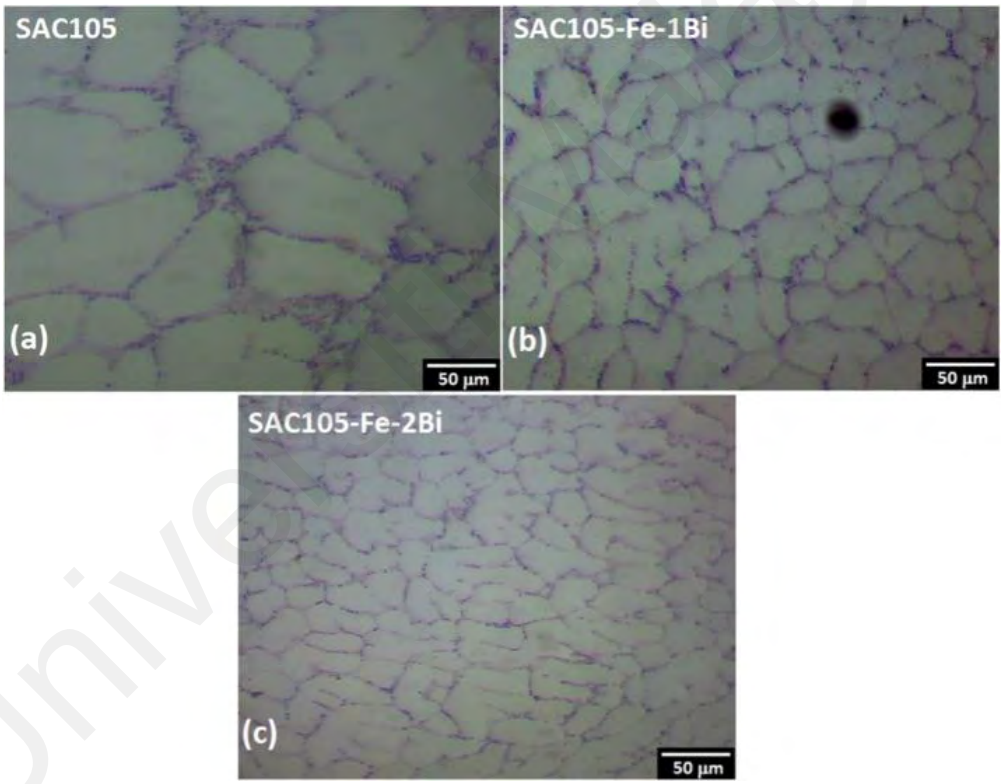

Figure 2.27: Grains size of: (a)SAC105, (b)SAC105-Fe-1Bi and (c)SAC105-Fe-2Bi (Ali et al., 2016).

Some key parameters of Fe/Bi added SAC105, such as hardness, and shear strength were also studied and compared with the base alloy SAC105 (Ali et al., 2016). Figure 2.28 shows the shear strength of SAC105-Fe-1Bi, SAC105-Fe-2Bi, and SAC105 solder alloys

comparison. SAC105 has a shear strength of 17.8 MPa. The shear strength of the basic alloy SAC105 is increased to 25 MPa by adding 0.05 wt.% Fe and 1 wt.% Bi. Additionally, adding the Bi content to 2% enhanced the shear strength to 34.3 MPa.

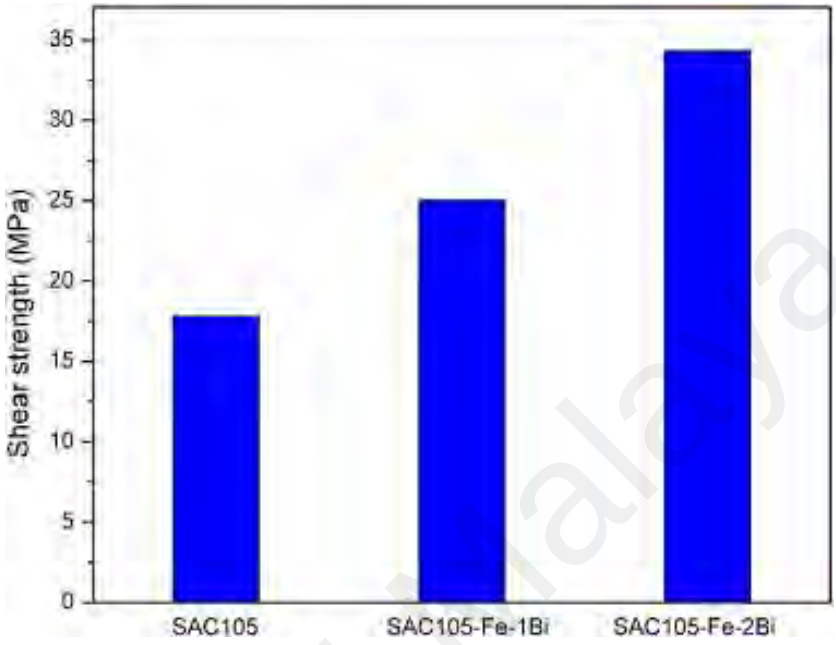

Figure 2.28: Shear strength of SAC105, SAC105-Fe-1Bi and SAC105-Fe-2Bi (Ali et al., 2016).

Bi addition in SAC increases its shear strength through a solid solution strengthening process. Bi dissolves in Sn matrix which strengthens the matrix and increases the shear performance eventually (Yang et al., 2013). The shear strength of SAC105 was modified from 29 MPa to 34.3 MPa by Fe and Bi additions (Fallahi et al., 2012; Liu et al., 2011). It was also found that adding 0.2 wt.% and 0.6 wt.% Fe to SAC369 raised the shear strength to 40 MPa and 53 MPa. This suggests that the Fe element helps SAC solder alloys enhance their shear strength. The improvement in shear strength for SAC105-Fe-1Bi and SAC105-Fe-2Bi alloys is a combined effect of Fe and Bi in the alloy, as both contribute to the shear strength. Moreover, the addition of Fe and Bi to SAC105 also upgraded the alloy hardness from 10.5 HV to 22.6 HV.

2.5.3 Multi element additions to SAC alloys

Along this line, multi additional elements were chosen and added into SAC solder to improve the performance under both thermal and mechanical challenges (Gyenes et al., 2017). Among these studies, a commercial alloy known as Innolot was reported. It contains 3 wt.% Ni, 1.5 wt.% Sb and 0.15 wt.% Bi in SAC387 based composition (Tao et al., 2016; Kang et al., 2021). β-Sn grains and same IMC phases were found in microstructures of both SACBiNi and bulk specimens of a commercial multicomponent solder called Innolot due to the similar chemical compositions of two materials by Tao et al., (2017). The microstructure of SACBiNi reveals globular and lamellar particles of Ag_3Sn in light grey and Cu_6Sn_5 in dark grey as shown in Figures 2.29(a-b). Since there are more Sb and Ni elements in Innolot solder, $Ag_3(Sn, Sb)$ and $(Cu, Ni)_6Sn_5$ as shown in Figures 2.29(c-d), in which Sn atoms are partly replaced by Sb atoms and Cu atoms are partially substituted by Ni atoms respectively. In addition, Ag_3Sn and Cu_6Sn_5 particles in SACBiNi solder are smaller and more concentrated, and strongly connected than in Innolot solder. For both solder alloys, Bi particles in white precipitate appear in the Sn matrix within tiny and isolated clusters.

Gyenes et al. (2017) investigated the microstructural properties of multicomponent Sn-Ag-Cu based solder alloys. A series of tensile tests and hardness tests were conducted, and comparisons were made among the solder alloys. The optical microscope pictures of SAC alloys with Bi, Sb and Ni addition are shown in Figure 2.30. Hypoeutectic microstructures containing β-Sn dendrites and variable amounts and kinds of IMC in the SAC307, SAC307+BiSbNi, SACX0807+Bi and SACX+BiSbNi.

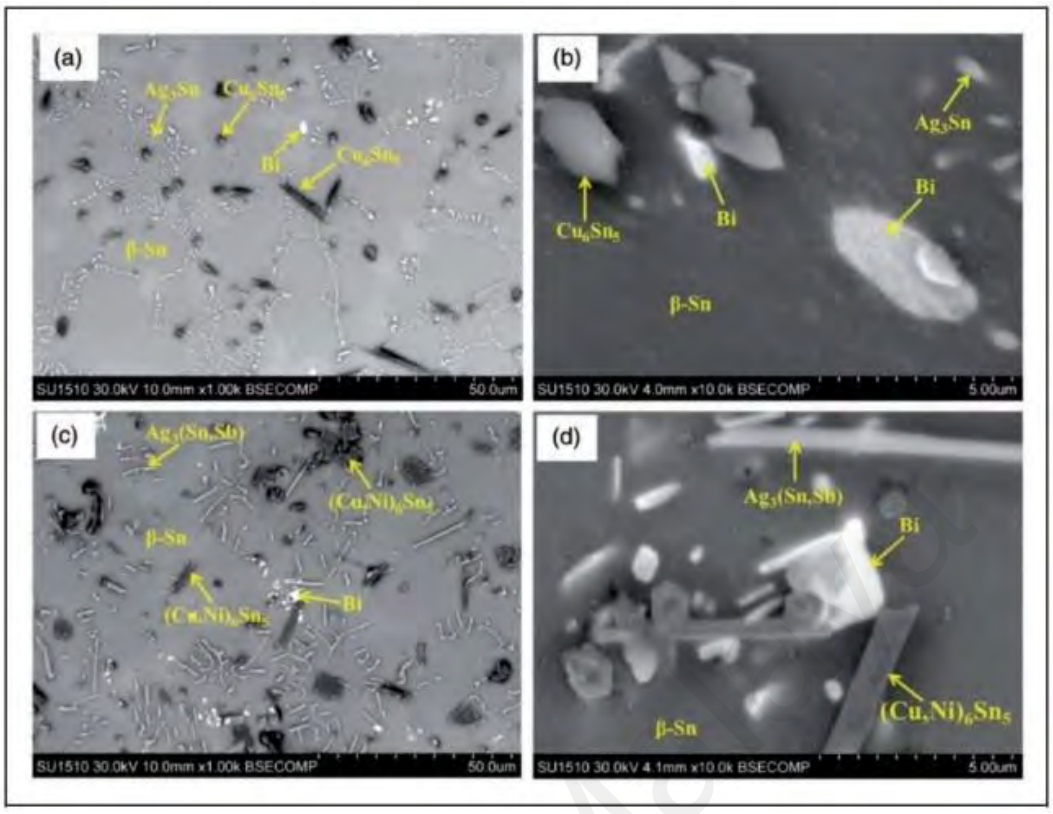

Figure 2.29: The as-cast microstructures: (a) overview and (b) magnified view for SACBiNi; (c) overview and (d) enlarged view for Innolot (Tao et al., 2017).

Figure 2.31 shows the SEM pictures of the alloys and the examined compositions. The SAC307 consists of a *β*-Sn solid solution and a fine eutectic IMC with atom Ag and Cu, according to the results. The Bi-containing eutectic emerges in the other three alloys. Particles of the Bi appear on SEM images. The different phases of the eutectic, particularly the *β*-Sn solid solution, Ag_3Sn, and $(Cu, Ni)_6Sn_5$ phases, are considerably easier to be detected in the SACX+BiSbNi alloy due to the high Cu and Ni percentage (Gyenes et al., 2017).

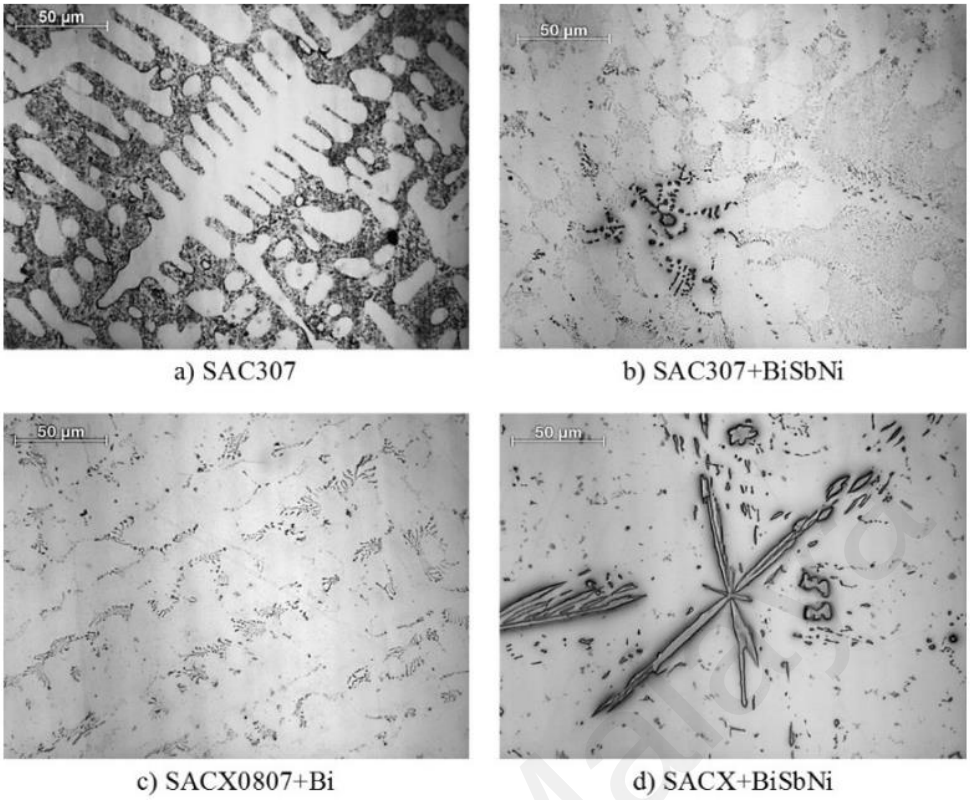

Figure 2.30: Optical microscopic images of the solder alloy (a) SAC307, (b) SAC307+BiSbNi, (c) SACX0807+Bi and (d) SACX+BiSbNi (Gyenes et al., 2017).

The effect on the mechanical performance for simultaneous additions of alloying elements added into SAC solders has also been studied, and comparisons between multicomponent solders and SAC solders have also been made. Among these studies, a commercial alloy known as Innolot was reported (Tao et al., 2016; Kang et al., 2021; Gyenes et al., 2017). It contains 3 wt% Bi, 1.5 wt% Sb and 0.15 wt% Ni in SAC387 based composition. The evaluations of the mechanical properties for Innolot alloy showed improved tensile, shear strength, and creep resistance. The UTS of Innolot increased 16.25 % and 121.4 % respectively as compared with SAC405 and SAC105, while the shear strength of this alloy increased 16.8 % in compared to SAC-Bi alloy (Chowdhury et al., 2016).

(a)

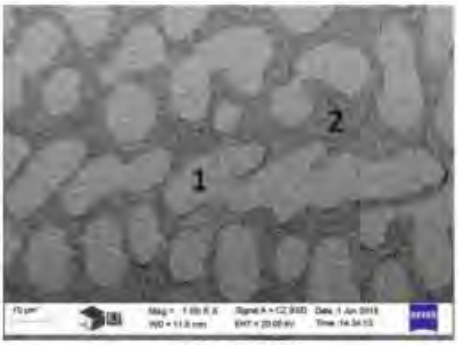

a) SAC307

Element	Analysed phases	
	1	2
	β-Sn	(β-Sn+ Ag_3Sn+Cu_6Sn_5)
Sn	99.50	87.85
Ag	0.50	7.48
Cu	-	4.67

(b)

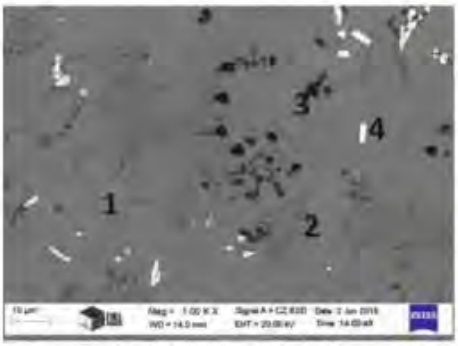

b) SAC307+BiSbNi

Element	Analysed phases			
	1	2	3	4
	β-Sn	Ag_3Sn	$(Cu,Ni)_6Sn_5$	(Bi)
Sn	95.05	30.93	51.58	15.13
Ag	0.25	66.33	-	-
Cu	-	2.74	41.19	-
Bi	2.89	-	-	84.87
Sb	1.81	-	-	-
Ni	-	-	7.23	-

(c)

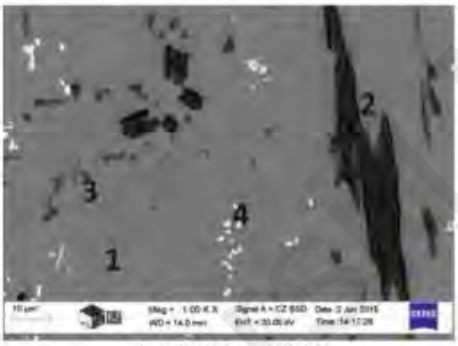

c) SACX+BiSbNi

Element	Analysed phases			
	1	2	3	4
	β-Sn	$(Cu,Ni)_6Sn_5$		(Bi)
Sn	94.25	46.78	61.89	46.00
Cu	-	45.41	36.03	-
Bi	2.76	-	-	54.00
Sb	2.99	-	-	-
Ni	-	7.81	2.08	-

(d)

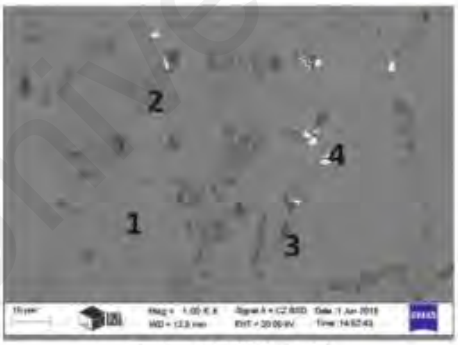

d) SACX0807+Bi

Element	Analysed phases			
	1	2	3	4
	β-Sn	Ag_3Sn	Cu_6Sn_5	(Bi)
Sn	96.09	49.35	71.17	34.02
Ag	0.65	50.65	-	-
Cu	1.12	-	28.83	-
Bi	2.14	-	-	65.98

Figure 2.31: SEM images of the (a)SAC307; (b)SAC307+BiSbNi; (c)SACX+BiSbNi; (d) SACX0807+Bi and measured compositions of the phases (Gyenes et al., 2017).

Furthermore, 5.12 % reduction of UTS for Innolot as compared to 14.99 % of SAC105 and 9.7 % of SAC305 was reported as after undergoing 60 days aging under 50 ℃ (Lall et al., 2013). As for creep behavior, Innolot possessed more resistance to creep at high temperatures with only 33 % of creep rate than SAC405 (Fahim et al., 2016). In addition, the thermal aging effect was also reported on the creep resistance. It was investigated that Innolot showed 5.25 times increase of steady-state creep rate during the first 30 thermal aging days but remains constant thereafter up to a year (Tao et al., 2015; Tao et al., 2019). Solid solution hardening and dispersion hardening were suggested as main mechanisms for the improvement of the creep performance (Fahim et al., 2016). Prior studies have also shown that Innolot is more reliable in thermal cycling since its fatigue exponent and coefficient increased 7.4 % and 131.9 % as compared with SAC387 (Tao et al., 2020). Tao et al. (2017) fabricated and tested lap-shear joining specimens for SACBiNi and Innolot solder alloys under different strain rates and temperatures. The effects on mechanical behavior and microstructure have been investigated. The shear stress–shear strain curves for SACBiNi and Innolot solder joints under three different strain rates and temperatures are shown in Figures 2.32 and 2.33.

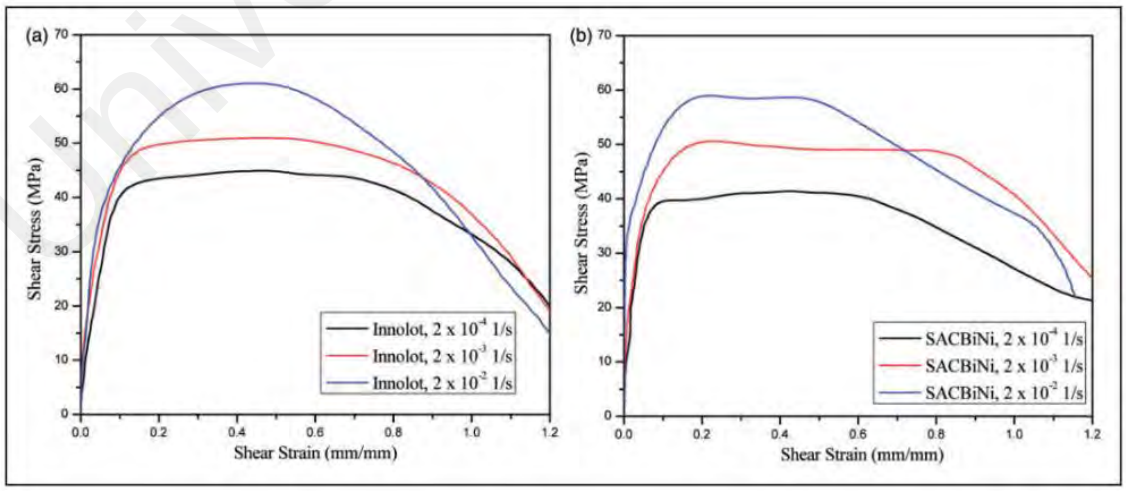

Figure 2.32: Shear stress vs. shear strain for SACBiNi and Innolot solder joints at 25°C with three strain rates (Tao et al., 2017).

Strain rates and temperatures have significant effects on the mechanical characteristics of SACBiNi and Innolot solder as shown in stress-strain curves. Under a strain rate of $2.0x10^{-4}$ s^{-1} and RT, the ultimate shear strength (USS) of the SACBiNi alloy is 41 MPa while the USS of the Innolot alloy is 45 MPa.

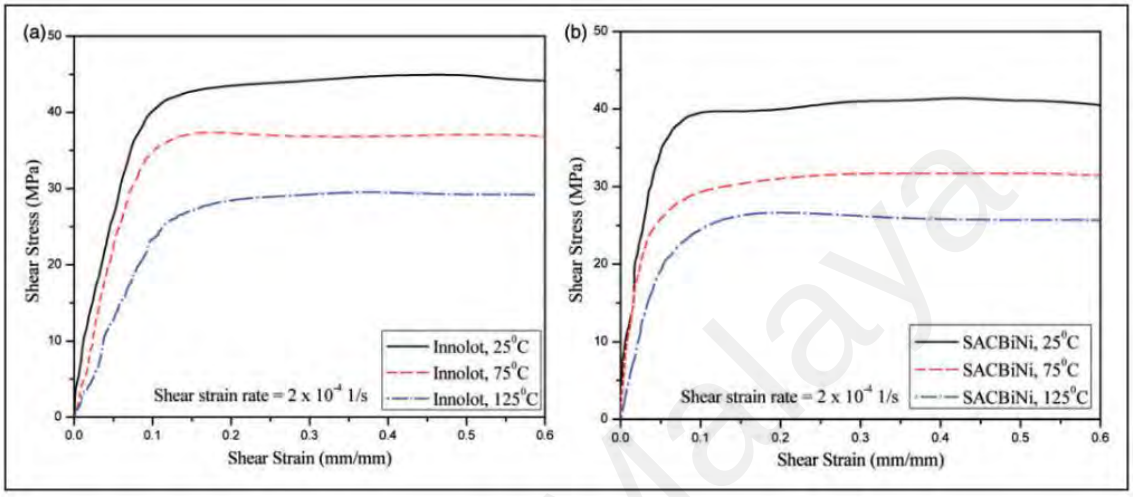

Figure 2.33: The shear stress-strain curves at strain rate $2.0x10^{-4}$ s^{-1} with three temperatures for SACBiNi and Innolot solder joints (adopted from Tao et al., 2017).

Besides Innolot solder, the SAC307+BiSbNi alloy has also doubled the UTS, YS, and hardness of SAC307, and its elongation is roughly half that of SAC307. These changes are attributable to the IMCs and Bi particle due to their effects of strength increasing (Gyenes et al., 2017). SACX+BiSbNi has the shortest elongation as shown in stress-strain curve of Figure 2.34.

SAC307+BiSbNi outperforms the other alloys in terms of strength, whereas SAC307 outperforms the others according to elongation. The YS, UTS, elongation, and Vickers hardness (HV) data are shown in Figure 2.35. YS, UTS and HV of SAC307+BiSbNi are roughly twice that of SAC307, while the elongation is about half of it. In comparison to SACX+BiSbNi, SACX0807+Bi has lower UTS and YS and greater elongation.

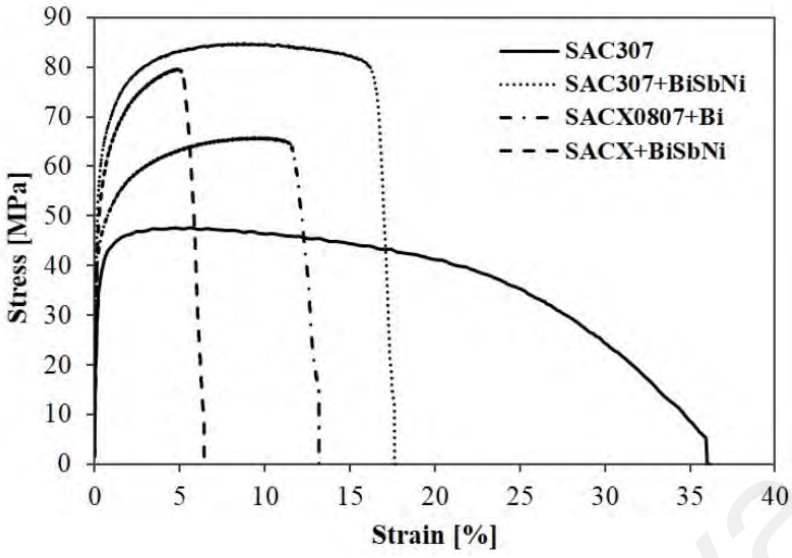

Figure 2.34: Stress-Strain curves of the SAC based multicomponent alloys (Gyenes et al., 2017).

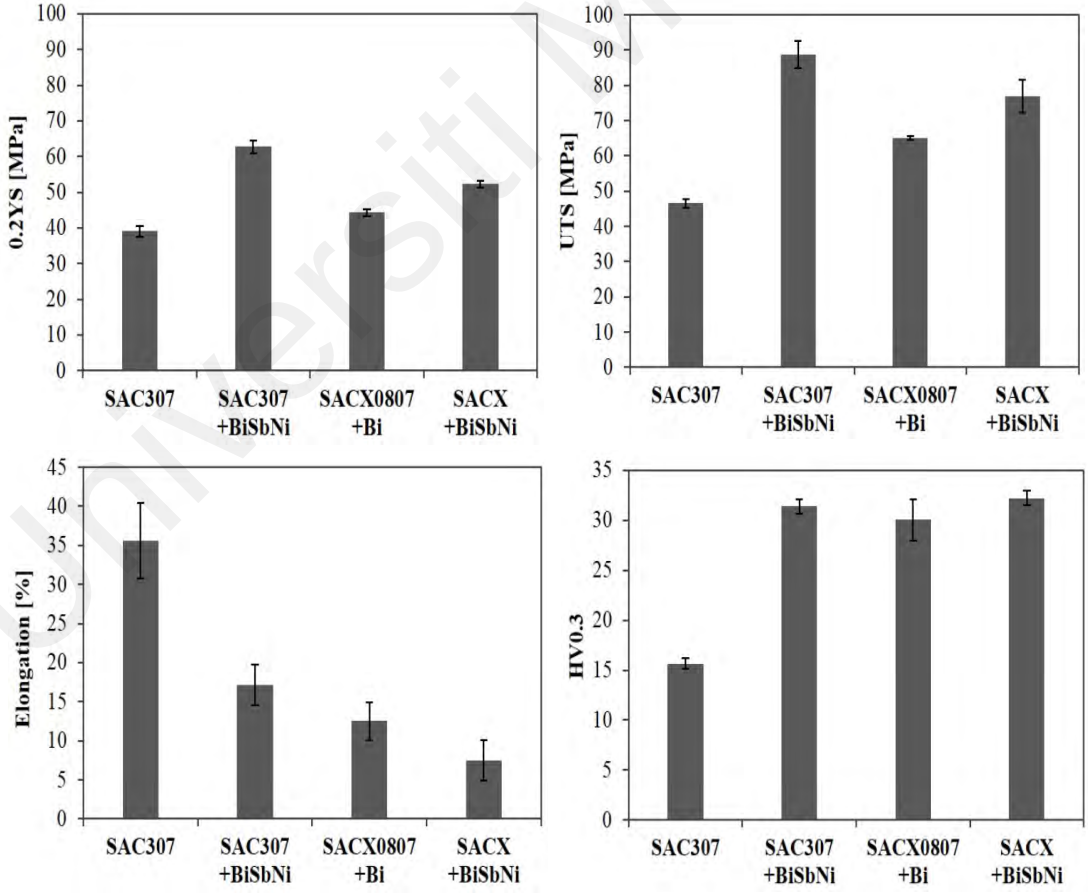

Figure 2.35: YS, UTS, Hardness Value and Elongation of the SAC based multicomponent alloys (Gyenes et al., 2017).

As for fracture behavior of the multicomponent solders, Figures 2.36 and 2.37 illustrate the fractography of the SACBiNi and Innolot alloys after shearing at RT with various zones of rupture under strain rate $2.0x10^{-4}$ s^{-1} (Tao et al., 2017). A mixed type of fracture occurs when a rupture begins within the solder joint and progresses to the interface with the thinnest IMC layer. Furthermore, few voids form in between the IMC layers and the solder connection. Indeed, the development of $(Cu, Ni)_6Sn_5$ and Cu_6Sn_5 IMC layers at the solder interface consumes a high percentage of Cu in solder, which may result in voids at the solder interface and mechanically weakening the solder joint.

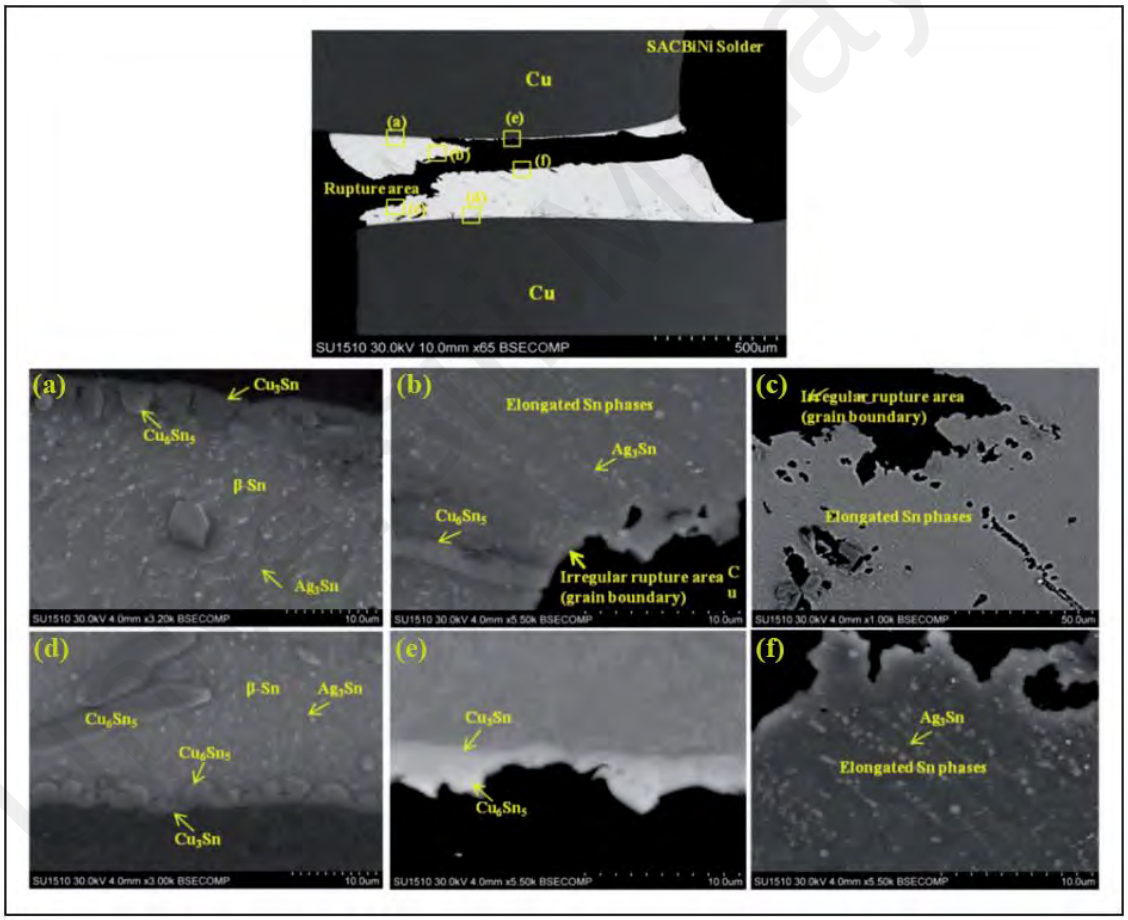

Figure 2.36: Cross-sectional SEM images of SACBiNi solder joint after shear testing at 2.0 x 10^{-4} s^{-1} (Tao et al., 2017).

Near rupture area inside the solder joint, the Sn phases which were originally globular before mechanical test became long orientated after undergone an axial growth activated by the mechanical energy applied during the test. The SEM images reveal the nature of the rupture in the two alloys which are more ductile in SACBiNi and more brittle in Innolot. Phase elongation found for both solders caused by mechanical action, and the fractures spread along the weakest route.

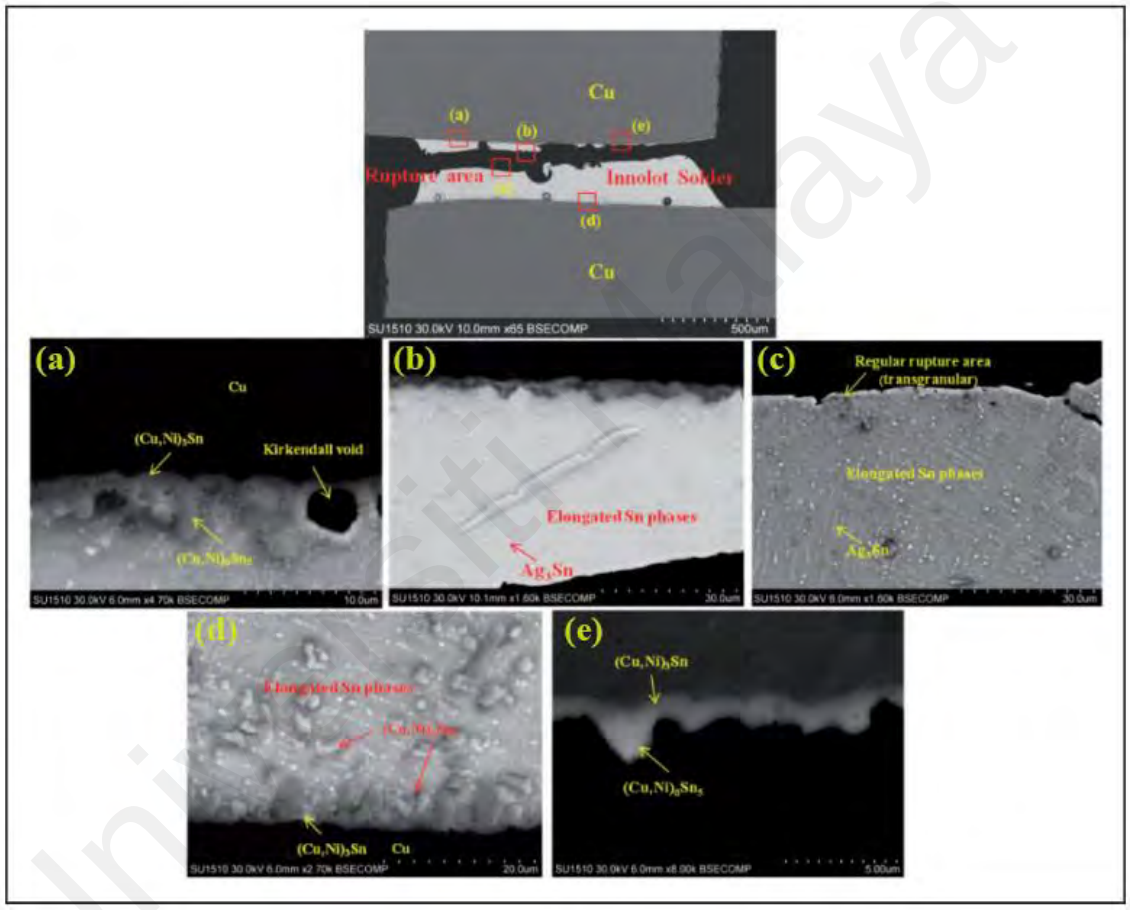

Figure 2.37: Cross-sectional SEM images of Innolot solder joint after shear testing at 2.0 x 10^{-4} s^{-1} (Tao et al., 2017).

2.6 Aging effects on solders

According to literature review, the properties of the solder are likely to degrade over long usage due to aging effects, especially in harsh conditions under high temperature and stress (Ma et al., 2006; Nabihah & Nurulakmal, 2019). For example, automotive

electronics manufacturers are facing significant challenges in respect to the thermo-mechanical reliability of solder joints. Solder joints display complex mechanical structure in electronic packaging. Up to date, several methods have been applied in improving the solder mechanical strength to ensure that the material properties remain after long-term services. One of the strategies that researchers used in their study is by adding multiple additional elements mentioned above to enhance the properties of the SAC solder alloys (Hammad, 2018; Mahdavifard et al., 2015).

2.6.1 Aging effects on bulk solders

Ali et al., (2021) explored the microstructure and mechanical characteristics of Bi-doped SAC305 solder alloys at high thermal aging temperature. The microstructure investigation and mechanical characteristics of the SAC alloys doped with varied compositions of Bi (1, 2 and 3 wt.%) were observed, compared, and studied. The improved microstructure was achieved by doping SAC305 with Bi, which lowered the IMC particle size, thereby preventing grain boundaries from expanding. On the other hand, the microstructure was changed by thermal aging at 100 °C and 200 °C, which increased the average particle size of the IMCs. Interestingly, even after thermal aging, the IMC size was determined to be smaller than SAC305, which suggests that Bi addition suppressed the change of microstructure of SAC305.

Microstructural study of SAC305 and Bi-doped SAC305 alloys is shown in Figure 2.38. IMCs were found to be dispersed across the Sn matrix in the form of Ag_3Sn and Cu_6Sn_5 (Osório et al., 2013). The addition of Bi improved the microstructure as observed in micrographs. In contrast to the earlier report by Hirai et al. (2019) and El-Daly et al. (2015), Bi particles were also present as solid-solved in the matrix, this investigation identified low amount Bi as solid particles in the Sn-matrix without producing any IMCs. Since dislocation motions and pinned grain boundaries are hindered by Bi particles at the

borders of the Sn matrix and inter dendritic regions, mechanical characteristics of SAC based solder have been enhanced. The reduction in particle size of the IMCs, according to Chen et al. (2014), resulted in a more refined microstructure and improved mechanical properties.

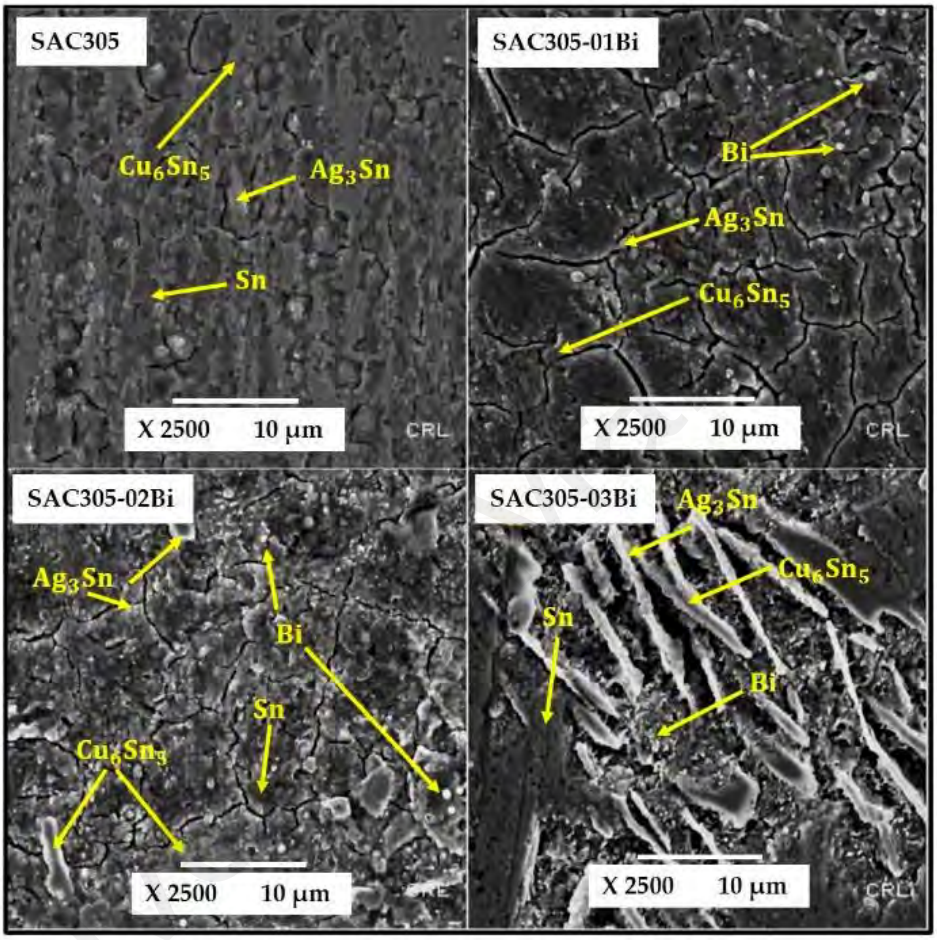

Figure 2.38: SEM of as-casted alloys SAC305, SAC305-01Bi, SAC305-02Bi and SAC305-03Bi (Ali et al., 2021).

SEM images of thermally aged specimens are shown in Figure 2.39. After thermal aging, the microstructure became coarser due to the dispersion of IMCs inside the grain (El-Daly et al., 2014b). During the grain growth, Cu_6Sn_5 particles changed shape from granular to whiskered and spherical, becoming larger than Ag_3Sn (El-Daly et al., 2014a). Comparing the SAC305 alloy and the Bi-doped with 1 and 2 wt.% alloys, the

microstructure of Bi at 3 wt.% revealed IMCs growing more slowly, with fewer dispersed grain boundaries. The solid solution containing the scattered Bi particles served as a pin to keep the fracture dislocation zones in phases (El-Daly et al., 2015). After thermal aging at high temperatures, the microstructure of Bi-added SAC305 was still refined compared to SAC305.

Meanwhile, Ali et al. (2021) also reported that the addition of Bi resulted in an increase of mechanical properties such as YS and UTS. The improvement of mechanical properties was linearly proportional to the percent of Bi doped in SAC305 (Witkin, 2012b). The findings of the tensile tests for the un-doped and Bi-doped SAC305 alloys as a function of various aging temperatures are shown in Figure 2.40. The addition of 1 wt.% Bi to SAC305 increased the YS to 55 MPa from 39.1 MPa. For 2 wt.% and 3 wt.% Bi addition, the value of YS improved to 72.5 and 83.4 MPa respectively. When the aging temperature rises from 100 °C to 200 °C, both YS and UTS decrease, indicating that the microstructure of the thermally aged specimens at high temperatures was severely impacted by IMC development, reducing solder reliability (Aamir et al., 2017).

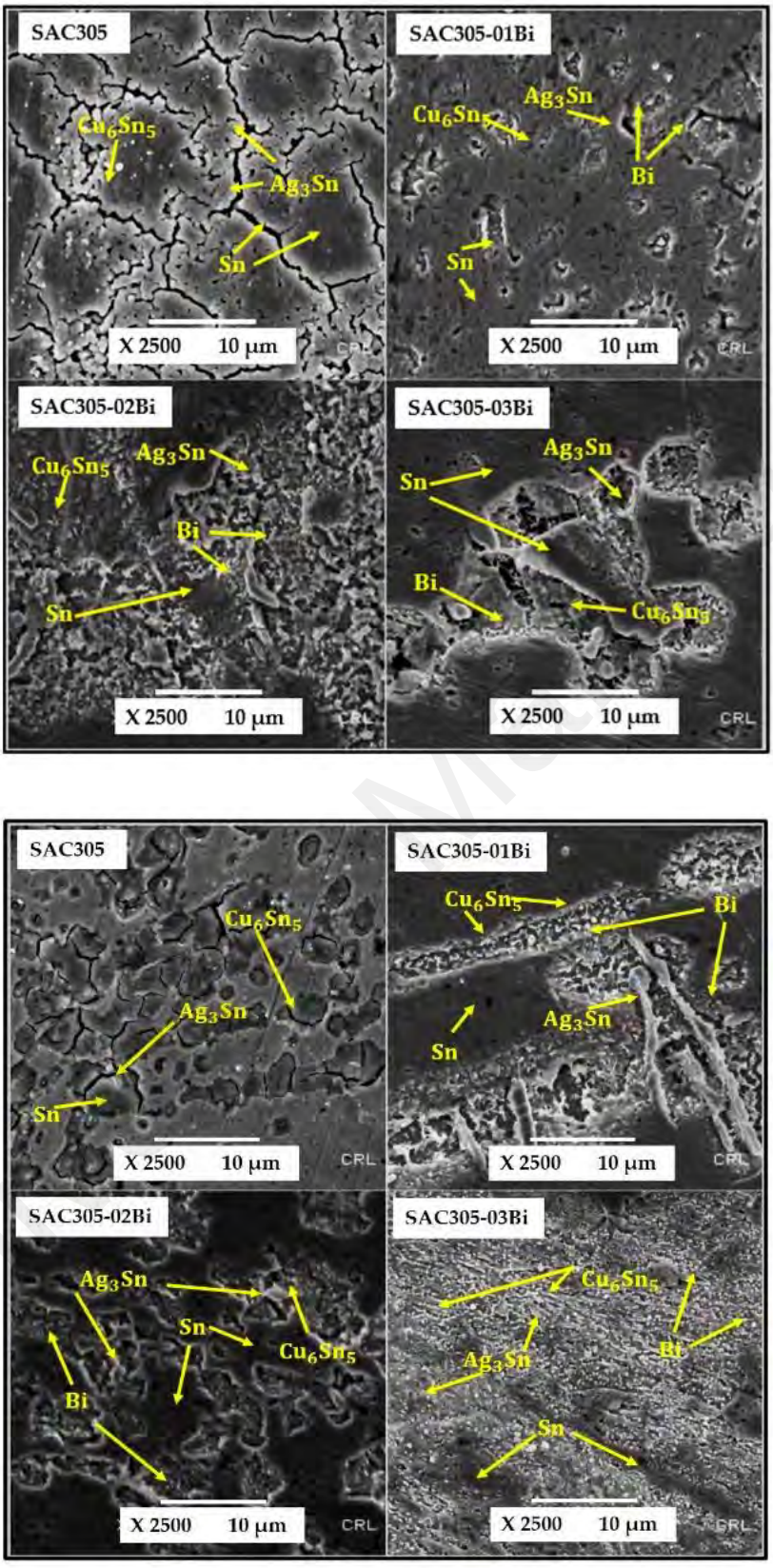

Figure 2.39: SEM images of thermally aged alloys SAC305, SAC305-01Bi, SAC305-02Bi and SAC305-03Bi at 100°C and 200°C (Ali et al., 2021).

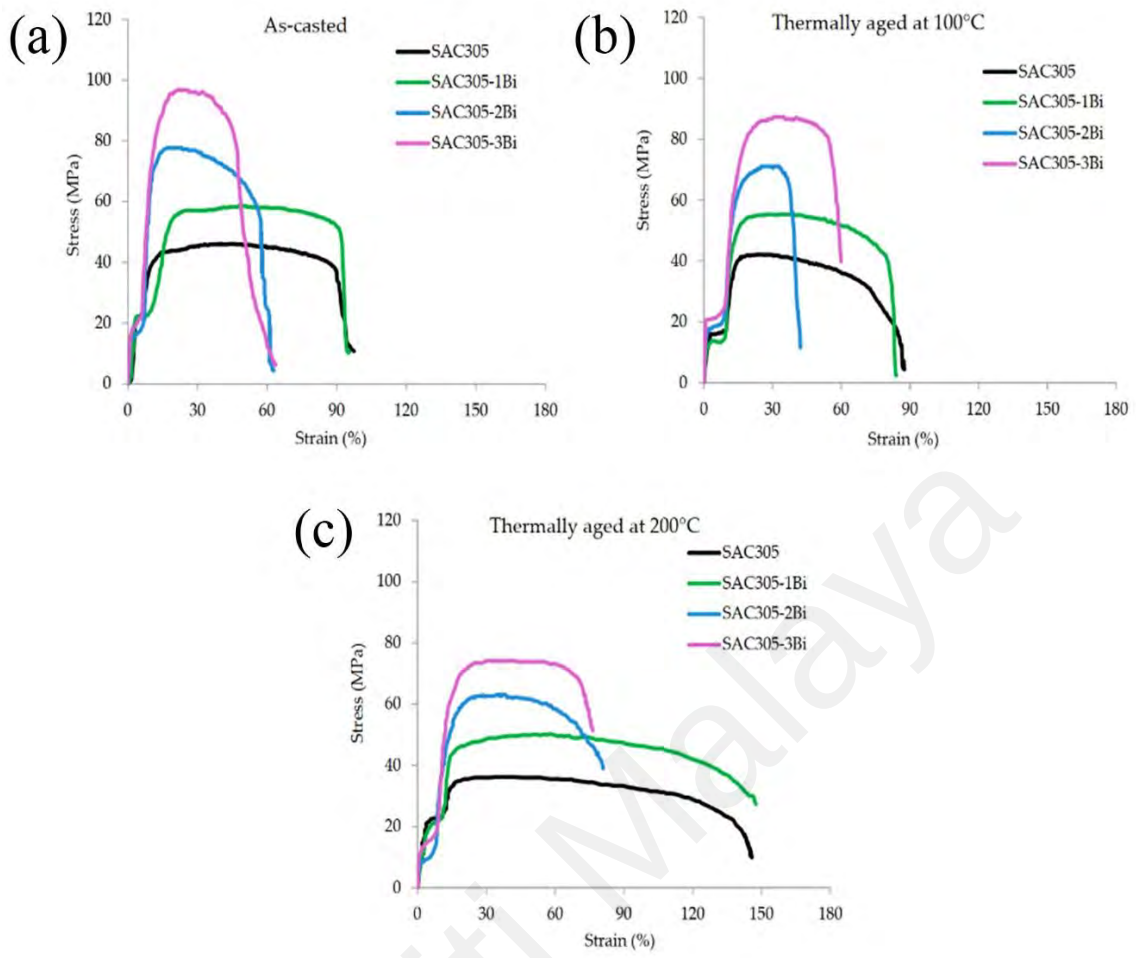

Figure 2.40: Stress-strain curves of thermally aged alloys SAC305, SAC305-1Bi, SAC305-2Bi and SAC305-3Bi at 0 °C, 100 °C and 200 °C (Ali et al., 2021).

2.6.2 Aging effects on solder joints

Li et al. (2006) studied the tensile strength of SAC357-xSb (x = 0, 1, 2 wt.%) solder joints aged at 150°C for 0, 200, 400, 600, 800, and 1000 hours, respectively. Figure 2.41 shows the tensile strength of SAC357 and SAC357-1Sb solder connections decline with increasing aging time. It can be observed that after 400 hours of aging, the rate of decline in strength slows down. The UTS values obtained for solders under different aging conditions and their corresponding total IMC layer thickness were studied by Li et al. (2006). The UTS of solder decreases as its IMC becomes thicker. After 600 hours of aging, the UTS of SAC357 solder connections reduces by 29 % with an increase of 4.5 μm in IMC layer thickness.

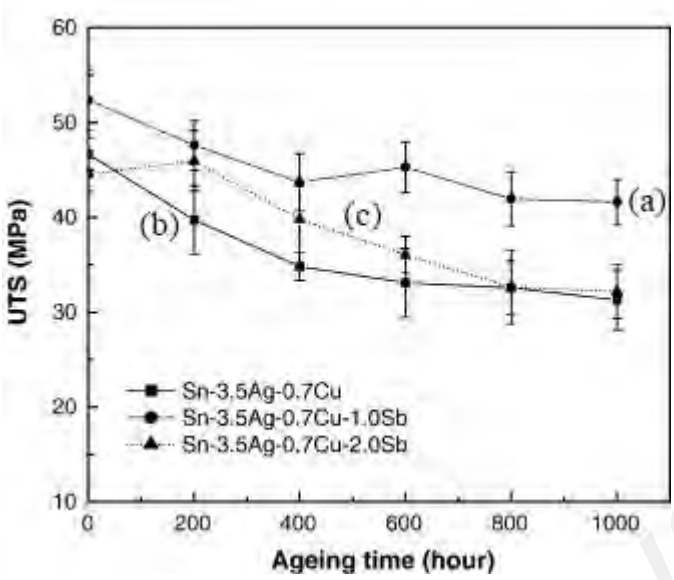

Figure 2.41: UTS vs. ageing time of SAC357-xSb solder joints. (a) x = 0.0, (b) x = 1.0, and (c) x = 2.0 (Li et al., 2006).

In SAC357-0.8Sb and SAC357-2Sb solder junctions, there are only a 13.5 % and 19.1 % strength drop for an increase of 1.7 μm and 2.51 μm in IMC thickness respectively. The findings show that the IMC formation at solder junctions has a considerable impact on tensile strength during the aging time (Prakash & Sritharan, 2004).

The IMC of Sb doped SAC solder alloy joint is thinner than the undoped SAC alloy which tells that refinement of microstructure has occurred. Addition of Sb also causes more $Ag_3(Sn, Sb)$ particles precipitate on the Cu_6Sn_5 layer, causing the solid solution hardening effect. Hence, this results in a higher UTS of Sb-doped SAC alloy compared to Sb free solder alloy joint. As the aging time rose, the decline slowed. The nonlinear relationship between aging time and UTS and YS of SAC-Sb is most likely owing to the precipitation strengthening of Sb-containing IMC in the Sn matrix (Kim et al., 2003).

The fractography of ductile fracture in solder is shown in Figure 2.42. The fracture route of as-soldered specimen is through the bulk solder. The Cu_6Sn_5 layer is detected to be the underlying layer of solder. The SAC357-0.8Sb solder joints exhibit both ductile and

brittle cracks after 600 hours of aging, as seen in Figure 2.43. Fracture occurred at the contact between the solder and the IMC layer in most locations after 1000 hours of aging. Thus, the hardening effect caused by more $Ag_3(Sn, Sb)$ particles precipitating on the Cu_6Sn_5 layer after adding Sb might be another explanation to prove Sb enhances the strength of the SAC357 solder joints (Li et al., 2006; Chen & Li, 2005).

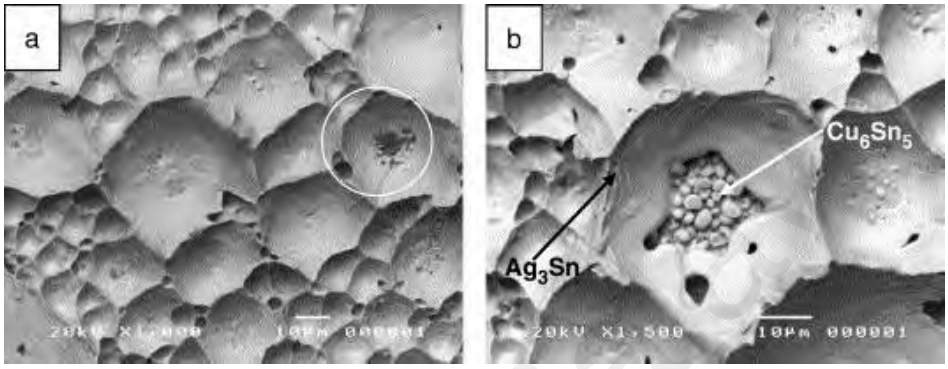

Figure 2.42: (a) SEM fractographies of SAC357-0.8Sb as-soldered solder joints and (b) enlarged SEM images in circle region (a) (Li et al., 2006).

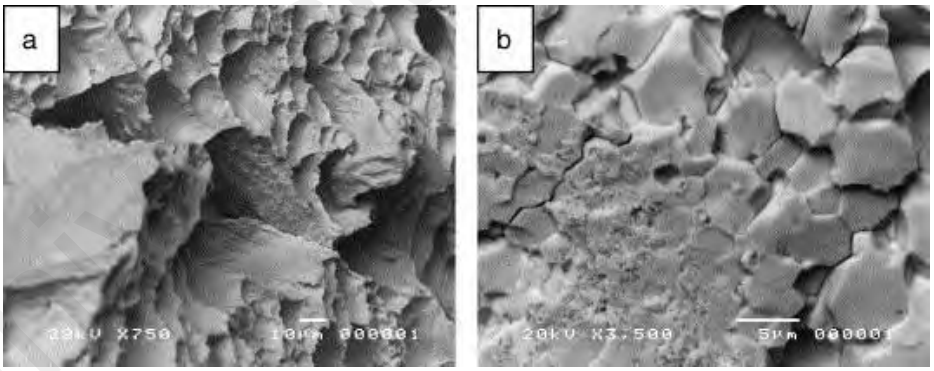

Figure 2.43: Different fracture fractographies of SAC357-0.8Sb solder joints aged at 150 °C for 600 h: (a) ductile fracture in the solder and (b) brittle fracture at the solder/IMC interface (Li et al., 2006).

2.7 Mechanical properties of soldering materials

2.7.1 Tensile property

In general, for mechanical reliability analysis of solder alloy, tensile tests are conducted to investigate the mechanical properties. Some previous studies have focused on the mechanical behavior of bulk and joint solders (Ali et al., 2016). The tensile properties of such SAC based Pb-free solder alloys were reported in many studies (Fallahi et al., 2012; Gyenes et al., 2017). Research on the effects of strain rate and temperature on the mechanical properties has been done on solders (Chowdhury et al., 2016; Lall et al., 2017). Some studies have focused on the effect of alloy additions in the microstructure and on the mechanical behavior of solder joints (Tao et al., 2019; Tao et al., 2020) Also, few research have confirmed that the multicomponent solders, which contain Bi and Sb, or contain Ni and Sb provide higher reliability under high operating temperatures and high stress conditions (Tao et al., 2016; Nabihah & Nurulakmal, 2019; Long et al., 2018). Eventually, Innolot as one of the multicomponent solders which is similar with the components of solder M was also characterized by microstructural refinement, solution strengthening and better toughness due to IMCs layers formed with Bi, Sb and Ni additions (Zhang et al., 2012; Xu & John, 2006; Kim et al., 2003). The evaluations of the mechanical properties for Innolot alloy showed the UTS increased 16.25% and 121.4% respectively as compared with SAC405 and SAC105 (Tao et al., 2016; Chowdhury et al., 2016). Furthermore, 5.12% reduction of UTS for Innolot as compared to 14.99% of SAC105 and 9.7% of SAC305 was reported as after undergoing 60 days aging under 50 °C (Lall et al., 2013). In Table 2.2, UTS under different aging time intervals or strain rates for Sn solders with different additions are compared of which of which the testing conditions are summarized. According to the UTS as a function of aging time, additions added in SAC solders increased the tensile strength of them and improved the reliability under thermal aging condition.

Table 2.2: UTS of Sn solders under different testing conditions.

Solders	Aging Time (h)	Aging temperature (°C)	Strain rate (s^{-1})	UTS before aging (MPa)	UTS after aging (MPa)	Sources
SAC305	0, 5, 24, 72, 144, 216, 504, 1008, 1512	RT	10^{-3}	47	38	(Ma et al., 2006)
SAC305	0, 2, 6, 12, 24, 48	80 125 165 210	$5x10^{-4}$	40 40 40 40	33 32 28 26	(Long et al., 2017)
SAC396	0, 72, 216	RT 180	$2x10^{-3}$	60 60	48 42	(Xiao et al., 2004)
SAC0307 **SAC0307-0.05Mn** **SAC0307-0.1Mn** **SAC0307-0.15Mn**	0, 144, 288, 576, 864, 1152	150	10^{-3}	53 56 58 55	34 38 40 35	(Tang et al., 2017)
SAC105 **Innolot**	0, 24, 720, 1440	50	10^{1}	41 74	36 70	(Lall et al., 2013)
SAC305	N/A	N/A	10^{-3} 10^{-2} 10^{-1}	40 48 57	N/A	(Tang et al., 2014)

Table 2.2: Continued.

Solders	Aging Time (h)	Aging temperature (°C)	Strain rate (s^{-1})	UTS before aging (MPa)	UTS after aging (MPa)	Sources
SAC305				26		
SAC305-0.5Ni	N/A	N/A	10^{-3}	27	N/A	(El-Daly et al., 2014)
SAC305-1Ni				25		
SAC305				35		(Chantaramanee & Sungkhaphaitoon, 2021)
SAC305-1Bi				48		
	N/A	N/A	10^{-4}		N/A	
SAC305-2Bi				60		
SAC357				37		
SAC357-1Sb	N/A	N/A	10^{-3}	42	N/A	(Li et al., 2006)
SAC357-2Sb				43		
SnPb				41		(Ding et al., 2014)
	N/A	N/A	10^{-3}		N/A	
SnPb-Cd				47		
Sn-6.5Zn				30		(El-Daly et al., 2015)
Sn-6.5Zn-0.5Cu	N/A	N/A	10^{-3}	37	N/A	
Sn-6.5Zn-1.5Cu				39		

2.7.2 Shear property

The shear strength of Pb-free alloys compared to eutectic Sn-Pb is shown in Figure 2.44. Sn-37Pb and Sn-0.7Cu solder bumps have similar shear strength values. The Sn-3.5Ag solder alloy has the highest shear strength, 25% higher than Sn-0.7Cu, while SAC387 is slightly weaker than Sn-3.5Ag. However, eutectic Sn-3.5Ag has been reported to be

susceptible to brittle interfacial delamination in surface mount interconnects (Frear & Vianco, 1994).

Tao et al. (2017) fabricated and tested lap-shear joining specimens for SACBiNi and Innolot solder alloys under different strain rates and temperatures. The effects on mechanical behavior and microstructure have been investigated. Strain rates and temperatures have significant effects on the mechanical characteristics of two solders. Under the strain rate of 2.0 x 10^{-2} s^{-1} and RT, the USS of the SACBiNi alloy is 58.9 MPa while the USS of the Innolot alloy is 61.1 MPa. Under the strain rate 2.0x10^{-4} s^{-1} and temperature of 125°C, the lowest shear strength values obtained for SACBiNi is 26.6 MPa and for Innolot is 29.5 MPa. Innolot alloy has stronger shear strength than SACBiNi because of its composition, which has larger proportions of Ni and Sb atoms.

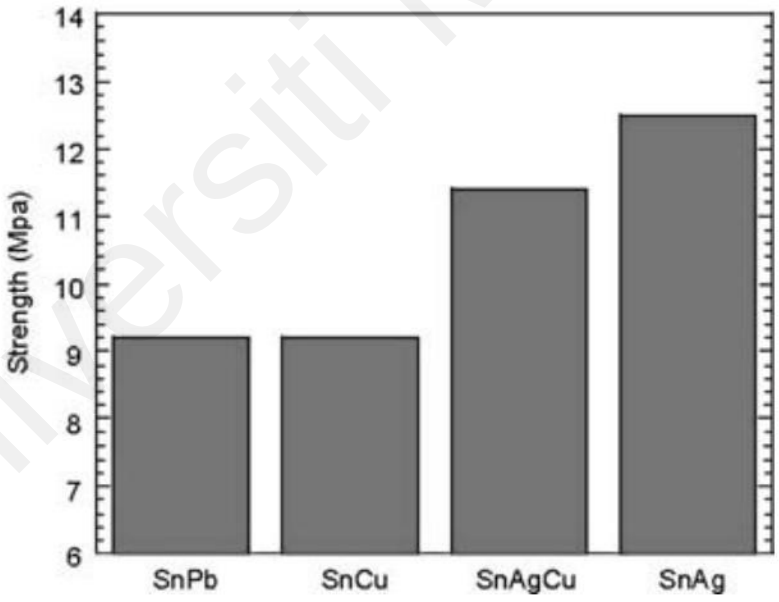

Figure 2.44: Shear strength of solder alloys (Frear & Vianco, 1994).

2.7.3 Creep property

During service, the creep behavior of the solder joint is a crucial issue due to it working under shear strain condition in the electronic packages or at high homologous temperature. When electronic packages are held at a constant stress which is in

interconnected solders, the solder deforms to relieve stress over time. There are three stages of creeping along timeline: primary stage, steady-state stage, and tertiary stage. Creep behavior of solder alloy is a time-dependent plastic deformation, and it would grow when a constant stress is applied (Zhang et al., 2007; Hidaka et al., 2009). Thus, the creep investigation of solder joint is an unavoidable concern to provide its reliability in electronic devices for long lifetime using target. previous work focused mostly on the bulk solder creep behavior and there was limited literature reported for real package on board level study during service (El-Daly et al., 2015; Witkin, 2012a). Recently, a bunch of Pb-free solders have been developed, and their creep behaviors have also been studied such as SAC105, SAC305, etc. (Burke & Punch, 2014; El-Daly et al., 2014; Chauhan et al., 2013; Haq et al., 2020). Nevertheless, only a few studies investigated the effects of strain rates and aging conditions on the creep behavior of multicomponent Pb-free solder alloys such as Innolot. As for Innolot, it possessed more resistance to creep at high temperatures with only 33% of creep rate than SAC405 (Lall et al., 2013). In addition, the thermal aging effect was also reported on the creep resistance. It was investigated that Innolot showed 5.25 times increase of steady-state creep rate during the first 30 thermal aging days but remains constant thereafter up to a year (Fahim et al., 2016; Tao et al., 2015). Solid solution hardening and dispersion hardening were suggested as main mechanisms for the improvement of the creep performance (Lall et al., 2013; Tao et al., 2015). It is likely that the dopants Bi, Sb and Ni can significantly block the movement of dislocations and thus increase the creep resistance of these solders, especially more resistant for SAC solders to creep at high temperatures (Fahim et al., 2016).

2.7.4 Hardness

A mechanical approach for assessing the resistance to plastic deformation of a material is known as hardness testing (Herrmann, 2011). The notion entails applying a load from an indenter to the sample surface. Then, by dividing the applied load on the anticipated

surface area, the values are numerically assessed. Vickers hardness is a measurement of the average hardness of the Pb-free solder alloy that is sectioned from the ingot or as-cast solder alloy for the bulk alloy. In the case of solder joints, the average hardness of the interconnections created by paste printing and reflowing was determined (Hu et al., 2015; Zhu et al., 2018). Due to the Vickers hardness with large tip size (200 nm), a higher load is often required (Cagliero and Maizza, 2011). Loading values of 25 g, 100 g, 300 g, and 10 gf were recently measured. In addition, since the Pb-free solders were readily bent, a shorter dwell time (10-20 s) was adequate for the indentation. The average hardness values are calculated by using measurements of up to 6, 30, and 40 indentation points (Negm et al., 2010; Chen et al., 2016; Hu et al., 2013; Gyenes et al., 2015; Chen et al.,2012). Prior to testing, samples are commonly placed in an epoxy resin for metallographic preparation (Han et al., 2013; Zhao et al., 2016; Sharmaet al., 2016). Characterization of hardness for Pb-free solders in bulk has brought in depth understanding as conducted by Tsao et al. (2016) and Yahaya & Mohamad (2017). The hardness of freshly made solder alloys derived from raw materials would have been determined. Besides, alloying resulted in the creation of novel IMC phases, which are often linked to increased hardness in the investigation. Furthermore, the solder alloy final hardness assessment after being exposed to various solidification circumstances was also important to be studied. Gyenes et al. (2015) tested Vickers hardness on a solidified Sn-0.7Cu-Ni solder ingot while researching the effects of Ni alloying. The maximum values of 15.2 HV were found at 0.08 ppm Ni in the average hardness test. The values decreased to 10.2 HV when the Ni concentration climbed to 0.18 ppm as shown in Figure 2.45.

The addition of an additional element Ni enabled the development of the new Ni_6Sn_5 IMC, which refined the present β-Sn and Cu_6Sn_5 phases. Higher dislocation motions were hampered by these improved IMCs, which explained the hardness gains. Increased

development of the bigger Ni_6Sn_5 IMC was favored by the loss in hardness caused by Ni addition, which weakened the overall structure inversely (Li et al., 2016).

However, not all additions in Pb-free solder resulted in favorable results. For example, adding a tiny quantity of In into the Sn-0.7Cu-0.2Ni solder alloy resulted in a drop in hardness values of 6.8%. As the In addition grew from 0 to 0.3 wt.%, a drop in hardness value could be found and resulted in a coarser IMC formation. (Li et al., 2014).

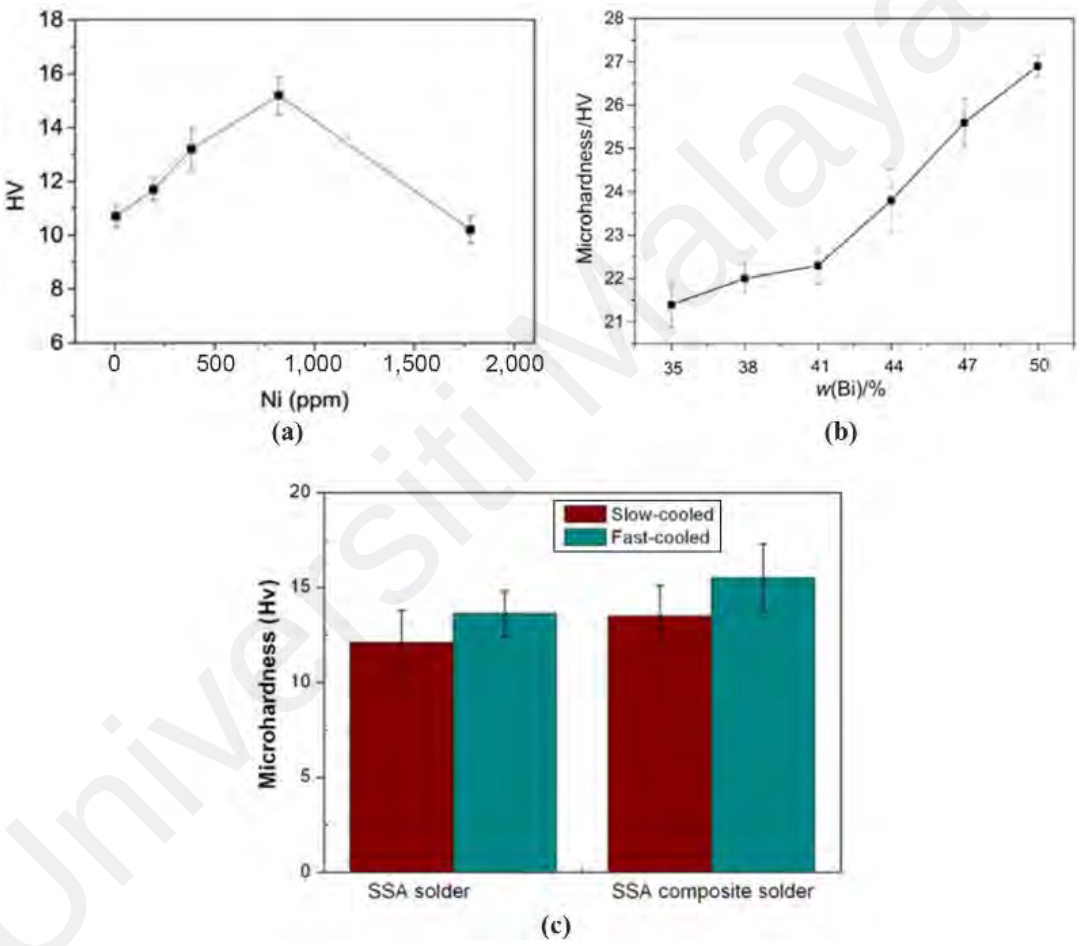

Figure 2.45: Vickers hardness values of bulk solder for (a) the Sn-0.7Cu-Ni solder alloy; (b) the Sn-Bi-In solder alloy with different Bi Wt.%.; (c) the pure and composite Sn-1.5Sb-1Ag composite solder with different cooling condition (Yahaya & Mohamad, 2017).

2.7.5 Fatigue failure

During service, harsh working environments with extreme cyclic temperatures applied on solders are critical. Thus, stress analysis is imperative to be studied to evaluate the reliability of the product (Erinc et al., 2008; Shah, 1990). Due to differences in CTE between the assembly materials and solder joint, stresses and strains are generated from thermal mismatch (Zhang et al., 2014; Vasudevan, 2008). A more challenging thermal issue is the thermal cyclic stress in components of packages during its operational life. When chips are running hotter, it increases the difference in temperature between itself and solder material. Plastic deformation or fatigue failure in solder joint frequently occur despite several new designs attempting to avoid it (Lau et al., 1990a; Lau, et al., 1990b; Enke et al., 1989). Heat generated from die would transfer to the solder joint. As package size shrinks, thermal stress on leads would be increased since the distance between die and solder joint becomes smaller. This reduced the heat transfer process and made the thermal mismatch more serious.

Hence, solder fatigue failure is required to be investigated to evaluate the mechanical degradation of solder due to deformation under cyclic loading (Vaynman, 1989; Frear 1989). As shown in Figure 2.46, the Sn-37Pb flip-chip interconnects failed due to crack formation and propagation through the heterogeneous roughened bands near the interface of UBM and solder (Fields et al., 1992). Heterogeneously coarsened regions are formed due to stress concentrations at weakly eutectic unit cell boundaries and cracks eventually form at these boundaries (Frear et al., 1988).

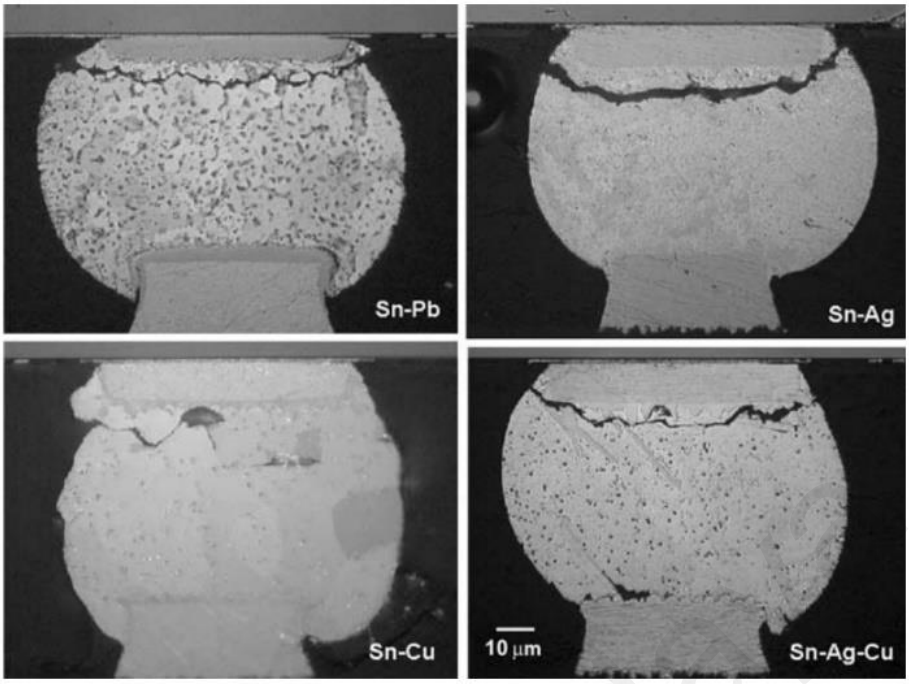

Figure 2.46: Optical micrographs of solder joint cross sections of solder joints Sn-Pb, Sn-Ag, Sn-Cu and Sn-Ag-Cu between Cu UBM and organic substrates after thermal cycling 0 °C to 100 °C (Fields, 1992).

Sn-0.7Cu solder deforms in thermomechanical fatigue via grain boundary sliding. Cracks were observed to propagate at grain boundaries where the interface between UBM and solder was significantly removed near the center of the joint (Frear et al., 1989). This solder is the optimal in terms of thermal fatigue and deforms a lot before failing due to crack growth. The failure behavior of the Sn-3.5Ag and SAC387 alloy showed both crack initiation and propagation through the IMC and interface between IMC and solder. Sn-3.5Ag solder has a shorter thermal fatigue life than other Pb-free alloys. The large Ag_3Sn IMC strengthens the joint and further reduced the compliance of the solder as reported, thereby shortening thermal fatigue life (Frear, 1992). Prior studies have also shown that multicomponent solder alloy like Innolot is more reliable in thermal cycling since its fatigue exponent and coefficient increased 7.4% and 131.9% as compare with SAC387 (Tao et al., 2019).

2.8 Constitutive modeling of soldering materials

In electronic packaging, stresses induced by thermal mismatch can cause extensive plastic deformation at solder joints, which is responsible for low-cycle thermal fatigue failure of solder materials. Expression of total strain was proposed by Pan (1991).

$$\varepsilon_t = \varepsilon_e + \varepsilon_p + \varepsilon_c \qquad (2.1)$$

or more explicitly by:

$$\varepsilon_t = \frac{\sigma}{E} + C_1\sigma^n + \gamma_T^{\left(1-e^{-B\dot{\varepsilon}_S^t}\right)} + C_2\dot{\varepsilon}_S^t \qquad (2.2)$$

Where,

σ = stress

ε = strain

E = modulus of elasticity

n = reciprocal of the strain hardening exponent

C_1 = reciprocal of the strength coefficient

$\dot{\varepsilon}_s$ = steady-state creep-rate as a function of the applied stress

γ_T = primary creep Amplitude of strain

B, C_2 = material constants for creep response under deformation mechanism

The four terms on the right-hand side of Equation (2.2) are the elastic, plastic, time-dependent primary creep, and steady-state creep strain components. This relationship is also often referred to as the classical elastoplastic creep constitutive equation. Electronic solders have been extensively studied over the past two decades (Lau & Pao, 1997). It serves as the basis for constitutive modeling of solder alloy material behavior, covering stress-strain curve modeling and creep deformation constitutive modeling.

2.8.1 Stress-strain curve modeling

Tensile testing is often used to evaluate the mechanical properties of solder alloys in electronic packaging, and the measured data are used to develop constitutive models to describe the stress-strain response and corresponding mechanical properties (Yang & Pang, 1996). Tensile strength decreases significantly with decreasing strain rate and increasing test temperature, as shown by the following two equations (Hertzberg, 1996; Jones et al., 1997):

$$\sigma = C\dot{\varepsilon}^n \quad (2.3)$$

$$\sigma = -\alpha T + \beta \quad (2.4)$$

Grain size is the main factor to study the effect of microstructure evolution on the mechanical properties of metallic materials. Its effect can be described by the well-known Hall-Petch equation, which states that the YS of polycrystalline materials is inversely proportional to its grain size (Hertzberg, 1996).

$$\sigma_y = \sigma_i + KD^{-0.5} \quad (2.5)$$

Where,

σ_y = yield strength

σ_i = material constant of overall resistance of the lattice to dislocation movement

K = constant measuring the contribution of grain boundary hardening

D = grain size

Nose et al. (2003) conducted a parametric study of the tensile strength of Sn-Pb solder as a function of chemical composition, strain rate, and temperature. They found that both the elastic modulus and YS increased with increasing Sn content.

Tensile strength is described as:

$$\sigma = A_0 + x \log_{10} \dot{\varepsilon} + y \log_{10} T \qquad (2.6)$$

Where,

σ = stress

$\dot{\varepsilon}$ = strain rate

T = test temperature (K)

A_0, x, y = functions of the weight percentage of Sn in the alloy

Pang et al. (2004) developed a modified Ramberg-Osgood model to describe the temperature and strain rate dependent stress-strain curves of SAC solder. The Ramberg-Osgood model of elastoplastic behavior can be expressed as:

$$\varepsilon = \frac{\sigma}{E} + \alpha \left(\frac{\sigma}{\sigma_0}\right)^n \qquad (2.7)$$

The modified temperature and strain rate dependent Ramberg-Osgood model is described as:

$$\varepsilon\,(T, \dot{\varepsilon}) = \frac{\sigma}{E} + \alpha \left(\frac{\sigma}{\sigma_0(T,\dot{\varepsilon})}\right)^{n\,(T,\dot{\varepsilon})} \qquad (2.8)$$

The hardening exponent n and the stress coefficient σ_0 depend on temperature and strain rate:

$$\sigma\,(T, \dot{\varepsilon}) = \sigma_0 + aT^* + b\dot{\varepsilon}^* \qquad (2.9)$$

$$n\,(T, \dot{\varepsilon}) = n_0 + cT^* + d\dot{\varepsilon}^* \qquad (2.10)$$

In these relationships,

$$T^* = \frac{T - T_r}{T_m - T_r} \text{ and } \dot{\varepsilon}^* = \ln\left(\frac{\dot{\varepsilon}}{\dot{\varepsilon}_r}\right). \qquad (2.11)$$

Where,

a, c = temperature coefficients

b, d = strain rate coefficients

T_r = real temperature

$\dot{\varepsilon}_r$ = strain rate

T_m = melting temperature

n_0 = strain hardening exponent

σ_0 = stress coefficient

2.8.2 Constitutive modeling of dislocation creep

One of the most common failure causes in electronic systems subjected to temperature cycling is solder joint fatigue. For mechanical design, reliability assessment, and process optimization, a reliable and complete solder constitutive equation to evaluate the material characteristics is required. In electronic packaging, the fundamental purpose of thermo-mechanical analysis is to anticipate the reliability of solder joints and compare with testing results. Although several constitutive models for Sn-Pb and Pb-free solders have been utilized, the power law for secondary creep stage has become popular since it has a strong dependence on the applied stress and the intrinsic activation energy and a weaker dependence on grain size, and it is integrated in multiple commercial finite element software.

Creep is a type of material deformation that best describes the increase in deformation with time under constant load. It usually occurs because of a long-term exposure to certain levels of stress that are still well below the yield stress of a material. Creep can be frequently observed in materials which undergo a long-term exposure to heat, and it tends to increase at elevated temperatures of a given material. A typical solder creep curve is shown in Figure 2.47 that represents strain vs. time response for a constant applied stress.

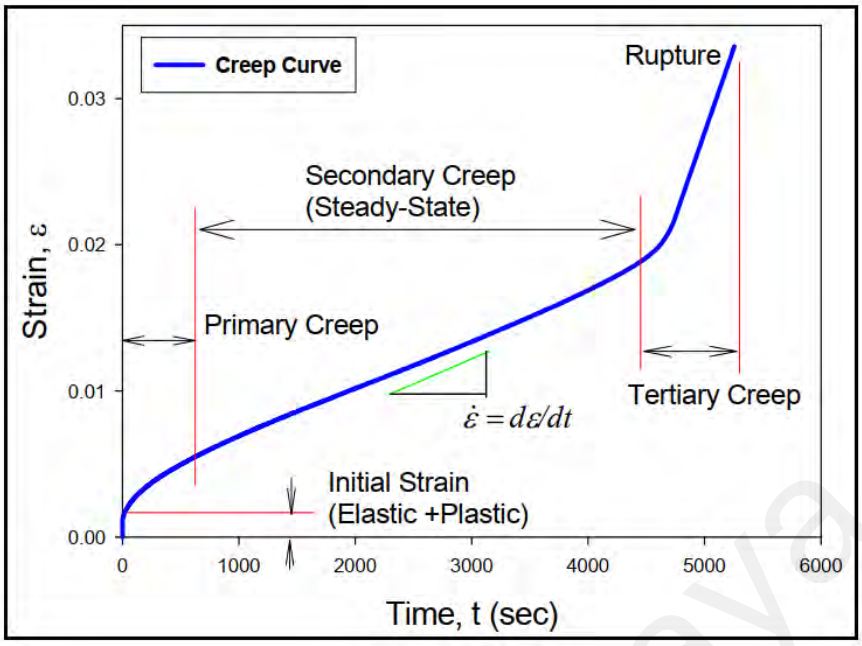

Figure 2.47: Typical SAC Solder Creep Curve (Motalab et al., 2012).

A typical creep curve consists of three distinct stages namely primary, secondary, and tertiary. At the primary stage, the strain rate is considerably high, but decreases with increasing time and strain. This is due to a process analogous to strain hardening at lower temperature. As the deformation further increases, the strain rate decreases and reaches the minimum value and becomes almost nearly constant. This is where the secondary creep stage starts to occur. The secondary stage is due to the balance achieved between work hardening and annealing process, also known as thermal softening process. The secondary creep zone is usually distinguished by a protracted period of almost constant slope. This slope is known as the steady state creep rate or creep compliance, and it is often applied as one of the essential material characteristics for solder in finite element simulations used to estimate solder joint durability by industries.

The lowest slope values in the secondary creep stage of the observed responses between $\dot{\varepsilon}$ (creep rate) and t (time) were used as the measured creep rates in most work and this study. The material is deformed plastically where the recovery effects such as high degree of strain hardening, and increased dislocation density are in concurrent as the creep rate

remains constant. As the tertiary creep region appears, a sudden transition to a virtually constant but greatly increased creep rate happens. At the third stage, the softening process is dominant. The increasing creep rate causes necking, cracking, and void formation within the material. Distributed damage occurs and eventually fracture can be observed. Ma & Suhling (2009) provided a review of the mechanical behavior and material characteristics of Pb-free solders. They demonstrated the need to use aging-dependent viscoplastic constitutive equations for SAC solders. There are several techniques to constitutive modelling of microelectronic solders in the literature. One classic work is done by Solomon (1990) who used a simple power law to define the connection between shear stress, shear strain, and shear strain rate. He demonstrated that a solder with a high Pb concentration was less temperature and strain rate sensitive than a Sn-Pb solder.

Busso et al. (1992) proposed a viscoplastic model based on continuum theory to evaluate the stress-dependence of the activation energy and the strong Bauschinger effect for Sn-Pb solder. In their models, they considered the kinematic hardening rule in plastic process, but they neglected isotropic hardening and static recover terms. By integrating grain boundary sliding and matrix dislocation deformation processes, Sung et al. (2002) created a novel viscoelastic model for Sn-Pb solder, highlighting the implications of grain and phase sizes on thermal fatigue life of eutectic solder connections. They also presented several internal stress tensor evolution models to characterize transient behaviors during tensile testing and first stage creep. In a unified constitutive model for Sn-Pb solder, Qian et al. (1997) used the back stress to represent the transient stage of a stress-strain curve.

For the solder with eutectic composition, Skipor (1996) used the Bodner Partom-constitutive relations to depict the internal inelastic deformation. Chen & Chen (2006) developed a constitutive model for Sn-Pb solder that included a kinematic hardening rule

and used it to predict isothermal cycle behavior under uniaxial and torsional pressure. For inelastic solder flow, an implicit constitutive integration approach was given.

For Sn-based solders, Darveaux and Banerji (1992) established a hyperbolic sine type power-law constitutive model that could predict creep flow for both low and high stresses. The Young's modulus and yield stress of Sn-Pb solder are significantly dependent on temperature and strain rate, according to Pang et al. (1998).

Creep mechanics emerged in the middle of the nineteenth century because of several unexpected failures of steam engines. Metals and alloys were the subject of the initial investigations. Due to technological demands, there was a growing interest in gaining a deeper understanding of creep occurrences. Norton (1929) looked at the secondary creep power law in respect to applications for different metals.

$$\dot{\varepsilon} = \frac{d\varepsilon}{dt} = A\sigma^m \qquad (2.12)$$

The introduced Equation (2.12) is for simple creep law, where ε represents the creep strain, $\dot{\varepsilon}$ the corresponding steady state creep rate, A is a material property based constant, and σ is the uniaxial stress.

Over the years, many researchers and engineers suggested various equations to describe creep mechanics. A general creep strain rate was then formulated as a function of the power law.

$$\dot{\varepsilon} = \frac{C\sigma^m}{D^h} e^{-\frac{Q}{kT}} \qquad (2.13)$$

Where,

C = constant which depends on the material and creep mechanism

D = grain size

h = constant which depends on creep mechanism

Q = activation energy of the material (J mol^{-1}),

k = Boltzmann constant (8.3145 J mol^{-1} K^{-1}),

T = Temperature

m = creep stress exponent

For m values which are within the range of 4-6, we can attribute it towards the dislocation creep mechanism. The movement of dislocations controls creep under high stresses which is relative to the shear modulus G. The activation energy Q is associated to self-diffusion for dislocation creep, the exponent, n is in the range 4-6, and $h = 0$ holds. It is proved that the applied stress and intrinsic activation energy have a substantial influence on dislocation creep, and the impact of grain size can be neglected.

Note that some alloys feature a very large stress exponent ($m > 10$). In this case, a threshold stress σ_{th} will be introduce and creep cannot be measured below this value. Equation (2.13) should be modified as follows:

$$\dot{\varepsilon} = \frac{A(\sigma-\sigma_{th})^m}{d^b} e^{-\frac{Q}{kT}} \qquad (2.14)$$

Where, A, Q and m can all be related to conventional mechanisms. The applied stress tends to drive the dislocations past the barrier. After bypassing an obstacle, dislocations get into a lower energy state. A significant part of the work required to overcome the energy barrier of passing an obstacle is provided by the applied stress, while the remaining impulse is provided by thermal energy. As a result, creep increases in these cases.

2.8.3 Diffusional creep mechanisms

Diffusion creeps can occur through two main deformation mechanisms. The first one was proposed by Nabarro and Herring and is shown in Figure 2.48(a). This mechanism

involves the flux of vacancies inside the grains. This migration of vacancies from the interior to the grain boundaries causes an increase in the grain length in the loading direction. Boundaries perpendicular to the loading direction are the source of vacancies. In contrast, boundaries parallel to this direction act as sinks for the flow of vacancies (Chawla & Meyers, 1999).

Another diffusion mechanism is proposed by Coble, as shown in Figure 2.48(b). In the case of Coble creep, the diffusion of vacancies occurs only at the grain boundaries and not within the grains. This diffusion process leads to grain boundary sliding. We can observe in Figure 2.48(b) that the grain elongation in the loading direction is caused by grain boundary sliding (Coble, 1963).

Diffusion creep is governed by the following constitutive equation:

$$\dot{\varepsilon} = \frac{\sigma\Omega}{kT}\left[A_{NH}\frac{D_L}{D^2} + A_C\frac{\delta D_{GB}}{D^3}\right] \qquad (2.15)$$

Where,

σ = stress

Ω = activation volume

k = the Boltzmann constant

T = temperature

δ = diffuse grain boundary width,

D_L, D_{GB} = diffusivities in the lattice and grain boundary

A_{NH}, A_C = Constants related to grain shape during Nabarro Herring and Coble creep

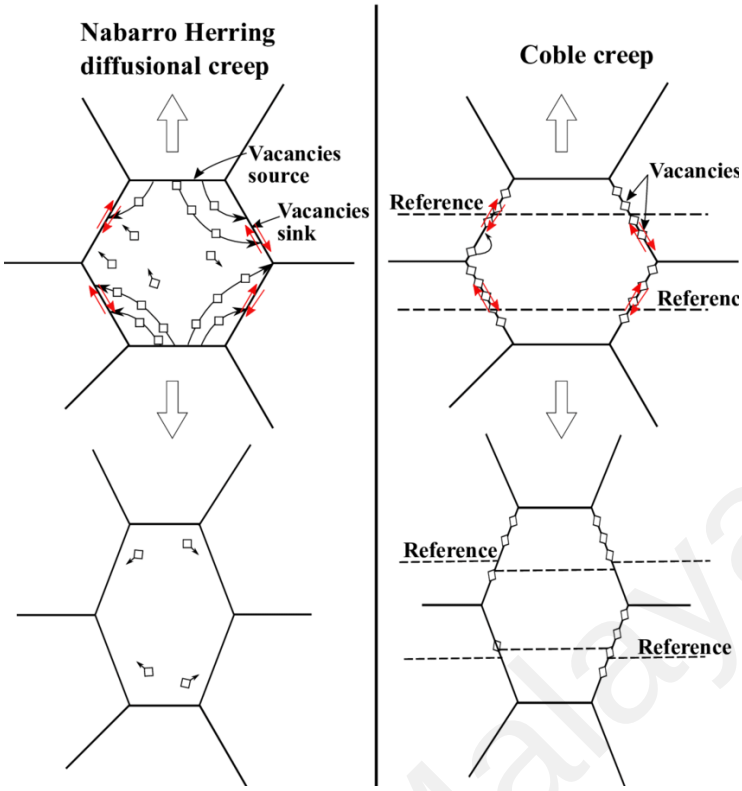

Figure 2.48: Grain boundary slides with respect to each other because of the diffusion of vacancies (a) from grain boundaries to the grain interior so-called "Nabarro Herring" diffusional creep mechanism, and (b) at grain boundaries Coble creep mechanism (Rida, 2018).

In Equation (2.15), the strain rate $\dot{\varepsilon}$ is proportional to the stress σ. Also, $\dot{\varepsilon}$ is proportional to D^{-2} for Nabarro-Herring creep and is directly proportional with D^{-3} for Coble creep. Therefore, to verify this mechanism, a series of creep tests should be performed at different stresses, grain sizes, and temperatures. Therefore, the slope of the log-log plot between σ and $\dot{\varepsilon}$ should be equal to one. Furthermore, the slope of the log-log plot between $\dot{\varepsilon}$ and d allows detection of which mechanism is active: Coble or Nabarro-Herring mechanism. Furthermore, to calculate the activation energy for grain boundary diffusion in the Coble mechanism or bulk diffusion in Nabarro-Herring mechanism, the Arrhenius diagram between $\dot{\varepsilon}$ and T should be studied at constants D and σ.

2.8.4 Garofalo creep model

Several models have been proposed to calculate creep parameters from the indentation depth versus time plots (Niranjani et al., 2012). However, recent studies have shown that among the various empirical creep models developed for characterizing primary and secondary stages creep behavior of metals and alloys used in electronic package on board level simulation, the Garofalo creep model is the most suitable model for analysis of softer materials and employed in the board level reliability simulation in ANSYS (Garofalo, 1963; Garofalo et. al., 1963). This model has been found which satisfies conditions for both high and low stresses and agrees well with experimental results. It also satisfies the linear relation found at temperatures near the melting point at low stresses (Lau et. al., 2018).

The generalized Garofalo creep model can be written as

$$\dot{\varepsilon}_{cr} = C_1[\sinh(C_2\sigma)]^{C_3} e^{\frac{-C_4}{T}} \qquad (2.16)$$

Where,

$\dot{\varepsilon}_{cr}$ = creep strain rate

σ = stress (Pa)

T = temperature (Kevin)

C_1, C_2, C_3, C_4 = material constant

2.9 Gap in the literature

The search for Pb-free replacements for Sn-Pb solders has been carried on for more than a decade. The alloy SAC305 has been widely accepted in Japan, SAC387 is now the leading Pb-free choice in the EU, and SAC396 has gained its popularity with the U.S. companies. However, the reliability of Pb-free solders, used in harsh conditions such as

in automotive, is still a serious concern. Simultaneous additions of multiple alloying elements like Bi, Sb, Ni etc. to conventional SAC based solders have recently been investigated to improve their reliability. Despite improvements brought by the effects of additional elements, the mechanical performances of multicomponent solder alloy have not been investigated. The effects of each additional element on the microstructural stability during thermal aging are lacking in literature.

Therefore, the effects of simultaneous additions of Bi, Sb and Ni to SAC305 solder on the evolution of microstructure and mechanical properties of the solder under thermal aging for long time should be investigated. Superior microstructural stability and improved mechanical strength of the multicomponent alloy at long aging time and its fracture behavior in tensile and creep testing should be discussed. To understand more knowledge about creep performance of multicomponent solder and its fracture behavior after creep testing, fractographies and corresponding EDX analysis should be studied to determine the creep mechanism and precipitates effects. Other than that, microhardness tests shall also be conducted on both solder samples to get further in-depth study on the hardness of material after the creep test. Lastly, only a few studies address stress distribution and creep strain analysis during temperature cycling test of SAC305 alloy applied in newly developed Pb-free packages. Thus, the simulation of application of SAC305 in a novel quad flat package by using FEM should be conducted and the stress distribution and creep strain analysis during temperature cycling test should be reported and compared with experimental results.

CHAPTER 3

RESEARCH METHODOLOGY

3.1 Overview of methodology

In this chapter, the experimental procedure and simulation process of this study is explained in detail. The materials and methods used for achieving the objectives are presented. The flowchart of research methodology used is schematically shown in Figure 3.1.

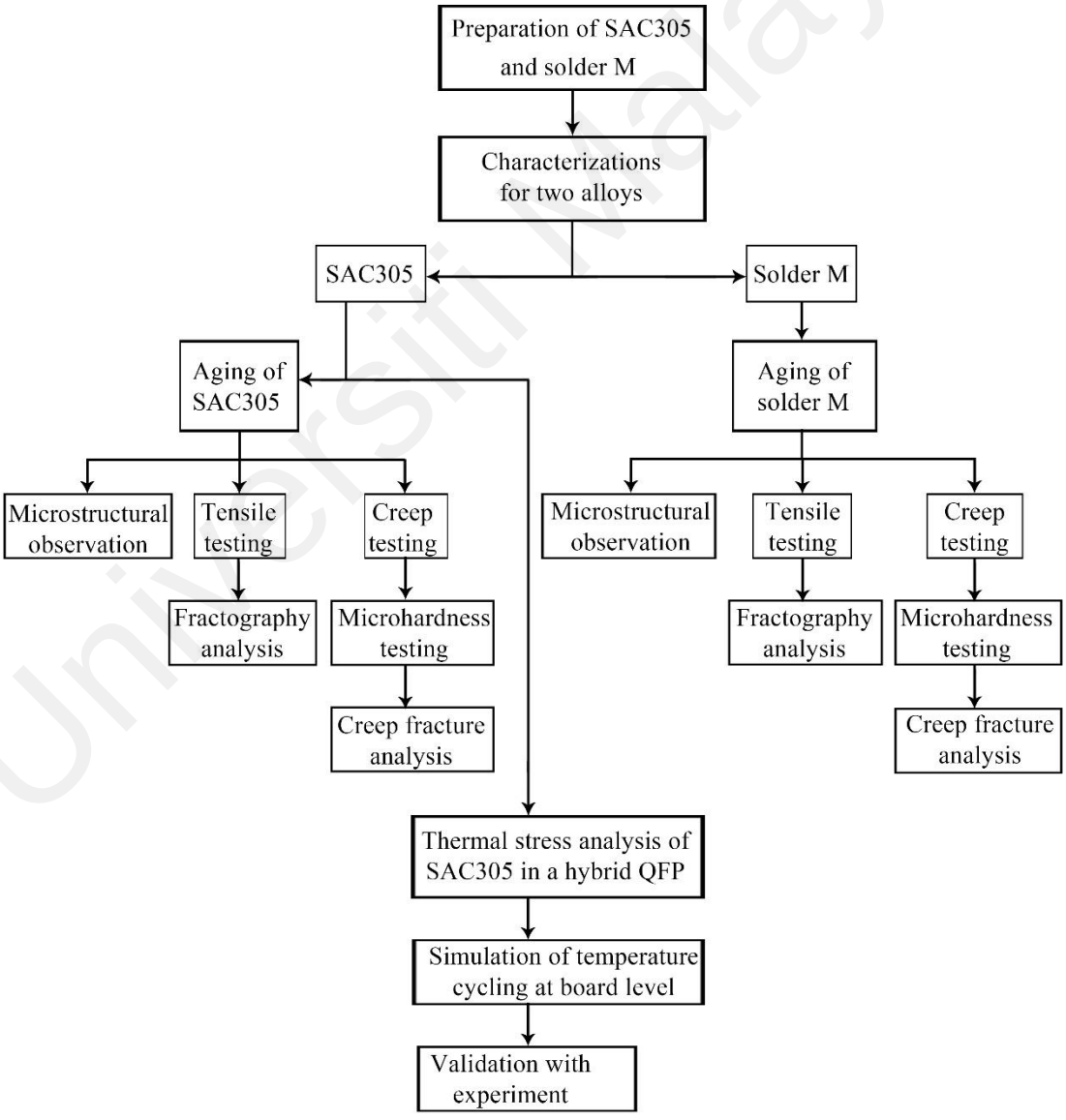

Figure 3.1: Flowchart of the research methodology used.

3.2 Raw materials and aging procedure

Two types of solder alloys, SAC305 and a SAC305 based multicomponent solder, referred to as solder M with composition of Sn-3.0Ag-0.5Cu-3.2Bi-2.95Sb-0.037Ni (SMIC Senju Metal Industry Co., Ltd.) were used in this study. Sheet-type specimen with 25 mm gauge length was prepared by following American Society for Testing and Materials (ASTM) standard (E8/E8M-13a). As-received solder bars were first compressed to 2 mm thick sheet plates by using a high accuracy rolling machine. The compressed sheet plates were cut into dog bone shape test samples by water jet with 100 mm total length and 10 mm width of grip section as shown in Figure 3.2. After that, samples were annealed for 24 h at 100 ℃ to eliminate any surface residual stresses. Thermal aging was performed on the solder samples in an oven at 125 ℃ for duration with 24 h, 168 h, and 1008 h, respectively.

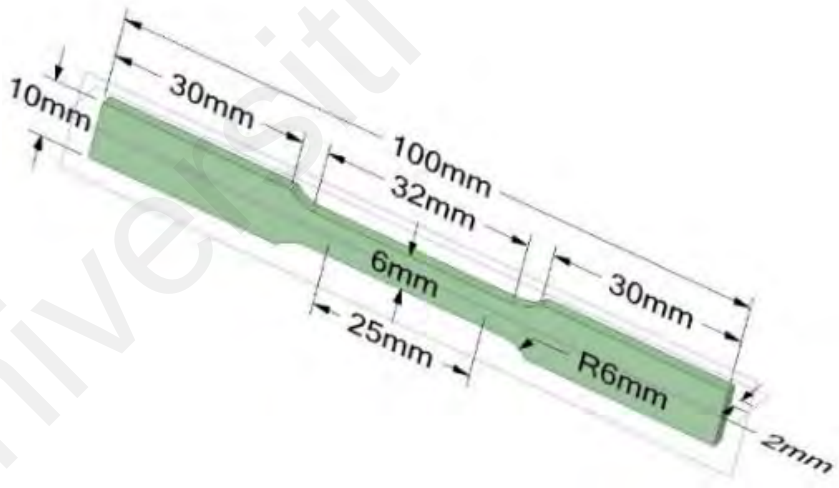

Figure 3.2: Tensile testing specimen with its dimension.

3.3 Characterizations of SAC305 and solder M

3.3.1 Chemical analysis in solder alloys

The bulk solder specimens were chemically analyzed by X-ray fluorescence spectroscopy (XRF, Rigaku NEX CG, Japan).

3.3.2 Examination of chemical compounds in solder alloys

The phase formations of the two solder alloys were analyzed in X-ray diffraction (XRD, Rigaku MiniFlex, Japan) examination. The XRD was operated at 40 kV and 15 mA using a Cu-Kα radiation source. The diffraction angle (2θ) was carried out from 3° to 90° with a scanning speed of 10°/min and a step size of 0.02. The crystal structures were identified by matching the XRD peaks with the database from the international center for diffraction data (ICDD).

3.3.3 Melting point examination of solder alloys

The melting points of SAC305 and solder M were determined by using differential scanning calorimetry (DSC, Mettler DSC 820, Switzerland). The sample (~ 10 to 15 mg) was placed on a 70 ml platinum crucible. It was heated in the DSC furnace at a rate of 10 ℃/min to 280 ℃. The melting points of two solder alloys were calculated from the onset temperature.

3.4 Microstructure observation procedure

3.4.1 Test specimen preparation

A small length of the sample was cut from the sheet-type specimen by using diamond cutter after each thermal aging interval, and the exposed cross-sectional area of the uniaxial specimen was then carefully polished within the molded resin which served as a convenient grip. Etching was performed for 20 seconds for both solders. The composition of etching solution for SAC305 is methanol (CH_3OH) and hydrochloric acid (HCl) within the volume ratio of 95:5, and etchant for solder M is a mixture of methanol (CH_3OH), hydrochloride acid (HCl), and nitric acid (HNO_3) in the volume ratio of 93:5:7.

After the specimens were polished and etched, carbon double-sided tape was attached surrounding the boundary of cross-sectional surface to provide good conduction for SEM analysis. The morphology of the surface of cross-section and fracture surface of sample

were investigated by SEM coupled with EDX. The grain on solder surfaces and IMC particles were taken over 10 backscattered electron images under 15kV from 5 samples at a magnification of 10k. Image J software (version 1.53t, LOCI, University of Wisconsin) was utilized to conduct the measurements of grain sizes and IMC particles.

3.4.2 Equipment set up

The etched samples for microstructural observation were tested by Phenom™ ProX Desktop SEM. The SEM image was operated by a software named Phenom ProSuite. The microstructural images and morphology figures of the solder alloys were displayed in the computer and saved in the computer.

3.5 Tensile testing procedure

3.5.1 Test specimen preparation

Uniaxial tensile tests were experimented on two types of solder samples with dog bone shape at RT by using Instron 3369 tensile tester. Strain rates of 10^{-4}/s, 10^{-3}/s and 10^{-2}/s were applied in tensile tests for samples with different thermal aging duration. Tensile testing was repeated 5 times by using 5 same solder specimens under each testing condition as listed in Table 3.1. The values of UTS, elongation, and toughness of 5 specimens were recorded and analyzed.

Table 3.1: Number of samples tested for two types of solders under different strain rates.

Strain rate / Aging time	**10^{-4}/s**	**10^{-3}/s**	**10^{-2}/s**
0h	5 pcs	5 pcs	5 pcs
24h	5 pcs	5 pcs	5 pcs
168h	5 pcs	5 pcs	5 pcs
1008h	5 pcs	5 pcs	5 pcs

3.5.2 Equipment set up

Tensile tests for dog bone shape specimens at RT were conducted by using Instron 3369 tensile tester. One integrated software package named Instron's Series IX/s software was applied for data acquisition, control, data analysis and report generation functionality of tensile testing.

3.6 Creep testing procedure

3.6.1 Test specimen preparation

Monotonic creep tests were experimented on two types of solder samples with dog bone shape at RT by using Shimadzu Autograph AGS-X 5kN universal testing machine. Variable creep stresses 20 MPa (24.2% of UTS), 30 MPa (36.5% of UTS) and 40 MPa (48.4% of UTS) were applied for solder M with different thermal aging duration in creep tests, whereas 11.3 MPa (24.2% of UTS), 17MPa (36.5% of UTS) and 20 MPa (42.9% of UTS) were applied for SAC305. The maximum creep testing time was up to 5×10^4 s. To reduce the experimental errors of the measurements and to get the most reliable results, creep testing was repeated 5 times by using 5 same solder specimens under each testing condition.

3.6.2 Equipment set up

Shimadzu Autograph AGS-X 5kN universal testing machine was used in creep experiments. The software named Trapezium X analyzed the creep result connecting to the universal testing machine of which the creep data was collected and processed during experiment.

3.6.3 Testing parameters

The number of samples of two solders under different creep stresses after variable thermal aging time are listed in Table 3.2 and 3.3. Noted the aging temperature was 125 °C, creep test was conducted at RT and test maximum period was up to 5×10^4 s.

Table 3.2: Number of samples tested for SAC305 under different creep stresses applied.

Stress / Aging time	**11.3MPa**	**17MPa**	**20MPa**
0h	5 pcs	5 pcs	5 pcs
24h	5 pcs	5 pcs	5 pcs
168h	5 pcs	5 pcs	5 pcs
1008h	5 pcs	5 pcs	5 pcs

Table 3.3: Number of samples tested for solder M under different creep stresses applied.

Stress / Aging time	**20MPa**	**30MPa**	**40MPa**
0h	5 pcs	5 pcs	5 pcs
24h	5 pcs	5 pcs	5 pcs
168h	5 pcs	5 pcs	5 pcs
1008h	5 pcs	5 pcs	5 pcs

3.7 Microhardness testing procedure

3.7.1 Test specimen preparation

Vickers microhardness tests were conducted for the fractured samples by using Shimadzu G-21 series microhardness tester after creep tests. The load 9.807 N and holding time 10s were set for the indenter. From the fracture tip to another side, 9 indentations were tested with 400μm in between them to avoid plastic deformation region. Microhardness tests

were repeated for 5 times along 5 straight lines with the same direction as shown in Figure 3.3.

The mean values of microhardness were recorded and analyzed. There were 45 indenters (9 spots along 5 lines) applied on each sample after creep tests.

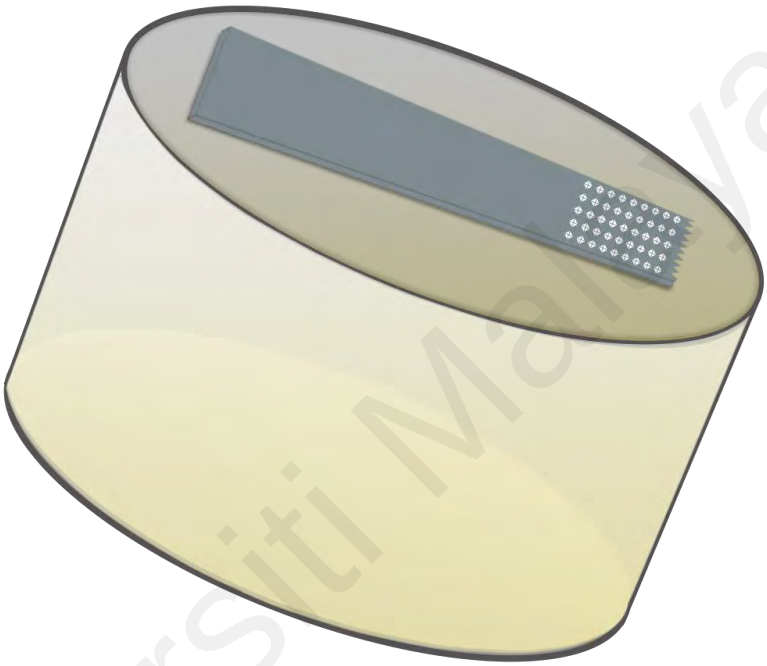

Figure 3.3: Diagram of microhardness testing specimen and indentations.

3.7.2 Equipment set up

The Vickers microhardness tests were conducted by using Shimadzu G-21 series microhardness tester.

3.7.3 Testing parameters

Figure 3.4 illustrates the four-sided pyramid of Vickers tip. The implanted indenter in the Pb-free solder alloy surfaces as indicated in the side view from the schematic imprinted the projected area utilized for the hardness assessments after the force applied (Yahaya & Mohamad, 2017).

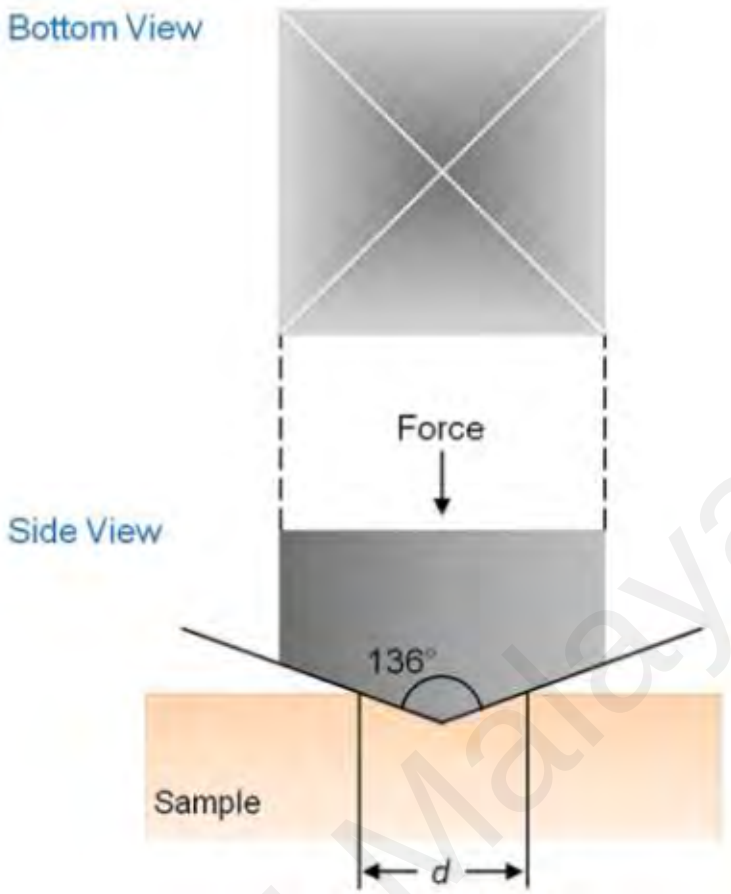

Figure 3.4: Schematic of Vickers microhardness indentation (Yahaya & Mohamad, 2017).

The equation for Vickers microhardness (HV) is as below:

$$\mathrm{HV} = \frac{2F\sin\frac{136^\circ}{2}}{p^2} = 1.854\frac{F}{p^2} \qquad (3.1)$$

Where,

F = indentation force (kgf)

p = average length of the diagonal left by the indenter (mm)

3.8 Statistical analysis of raw data

The data obtained were analyzed by using Statistical Package for the Social Science (version 26, SPSS Inc., Chicago, USA) for Windows. A repeated measures (RM) ANOVA test was performed to statistically analyze the size values of the grain and IMCs

in treatment groups at different thermal aging durations. Based on the Shapiro-Wilk test, the data of measured sizes of grain and IMCs of two solder alloys distributed was evaluated at each thermal aging timepoint. Furthermore, a Mauchly's test indicated assumption of sphericity had not been violated ($p > 0.05$). Hence, the data were analyzed without any correction for sphericity. Following RM ANOVA test, a pairwise comparison among mean grain sizes of all the possible group pairs followed with Bonferroni correction was performed.

3.9 Modelling of thermal fatigue failure in ANSYS

A quarter of PCB assembly of the QFP package was modeled in ANSYS software of which SAC305 alloy was applied in the package as shown in Figure 3.5. The newly designed hybrid 10 mm x 10 mm QFP with 100 I/O having two layers of different types of leads (inner J-lead, outer gull wing) are placed in an interdigitated trace pattern. Due to the symmetry about the vertical midplane of a whole QFP package, a quarter of the square model would be enough to reflect the performance in thermal analysis. Coupled in-plane translations were applied to the other symmetry plane to produce a state of generalized plane strain. The boundary condition was set as a fixed plane for the cross sections of the model in Figure 3.5.

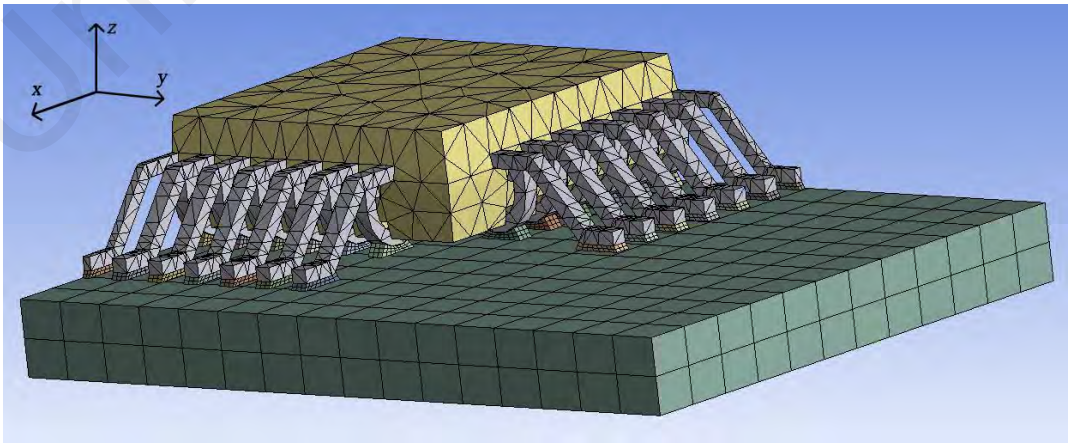

Figure 3.5: 3D QFP model for thermal analysis after meshing.

The properties of materials used in this study are listed in Table 3.4.

Table 3.4: Properties of materials used in fatigue failure modelling.

Materials	Young's modulus (GPa)	Poisson's ratio	CTE (ppm/ ˚C)
SAC305	43.25	0.3	21.725
Copper alloy lead	117	0.33	16.7
Silicon	131	0.278	2.8
PCB	E_x=20	$\nu_{xy} = 0.11$	α_x=12.5
	E_y=18	$\nu_{yz} = 0.09$	α_y=11.4
	E_z=15	$\nu_{xz} = 0.14$	α_z=82
Epoxy mold compound (EMC)	19	0.25	10 (<150 ˚C)

SAC305 was applied as solder joint to connect the QFP and PCB as shown in Figure 3.6. The footprint of J-lead is on the inner side on printed circuit board and gull wing lead is on outer side. Using exclusively hexahedral solid elements, the model could capture the precise shape of the SAC305 solder joint applied in the package and potential effects of distance to neutral point (DNP) while retaining significant computational efficiency over full octant models. To have fine meshing for convergence and accurate results, the meshing size for both two types of lead were 0.01 mm based on the small size of the models.

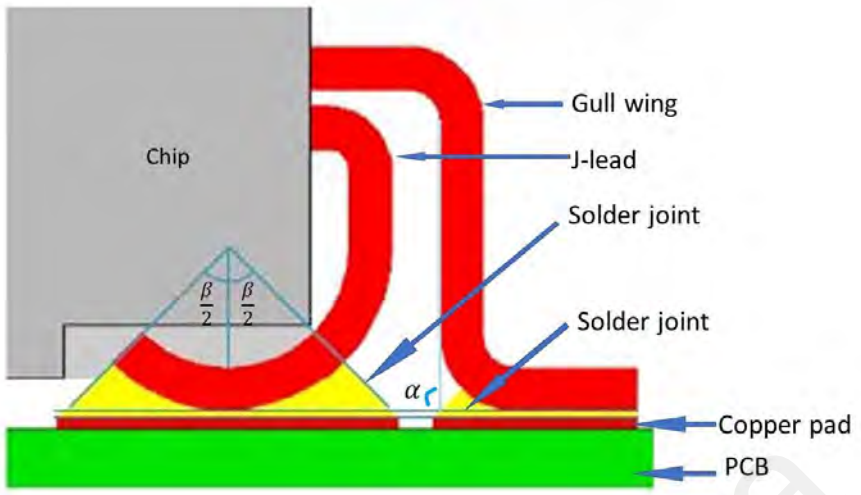

Figure 3.6: Schematic of SAC305 applied in QFP package.

In Figure 3.7, heating and cooling are achieved by forced convection, and the maximum ramp rate is 11 ℃ per minute. The temperature cycling is from -40 ℃ to 125 ℃ and dwells for 15 minutes, then ramps down to -40 ℃ and dwells for another 15 minutes, then ramps up to 125 ℃ and dwells for 15 minutes again, and so for. The ramp up and ramp down times are 15 minutes each. The temperature cycling simulation started from stress free status within 175 ℃ where there was no compression between each material in the assembly. Five temperature cycles were executed.

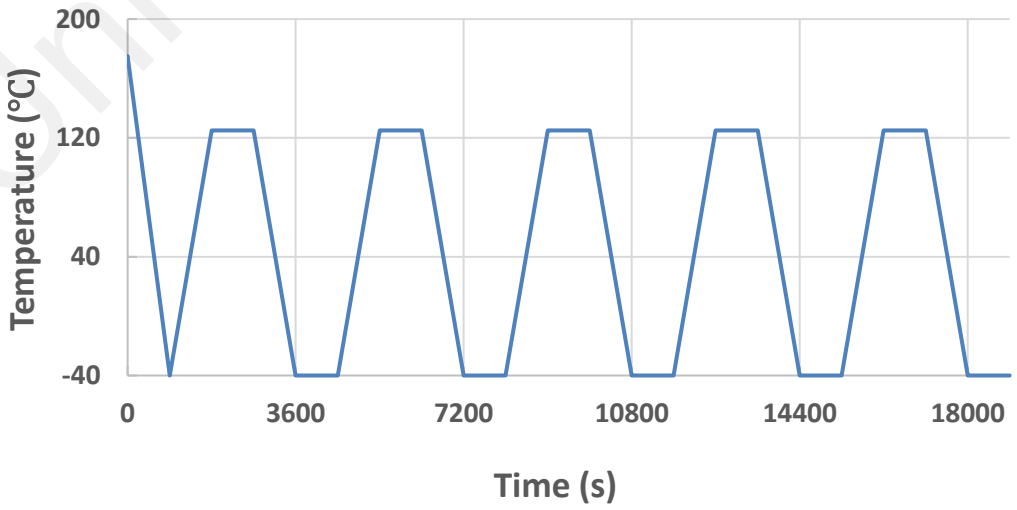

Figure 3.7: Temperature cycling setup and profile.

The creep behavior of solder was summarized empirically using the following equation:

$$\dot{\varepsilon}_{cr} = A\sigma^{m} e^{-Q/RT} \qquad (3.2)$$

Where,

$\dot{\varepsilon}_{cr}$ = creep strain rate

A = material constant

σ = flow stress

m = stress exponent

Q = creep activation energy

R = gas constant

The SAC305 solder material is assumed to follow the generalized Garofalo creep model:

$$\dot{\varepsilon}_{cr} = C_1[\sinh(C_2\sigma)]^{C_3} e^{\frac{-C_4}{T}} \qquad (3.3)$$

Where,

$\dot{\varepsilon}_{cr}$ = creep strain rate

σ = stress (Pa)

T = temperature (Kevin)

C_1, C_2, C_3, C_4 = material constant

To evaluate the number of cycles to failure of solder joint under chip corner, Coffin Manson criterion was applied where creep strain accumulated over thermal cycles is expressed as an empirical relation in:

$$N_f = \Theta(\Delta\varepsilon_{cr})^{-c_5} \quad (3.4)$$

Where,

N_f = number of cycles to failure

$\Delta\varepsilon_{cr}$ = creep strain per cycle

Θ, C_5 = corresponding coefficients of SAC305

3.10 Experimental validation of thermal fatigue failure simulation

To validate the simulation results, 100 hybrid QFPs mounted on PCBs in daisy chain setting up were placed in temperature chamber for board level temperature cycling test as shown in Figure 3.8(a). Surface mount technology has been applied and SAC305 solder material was chosen on this research to mechanically support and electronically connect this hybrid quad flat package to a printed circuit board. The quad flat packages and the printed circuit boards were baked under 125 °C for 24 hours to avoid the popcorn effect of the board. Prior to soldering, the solder paste with flux was printed onto the printed circuit board with a stencil particularly designed for the sample. The reflow process was carried out at 240 °C for 60 seconds.

The temperature profile was the same as shown in Figure 3.7, and 9928 cycles were proceeded by following JEDEC standard (JESD22-A104-B). The samples for the temperature cycling test were vertically socketed in standoff of temperature chamber in cascade way as shown in Figure 3.8(b).

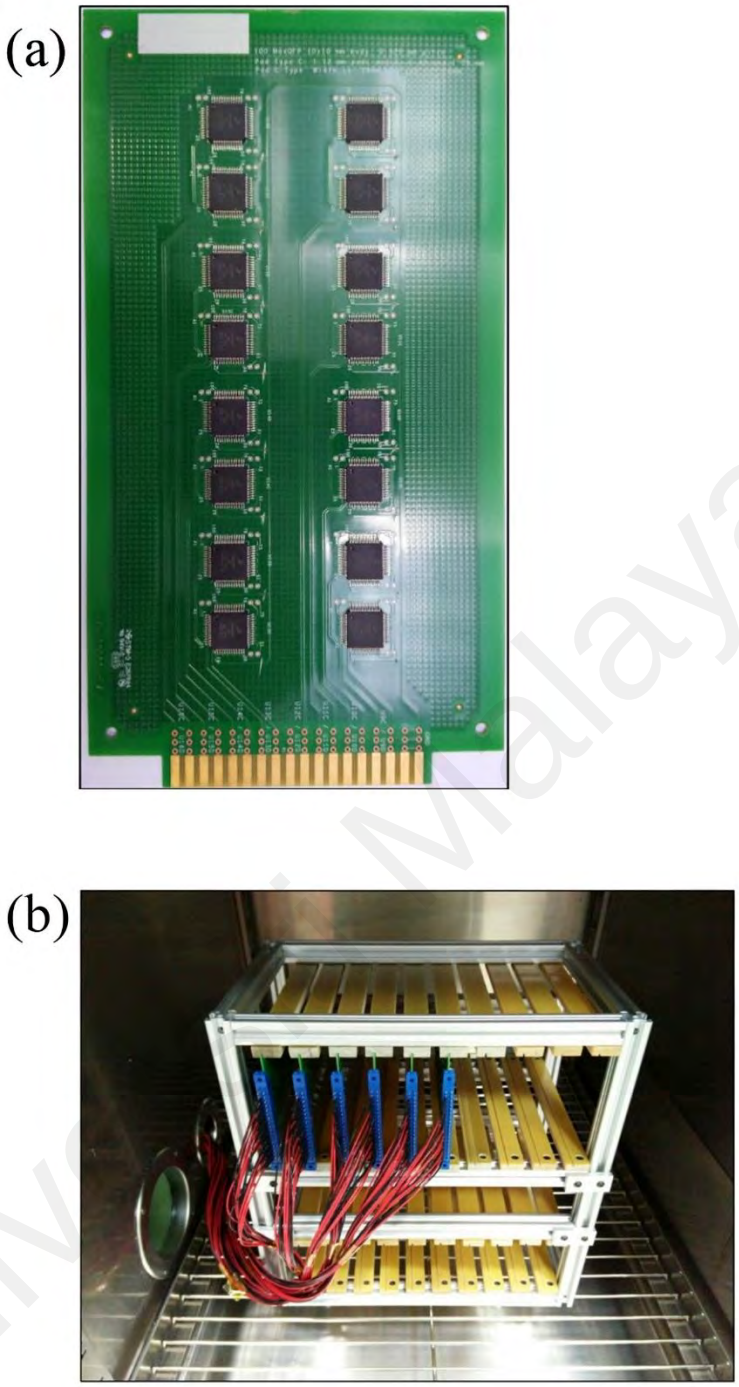

Figure 3.8: (a) QFP test units mounted on PCBs by using SAC305; (b) QFP board level test units in daisy chain setting up placed in temperature chamber.

CHAPTER 4

RESULTS AND DISCUSSIONS

4.1 Characterization of solders

4.1.1 Chemical analysis of solders

The bulk solder specimens were subjected to XRF analysis, and their chemical components were examined and given in Table 4.1. The result is confirmed within the range of the inspection report from the supplier.

Table 4.1: The chemical compositions of SAC305 and solder M (wt.%).

	Ag (%)	Cu (%)	Bi (%)	Sb (%)	Ni (%)	Sn (%)
SAC305	2.97	0.56	-	-	-	Balance
Solder M	3.25	0.67	3.2	2.8	0.037	Balance

4.1.2 Phases present in the solders

Figure 4.1 shows the XRD analysis results of solder M and SAC305 alloy. According to XRD analysis, the IMC Ag_3Sn and Cu_6Sn_5 were formed in β-Sn matrix of both solder alloy structures. Solder M contains all these three phases, in addition, it also contains IMC SbSn, and Bi phase. The phases remain the same during aging at 125℃ for up to 1008h. This indicated that the thermal aging did not result in new IMC formed in both solder alloys.

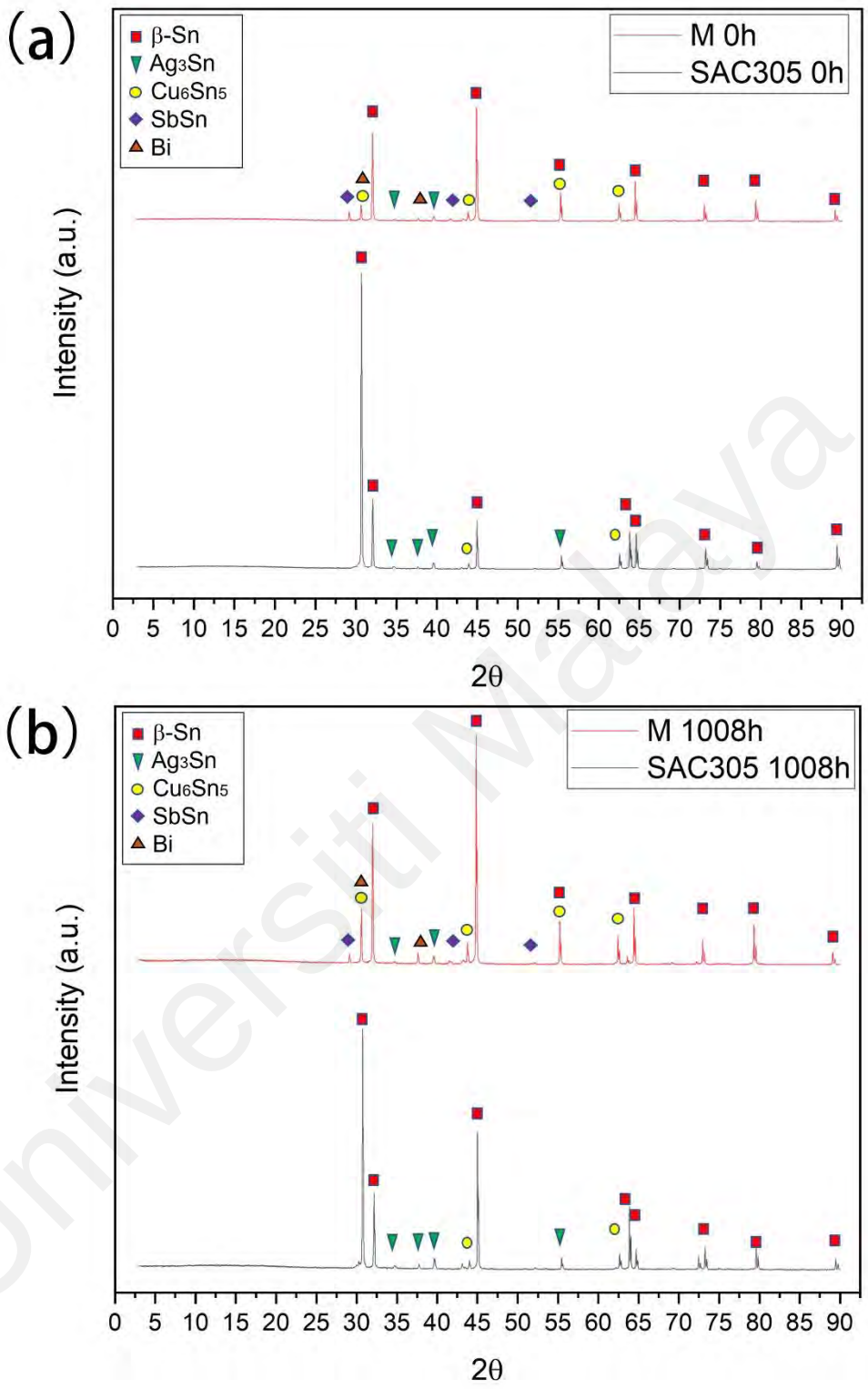

Figure 4.1: XRD analysis results of SAC305 and solder M after (a) 0h aging and (b) 1008h aging at 125 ℃.

4.1.3 Melting points of solders

As shown in Figure 4.2, melting temperatures were measured as 223.9 ℃ for solder M and 223 ℃ for SAC305 alloy according to DSC analysis results. According to the results obtained, the melting temperature of solder M is higher than SAC305. Hence, the simultaneous additions of multiple alloying elements like Bi, Sb, Ni slightly increased the melting point of SAC solder. This slight increase is unlikely to have an impact on the manufacturing process.

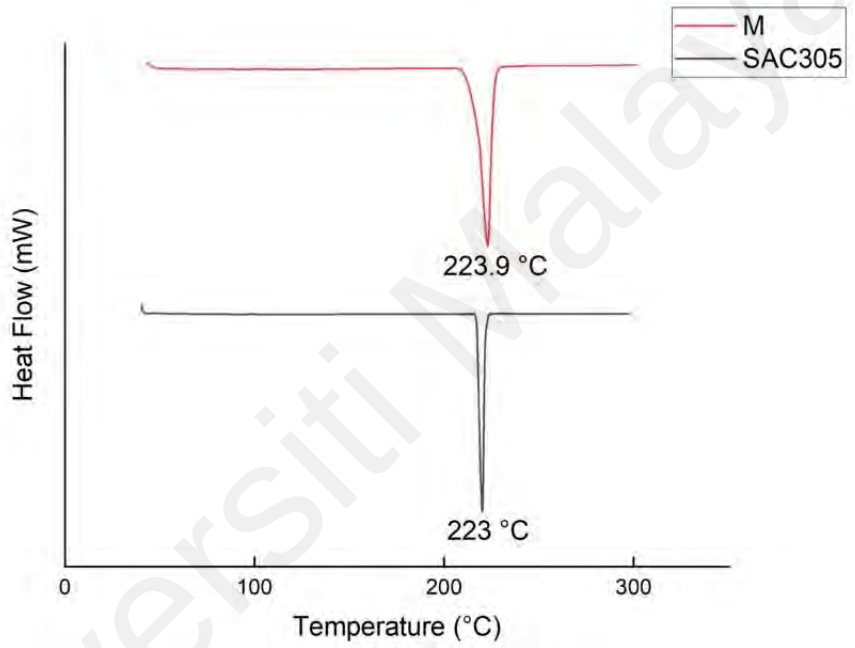

Figure 4.2: Melting temperatures of SAC305 and solder M from DSC testing.

4.2 Thermal aging effects on tensile properties of SAC305 and solder M

4.2.1 Microstructure evolution during thermal aging

The grains of solder M are clearly seen in SEM after etching. Grains with dark line boundary are identified in Figures 4.3(a-d). At 24 h aging time under 125℃, the grain diameter increased to 2.38 µm as compared to the as-received sample of 1.42 µm as shown in Figure 4.3(a). After 24 hours, the grain diameter continued to increase with aging time. The average grain diameter increased to 3.59 µm at 168h and 3.98 µm at 1008h, respectively. However, the rate of grain growth reduces after 168 h. The difference

of grain sizes is lesser between thermal aging of 168h in Figure 4.3(c) and 1008 h in Figure 4.3(d). During the grain growth, grain boundaries expanded, and small grains coalesced, thus formed a larger grain.

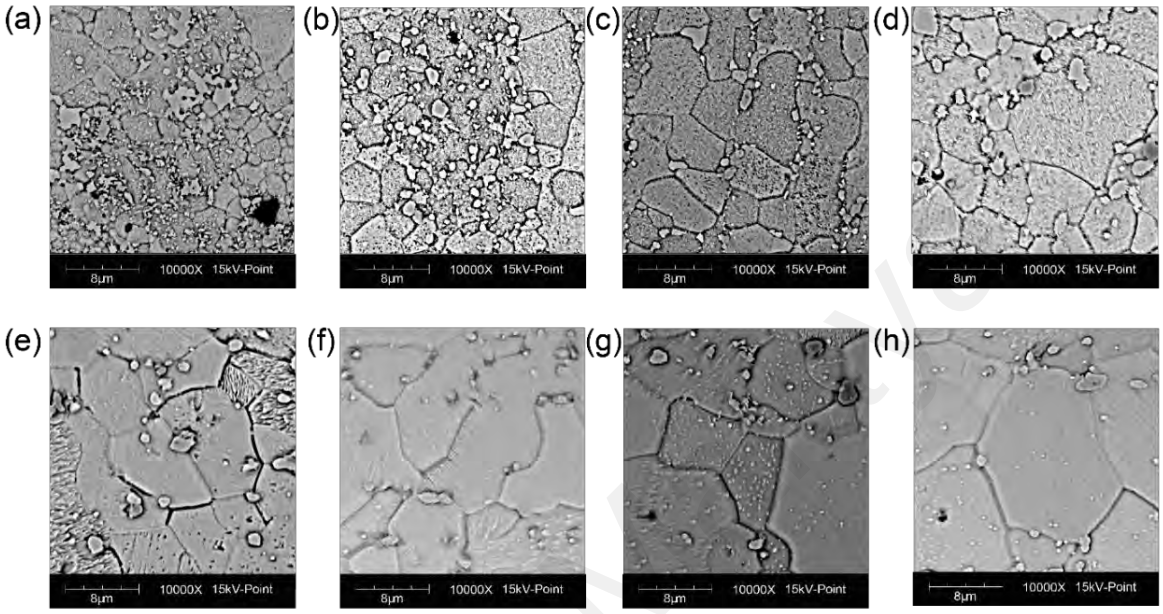

Figure 4.3: SEM images of solder cross section after 125°C aging: (a) solder M 0 h; (b) solder M 24 h; (c) solder M 168 h; (d) solder M 1008 h; (e)SAC305 0 h; (f) SAC305 24 h; (g) SAC305 168 h; (h) SAC305 1008 h.

The change of grains size as a function of thermal aging time is plotted in Figure 4.4. Average grain diameter of solder M increased by 180.3% after 1008 h thermal aging. In comparison with solder M, the average grain diameter of as-received SAC305 is 3.53 μm which is 2.5 times larger than solder M shown in Figure 4.3(e). After 24 h thermal aging, the grain diameter of SAC305 increased to 4.74 μm. However, the grain growth rate of SAC305 consistently increases to 6.53 μm and 10.6 μm after 168 h and 1008 h, respectively. The trend of grain growth of SAC305 against thermal aging time is also plotted in Figure 4.4. The average grain diameter of SAC305 increased by 200.3% of the as-received sample after 1008 h of thermal aging. The grain growth rate of SAC305 is like solder M during the first 24h thermal aging. However, the grain growth rate of solder

M is reduced after 168 h while the rate of SAC305 is still increasing till the end of thermal aging.

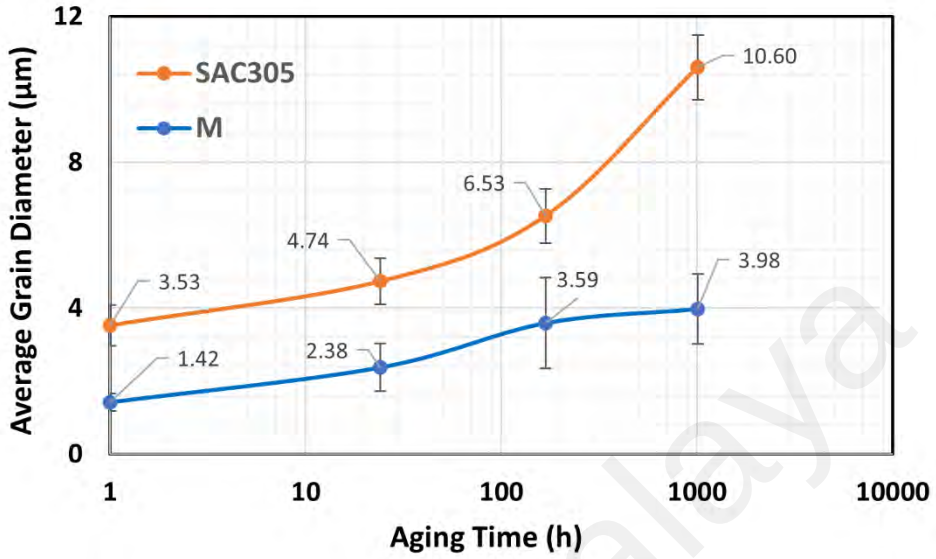

Figure 4.4: Change of grain size of SAC305 and solder M during thermal aging.

RM ANOVA showed that there was significant difference between the mean grain sizes of solder M and SAC305 at each thermal aging timepoint ($p < 0.05$). Furthermore, a pairwise comparison showed significant differences between the mean grain sizes of two solder alloys at each thermal aging timepoint.

It was observed that high temperature aging caused significant grain growth. The change of grain size during thermal aging indicated the occurrence of dynamic recrystallization. It is well known that when alloy is subjected to hot deformation (temperature higher than half of the melting point), the processes of strain-hardening and softening are concurrent (Xu & Pang, 2006; Kim et al., 2003). Hot deformation may involve in the process of dislocation redistribution due to vacancy climb, the formation of recrystallization nuclei, and their growth by migration of large angle boundaries under appropriate condition (temperature, amount, and rate of deformation). However, after the thermal aging, the solder M displayed a slower rate of grain growth than SAC305, and finer microstructure

with clearer grain boundary. It showed that the additional elements of Bi, Sb, and Ni could suppress grain growth rate and improved microstructural refinement during thermal aging (Tao et al., 2019; Tao et al., 2020; El-Daly et al., 2013).

Besides the observation of grain in Figure 4.3, the precipitations on both solders were investigated. The size of IMCs increased as observed on both solders during thermal aging. The majority compound on cross section of solder M is β-Sn. IMCs contained Ag, and Cu were found on the surface of both solder M and SAC305. In addition, particle Bi, and IMCs contained Sb and Ni were found on solder M surface. Sb and Ni acted as nucleation sites, leading to accelerated solidification of Sn and shorter time spans for IMC growth, which resulted in microstructural refinement and suppression of IMC growth (Hammad, 2018; Tao et al., 2015; Tao et al., 2019; Li et al., 2020).

Furthermore, Sb atoms were found in SbSn phase which not only contributed to suppressing the coarsening of the β-Sn matrix, but also provided precipitation strengthening (El Basaty et al., 2017). Moreover, the addition of minor Ni element in the solder M significantly decreased the grain size of the IMC phase. This was caused by the Cu atoms were replaced by Ni atoms during the crystallization of Cu_6Sn_5 due to the similar atom size between Cu and Ni (Tao et al., 2016). A small amount of dispersed $(Cu,Ni)_6Sn_5$ phase can be formed in the primary phase and network eutectic structure, which can refine the primary β-Sn phase (Zhao et al., 2019).

4.2.2 Aging effects on stress-strain response of SAC305 and solder M

The effect of 125°C aging on the stress-strain behavior of solder M and SAC305 samples under strain rate 10^{-3}/s are illustrated in Figures 4.5(a-b). Overall, the initial linear behavior of the average stress-strain curves is slightly affected by thermal aging time, while the post yield behavior changes dramatically with aging. Plots of the variation of UTS and percentage of elongation during thermal aging are shown in Figures 4.6(a-b)

respectively. UTS of solder M is higher than SAC305 during thermal aging. UTS of solder M increased 2% after the first 24 h of thermal aging in compared to as-received sample of 82.7 MPa (lower than the UTS 95 MPa of Innolot), then it reduced another 3% to 80.2 MPa in the end of 1008 h (Gyenes et al., 2017). In contrast, UTS of SAC305 kept reducing from 46.6 MPa to 26.6 MPa during 1008h thermal aging, which showed 44.2% reduction. As for elongation, as-received solder M showed 8% larger than SAC305. The change of solder M elongation showed a decreasing trend during 1008 h of thermal aging, while the elongation of SAC305 increases. After 1008 h thermal aging, percentage of SAC305 elongation was 26.1% larger than solder M. Besides aging time, the mechanical properties of solders were greatly affected by the alloying elements.

Overall, Bi, Sb and Ni can individually improve the strength of SAC solder which was investigated in previous studies. Bi was suggested to improve the strength of tin due to solid solution and precipitation strengthening, while Sb was suggested to cause precipitation strengthening (El-Daly et al., 2015; Kang et al., 2021; Miric, 2010; El-Daly et al., 2014; Hammad, 2018). Besides, the microstructural refinement caused by Sb and Ni further improved the strength of SAC solder (Miric, 2010; El-Daly et al., 2014; Lopez et al., 2010). For addition at lower than 2 wt.%, Bi dissolves in the β-Sn matrix according to the binary Bi-Sn phase diagram and causes solid solution strengthening.

The addition of Bi greater than 2 wt.% results in Bi precipitation in the β-Sn matrix (El Basaty et al., 2017; Okamoto, 2010; Shen, et al., 2015; Tateyama, et al., 2000). Both mechanisms improved the UTS of SAC solder. However, the UTS reduced when the weight percentage of Bi increased to 5 wt.% (Ali et al., 2021). Therefore, 3.2 wt.% of Bi in solder M is expected to enhance the tensile strength of the SAC solder as it was observed in the present study.

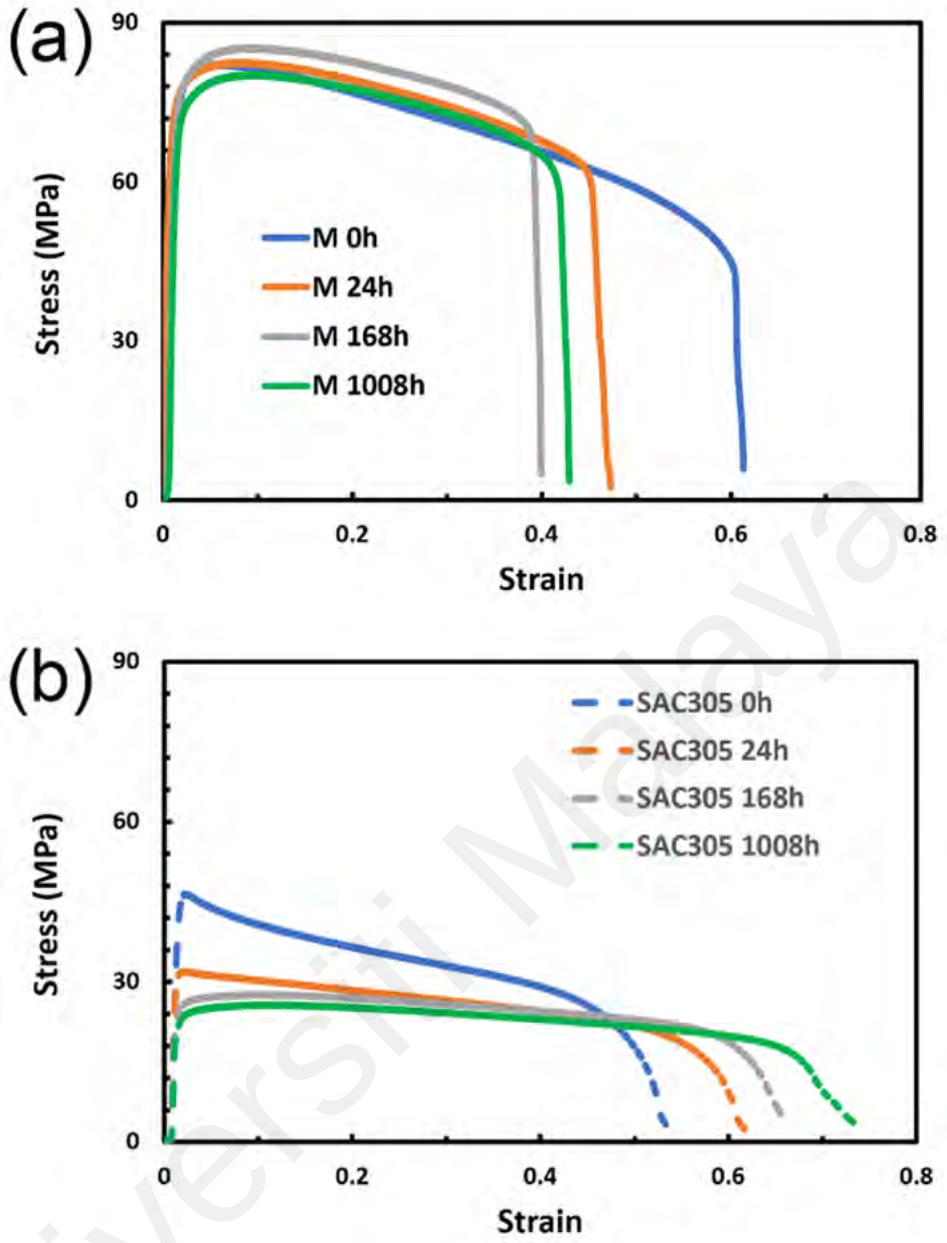

Figure 4.5: Stress-strain curves of two solders under strain rate 10^{-3}/s after 125℃ aging: (a) solder M; (b) SAC305.

According to the binary Sn-Sb phase diagram, Sb has negligible solid solubility in *β*-Sn (Sayyadi & Naffakh-Moosavy, 2019). However, Sb addition could form SbSn precipitates thus increased the UTS of SAC solder when the weight percentage of Sb increased from 0 wt.% to 2 wt.% (Sayyadi & Naffakh-Moosavy, 2019; Okamoto, 2012). In addition, Sb leads to accelerated solidification of Sn and shorter time spans for IMC

growth as it acts as nucleation sites, resulting in microstructural refinement and suppression of IMC growth during thermal aging (Okamoto, 2012). Moreover, the finer precipitates of SbSn could effectively obstruct the dislocation movement initiated in Sn matrix which also led to improved strength (Okamoto, 2012; Borzone, et al., 2021). Hence, the solder M with 2.8 wt.% Sb addition performed higher strength in tensile tests.

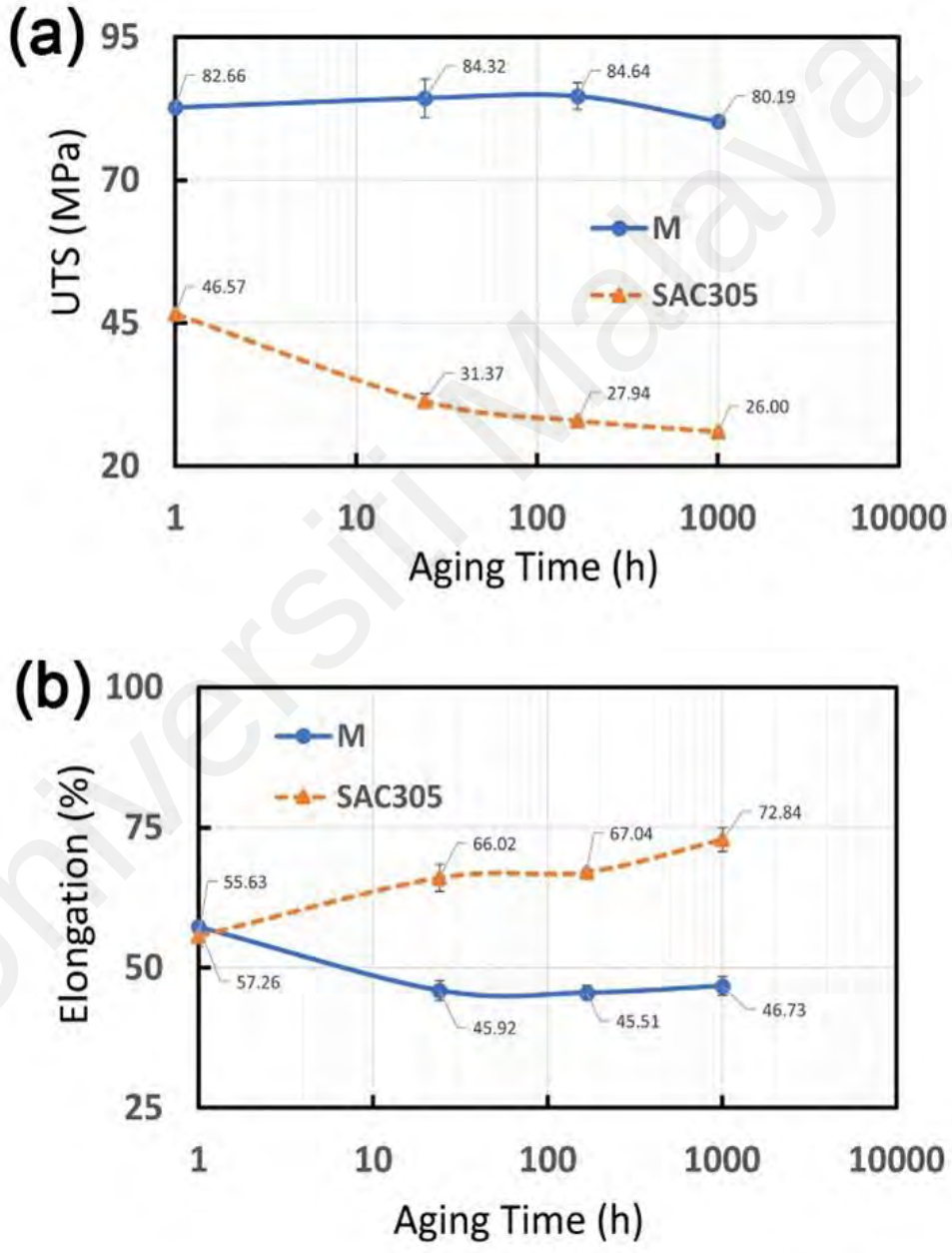

Figure 4.6: Solder M and SAC305 under strain rate 10^{-3}/s during 125℃ aging: (a) ultimate tensile strength; (b) Percentage of elongation.

As for Ni, its solid solubility in β-Sn is very low, thus it is not expected to lead to solid solution strengthening to any appreciable extent (Li, et al., 2006; Okamoto, 2008). However, the addition of Ni leads to the formation of smaller and more uniformly distributed $(Cu, Ni)_6Sn_5$ (Lopez, et al., 2010). Since the fine precipitates are dispersed in primary β-Sn grains, Ni plays an important role in the formation of $(Cu, Ni)_6Sn_5$ IMCs. According to previous study, when small amount of Ni (less than 0.05 wt.%) is added to the solder alloy, the Sn-rich phase is smaller in size, and the IMCs are more uniformly distributed.

Based on this evidence, it is expected that 0.037 wt.% of Ni addition improves the tensile strength of SAC solder. However, when Ni addition reaches 0.05 wt.%, it has an even higher fraction of the primary β-Sn phase and the IMCs appeared coarse within the matrix as compared to the former case. A few short rod shape $(Cu, Ni)_6Sn_5$ IMCs are generated mainly inside the β-Sn phase. Moreover, the standard Gibbs energy of formation of Cu-Sn is lower than that of Ni-Sn. In addition, the solubility of Ni could stabilize $(Cu, Ni)_6Sn_5$ significantly (Hammad, 2013). In turn, if Ni addition added in SAC solder were higher than 0.05 wt.%, it exhibits a low UTS and a large elongation, which produces a soft and highly compliant bulk solder (El-Daly & El-Taher, 2013).

In summary, the mechanical strength of solder M with 0.037 wt.% Ni solder has the optimal performance in improving the strength, owing to the optimal volume fraction of Sn, and a large volume fraction of eutectic region. The strength of solder M benefited from solid solution strengthening by Bi. The precipitation strengthening of Bi, and IMC of SnSb contributed to its UTS improvement. As compared with SAC305, SbSn, and $(Cu, Ni)_6Sn_5$ have also improved microstructural refinement concurrently.

In order to have a more complete view of the thermal aging effects on strength of two solder alloys, the UTS and elongation are considered in evaluation of the overall strength

extent of the solder. Toughness represents a balance of strength and ductility, and it is related to the area under the stress–strain curve. The areas under stress-strain curves of Figure 4.5 are plotted against thermal aging time under strain rates 10^{-3}/s are shown in Figure 4.7. After 1008 h thermal aging, the toughness of as-received solder M decreased from 41.5 MJ/m^3 to 30.9 MJ/m^3, while the toughness of SAC305 decreased slightly from 17.2 MJ/m^3 to 16.3 MJ/m^3.

The value of toughness (area under stress-strain curve) for solder M is always larger than SAC305 even though the toughness of solder M was decreasing. This proved that the overall strength of solder M is higher than SAC305 during thermal aging due to the additions of element Bi, Sb, and Ni.

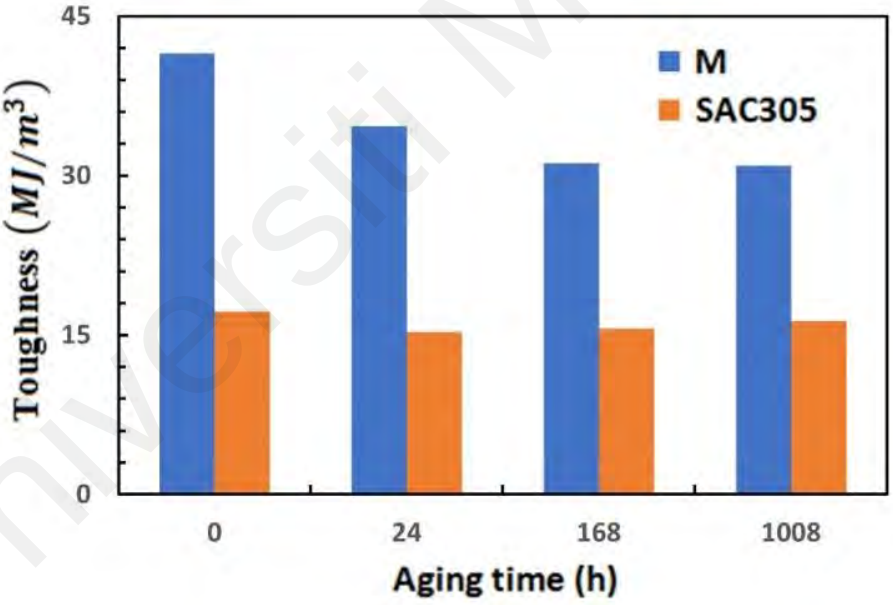

Figure 4.7: Toughness of solder M and SAC305 under stress-strain curve at strain rate 10^{-3}/s during 125℃ aging.

To find out the relationships between mechanical properties and the grain diameter, UTS, elongation and toughness as dependencies have been plotted against the grain diameter of two solder alloys. Figure 4.8(a) shows that the grain growth has less effect on the UTS

of solder M, while the elongation reduces with the increased grain diameter. Besides, the toughness of solder M is affected strongly when its grain diameter increases as shown in Figure 4.8(b). As for SAC305, Figure 4.9(a) shows the increased grain size leads to the decrease of its UTS and increased elongation. However, the toughness has less effect from the grain growth as shown in Figure 4.9(b).

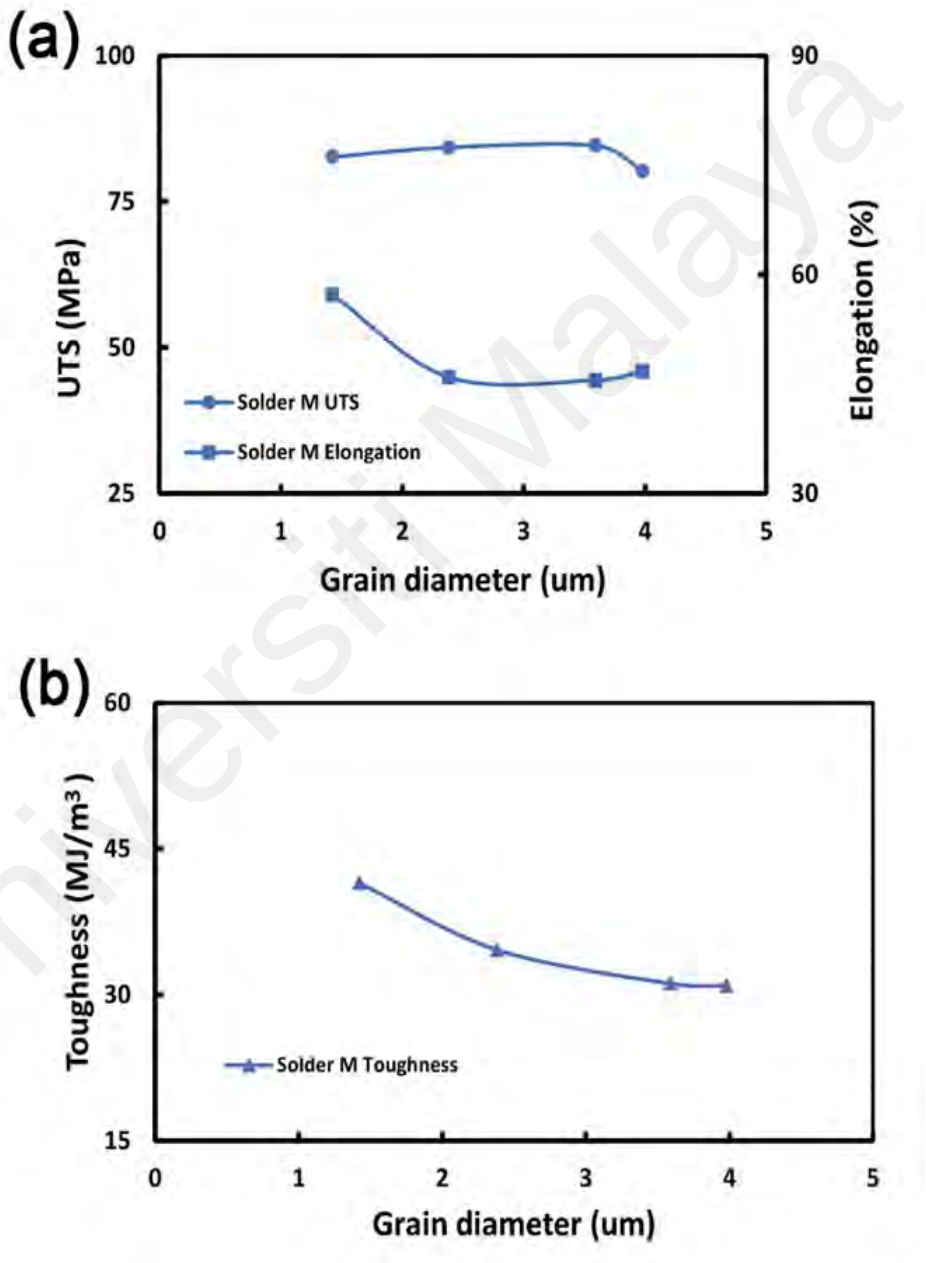

Figure 4.8: The dependence of elongation, UTS and toughness on grain size of solder M.

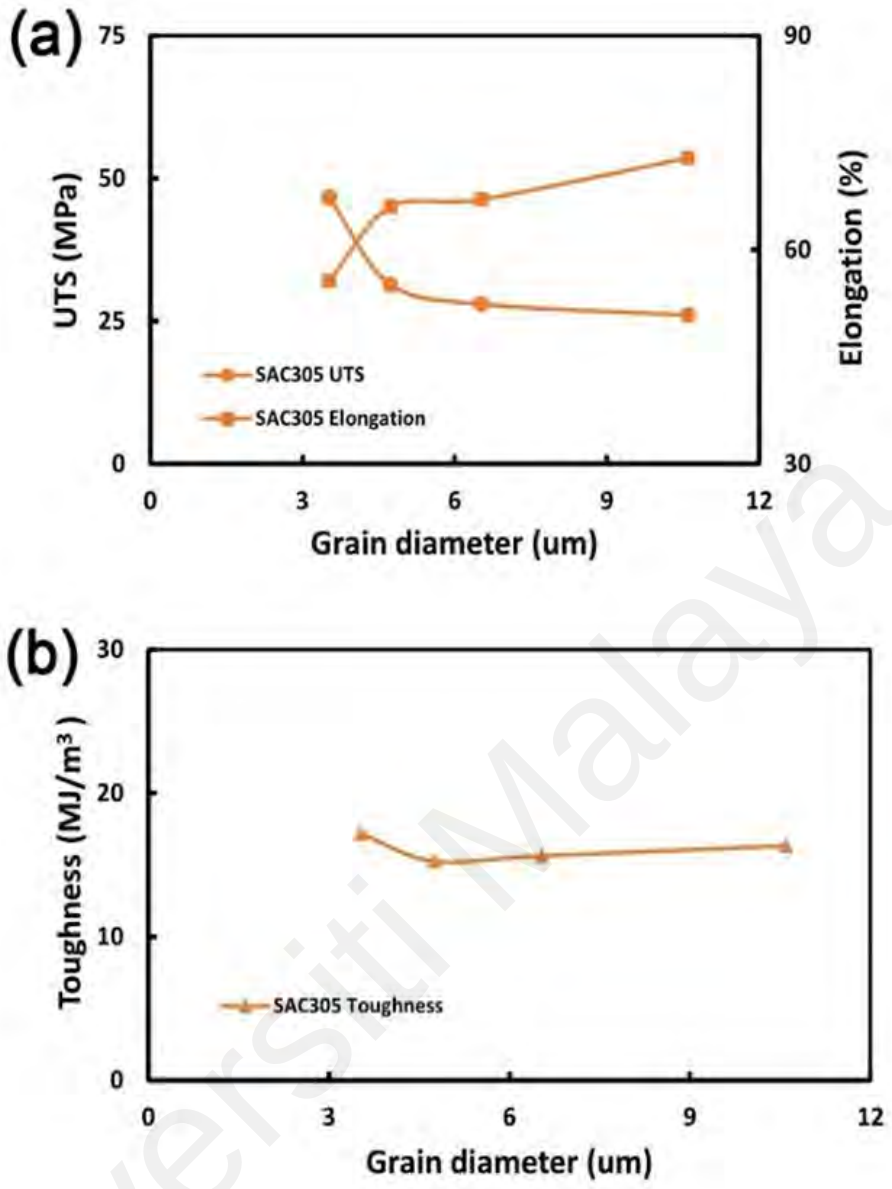

Figure 4.9: The dependence of elongation, UTS and toughness on grain size of SAC305.

4.2.3 Strain rate effects on tensile properties under thermal aging conditions

For solder materials under tensile loading, when the applied stress goes beyond the YS, σ_y, it continues to deform plastically until instability is reached. The stress, at which instability occurs, σ_{UTS}, is the UTS. A stress strain curve of solder material under tensile condition shows that up to σ_{UTS}, the strain is distributed uniformly in the specimen and beyond σ_{UTS}, it is concentrated in the region where a

neck develops and eventually fracture occurs. The common ranges for strain rate testing are between 10^{-4}/s and 10^{-1}/s (quasi-static) and 10^{-1}/s to 10^{3}/s (dynamic) (Chen et al., 2002; Witkin, 2012b).

Due to equipment constraint in the lab, the highest strain rate that can be used is 10^{-2}/s. The strain rate used in this study ranged between 10^{-4}/s and 10^{-2}/s, which is the range for quasi-static loading. In this section, constant strain rate tensile tests on bulk solder dog-bone type sheet plate tensile specimens under different thermal aging conditions were investigated. Tensile tests were carried out on the universal tester at room temperature of 25 ℃, for three different strain rate conditions of 10^{-4}/s, 10^{-3}/s, and 10^{-2} /s, respectively.

The apparent elastic modulus, YS and UTS plots against strain rate are shown in Figures 4.10 to 4.12 respectively. As observed, solder M showed higher elastic modulus, YS and UTS than SAC305 at strain rates of 10^{-4}/s, 10^{-3}/s, and 10^{-2}/s, when strain rate increases the stress strain curves move upwards and with an increase in the apparent elastic modulus, YS and UTS. The strain rate effects on the apparent elastic modulus, YS and UTS for solder M and SAC305 under thermal aging conditions can be expressed in power law equations from Equations (4.1) to (4.3) respectively. In the meantime, the constants of relation between elastic modulus, YS, UTS and strain rate for solder M and SAC305 to fit into the power law equations are listed in Tables 4.2 to 4.4.

The strain rate sensitivity of solder M and SAC305 shows a dependence on strain rate resulting from dynamic hardening strain rate effects on the on elastic modulus, YS and UTS. It is very clear that the strain rate played a significant role and affected the strength of the solders. The elastic modulus, YS and UTS increase with increasing strain rate for both solder alloys. This is because an increase in strain rate is accompanied by an increase in the dislocation density. It is then more difficult for other dislocations to glide through the material, especially at the lower deformation temperatures (Hammad, 2018).

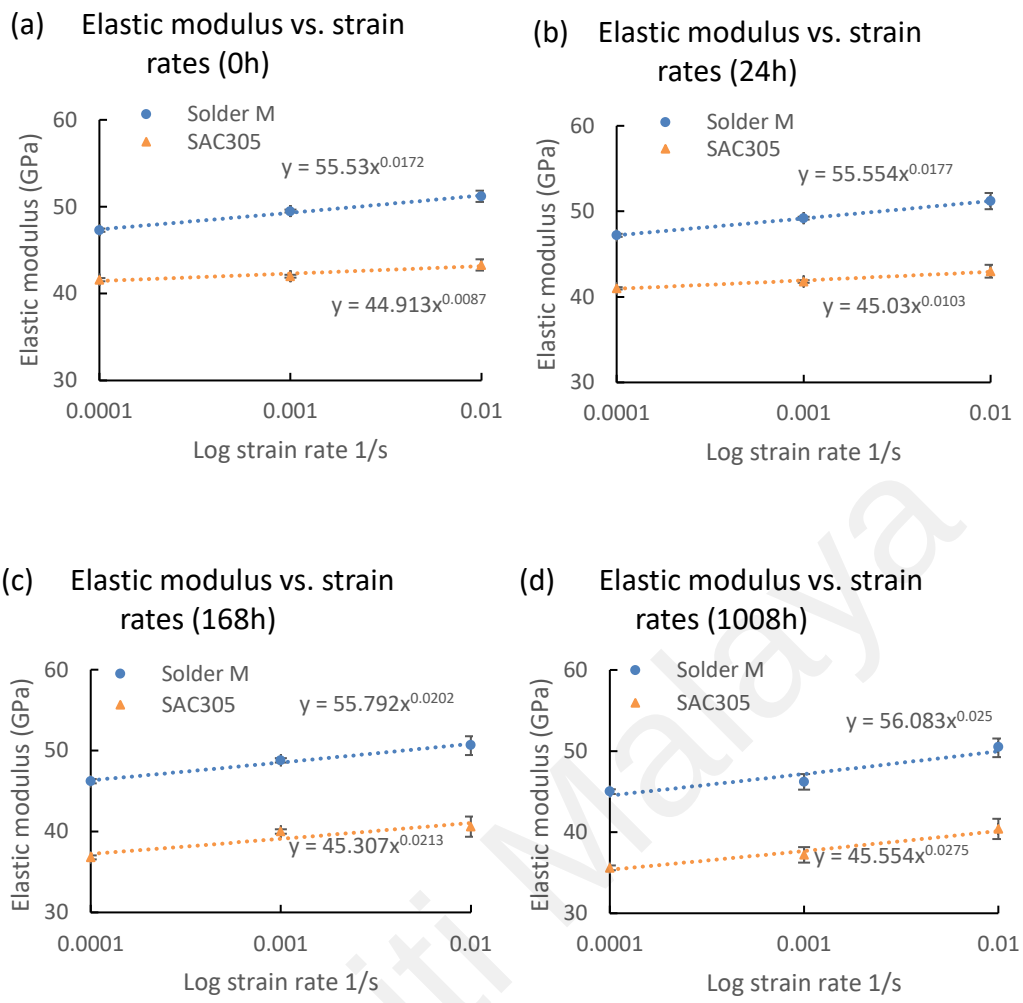

Figure 4.10: The comparison of elastic modulus of solder M and SAC305 as a function of strain rate after (a) 0h (b) 24h (c) 168h (d) 1008h aging at 125°C.

The strain rate effect on the apparent elastic modulus for solder M and SAC305 under thermal aging conditions can be expressed in power law equation as follows:

$$E = \alpha_1 \dot{\varepsilon}^{\alpha_2} \qquad (4.1)$$

Where,

E = elastic modulus

$\dot{\varepsilon}$ = strain rate

α_1 = constant in power law between elastic modulus and strain rate

α_2 = constant in power law between elastic modulus and strain rate

Table 4.2: Constants fitted in power law equation for the relation between elastic modulus and strain rate.

Aging time (h)	α_1	α_1	α_2	α_2
	Solder M	SAC305	Solder M	SAC305
0	55.53	44.91	0.0172	0.0087
24	55.55	45.03	0.0177	0.0103
168	55.79	45.31	0.0202	0.0213
1008	56.08	45.55	0.025	0.0275

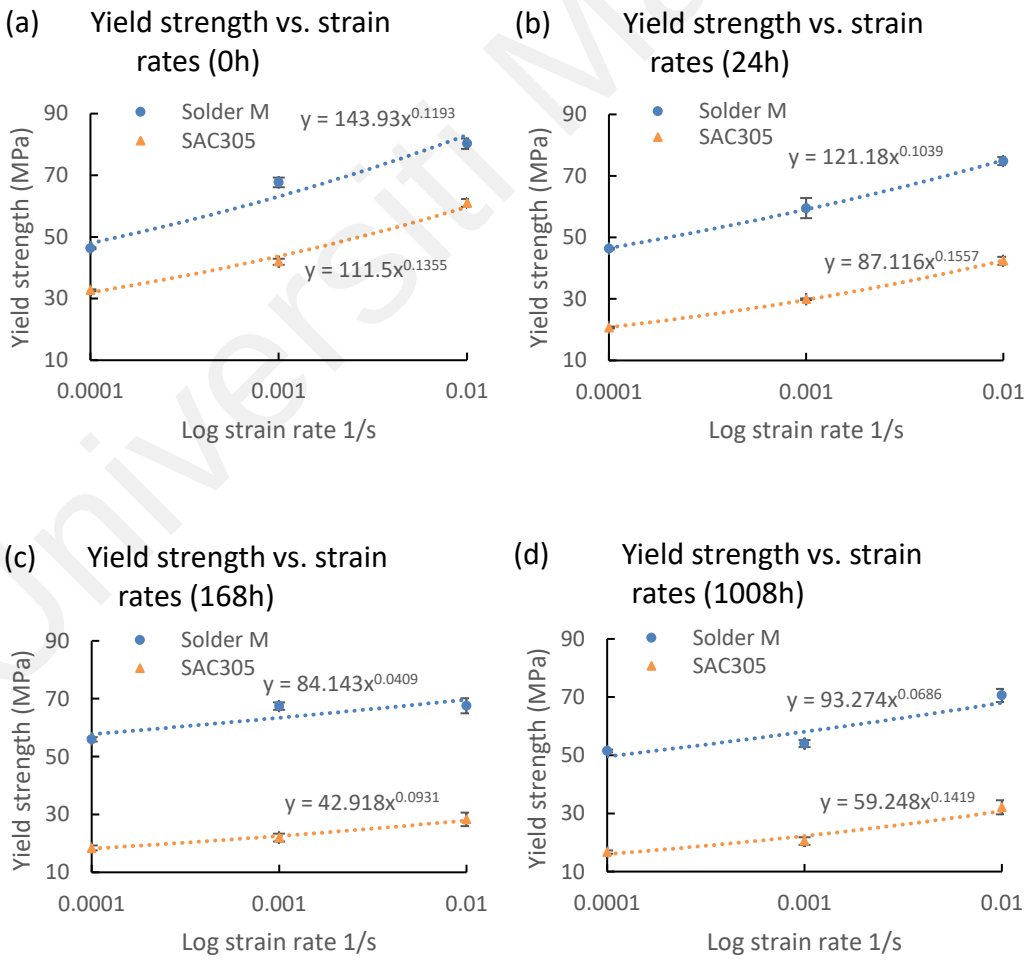

Figure 4. 11: The comparison of yield strength of solder M and SAC305 as a function of strain rate after (a) 0h (b) 24h (c) 168h (d) 1008h aging at 125℃.

The strain rate effect on the YS for solder M and SAC305 under thermal aging conditions can be expressed in power law equation as follows:

$$\sigma_y = \alpha_3 \dot{\varepsilon}^{\alpha_4} \quad (4.2)$$

Where,

σ_y = yield strength

$\dot{\varepsilon}$ = strain rate

α_3 = constant in power law between YS and strain rate

α_4 = constant in power law between YS and strain rate

Table 4.3: Constants fitted in power law equation for the relation between YS and strain rate.

Aging time (h)	α_3	α_3	α_4	α_4
	Solder M	SAC305	Solder M	SAC305
0	143.93	111.15	0.1193	0.1355
24	121.18	87.12	0.1039	0.1557
168	84.14	42.92	0.0409	0.0931
1008	93.27	59.25	0.0686	0.1419

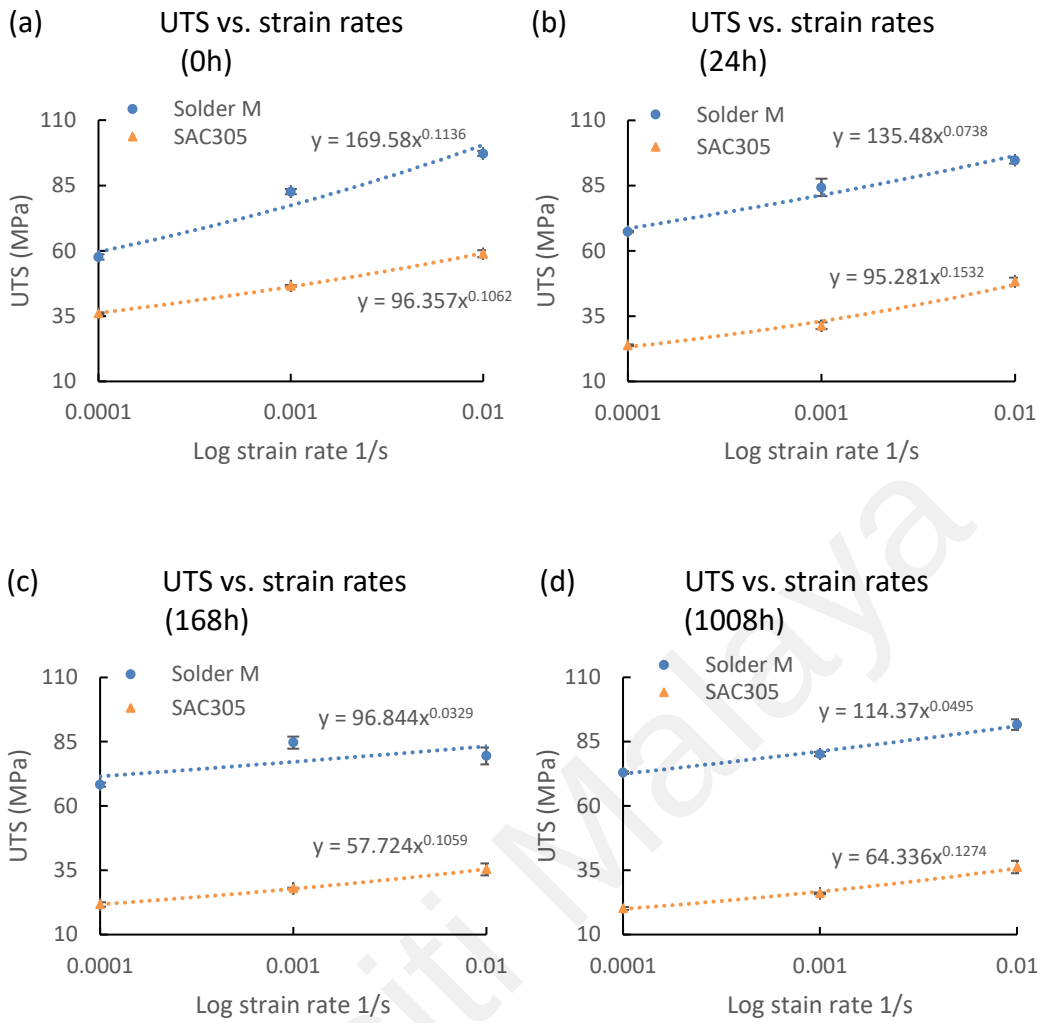

Figure 4.12: The comparison of ultimate tensile strength of solder M and SAC305 as a function of strain rate after (a) 0h (b) 24h (c) 168h (d) 1008h aging at 125℃.

The strain rate effect on the UTS for solder M and SAC305 under thermal aging conditions can be expressed in power law equation as follows:

$$\sigma_{UTS} = \alpha_5 \dot{\varepsilon}^{\alpha_6} \qquad (4.3)$$

Where,

σ_{UTS} = ultimate tensile strength

$\dot{\varepsilon}$ = strain rate

α_5 = constant in power law between UTS and strain rate

α_6 = constant in power law between UTS and strain rate

Table 4.4: Constants fitted in power law equation for the relation between UTS and strain rate.

Aging time (h)	α_5	α_5	α_6	α_6
	Solder M	SAC305	Solder M	SAC305
0	169.58	96.36	0.1136	0.1062
24	135.48	95.28	0.0738	0.1532
168	96.84	57.72	0.0329	0.1059
1008	114.37	64.34	0.0495	0.1274

4.2.4 Strain rate effects on plastic strain

Conventional strength and strain-hardening parameters have been derived for idealized true-stress/true-strain curves obeying the Hollomon equation $\sigma = K\epsilon^n$, where K and n are material constants, σ represents the applied true stress on the material, ε is the true strain, and K is the strength coefficient. The strain hardening exponent (also called the strain hardening index), noted as n, a constant often used in calculations relating to stress-strain behavior in work hardening. The true tensile strength is almost independent of n, but the stress at 0.2% plastic strain is strongly dependent on n. The value of the strain hardening exponent lies between 0 and 1, with a value of 0 implying a perfect plastic solid and a value of 1 representing a perfectly elastic solid. Most metals have an n value between 0.1 and 0.5.

In most of the physical approaches the evolution of the flow stress is governed by the dislocation kinetics. For most material such as solder alloy, the shape of stress strain curves are usually represented by a simple power law expression, known as the Holloman equation:

$$\sigma_t = K\varepsilon_t^n \quad (4.4)$$

Where,

σ_t = true flow stress

K = strength coefficient

ε_t = true plastic strain

n = strain hardening exponent

By manipulating the equation, implication showed that the increase in stress caused by a small plastic strain can be significant. The larger the stress increment, for a given strain, the larger the cold worked yield strength, this useful parameter n known as the work hardening exponent and can be derived by plotting Equation (4.5) in logarithmic mode as:

$$\ln(\sigma) = \ln(K) + n \cdot \ln(\varepsilon) \quad (4.5)$$

Strength coefficient K and strain hardening exponent n as a function of aging time under different strain rates are plotted in Figures 4.13 and 4.14 respectively. The strength coefficient K of solder M is around 3 times higher than SAC305 at different strain rates. There is a consistent trend involving an increase in the value of K with higher strain rates for both solder M and SAC305. For the as-received solder M, the K value is 93.5 at strain rate 10^{-4}/s, and it increases to 132.7 when the strain rate becomes 10^{-3}/s. This trend remains for the strain rate at 10^{-2}/s which shows 164 of the K value. Meanwhile, the K value of SAC305 is 36.3 at strain rate 10^{-4}/s, it also shows the higher value under increased strain rates which are 40.2 and 54.8 under strain rate of 10^{-3}/s and 10^{-2}/s respectively. At strain rate 10^{-4}/s, the K value of solder M keeps increasing during the thermal aging. There is 34% increase of solder M after 1008h thermal aging as compared to the as-received sample. However, strength coefficient of SAC305 remains at the similar value after 1008h aging at 125 ℃. It indicates that the thermal aging improved the strength of solder M as

the simultaneously added additional elements have contributed to the mechanism of both precipitation strengthening and solid solution strengthening. At strain rate of 10^{-3}/s and10^{-2}/s, solder M also show the enhanced strength coefficient after thermal aging at 125 ℃. However, the extent of increased *K* value under higher strain rates are not as apparent as low strain rate 10^{-4}/s. As compared to solder M, the increased strain rate has no effect on the *K* value of SAC305 which remains stable during thermal aging.

The strength coefficient *K* numerically equals the extrapolated value of true stress at a true strain of 1.0. It was found to correlated well with UTS and hardness which are shown in Table 4.2 and 4.3 (Roessle & Fatemi, 2000; Li et al., 2019). The strength coefficient of solder M increased during 125℃ aging up to 1008h. In corresponding to the improvement of the strength of solder M, UTS has the same trend of which the value increased from 57.65 MPa at 0h to 72.93 MPa after thermal aging as shown in Table 4.5. As for SAC305, its *K* value showed a decrease, and its UTS has the same performance during thermal aging. Furthermore, the hardness of two solder alloys showed the same trend where solder M increased during thermal aging whereas SAC305 decreased as shown in Table 4.6.

Table 4.5: UTS (MPa) of solder M and SAC305 at strain rate 10^{-4}/s after thermal aging.

UTS (MPa)	0 h	24 h	168 h	1008 h
Solder M	57.65	67.42	68.3	72.93
SAC305	36.1	23.85	21.71	20.17

Table 4.6: Hardness (HV) of solder M and SAC305 after thermal aging.

Hardness (HV)	0 h	24 h	168 h	1008 h
Solder M	28.66	29.4	31.22	31.62
SAC305	13.16	12.29	11.86	10.72

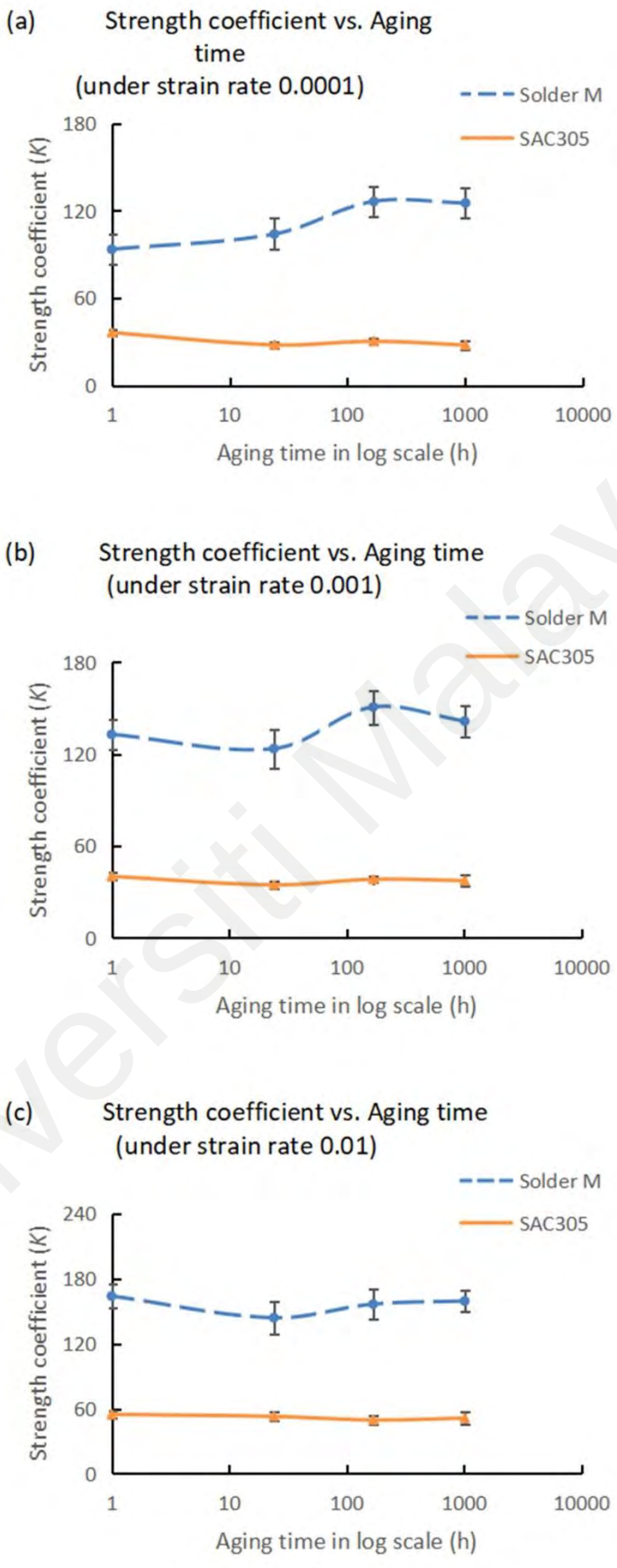

Figure 4.13: The comparison of strength coefficient *K* of two solders as a function of aging time at 125°C under strain rate (a) 10^{-4}/s (b) 10^{-3}/s (c) 10^{-2} /s.

Strain hardening exponent *n* as a function of aging time under different strain rates are plotted in Figure 4.14. *n* value of solder M is as high as 10 times that of SAC305 under different strain rates which indicates that the solder M became stronger as it undergoes plastic deformation.

The strain hardening exponent of solder M fluctuated during thermal aging but remained at the similar level after 1008h at 125 ℃. However, *n* value of SAC305 kept decreasing during thermal aging with less effect of strain rate. It decreased from 0.024 to 0.019 at strain rate of 10^{-4}/s after 1008h thermal aging as shown in Figure 4.14(a). When the strain rate increases, strain hardening exponent increases as well and shows similar decreasing trend after thermal aging as shown in Figures 4.14(b-c), *n* value decreases 18.2% and 23.4% at strain rate 10^{-3}/s and 10^{-2}/s respectively. According to the hardness value of SAC305 in Table 4.3, the 22.8% reduction of hardness after thermal aging indicates that SAC305 became more ductile which is in good agreement with the change of strain hardening exponent.

During thermal aging, the strain hardening exponent of SAC solders may change depending on the microstructural evolution. The *n* value decreases as the solder ages, indicating a decreased ability to sustain plastic deformation (Libot et al., 2018). This can be attributed to the evolution of the microstructure, including the coarsening of IMCs, which can act as obstacles to dislocation motion, leading to a more pronounced strain hardening effect. Furthermore, the formation and growth of IMCs can also influence the strain hardening behavior, with different IMC phases having varying effects. The size, distribution, and composition of IMCs in solder M can vary with aging conditions, affecting the dislocation dynamics and strain hardening exponent. The presence of IMCs can lead to a change in the strain hardening exponent (Kanda et al. 2012; Ali et al. 2021).

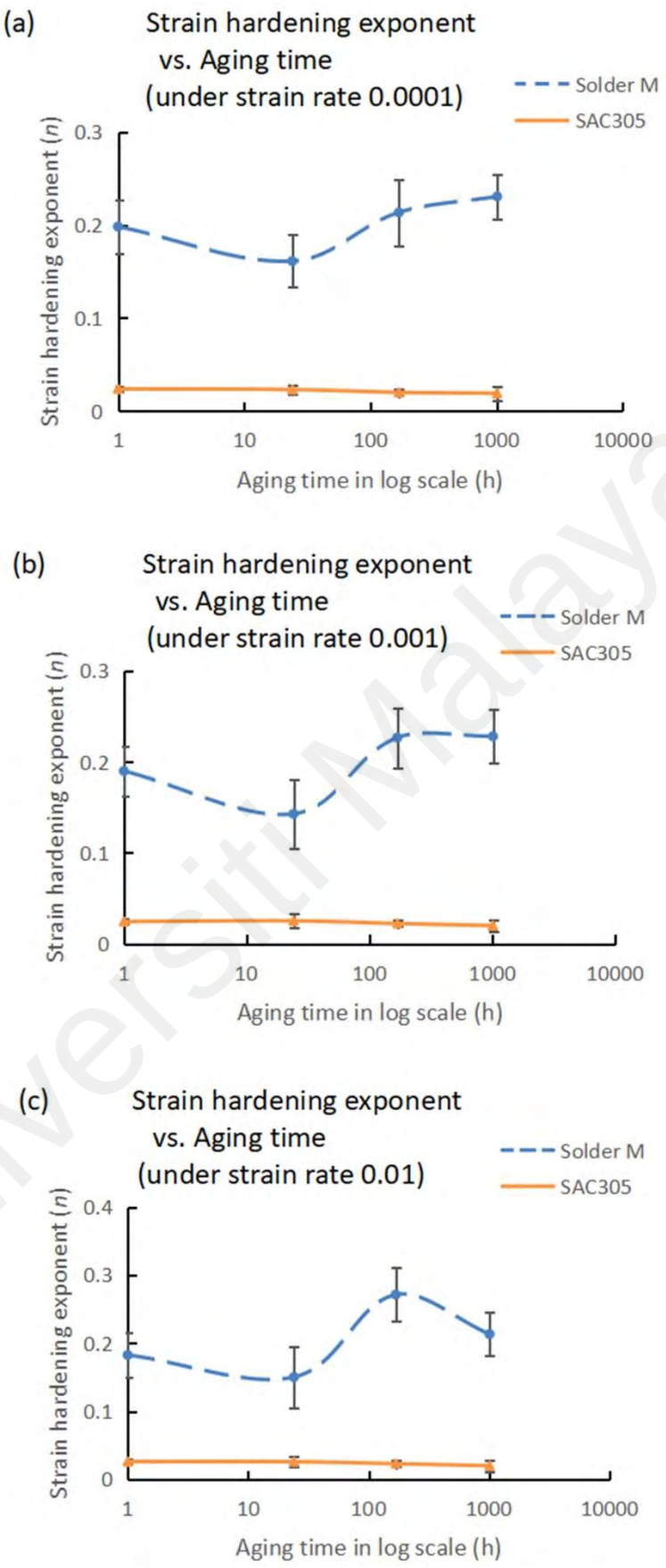

Figure 4.14: The comparison of strain hardening exponent *n* of two solders as a function of aging time at 125°C under strain rate (a) 10^{-4}/s (b) 10^{-3}/s (c) 10^{-2} /s.

During the first 24h, the grain size increased due to thermal aging which caused the strain hardening exponent decrease for both solder M and SAC 305. However, after 24h thermal aging, the IMCs formed in solder M by additional elements, leading to changes in their size and distribution. This coarsening can affect the dislocation motion and change the strain hardening ability, resulting in a retain in the strain hardening exponent as observed in Figure 4.14.

4.2.5 Effect of different percentage of additional element

The addition of Bi less than 2 wt.% could dissolve in the β-Sn matrix and form a solid solution strengthening mechanism. Bi addition greater than 2 wt.% resulted in Bi precipitation in the β-Sn matrix and the formation of a precipitation strengthening mechanism in term of binary phase diagram of Bi-Sn (Okamoto, 2010). Both mechanisms improved the strength of the SAC solder. The stress-strain curves of SAC305-xBi (x= 0, 1, 2, 3) are shown in Figure 4.15, Bi is inherently brittle, dissolves in lesser than 2 wt.% in the Sn matrix and the high percentage of Bi in the Sn alloy forms large precipitates in the matrix by solid state precipitation of Bi (Ali et al., 2021). Therefore, the high amount of Bi is detrimental for the mechanical properties as the ultimate tensile strength of solder M in compare with SAC305 solder with lower amount of Bi added. According to the trend of UTS increase with variable weight percentage of Bi addition, the polynomial relation between UTS and wt.% of Bi is followed the Equation (4.6).

$$y = 3.58x^2 + 26.49x - 0.72 \qquad (4.6)$$

Hence, the expected UTS of SAC305 solder with 3.2 wt.% Bi added in supposed to be 120.7MPa. However, the real UTS value of solder M is 82.3MPa which is 31.8% lower than expected UTS.

To validate the explanation of mechanical performance of SAC solder added with high weight percentage (larger than 3.2 wt.%) of Bi addition, the tensile test results of the SAC257-xBi alloy solder are given in Figure 4.15 (Sayyadi & Naffakh-Moosavy, 2019). According to the results, for the alloy solders with Bi up to 2.5 wt.%, the UTS increased. However, the UTS reduced when the weight percentage of Bi increased from 2.5 wt.% to 5 wt.%. Therefore, within low percentages of Bi (lower than 5 wt.%), the strength of SAC solder can be benefited through both the formation of a solid solution with Sn matrix and formation of fine precipitates of Bi addition.

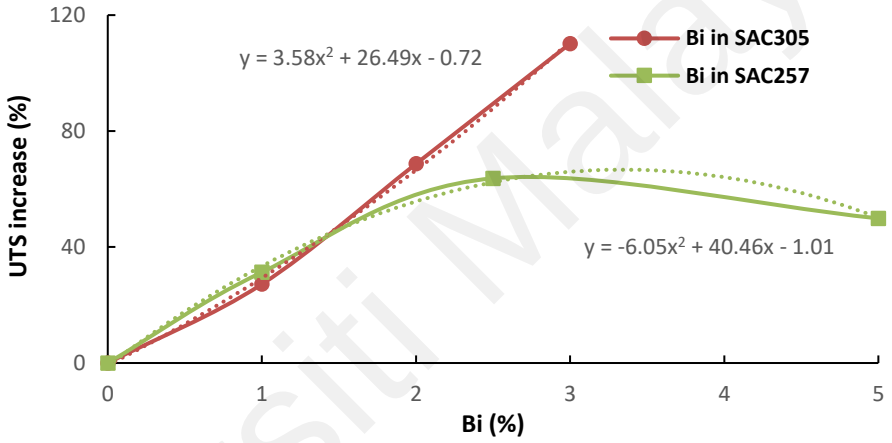

Figure 4.15: Effect of Bi with different percentage in SAC solders (Ali et al., 2021; Sayyadi & Naffakh-Moosavy, 2019).

The addition of Sb could not dissolve in the β-Sn matrix or form a solid solution strengthening mechanism. Due to the low solubility of Sb in Sn, Sb addition could form SbSn precipitation strengthening as shown in binary phase diagram of Sb-Sn (Okamoto, 2012) and new Sb-Sn phase diagram (Borzone et al., 2021). However, finer strengthening IMC precipitates SbSn could effectively obstruct the dislocation movement initiated in Sn matrix which led to an increase to the effective properties of the alloy and contributes to suppress the coarsening of Ag_3Sn phase (Hammad, 2018).

Hence, the solder M with 2.8 wt.% Sb addition performed even higher strength in tensile tests as shown in Figure 4.16 (Li et al., 2006).

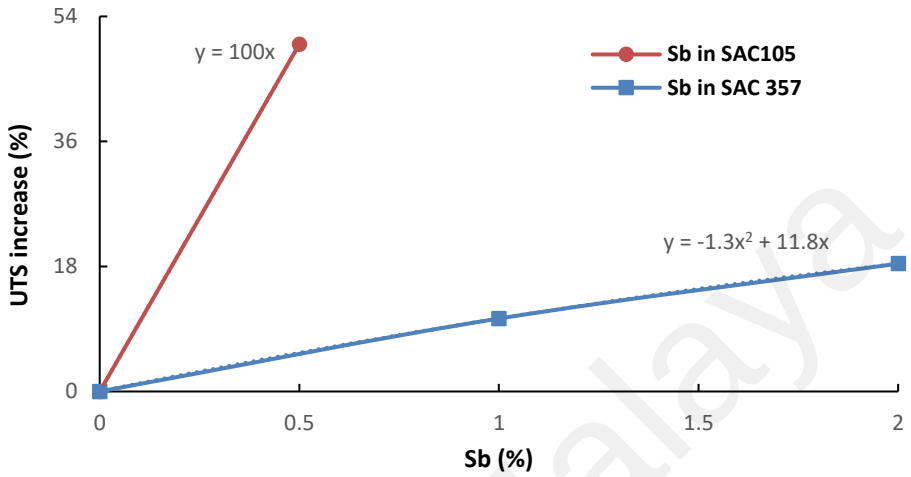

Figure 4.16: Effect of Sb with different percentage in SAC solders (Hammad, 2018; Li et al., 2006).

Ni is hard to dissolve in Sn matrix according to the binary Sn-Ni phase diagram (Okamoto, 2008). The addition of Ni added into SAC solder alloy leads to the formation of $(Cu, Ni)_6Sn_5$ IMC, Ni with 0.05 wt.% addition produced smaller contribution in Sn-rich phase and the more uniform distribution of IMCs. Ni with 0.1 wt.% into SAC solder has high fraction of the primary β-Sn phase due to the low solubility of Ni in Sn (Hammad, 2018). The solid solution strengthening of solder M would not be benefited much by adding 0.037 wt.% Ni, thus the UTS would not be increased as shown in Figure 4.17 (Hammad, 2013).

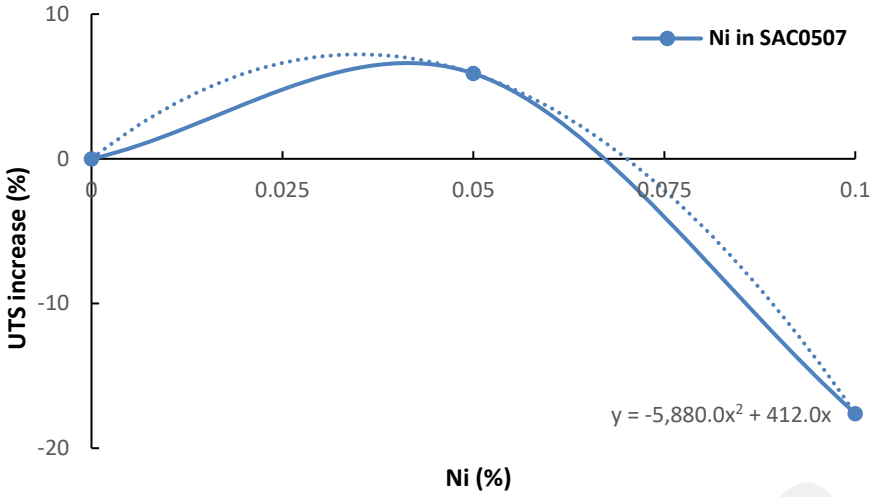

Figure 4.17: Effect of Ni with different percentage in SAC0507 (Hammad, 2018).

4.2.6 Fractography analysis of SAC305 and solder M

Figures 4.18 and 4.19 showed the top views of the fracture surfaces of two types of solder samples aged at 125℃ at different time intervals. The magnification is 500x for the overall observation in the left-side fractography, and the selected fracture surface in green box is enlarged to 2000x magnification as shown in the right-side image. The fracture mode of SAC305 was more ductile than solder M as the fractography of cross-sectional area of SAC305 showed necking and consisted large ductile dimples. Dimples have been detected on the top view of the fracture interface of the as-received samples, as indicated in Figures 4.18(a) and 4.19(a).

Tiny dimples were shown on the fracture surface of solder M, whereas larger and deeper dimples were observed on the surface of SAC305. Dimples with slightly increased sizes were detected in solder M thermally aged for 24h, and 1008h as displayed in Figures 4.18(b) and 4.20(c). As for SAC305, larger dimple sizes on fracture surface from top view were observed, as illustrated in Figure 4.19.

The dimple size of SAC305 thermally aged for 1008h increases as shown in Figure 4.19(c). At short aging duration, Hu et al. (2007) observed a similar ductile dimple

fracture morphology in the case of lap shear test. However, for longer aging duration, the authors found a transition of fracture morphology to cleavage in SAC305. For as-received SAC305 samples, the work hardening could restrain re-crystallization or recovery of sub-microstructures during tensile deformation. Once the initial cracks of surface nucleated, the fracture failure of specimen would have occurred for the crack cleavage. The effect of 125℃ thermal aging changes the dynamic behavior of SAC305 solder such as accelerating deformation, grain boundary sliding, and re-crystallization would occur (Hammad, 2013; Hu, et al., 2016). In the tensile tests, the testing temperature seriously affected the fracture behaviors and morphology of specimen fracture surfaces (Hammad, 2018; Xu & Pang, 2006). Lesser ductility of solder M is caused by the brittleness within various IMCs. Previous works showed that adding Bi, Sb, and Ni to Sn-Ag-Cu solder formed particle Bi, IMC SbSn and $(Cu, Ni)_6Sn_5$ inside the bulk solder and progressed the failure of the nucleation sites, and decreased ductility (Miric, 2010; Hammad, 2018; Zhu, et al., 2007; Hu, et al., 2014; Tao, et al., 2017). The lesser ductile fracture behavior could be attributed to Bi, which was scattered in β-Sn and prevented solder to deform in β-Sn. In addition, the reduction of elongation of solder M could be justified by Bi brittle properties (Hammad, 2018; Alam et al., 2019; El-Daly, et al., 2013). Therefore, the fracture modes between two solder alloys were non-identical.

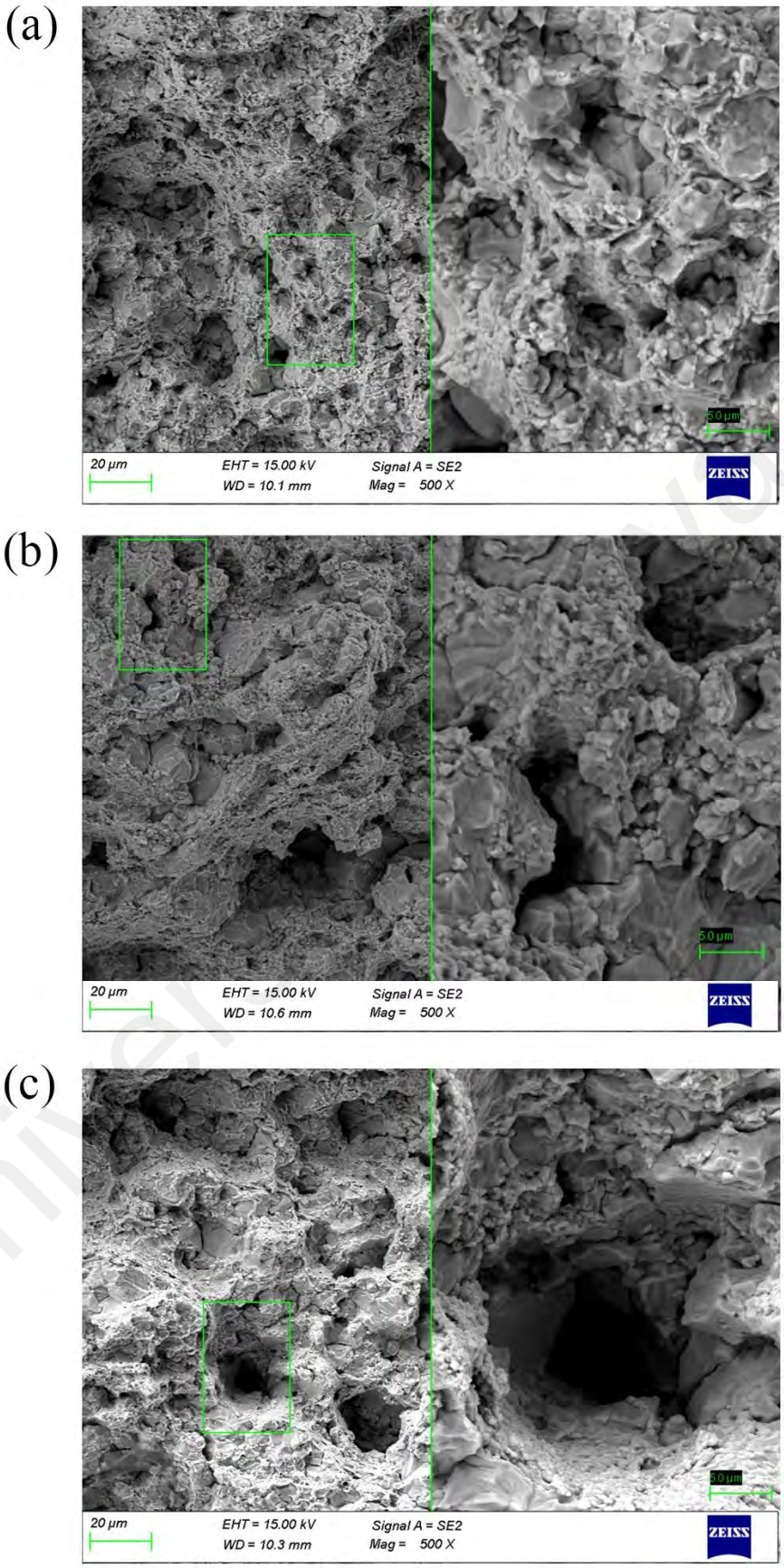

Figure 4.18: Fractography of solder M in tensile testing after 125 °C thermal aging: (a) 0 h aged; (b) 24 h aged; (c) 1008 h aged.

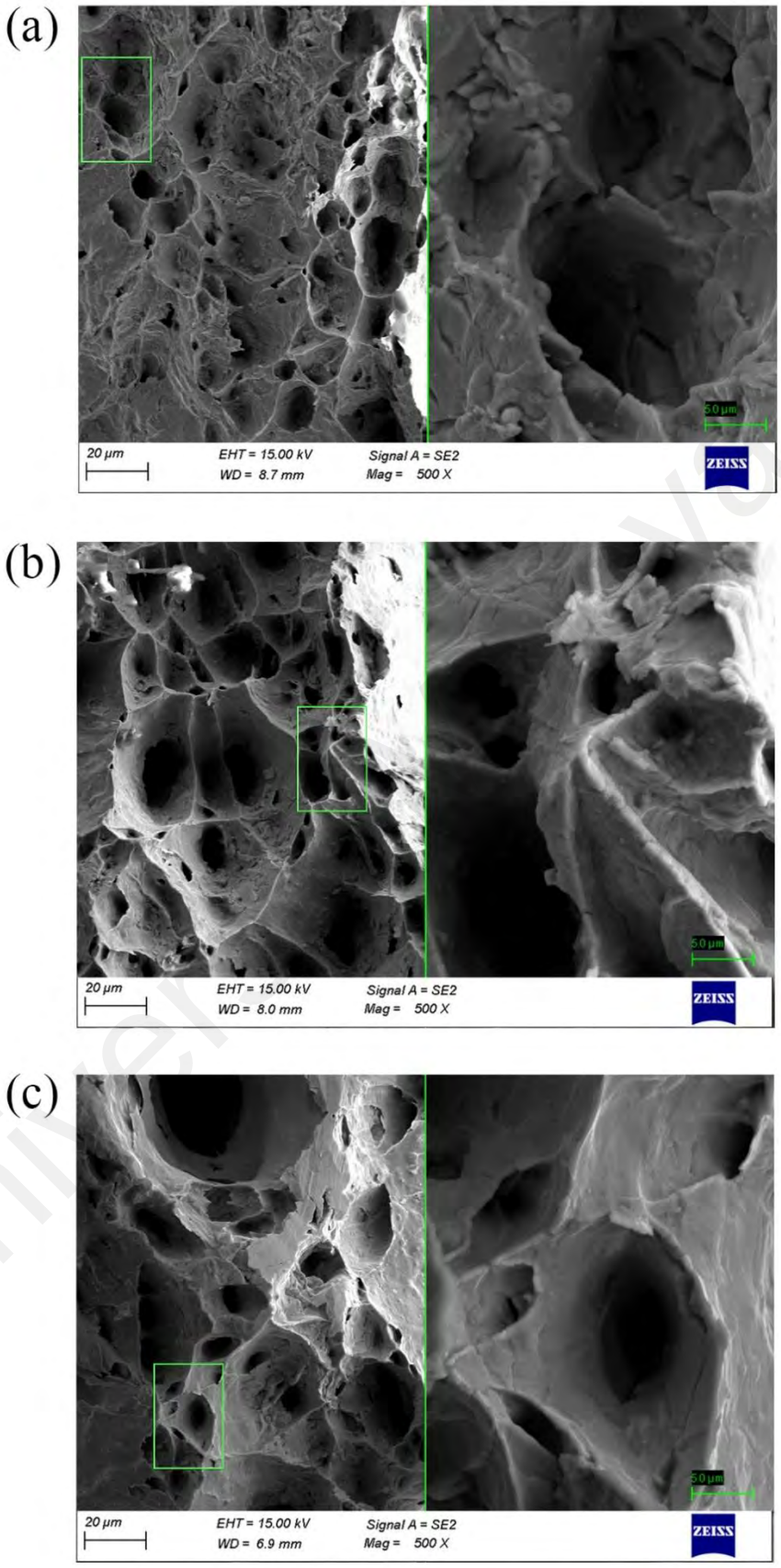

Figure 4.19: Fractography of SAC305 in tensile testing after 125 °C thermal aging: (a) 0 h aged; (b) 24 h aged; (c) 1008 h aged.

4.2.7 Summary of thermal aging effects on tensile properties

In this section, the effects of simultaneous additions of Bi, Sb, and Ni to SAC305 solder on the microstructural and mechanical properties in tensile testing during thermal aging at 125 ℃ for up to 1008 hours were investigated. The characterizations of SAC305 and solder M were reported. Microstructural observations for both solders were analyzed and compared through SEM analysis. In addition, the mechanical performances and fracture behaviors in tensile testing were studied. The main findings of the investigation are summarized as following:

- The average grain diameter of as-received solder M is 1.42 μm, which is 2.5 times smaller of SAC305. After 1008h aging at 125℃, the grain diameter of solder M increased to 3.98 μm while SAC305 increased to 10.6 μm. Overall, the addition of Bi, Sb, and Ni improved microstructural refinement, suppressed the grain growth of solder M, and reduced the grain growth rate in comparison with SAC305.
- During thermal aging, UTS of solder M retained its strength in comparison to as-received sample under different strain rates, whereas SAC305 decreased of as-received sample. However, the elongation of solder M decreased in contrast with an increase of SAC305. The additional element Bi, Sb and Ni resulted in the higher UTS of solder M due to their solid solution strengthening and precipitation strengthening mechanisms.
- The toughness of solder M is higher than SAC305 at all thermal aging conditions. This is despite the toughness of solder M decreased from 41.5 MJ/m^3 to 30.9 MJ/m^3 at strain rate 10^{-3}/s during 1008h thermal aging, while the toughness of SAC305 only slightly reduced from17.2 MJ/m^3 to 16.3 MJ/m^3 with as-received sample.
- SAC305 showed more ductile fracture behavior and the dimple size increased faster resulting from the thermal aging effect in compared to solder M.

4.3 Thermal aging effects on the creep behavior of SAC305 and solder M

4.3.1 Thermal aging effects on creep response of SAC305 and solder M

Figure 4.20 shows the creep behaviors of solder M after different thermal aging intervals with variable creep stresses applied. The creep strain increased during $5x10^4$ s for samples in all conditions. The overall trend of solder M with different aging time shows that 125℃ aging resulted in the decreased creep rate during 1008h.

Figure 4.20(a) shows creep behavior of solder M under 20 MPa after 0h, 24h, 168h and 1008h aging at 125℃. The creep strain at the end of creep test for 0h aged sample is 0.075. It is observed that 125℃ aging reduced the creep strain rapidly after 24h with 20% decrease. After that, the creep strain kept reducing till 1008h. However, the creep performance of 168h thermal aging for solder M did not show much difference with 1008h. The creep strains in the end of creep tests are 0.054 and 0.051 respectively, which have 29.2% and 32% decrease as compared to non-aged sample.

Figure 4.20(b) shows a higher value of creep strain in the end of creep testing which is 0.37 for 0h thermally aged solder M. Due to the higher stress of 30 MPa applied on the sample, the creep strain increased 393.3% as compared with lower creep stress of 20 MPa applied on solder M in Figure 4.20(a). Higher stress accelerates the movement of dislocations, which includes dislocation gliding and climbing. Higher stress also induces greater grain boundary sliding. The dislocation gliding and grain boundary sliding are the major creep mechanisms for creep deformation (Kerr & Chawla, 2004). It is apparent that both the creep strain rate and rupture time are sensitive to the applied stress. Nevertheless, the thermal aging showed an improved effect on creep resistance of solder M in Figures 4.20(b-c). At the first 24h thermal aging, the creep resistance increased rapidly, and the creep performances are almost the same after that till 1008h thermal aging. Creep stain in

the end of creep testing for 1008h thermal aging sample reduced 64.9% than the sample at 0h.

When the stress applied on solder increased to 40 MPa as shown in Figure 4.20(c), the tertiary creep stage was observed clearly. Apart from this, all the samples fractured after creep testing. The higher stress applied on solder M increased the creeping rate which has shown typically with the sample at 0h thermal aging. The creep strain for the non-aged sample reached the maximum value with 0.49 under 40 MPa. Thermal aging had the same effect under this creep condition with the previous cases, and the creep strain decreased 30.6% after 1008h.

However, the creep performance of SAC305 shows an opposite behavior as compared to solder M in Figure 4.21. The overall effect of thermal aging on SAC305 did not increase the creep resistance but accelerated the creeping rate for all the conditions. Figure 4.21(a) shows the creep behavior of SAC305 under 11.3 MPa for different thermal aging time intervals. The creep strain of SAC305 with 1008h thermal aging has increased 20% compared to the sample with 0h thermal aging in the end of creep testing.

Furthermore, the higher stress increased the creeping rate, especially those with long thermal aging time. As Figure 4.21(b) shows, the creep stains at the end of testing of 0h and 1008h thermal aging are 0.16 and 0.4 respectively under 17 MPa. This load has resulted in the tertiary creep behavior for 168h and 1008h thermally aged samples. In addition, with the same creep stress 20 MPa applied on the samples, SAC305 samples with different thermal aging time were all fractured as shown in Figure 4.21(c). Besides, samples with 168h and 1008h thermal aging have reached tertiary creep stage quickly within 2700s after the load applied.

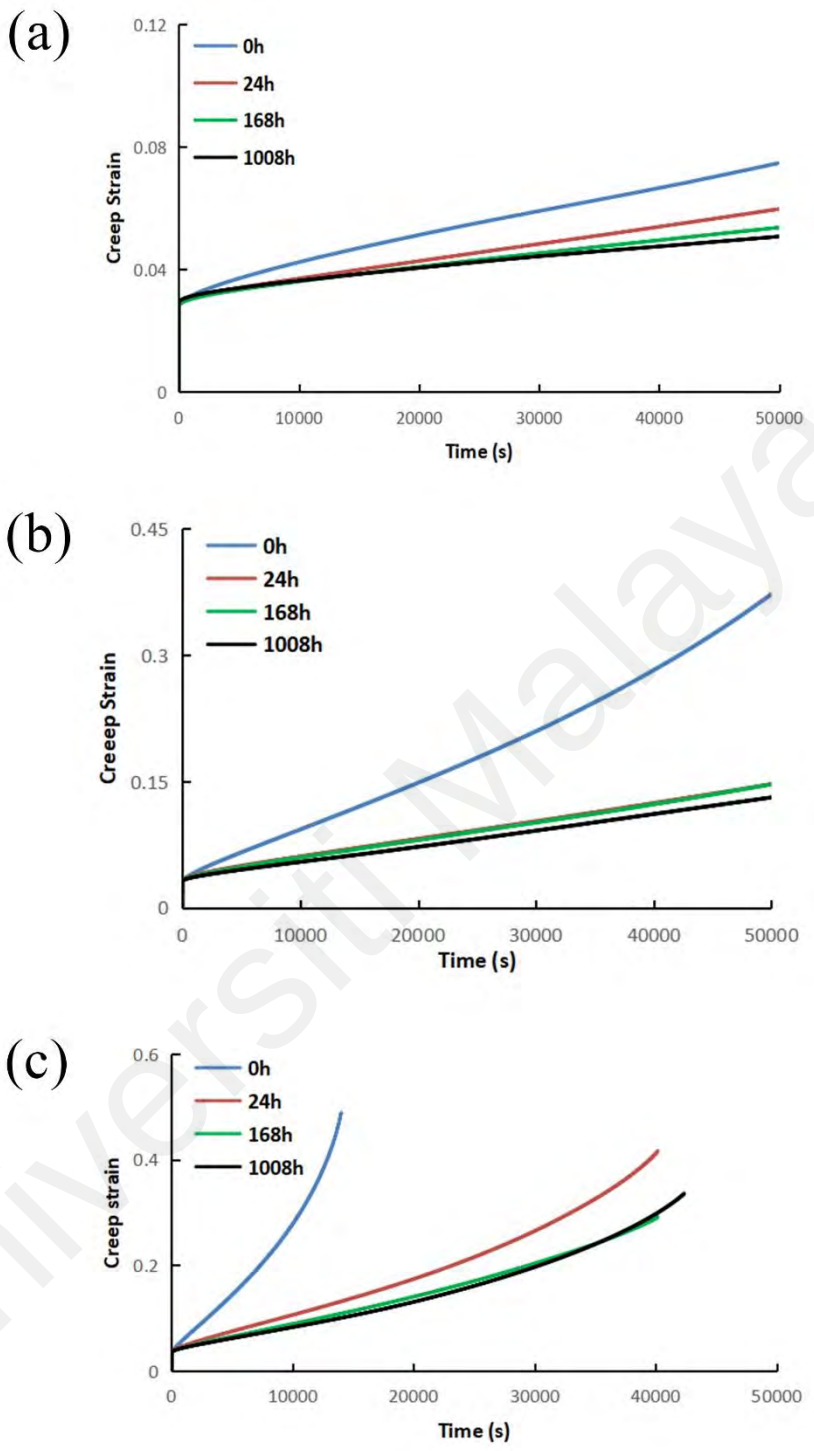

Figure 4.20: Creep behavior of solder M under (a) 20 MPa; (b) 30 MPa and (c) 40 MPa after aging at 125℃.

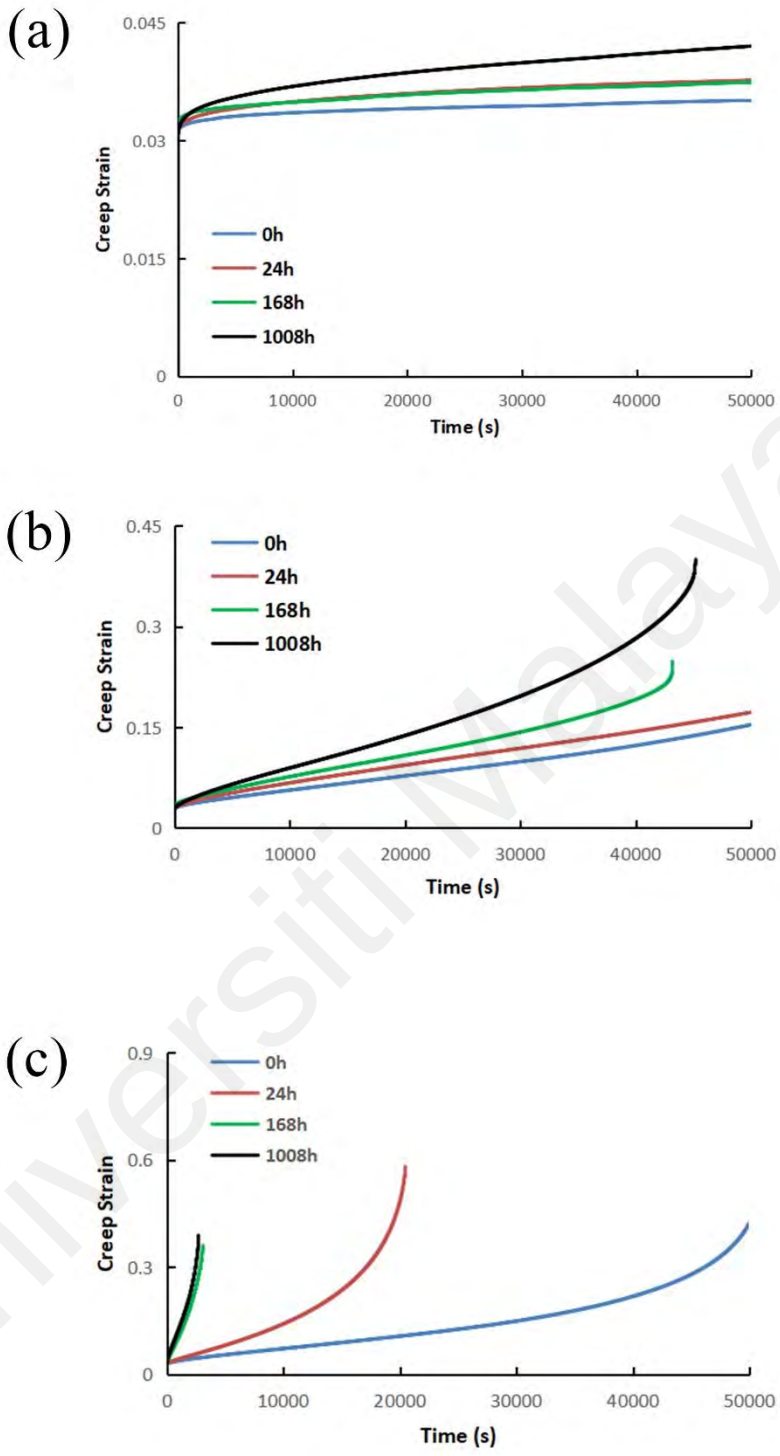

Figure 4.21: Creep behavior of SAC305 under (a) 11.3 MPa; (b) 17 MPa; (c) 20 MPa after aging at 125℃.

As secondary regime is the longest in duration and thus represents the lifetime of solder, Figure 4.22 shows the steady-state creep rate which is plotted in as function of aging time under various stress levels at room temperature. The creep deformation increases with increasing creep stress applied since higher stresses accelerate the dislocation gliding and climb and induce greater grain boundary sliding. As Figure 4.22(a) shows, thermal aging reduced the creep rate on the secondary stage which improved the creep rupture life of solder M. After first 24h aging at 125℃, the steady-state creep rates reduced 25% 67% and 70% under creep stress of 20MPa, 30MPa and 40MPa, respectively.

Thereafter, the creep rate remains remarkably constant, even over periods as long as 1008h. This phenomenon indicated that Bi, Sb and Ni added in solder M has strengthened its creep resistance and improved the mechanical properties. In contrast, the increase in the steady-state creep rate is extremely large for SAC305 under different creep stresses applied as shown in Figure 4.22(b). During the 1008h thermal aging, the creep rates under all creep stress levels increase more than 3 times as compared to the non-aged samples which indicates the resistance to creep deformation dramatically declines.

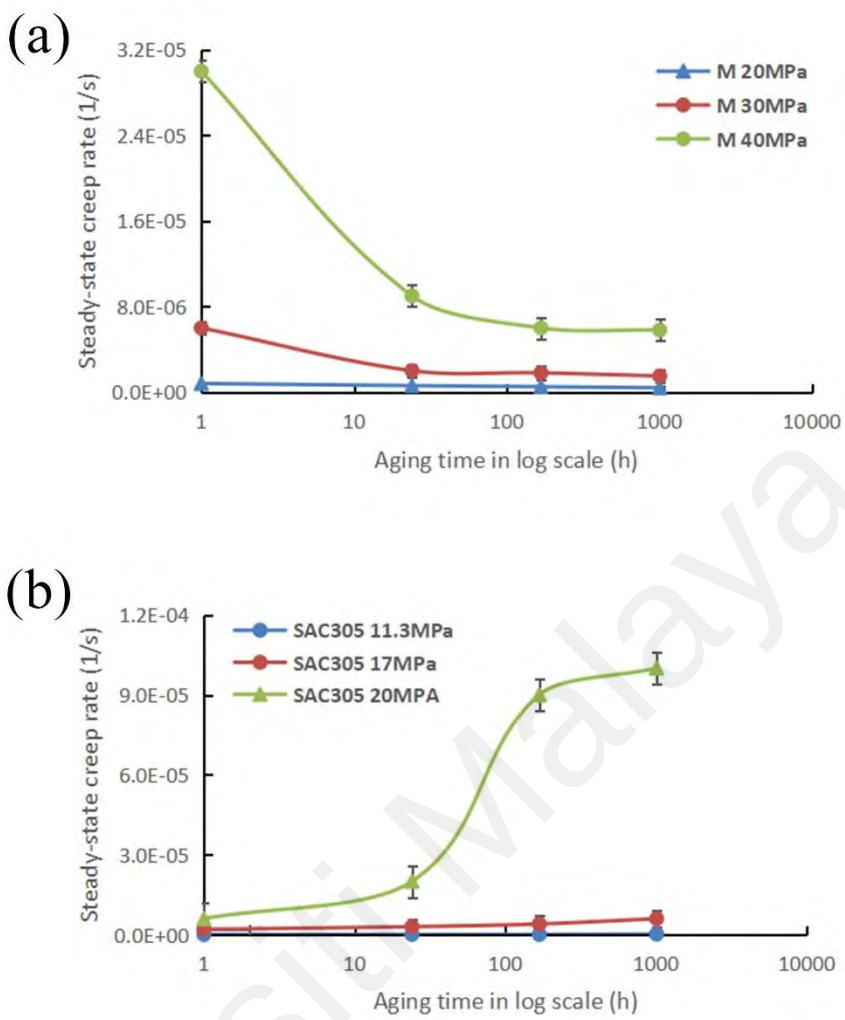

Figure 4.22: The steady-state creep strain rate of (a) solder M and (b) SAC305 with respect to aging time in log scale under variable creep stresses.

4.3.2 Hardness change during thermal aging

Figure 4.23 shows the microhardness indenters on the fracture tip area and with 3.2mm from fracture tip of solder M after creep testing. All the tested specimens fractured in the end of creep testing with 40 MPa creep load applied (whereas all the tested specimens of SAC305 fractured with 20 MPa creep load applied). According to Figure 3.3, the graph of hardness change was plotted against the distance between the indenter and creep fracture tip of solder M aged at different time intervals. Fracture mode of solder M was

ductile as the cross-sectional area showed necking and maximum deformed part is the fracture tip.

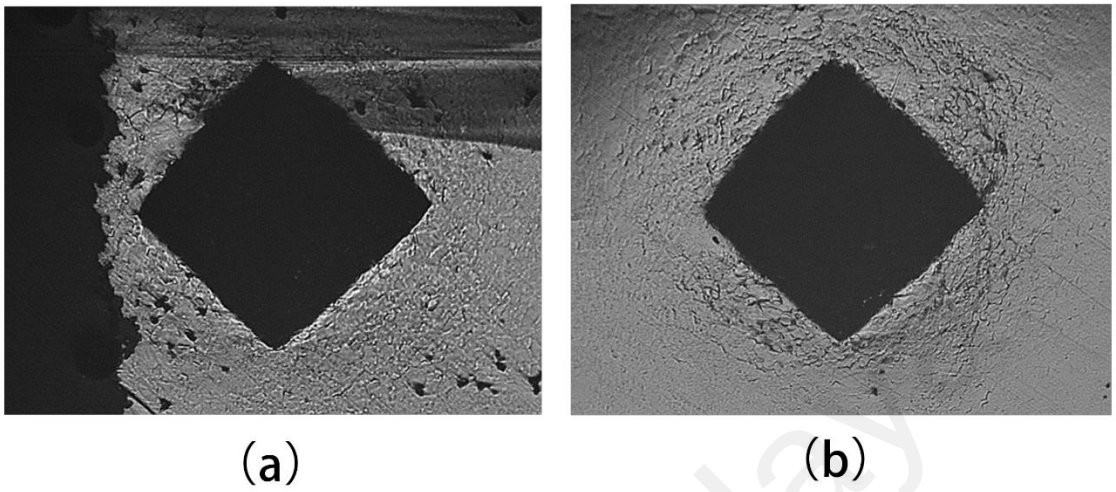

Figure 4.23: (a) Microhardness indentation of solder M at the fracture tip after creep testing with 40 MPa applied; (b) Microhardness indentation with 3.2mm in between fracture tip and indenter on solder M after creep testing.

Thermal aging has the effect of increasing the hardness of solder M. Away from the fracture tip, hardness showed larger when the distance between fracture tip and indenter increased. The sample with 0h thermal aging time has Vicker hardness with 28.7 HV, and the hardness was not increased much after the sample has been thermally aged for 24h. Referring to the change of strain hardening in Figure 4.14, 125℃ aging for 24h has shown a decrease in the strain hardening exponent. Thus, the hardness would not have been increased at the first 24h. However, after that, the hardness kept increasing 10.1% to 31.6 HV after 1008h aging at 125℃ as the strain hardening effect improved the strength of solder M. The solid solution strengthening from Bi, and precipitation strengthening of Bi and Sb improved the hardness of solder M during thermal aging. During thermal aging, SAC305 undergoes microstructural changes, including grain growth and coarsening of the IMCs. These changes can affect the mechanical properties of the solder which leads to the reduction of its hardness.

However, the presence of IMCs can strengthen the solder alloy and increase its resistance to deformation, leading to higher hardness values of solder M with additional elements added. The strain hardening exponent (*n* value) characterizes the rate at which a material hardens as it undergoes plastic deformation. It is often determined through tensile testing and reflects the ability of the material to sustain plastic deformation without fracturing. The minimum hardness values obtained for all the samples with variable thermal aging time are all on the fracture tips, the hardness increased away from fracture tip to another side of sample as shown in Figure 4.24. Due to the ductile property of two solders, voids are generated around inclusions, matrix interfaces, and at the center of the necking part before the solder raptured, where the hydrostatic stress is maximized and stress triaxiality dominates. The process of fracture starts with void nucleation, then develops by void growth, and void would link with each other and finally coalescence as bigger ones (Pantazopoulos, 2019). The inclusion density affects the micro-void nucleation rate, leading to a higher number of nucleation sites and lower growth potential, resulting in a high void distribution density and lower size dimples, signifying lower overall plasticity (Hosford, 2013). During third stage creep, an effective reduction of cross-section happens, and various microscopic degradation phenomena take place, such as massive void formation, cavitation generation while microstructural changes driven by diffusion processes and recrystallization. The micro-void coalescence gives rise to the evolution of ductile fracture, which creates fracture surface patterns with a lot of dimples (Pantazopoulos et al., 2016). The growth of coarse voids proceeds against fine ones. As void evolution advances, the un-fractured metal links between the holes are consecutively strained until final failure occurs, creating lower size secondary dimples and leading to an assigned distribution of cavities (Hull, 1999). Thus, these voids near the fracture tip results in a lower hardness value as compared to other parts of the sample.

The Vicker hardness at the fracture tip for 0h aged sample is 25.8 HV, is increased 2.3% after 24h, and reached to the maximum value at 168h with 28 HV, then the hardness stayed the same after that till 1008h thermal aged status. As for SAC305, the Vicker hardness at the fracture tip is 12.6 HV for the as-received sample, and it dropped to 11.1 HV after 1008h aging at 125 ℃ as shown in Figure 4.24(b). Therefore, the improved hardness of solder M near the fracture tips after thermal aging still resulted from the simultaneously added additional elements.

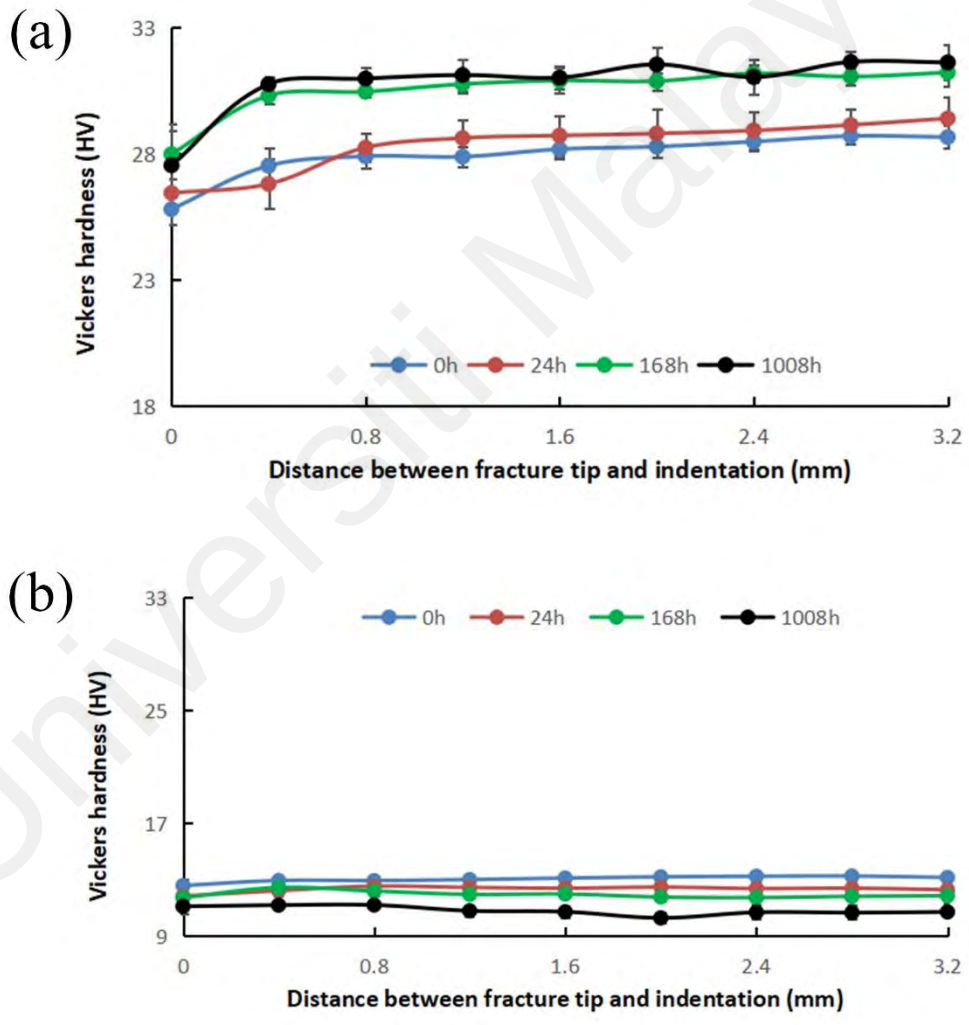

Figure 4.24 Microhardness of thermally aged (a) solder M and (b) SAC305 from the fracture tip to another side of sample after creep testing.

4.3.3 Creep fracture analysis of SAC305 and solder M

Figure 4.25(a) shows the fractography at 1000x magnification of as-received solder M after creep test under 40 MPa. This fractography shows cracks occurring on the grain boundaries of the fracture surfaces. Besides, all the other FESEM images on different locations of the fracture surface have shown the same behavior as observed. Hence, the fracture characteristics of the creep failures can be defined as intergranular for most cases. Moreover, dimples were observed on fractographies which has shown also in the tensile fracture surfaces. These dimples were caused by the growth and coalescence of microscopic voids during creep deformation. In the later stages of creep deformation, micro-voids formed and grew within the material. As these micro-voids coalesce, they lead to crack propagation and eventual fracture. The fracture surface revealed the presence of grain boundaries as some smooth and ball like facets were observed. These facets between individual grains can act as barriers to dislocation movement and influence the fracture behavior. Therefore, the creep failures are intergranular ductile fractures.

Figure 4.25(b) provides more details of the creep fracture characteristics, which is the enlarged aera of selected fracture surface in the red box of Figure 4.25(a). Grain boundary sliding was observed in Figure 4.25(b) from where the deformation mechanism of solder M after creep testing showed its grains slide against each other. This behavior occurs in polycrystalline material under external stress at high homologous temperature (above 0.4) and low strain rate and is intertwined with creep.

In addition, Sherby and Burke (1968) suggested the inconsistency in the activation energy values for pure tin from the well-established equality between the values of the activation energy for creep and the activation energy value for self-diffusion. It is generally observed that the activation energy for creep is equal to the activation energy for self-diffusion through the lattice, when T/T_m is larger than the homologous temperature of the transition

between pipe diffusion and lattice diffusion. Homologous temperature describes the operating temperature relative to the melting temperature of the material. The value of T/T_m is usually about 0.5 to 0.6 for most Pb-free alloy. According to the DSC results in Figure 4.2, T/T_m of solder M and SAC305 are both 0.6 during the creep testing which is high temperature creep. Thus, both lattice and pipe diffusion take place simultaneously. Moreover, the creep temperature at $T/T_m = 0.6$ has been taken to signify a change from processes controlled by lattice diffusion to mechanisms involving preferential diffusion along dislocations or grain boundaries (Feltham & Meakin, 1959). Furthermore, with polycrystalline Sn alloy, creep occurs by diffusion-controlled dislocation processes when creep exponent higher than 4 (*m* falls within the range of 4 to 6 for SAC305), generally attributed to a transition to diffusional creep mechanisms (Burton & Greenwood, 1970; Witkin, 2013).

Since the creep deformation is diffusion controlled, Coble creep is a type of diffusion-controlled creep mechanism that predominantly occurs in polycrystalline materials. It is more pronounced in materials with small grain sizes, as smaller grains have more grain boundaries, providing more opportunities for diffusion along the grain boundaries. The creep mechanism of solder M can be determined as grain boundary sliding aided by grain boundary diffusion (Coble creep).

Furthermore, in Figure 4.25(b), Sn was the main element detected on two grains in the EDX analysis. It indicates that Sn grains stretched along that direction where the creep stress was applied. This led to the creation of voids and cavities and a loss of coherency. To prevent void formation, the grains slide relative to each other to fill in these unfavorable gaps as observed.

However, there are also precipitates of which the grain size is much smaller than Sn grain size as found in selected fracture surface in the red box of Figure 4.26(a). Figure 4.26(b) enlarged this area with 10000x magnification. Ag was detected with an unusually high weight percentage of 15.42 wt.% in EDX analysis as shown in Figure 4.26(c). This observation proved that the IMC precipitates exist on solder M fracture surface and the deformation mechanism in creep testing tends to show as grain boundary sliding as well. However, the creep mechanism and fracture behavior of the IMC precipitates need to be further studied since the size is too small to be observed by using current equipment.

Creep fractographies of solder M under 40MPa after aging at 125℃ are shown in Figure 4.27. Since the creep deformation is diffusion controlled, grain boundary sliding aided by grain boundary diffusion (Coble creep) is observed for all the samples during thermal aging. FESEM images show cracks occurring on the grain boundaries of the fracture surfaces. Hence, the fracture characteristic of the creep failures in solder M is intergranular. Moreover, tiny dimples were observed on fractographies for all the samples of solder M at 125℃ aging. Hence, the creep failures are intergranular ductile fractures.

Intergranular fracture mechanism is common for creep failures. The tensile strength of the grain boundaries is higher than the interior of grains for low temperatures. However, the tensile strength of the interior of grains is higher than the grain boundaries for elevated temperatures (Gaffard et al., 2005; Sasikala et al., 1999). Therefore, high temperature creep failure tends to occur at grain boundaries. When solder M experienced dislocation climb creep controlled by lattice diffusion, it means that deformation occurs primarily due to dislocation movement within the crystal lattice of the material.

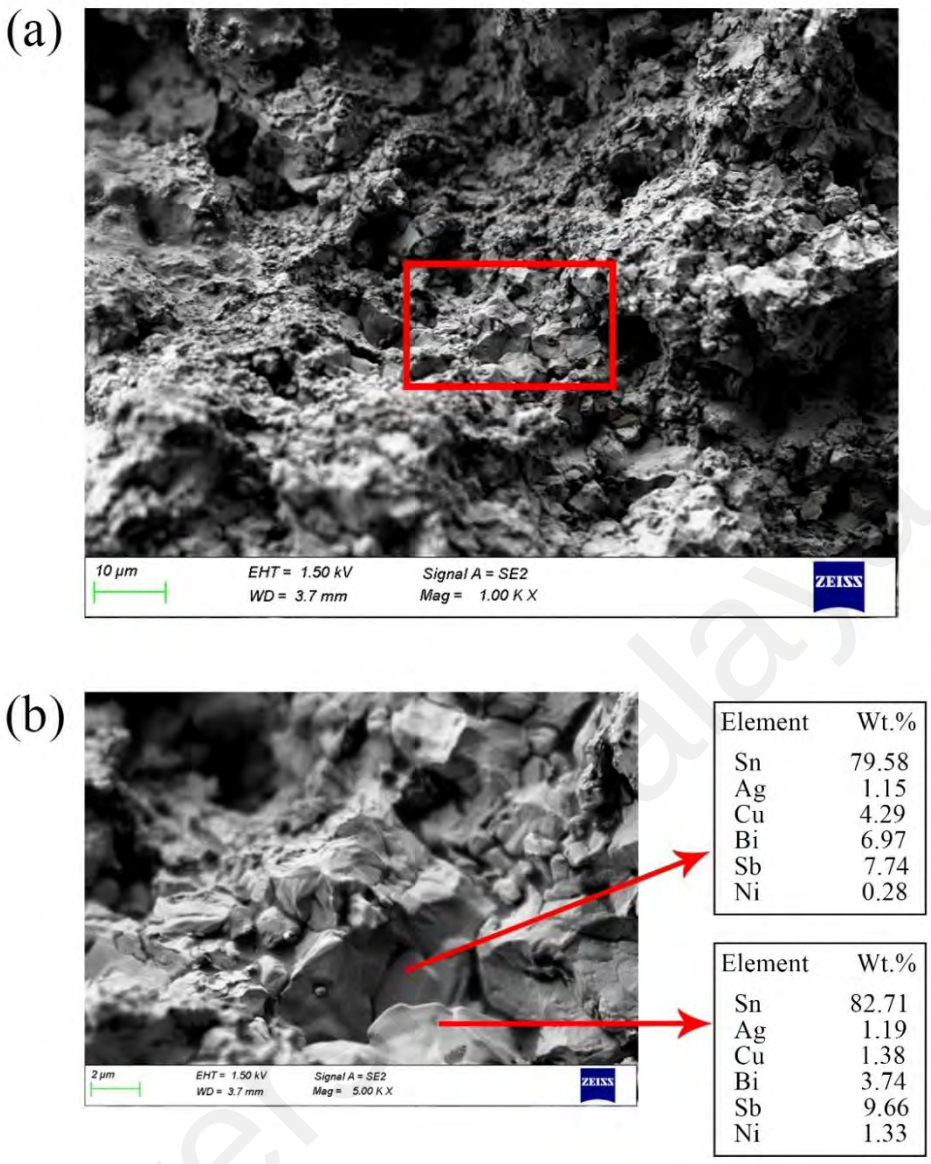

Figure 4.25: (a) Fractography at 1000x magnification of as-received solder M after creep testing under 40MPa; (b) Zoomed in creep fracture surface of (a) at 5000x magnification and corresponding EDX analyses.

After creep stress (40MPa) was applied for some time, dislocations climb and rearrange, causing the material to undergo plastic deformation, leading to fracture. Since creep under lattice diffusion-controlled mechanisms involves atomic movement and diffusion, there was grain boundary sliding and might have atomic rearrangement near the fracture surface.

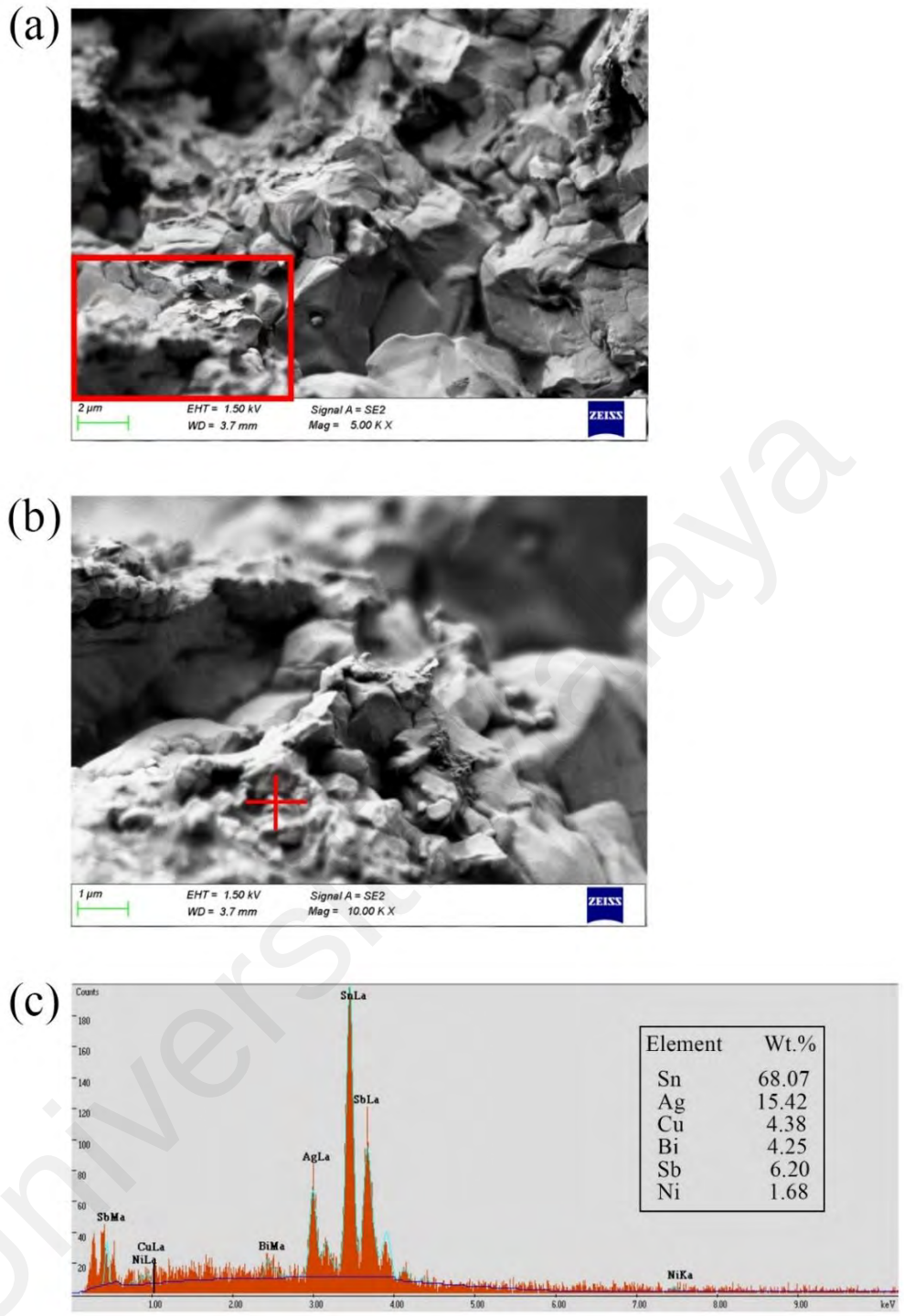

Figure 4.26: (a) Fractography at 5000x magnification of as-received solder M after creep testing under 40MPa; (b) Zoomed in creep fracture surface of (a) at 10000x magnification; (c) Corresponding EDX analyses of (b).

The fracture surface in Figure 4.27(a) exhibits a characteristic region where the final fracture occurred. This area appears rough and granular due to the gradual accumulation of deformation and the formation of voids and microcracks. When solder M was subjected to high temperatures during creep testing, atoms near the grain boundaries diffused from regions of high stress to regions of lower stress. This diffusion process caused the grains to grow or elongate in the direction of the applied stress, leading to creep deformation. During the thermal aging, grain size in Figures 4.27(b-c) increased as compared to Figure 4.27(a). The size and distribution of IMCs have also changed over time. In addition to grain boundary sliding occurred in solder M, the precipitate strengthened microstructure of multicomponent alloys would seem to preclude sliding as a possibility, due to pinning of the grain boundaries by these precipitates, such as Bi, SbSn, $(Cu, Ni)_6Sn_5$, Ag_3Sn (Mavoori & Jin, 1998; Kerr & Chawla, 2004).

As for SAC305 creep fracture behavior, the necking phenomenon was observed in all tested specimens at 125℃ aging, indicating that the fracture is ductile. The fractographies of aged SAC305 in Figure 4.28 showed dimpled pattern which was observed on all fracture surfaces. The fracture surfaces of the SAC305 show ductile dimples with increased size after 24h thermal aging in Figure 4.28(b) and 1008h thermal aging in Figure 4.28(c) as compared to as-received SAC305 in Figure 4.28(a), which indicated that a plastic deformation mechanism dominated the fracture. The dimpled fracture surface on SAC305 indicated that the failure was ductile and occurred by micro-void nucleation and growth within the solder. The initial micro-voids nucleated preferentially within regions of stress concentration near the fracture tips, and subsequently the crack propagated by further micro-void nucleation and growth through the intervening regions. Once the initial micro-voids were formed, they rapidly grew, and eventually the intervening matrix fractured via micro-void nucleation, growth, and coalescence through the solder matrix.

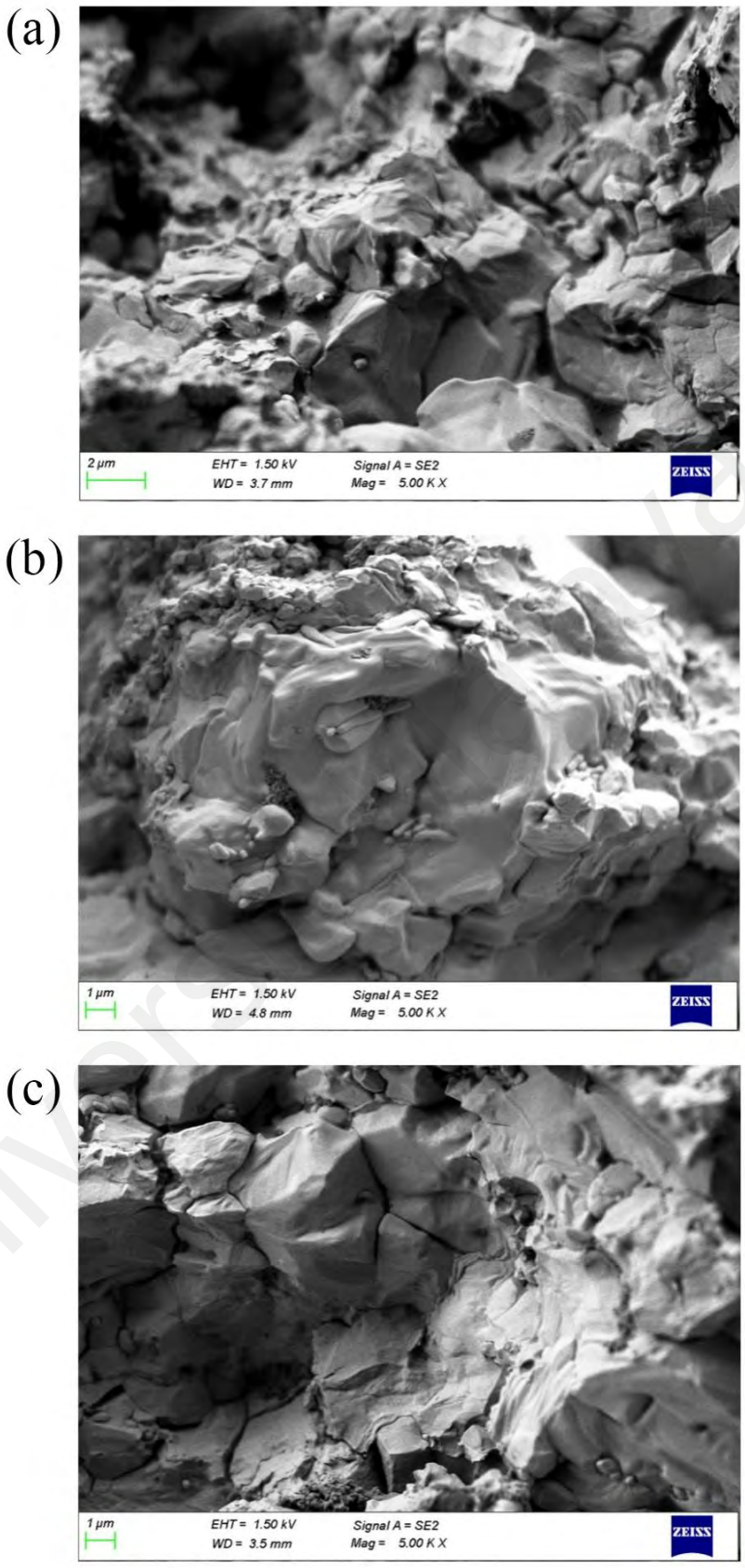

Figure 4.27: Fractography at 5000x magnification of solder M in 40 MPa creep testing after 125 ℃ thermal aging: (a) 0 h aged; (b) 24 h aged; (c) 1008 h aged.

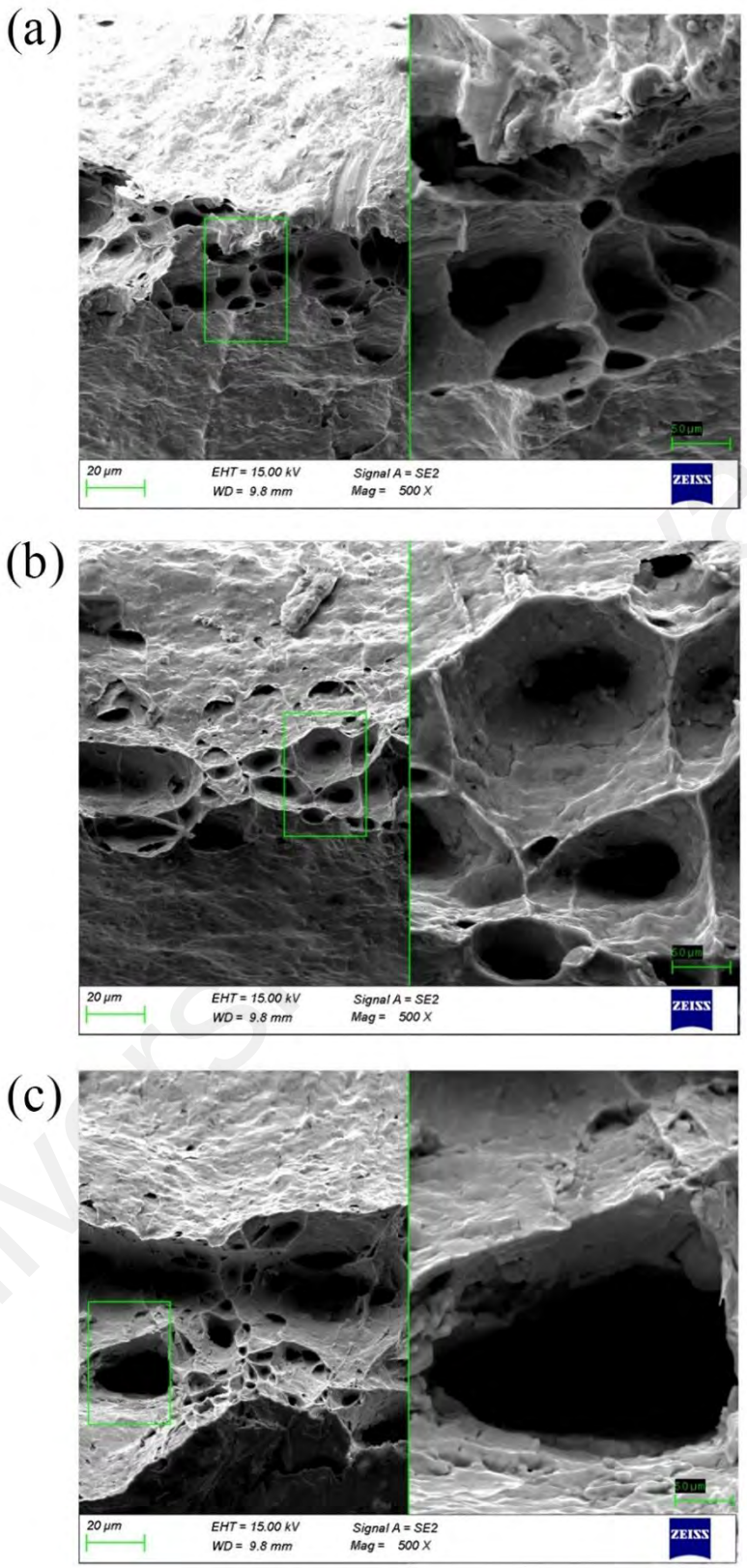

Figure 4.28: Fractography at 500x magnification (2000x magnification at right-side for zoomed in area in green box at left-side) of SAC305 at 20 MPa creep testing after 125 °C thermal aging: (a) 0 h aged; (b) 24 h aged; (c) 1008 h aged.

4.3.4 Summary of thermal aging effects on the creep behavior

In this study, the effects of simultaneous additions of Bi, Sb, and Ni to SAC305 solder on the creep behavior and microhardness change from creep fracture tip to another side after thermal aging at 125 ℃ for up to 1008 hours were investigated. The element composition characterizations of the novel solder M and SAC305 were reported. Creep performances for both solders were analyzed and compared. In addition, the mechanical performances and hardness near creep fracture tip after creep tests were studied. The main findings of the investigation are summarized as following:

- 125℃ aging resulted in the decreased creep rate during 1008h for solder M, but the opposite performance of SAC305. The first 24h thermal aging has the most obvious change on creep performance on both solder alloys, and solder M stayed stable with its creep performance after 168h thermal aging.
- With 20 MPa creep stress applied, solder M has performed higher creep resistance during $5x10^4$ s creep testing, but SAC305 showed lower creep resistance. The steady-state creep rate of solder M reduced after aging at 125℃ whereas SAC305 in an opposite performance.
- The additional elements Bi, Sb and Ni improved the creep resistance and lifetime of solder M as compared to SAC305.
- The hardness increased 10.1% after 1008h thermal aging for solder M due to Bi, Sb and Ni added.
- The fracture tip with maximum deformation has the lowest hardness value as compared to other parts of solder M after creep testing with 40 MPa applied.
- The creep mechanism of solder M can be determined as grain boundary sliding aided by grain boundary diffusion (Coble creep), whereas dimpled fractography of SAC305 indicated that a plastic deformation mechanism dominated the fracture.

4.4 Simulations of reliability of SAC305 applied in a novel package

Due to the variation of temperature during service, the solder in QFP and PLCC undergo high thermal stress, which can lead to large deformation and failure. Thus, the prediction of thermal stress and strain distributions is a prerequisite for reliability analysis of such components. Along this line, this part of the work analyzed the performances of SAC305 applied in a novel hybrid package with two types of leads (gull wing and J-lead). The thermal stress and strain distributions of SAC305 were determined by using FEM in software ANSYS. Simulation work of package under thermal cyclic loading has been done, accumulated creep strain was found in the critical location of solder in package, and lifetime was predicted.

4.4.1 Thermal stress analysis of SAC305 used in a hybrid QFP

SAC305 solder applied in the hybrid 100-pin QFP which consists of gull wing and J-lead in a single package. These leads are the electrical and mechanical connections of the package and are soldered to the surface of a PCB. Two types of lead are designed: gull wing is mounted with 45° inclined with vertical direction while J-lead is vertically mounted on PCB. The newly designed package was depicted in Figure 4.29 where the package constituted gull wing and J-lead placed side by side.

Figure 4.29: Hybrid QFP with two types of lead.

In board level temperature cycling simulation, the maximum value of von Mises stress of 55.6 MPa is found in the solder joints near the chip corner as shown in Figure 4.30(a).

The location is at the interface between the bottom of the solder under J-lead in the corner of QFP and the PCB. This maximum von Mises stress is found at -40 °C at the end of the thermal cycling profile. Thus, any failure is expected to occur at this location. There is also warpage found in PCB as shown in Figure 4.30(b) due to the deformation under thermal loading condition. The maximum deformation with value 0.033 mm is found in the corner of PCB edge, and the displacement direction of the maximum deformed location is facing up. Besides, the warpage of the PCB board is shown in concave shape.

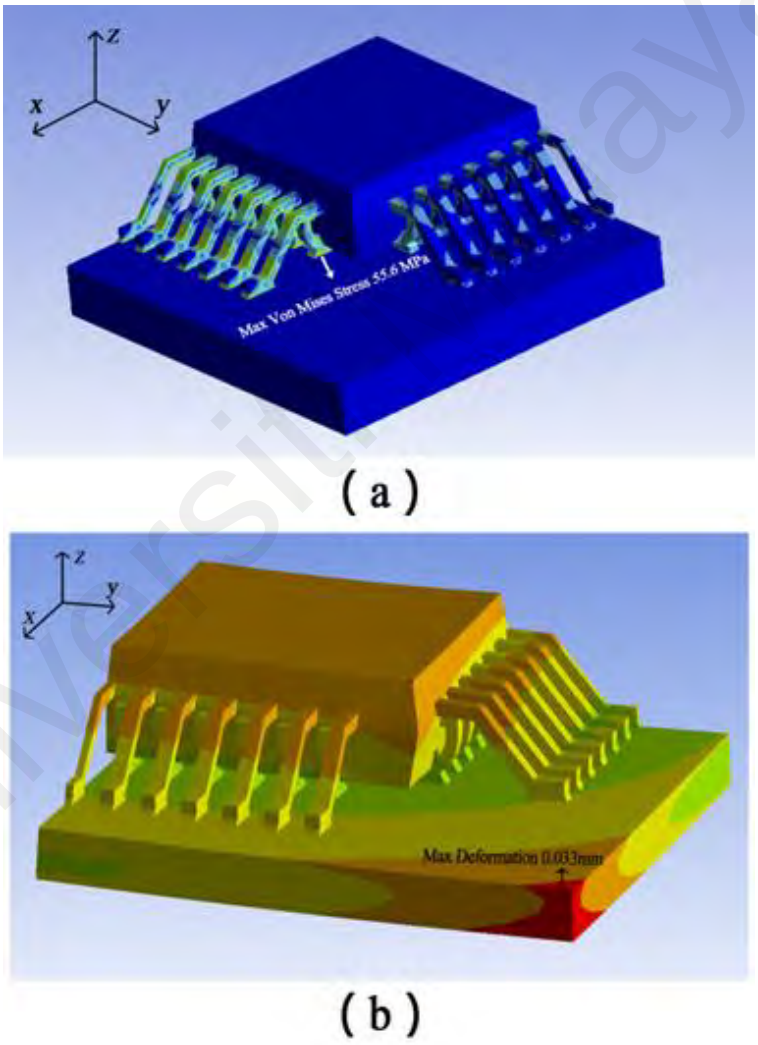

Figure 4.30: Maximum von Mises stress and deformation of hybrid QFP on PCB at -40 °C. (a) Maximum von Mises stress in solder under J-lead in the package corner and (b) Maximum deformation of hybrid QFP on PCB.

4.4.2 Temperature cycling simulation results at board level

Maximum creep strain is found in solder corner at the interface between the bottom of the solder under J-lead in the corner of QFP and PCB as shown in Figure 4.31. This is also the same location where the maximum von Mises stress was found in Figure 4.30(a).

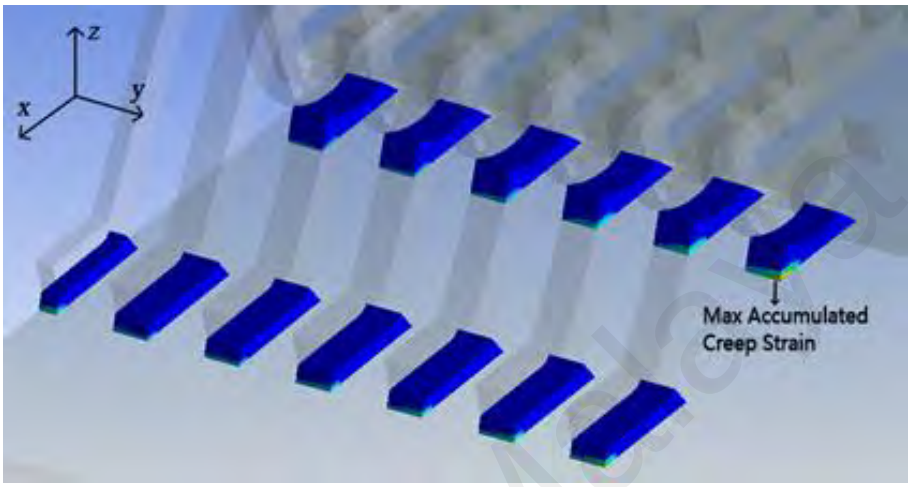

Figure 4.31: Maximum accumulated creep strain of J-lead solder joint under chip corner.

The creep behavior of SAC305 solder material was simulated by following the generalized Garofalo creep model where the parameters were provided by NXP:

$$\dot{\varepsilon}_{cr} = C_1[\sinh(C_2\sigma)]^{C_3} e^{\frac{-C_4}{T}} \qquad (4.7)$$

Where,

$\dot{\varepsilon}_{cr}$ = creep strain rate

σ = stress (Pa)

T = temperature (Kevin)

$C_1 = 5 \times 10^5$ (material constant)

$C_2 = 10^{-8}$ (material constant)

$C_3 = 5$ (material constant)

C_4 = -5807 (material constant)

Shear stress and creep shear strain hysteresis loops on the solder joint near the package corner were plotted in Figure 4.32(a). It is shown that the creep responses converged after three cycles, which indicates the creep behavior becomes stabilized from the fourth cycle. In addition, from the plotting between accumulated creep strain and time in Figure 4.32(b), it can be observed that the creep strain per cycle is 8.55×10^{-5}.

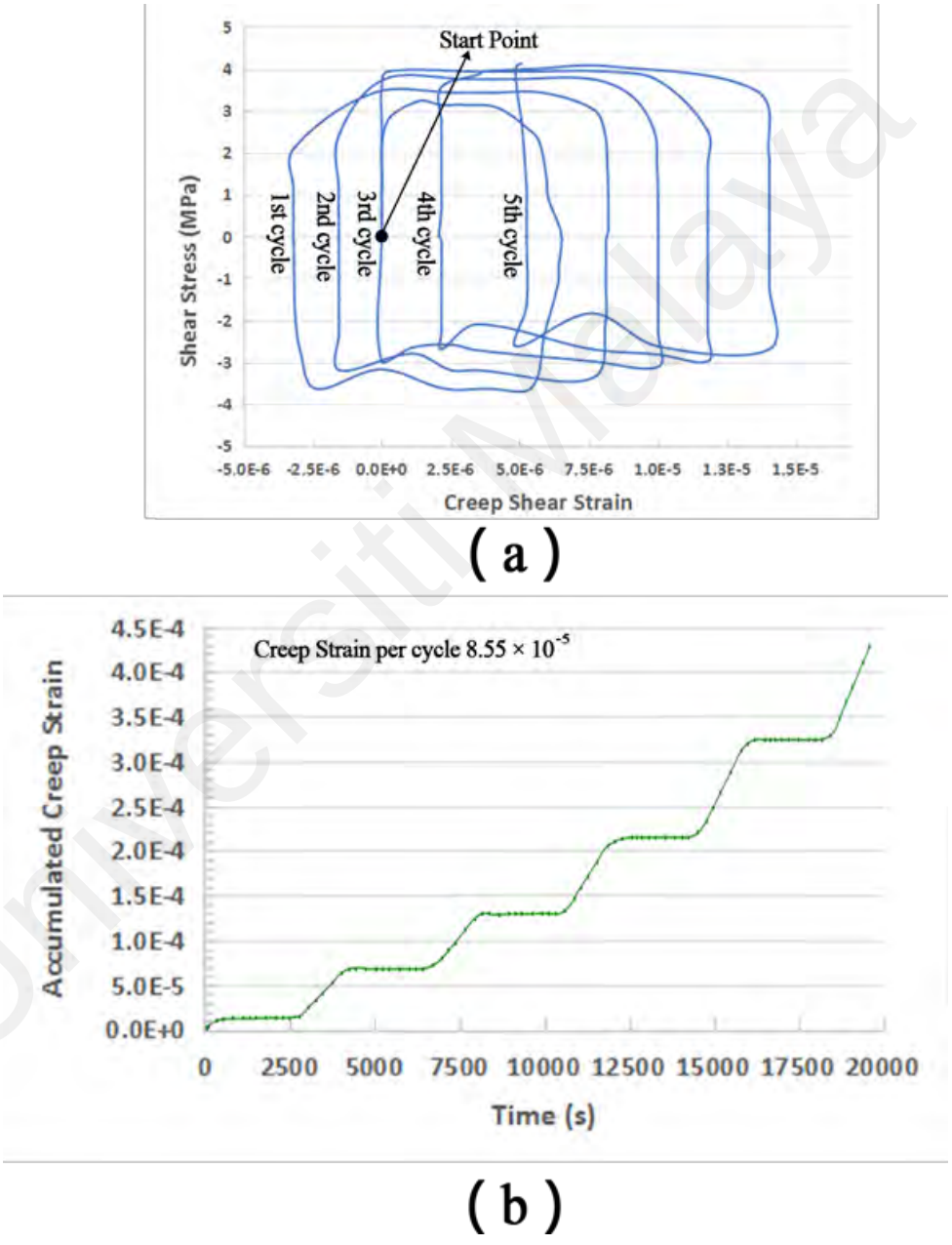

Figure 4.32: Simulation results of creep shear strain hysteresis loops and accumulated creep strain of J-lead solder joint under chip corner. (a) Shear stress vs. creep shear strain hysteresis loops and (b) Accumulated creep strain vs. time.

To evaluate the number of cycles to failure of solder joint under chip corner, Coffin Manson criterion is applied where creep strain accumulated over thermal cycles is expressed as an empirical relation in Equation (4.8) (Dudek et al., 2004):

$$N_f = \Theta(\Delta\varepsilon_{cr})^{-C_5} \quad (4.8)$$

Where,

N_f = number of cycles to failure

$\Delta\varepsilon_{cr} = 8.55 \times 10^{-5}$ (creep strain per cycle)

Θ = 4.5 (corresponding coefficients of SAC305) (Dudek et al., 2004)

C_5 = 1.295 (corresponding coefficients of SAC305) (Dudek et al., 2004).

Using this criterion, the expected number of cycles to failure is 8.34×10^5.

To validate the simulation results, board level temperature cycling test has been conducted with same temperature profile from -40 ℃ to 125 ℃ in Figure 3.7. The test results in Figure 4.33 show that the failed package is lower than 15% after 9928 cycles in this extreme testing condition. The package failed percentage for this hybrid QFP is lower than the designed value in NXP which is 25%. However, the large difference between the predicted lifetime and the experimental results could be attributed to the limitation of the Coffin-Manson model. Indeed, the model considers only accumulated creep strain as the driving force for failure. Thus, other modes of failures commonly found experimentally including electrical disconnection due to voids forming and growing or wire bonding failure are not considered.

Overall, the addition of Bi, Sb, and Ni improved microstructural refinement, suppressed the grain growth of solder M, and reduced the grain growth rate in comparison with SAC305. During thermal aging, UTS of solder M retained its strength in comparison to as-received sample, whereas SAC305 decreased of as-received sample. Thus, solder M

shall perform better in terms of its strength as compared to SAC305 since the additional element Bi, Sb and Ni resulted in the higher UTS of solder M due to their solid solution strengthening and precipitation strengthening mechanisms.

In addition, the toughness of solder M is higher than SAC305 at all thermal aging conditions. Also, 125℃ aging resulted in the decreased creep rate during 1008h for solder M, but the opposite performance of SAC305. The first 24h thermal aging has the most obvious change on creep performance on both solder alloys, and solder M stayed stable with its creep performance after 168h thermal aging. With creep stress applied, solder M has performed higher creep resistance during creep testing, but SAC305 showed lower creep resistance. The steady-state creep rate of solder M reduced after aging at 125℃ whereas SAC305 in an opposite performance.

In summary, the life span of solder M is supposed to be much longer than SAC305 during the hybrid QFP service in temperature cycling, and it can be the replacement of SAC305 serving in the harsh condition. The main reason is that the additional elements Bi, Sb and Ni improved the creep resistance and lifetime of solder M as compared to SAC305.

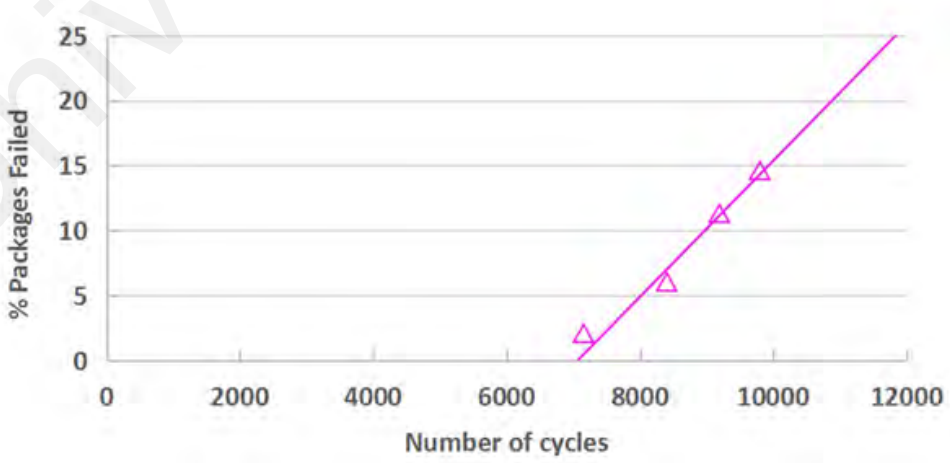

Figure 4.33: Percentage of failed hybrid QFP at board level temperature cycling test.

4.4.3 Summary of simulations of SAC305 applied in a novel QFP

Stress distributions in SAC305 were evaluated by using FEA in ANSYS, and maximum local stress was analyzed. The creep of SAC305 solder joints under thermal cycling condition has been determined by non-linear and time dependent 3D finite element simulation. A few statements may be fairly drawn as follows:

- The maximum von Mises stress and creep strain were found to occur near the interface between SAC305 solder under J-lead and PCB near the package corner in temperature cycling simulation.
- Warpage occurred in temperature cycling simulation and the maximum deformation was found in PCB corner.
- Temperature cycling experimental test validated lifetime of SAC305 applied this QFP and the value is lesser than simulation result, but the product is still considered reliable as test results passed NXP criterion.

CHAPTER 5

CONCLUSIONS AND RECOMMENDATIONS

5.1 Conclusions

In this study, the effects of simultaneous additions of Bi, Sb, and Ni to SAC305 solder on the microstructural and mechanical properties during thermal aging at 125 ℃ for up to 1008 hours were investigated. The characterizations of the novel solder M and SAC305 were reported. Microstructural observations for both solders were analyzed and compared through SEM analysis. In addition, the mechanical performances and fracture behaviors in tensile and creep testing were studied. Moreover, stress distributions in SAC305 applied in a novel hybrid QFP package were evaluated by using FEA in ANSYS, and maximum local stress was analyzed. The creep of SAC305 solder joints under thermal cycling condition has been determined by non-linear and time dependent 3D finite element simulation. The conclusions of this thesis can be drawn as follows based on the objectives that have been set in the beginning of the work:

Objective 1: *To investigate the effect of thermal aging on mechanical properties and creep characteristics of SAC305 and Solder M at room temperature.*

- During thermal aging, UTS of solder M retained its strength in comparison to as-received sample under different strain rates, whereas SAC305 decreased of as-received sample. However, the elongation of solder M decreased in contrast with an increase of SAC305.
- The toughness of solder M is higher than SAC305 at all thermal aging conditions. This is despite the toughness of solder M decreased from 41.5 MJ/m^3 to 30.9 MJ/m^3 at strain rate 10^{-3}/s during 1008h thermal aging, while the toughness of SAC305 only slightly reduced from17.2 MJ/m^3 to 16.3 MJ/m^3 with as-received sample.

- 125℃ aging resulted in the decreased creep rate during 1008h for solder M, but the opposite performance of SAC305. The first 24h thermal aging has the most obvious change on creep performance on both solder alloys, and solder M stayed stable with its creep performance after 168h thermal aging.
- With 20 MPa creep stress applied, solder M has performed higher creep resistance during $5x10^4$ s creep testing, but SAC305 showed lower creep resistance. The steady-state creep rate of solder M reduced after aging at 125℃ whereas SAC305 in an opposite performance.
- The hardness increased 10.1% after 1008h thermal aging for solder M due to Bi, Sb and Ni added.
- The creep fracture tip with maximum deformation has the lowest hardness value as compared to other parts of solder M after creep testing with 40 MPa applied.

Objective 2: *To evaluate the effect of thermal aging on the microstructure and fracture surface of SAC305 and Solder M.*

- The average grain diameter of as-received solder M is 1.42 μm, which is 2.5 times smaller of SAC305. After 1008h aging at 125℃, the grain diameter of solder M increased to 3.98 μm while SAC305 increased to 10.6 μm. Overall, the addition of Bi, Sb, and Ni improved microstructural refinement, suppressed the grain growth of solder M, and reduced the grain growth rate in comparison with SAC305.
- SAC305 showed more ductile fracture behavior and the dimple size increased faster resulting from the thermal aging effect in compared to solder M in tensile testing.
- The creep fracture surface of solder M showed the creep mechanism of it can be determined as grain boundary sliding aided by grain boundary diffusion (Coble creep).

- The creep fracture surface of SAC305 indicated that a plastic deformation mechanism dominated the fracture.

Objective 3: *To analyze the effect of additional elements Bi, Sb and Ni on the mechanical properties of SAC305 alloy.*

- The additional element Bi, Sb and Ni resulted in the higher UTS of solder M due to their solid solution strengthening and precipitation strengthening mechanisms.
- The additional elements Bi, Sb and Ni improved the creep resistance and lifetime of solder M as compared to SAC305.

Objective 4: *To assess the reliability of SAC305 used in a novel QFP under thermal cyclic loading.*

- The maximum von Mises stress and creep strain were found to occur near the interface between SAC305 solder under J-lead and PCB near the package corner in temperature cycling simulation.
- Temperature cycling experimental test validated lifetime of SAC305 applied this QFP and the value is lesser than simulation result, but the product is still considered reliable as test results passed NXP criterion.

5.2 Recommendations

- In the present study, the effects of simultaneous additions of Bi, Sb, and Ni to SAC305 solder on the microstructural and mechanical properties during thermal aging at 125 ℃ for up to 1008 hours were investigated. However, the tensile and creep tests were conducted at room temperature. It is recommended that the elevated temperatures to be applied in the tensile and creep testing since it is another variable that leads to primary failure mechanism for solders.

- Once the experimental data of creep testing under elevated temperatures can be collected for future work. It is recommended that the mathematical modelling of creep behavior of solder M to be explored to understand the effects of different creep parameters of this alloy such as activation energy, creep stress exponent, etc.
- Stress distributions, accumulated creep strain and lifetime of solder M applied in the novel hybrid QFP package is recommended for future work to compare with SAC305 performance by using FEA in ANSYS.

REFERENCES

Aamir, M., Waqas, M., Iqbal, M., Hanif, M. I., & Muhammad, R. (2017). Fuzzy logic approach for investigation of microstructure and mechanical properties of Sn96. 5-Ag3. 0-Cu0. 5 lead free solder alloy. *Soldering & Surface Mount Technology*.

Abtew, M., & Selvaduray, G. (2000). Lead-free solders in microelectronics. *Materials Science and Engineering: R: Reports, 27*(5-6), 95-141.

ahir Rizvi, M. J. (2007). Experimental and Modelling Studies of Electronic Packaging Interconnections formed with Lead-free Materials.

Aisha, I. S. R., Ourdjini, A., Astuty, A., & Saliza, O. (2011). Effect of Surface Finish On Intermetallic Compound Formation During Soldering With Ni-Doped Solders. *Solid State Sci. Technol, 19,* 319-329.

Ahn, B. (2021). Recent advances in brazing fillers for joining of dissimilar materials. *Metals, 11*(7), 1037.

Alam, M. S., Hassan, K. R., Suhling, J. C., & Lall, P. (2019, May). High Temperature Aging Effects in SAC and SAC+ X Lead Free Solders. In *2019 IEEE 69th Electronic Components and Technology Conference (ECTC)* (pp. 1815-1825). IEEE.

Ali, B. (2015). Advancement in microstructure and mechanical properties of lanthanum-doped tin-silver-copper lead free solders by optimizing the lanthanum doping concentration. *Soldering & Surface Mount Technology, 27*(2), 69-75.

Ali, B., Sabri, M. F. M., Jauhari, I., & Sukiman, N. L. (2016). Impact toughness, hardness and shear strength of Fe and Bi added Sn-1Ag-0.5 Cu lead-free solders. *Microelectronics Reliability*, *63*, 224-230.

Ali, L. F., Kuppuswamy, N., Soundararajan, R., Ramkumar, K. R., & Sivasankaran, S. (2021). Microstructural evolutions and mechanical properties enhancement of AA 6063 alloy reinforced with Tungsten (W) nanoparticles processed by friction stir processing. *Materials Characterization*, *172*, 110903.

Ali, U., Khan, H., Aamir, M., Giasin, K., Habib, N., & Owais Awan, M. (2021). Analysis of microstructure and mechanical properties of bismuth-doped SAC305 lead-free solder alloy at high temperature. *Metals, 11*(7), 1077.

An, T., & Qin, F. (2011). Cracking of the intermetallic compound layer in solder joints under drop impact loading.

Anderson, I. E., Cook, B. A., Harringa, J. L., & Terpstra, R. L. (2002). Microstructural modifications and properties of Sn-Ag-Cu solder joints induced by alloying. *Journal of electronic materials*, *31*, 1166-1174.

Anderson, I. E., Cook, B. A., Harringa, J. L., & Terpstra, R. L. (2002). Sn-Ag-Cu solders and solder joints: Alloy development, microstructure, and properties. *Jom*, *54*, 26-29.

Ara, A., & Usmani, J. A. (2015). Lead toxicity: a review. *Interdisciplinary toxicology, 8*(2), 55-64.

Armstrong, R. W. (2014). Engineering science aspects of the Hall–Petch relation. *Acta Mechanica*, *225*, 1013-1028.

Artaki, I., Noctor, D., Mather, J., Schroeder, S., Napp, D., Desantis, C., ... & Handwerker, C. (1999, February). Research trends in lead-free soldering in the US: NCMS Lead-Free Solder Project. In *Proceedings First International Symposium on Environmentally Conscious Design and Inverse Manufacturing* (pp. 602-605). IEEE.

Bai, Z., Wang, H., & Yao, J. (2015). *U.S. Patent No. 9,190,351*. Washington, DC: U.S. Patent and Trademark Office.

Bashir, M. N., Haseeb, A. S. M. A., Rahman, A. Z. M. S., & Fazal, M. A. (2016). Effect of cobalt doping on the microstructure and tensile properties of lead free solder joint subjected to electromigration. *Journal of Materials Science & Technology*, *32*(11), 1129-1136.

Billah, M. M., & Chen, Q. (2016). Strength of MWCNT-reinforced 70Sn-30Bi solder alloys. *Journal of Electronic Materials*, *45*, 98-103.

Body, P. E., Inglis, G., Dolan, P. R., & Mulcahy, D. E. (1991). Environmental lead: a review. *Critical Reviews in Environmental Science and Technology, 20*(5-6), 299-310.

Boesenberg, A. J. (2011). *Development of aluminum, manganese, and zinc-doped tin-silver-copper-X solders for electronic assembly.* Iowa State University.

Boettinger, W. J., Handwerker, C. A., & Kattner, U. R. (1993). Reactive wetting and intermetallic formation. *The mechanics of solder alloy wetting and spreading*, 103-140.

Borzone, G., Delsante, S., Li, D., & Novakovic, R. (2021). New insights into phase equilibria of the Sb-Sn system. *Journal of Phase Equilibria and Diffusion*, *42*, 63-76.

Braga, M. H., Vizdal, J., Kroupa, A., Ferreira, J., Soares, D., & Malheiros, L. F. (2007). The experimental study of the Bi–Sn, Bi–Zn and Bi–Sn–Zn systems. *Calphad*, *31*(4), 468-478.

Brand, M. J., Kolp, E. I., Berg, P., Bach, T., Schmidt, P., & Jossen, A. (2017). Electrical resistances of soldered battery cell connections. *Journal of Energy Storage, 12*, 45-54.

Burke, C., & Punch, J. (2014). A comparison of the creep behavior of joint-scale SAC105 and SAC305 solder alloys. *IEEE Transactions on Components, Packaging and Manufacturing Technology, 4*(3), 516-527.

Burton, B., & Greenwood, G. W. (1970). The limits of the linear relation between stress and strain rate in the creep of copper and copper-zinc alloys. Acta Metallurgica, 18(12), 1237-1242.

Cagliero, R., & Maizza, G. (2011). Influence of Vickers Indenter Tip Geometry on the Macro-indentation Properties of γ-TiAl Alloys. In *Proceedings of the 2011 COMSOL Conference, Stuttgart*.

Cai, Z., Suhling, J. C., Lall, P., & Bozack, M. J. (2012, May). Mitigation of lead free solder aging effects using doped SAC-X alloys. In *13th InterSociety Conference on Thermal and Thermomechanical Phenomena in Electronic Systems* (pp. 896-909). IEEE.

Cai, Z., Zhang, Y., Suhling, J. C., Lall, P., Johnson, R. W., & Bozack, M. J. (2010, June). Reduction of lead free solder aging effects using doped SAC alloys. In *2010 Proceedings 60th Electronic Components and Technology Conference (ECTC)* (pp. 1493-1511). IEEE.

CHANTARAMANEE, S., & SUNGKHAPHAITOON, P. (2021). Influence of bismuth on microstructure, thermal properties, mechanical performance, and interfacial behavior of SAC305-xBi/Cu solder joints. *Transactions of Nonferrous Metals Society of China*, *31*(5), 1397-1410.

Charles Jr, H. K., & Clatterbaugh, G. V. (1990). Solder joint reliability—Design implications from finite element modeling and experimental testing.

Chauhan, P., Mukherjee, S., Osterman, M., Dasgupta, A., & Pecht, M. (2013, July). Effect of isothermal aging on microstructure and creep properties of SAC305 solder: a micromechanics approach. In *International Electronic Packaging Technical Conference and Exhibition* (Vol. 55751, p. V001T07A009). American Society of Mechanical Engineers.

Che, F., Zhu, W., Poh, E. S., Zhang, X., & Zhang, X. (2010). The study of mechanical properties of Sn–Ag–Cu lead-free solders with different Ag contents and Ni doping under different strain rates and temperatures. *Journal of Alloys and Compounds, 507*(1), 215-224.

Chen, H., Han, J., Li, J., & Li, M. (2012). Inhomogeneous deformation and microstructure evolution of Sn-Ag-based solder interconnects during thermal cycling and shear testing. *Microelectronics Reliability*, *52*(6), 1112-1120.

Chen, H., Lee, H. Y., Ku, C. S., & Wu, A. T. (2016). Evolution of residual stress and qualitative analysis of Sn whiskers with various microstructures. *Journal of materials science*, *51*, 3600-3606.

Chen, W., Lu, F., & Cheng, M. (2002). Tension and compression tests of two polymers under quasi-static and dynamic loading. *Polymer testing*, *21*(2), 113-121.

Chen, W. M., Kang, S. K., & Kao, C. R. (2012). Effects of Ti addition to Sn–Ag and Sn–Cu solders. *Journal of alloys and compounds*, *520*, 244-249.

Chen, W.-Y., Yu, C.-Y., & Duh, J.-G. (2014). Improving the shear strength of Sn–Ag–Cu–Ni/Cu– Zn solder joints via modifying the microstructure and phase stability of Cu–Sn intermetallic compounds. *Intermetallics, 54*, 181-186.

Chen, X., Zhou, J., Xue, F., & Yao, Y. (2016). Mechanical deformation behavior and mechanism of Sn-58Bi solder alloys under different temperatures and strain rates. *Materials Science and Engineering: A*, *662*, 251-257.

Chen, Z., Ma, K., Liu, L., Lee, N.-C., Liu, G., Yan, J., Li, H., Liu, S., Ruan, M., & Pan, H. (2021). Mechanical Performance and Reliability of a Sn–Ag–Cu–Sb Alloy at Elevated Temperatures. *IEEE Transactions on Components, Packaging and Manufacturing Technology, 11*(7), 1081-1087.

Cheng, F., Nishikawa, H., & Takemoto, T. (2008). Microstructural and mechanical properties of Sn–Ag–Cu lead-free solders with minor addition of Ni and/or Co. *Journal of materials science, 43*, 3643-3648.

Cheng, S., Huang, C. M., & Pecht, M. (2017). A review of lead-free solders for electronics applications. *Microelectronics Reliability, 75,* 77-95.

Chinnam, R. K., Fauteux, C., Neuenschwander, J., & Janczak-Rusch, J. J. A. M. (2011). Evolution of the microstructure of Sn–Ag–Cu solder joints exposed to ultrasonic waves during solidification. *Acta Materialia*, *59*(4), 1474-1481.

Choi, S., Lucas, J., Subramanian, K., & Bieler, T. (2000). Formation and growth of interfacial intermetallic layers in eutectic Sn-Ag solder and its composite solder joints. *Journal of Materials Science: Materials in Electronics, 11*(6), 497-502.

Chowdhury, M. R., Ahmed, S., Fahim, A., Suhling, J. C., & Lall, P. (2016, May). Mechanical characterization of doped SAC solder materials at high temperature. In *2016 15th IEEE Intersociety Conference on Thermal and Thermomechanical Phenomena in Electronic Systems (ITherm)* (pp. 1202-1208). IEEE.

Chroneos, R. J., Mallik, D., & Prough, S. D. (1993). Packaging alternatives for high lead count, fine pitch, surface mount technology. *IEEE transactions on components, hybrids, and manufacturing technology*, *16*(4), 396-401.

Chuang, T. H. (2006). Rapid whisker growth on the surface of Sn–3Ag–0.5 Cu–1.0 Ce solder joints. *Scripta Materialia*, *55*(11), 983-986.

Chudnovsky, B. H. (2012). *Electrical power transmission and distribution: aging and life extension techniques.* CRC Press.

Clech, J. P. M., Coyle, R. J., & Arfaei, B. (2019). Pb-free solder joint thermo-mechanical modeling: state of the art and challenges. *JOM, 71*, 143-157.

Cohn, C., & Harper, C. (2004). *Failure-free integrated circuit packages*. McGraw-Hill, Inc..

Coyle, R., Parker, R., Arfaei, B., Mutuku, F., Sweatman, K., Howell, K., ... & Benedetto, E. (2014, May). The effect of nickel microalloying on thermal fatigue reliability and microstructure of SAC105 and SAC205 solders. In *2014 IEEE 64th Electronic Components and Technology Conference (ECTC)* (pp. 425-440). IEEE.

Crandall, M. A. (2011). *Effect of intermetallic growth on durability of high temperature solders (tin-silver, SAC305, SAC+ manganese, tin-silver+ copper Nano) in thermal and vibration environments* (Doctoral dissertation, University of Maryland, College Park).

Damalas, C. A., & Eleftherohorinos, I. G. (2011). Pesticide exposure, safety issues, and risk assessment indicators. *International journal of environmental research and public health, 8*(5), 1402-1419.

Dariavach, N., Callahan, P., Liang, J., & Fournelle, R. (2006). Intermetallic growth kinetics for Sn-Ag, Sn-Cu, and Sn-Ag-Cu lead-free solders on Cu, Ni, and Fe-42Ni substrates. *Journal of Electronic Materials*, *35*, 1581-1592.

Das, V. K. (2014). *Tin In Applications Meeting the Green Challenge.* The University of Malaya Press.

Darveaux, R. F. (1993). *Mechanical evaluation of indium for die attachment in a multichip package.* North Carolina State University.

Depiver, J. A., Mallik, S., & Harmanto, D. (2021). Solder joint failures under thermo-mechanical loading conditions–A review. *Advances in Materials and Processing Technologies*, *7*(1), 1-26.

Ding, Y., Wu, G. D., Wang, X. L., Yan, G. S., & Hang, C. J. (2014, August). Tensile testing and microstructure analysis on Sn-Pb-Cd and Sn-Pb eutectic solder. In *2014 15th International Conference on Electronic Packaging Technology* (pp. 893-897). IEEE.

Dong, W., Shi, Y., Lei, Y., Xia, Z., & Guo, F. (2009). Effects of small amounts of Ni/P/Ce element additions on the microstructure and properties of Sn3. 0Ag0. 5Cu solder alloy. *Journal of Materials Science: Materials in Electronics*, *20*, 1008-1017.

Dudek, R., Walter, H., Doering, R., & Michel, B. (2004, May). Thermal fatigue modelling for SnAgCu and SnPb solder joints. In *5th International Conference on Thermal and Mechanical Simulation and Experiments in Microelectronics and Microsystems, 2004. EuroSimE 2004. Proceedings of the* (pp. 557-564). IEEE.

El-Daly, A. A., Al-Ganainy, G. S., Fawzy, A., & Younis, M. J. (2014). Structural characterization and creep resistance of nano-silicon carbide reinforced Sn–1.0 Ag–0.5 Cu lead-free solder alloy. *Materials & Design, 55*, 837-845.

El-Daly, A. A., Desoky, W. M., Saad, A. F., Mansor, N. A., Lotfy, E. H., Abd-Elmoniem, H. M., & Hashem, H. (2015). The effect of undercooling on the microstructure and tensile properties of hypoeutectic Sn–6.5 Zn–xCu Pb-free solders. *Materials & Design*, *80*, 152-162.

El-Daly, A. A., & El-Taher, A. M. (2013). Evolution of thermal property and creep resistance of Ni and Zn-doped Sn–2.0 Ag–0.5 Cu lead-free solders. *Materials & Design*, *51*, 789-796.

El-Daly, A. A., & El-Taher, A. M. (2013). Improved strength of Ni and Zn-doped Sn–2.0 Ag–0.5 Cu lead-free solder alloys under controlled processing parameters. *Materials & Design*, *47*, 607-614.

El-Daly, A. A., El-Taher, A. M., & Dalloul, T. R. (2014). Enhanced ductility and mechanical strength of Ni-doped Sn–3.0 Ag–0.5 Cu lead-free solders. *Materials & Design*, *55*, 309-318.

El-Daly, A. A., Eid, N. A. M., & Ibrahiem, A. A. (2022). Synergic effect of Te, Ni and MWCNT on creep behavior and microstructural evolution of Sn-1.0 Ag-0.7 Cu low-Ag solder. *Journal of Alloys and Compounds, 902,* 163808.

El-Daly, A. A., & Hammad, A. E. (2010). Elastic properties and thermal behavior of Sn–Zn based lead-free solder alloys. *Journal of Alloys and Compounds, 505*(2), 793-800.

El-Daly, A. A., Hammad, A. E., Fawzy, A., & Nasrallh, D. A. (2013). Microstructure, mechanical properties, and deformation behavior of Sn–1.0 Ag–0.5 Cu solder after Ni and Sb additions. *Materials & design*, *43*, 40-49.

El-Daly, A. A., Ibrahiem, A. A., & Eid, N. A. M. (2021). Development of Sn-1.0 Ag-0.7 Cu composite solder with improved resistivity and strength–ductility synergy through additions of Ni, Te and MWCNT. *Journal of Materials Science: Materials in Electronics, 32,* 19871-19889.

El-Daly, A., El-Taher, A., & Dalloul, T. (2014). Improved creep resistance and thermal behavior of Ni-doped Sn-3.0 Ag-0.5 Cu lead-free solder. *Journal of Alloys and Compounds, 587*, 32-39.

El-Daly, A., El-Taher, A., & Gouda, S. (2015). Development of new multicomponent Sn-Ag-Cu-Bi lead-free solders for low-cost commercial electronic assembly. *Journal of Alloys and Compounds, 627*, 268-275.

El-Daly, A., Hammad, A., Al-Ganainy, G., & Ragab, M. (2014a). Influence of Zn addition on the microstructure, melt properties and creep behavior of low Ag-content Sn-Ag-Cu lead-free solders. *Materials Science and Engineering: A, 608*, 130-138.

El-Daly, A., Hammad, A., Al-Ganainy, G., & Ragab, M. (2014b). Properties enhancement of low Ag-content Sn-Ag-Cu lead-free solders containing small amount of Zn. *Journal of Alloys and Compounds, 614*, 20-28.

Enke, N. F., Kilinski, T. J., Schroeder, S. A., & Lesniak, J. R. (1989). Mechanical behaviors of 60/40 tin-lead solder lap joints. *IEEE transactions on components, hybrids, and manufacturing technology*, *12*(4), 459-468.

Erer, A. M., Oguz, S., & Türen, Y. (2018). Influence of bismuth (Bi) addition on wetting characteristics of Sn-3Ag-0.5 Cu solder alloy on Cu substrate. *Engineering Science and Technology, an International Journal, 21*(6), 1159-1163.

Erinc, M., Schreurs, P. J. G., & Geers, M. G. D. (2008). Intergranular thermal fatigue damage evolution in SnAgCu lead-free solder. *Mechanics of Materials*, *40*(10), 780-791.

Erinc, M., Schreurs, P., Zhang, G., & Geers, M. (2005). Microstructural damage analysis of SnAgCu solder joints and an assessment on indentation procedures. *Journal of Materials Science: Materials in Electronics, 16*(10), 693-700.

Evans, J. W. (2007). *A guide to lead-free solders: physical metallurgy and reliability.* Springer Science & Business Media.

Fahim, A., Ahmed, S., Chowdhury, M. R., Suhling, J. C., & Lall, P. (2016, May). High temperature creep response of lead free solders. In *2016 15th IEEE Intersociety Conference on Thermal and Thermomechanical Phenomena in Electronic Systems (ITherm)* (pp. 1218-1224). IEEE.

Fallahi, H., Nurulakmal, M., Arezodar, A. F., & Abdullah, J. (2012a). Effect of iron and indium on IMC formation and mechanical properties of lead-free solder. *Materials Science and Engineering: A, 553*, 22-31.

Fallahi, H., Nurulakmal, M., Fallahi, A., & Abdullah, J. (2012b). Modifying the mechanical properties of lead-free solder by adding iron and indium and using a lap joint test. *Journal of Materials Science: Materials in Electronics, 23*(9), 1739-1749.

Feltham, P., & Meakin, J. D. (1959). Le fluage dans les métaux cubiques a faces centrées et spécialement dans le cuivre. *Acta Metall*, *7*, 614.

Fields, R. J., Low III, S. R., Lucey Jr, G. K., Cieslak, M. J., Perepezko, J. H., & Kang, S. (1992). The metal science of joining. In *TMS Symp. Proc.(The Metallurgical Society, 1992)* (p. 165).

Frear, D. R. (1989). Thermomechanical fatigue of solder joints: A new comprehensive test method. *IEEE transactions on components, hybrids, and manufacturing technology*, *12*(4), 492-501.

Frear, D., Grivas, D., & Morris, J. W. (1988). A microstructural study of the thermal fatigue failures of 60Sn-40Pb solder joints. *Journal of Electronic Materials*, *17*, 171-180.

Frear, D., Grivas, D., & Morris, J. W. (1989). Parameters affecting thermal fatigue behavior of 60Sn-40Pb solder joints. *Journal of Electronic Materials*, *18*(6), 671-680.

Frear, D. R., Jang, J. W., Lin, J. K., & Zhang, C. (2001). Pb-free solders for flip-chip interconnects. *Jom*, *53*(6), 28-33.

Frear, D. R., & Vianco, P. T. (1994). Intermetallic growth and mechanical behavior of low and high melting temperature solder alloys. *Metallurgical and Materials Transactions A, 25*, 1509-1523.

Fu, N., Suhling, J. C., & Lall, P. (2016, May). Cyclic Stress-Strain Behavior of SAC305 Lead Free Solder: Effects of Aging, Temperature, Strain Rate, and Plastic Strain Range. In *2016 IEEE 66th Electronic Components and Technology Conference (ECTC)* (pp. 1119-1127). IEEE.

Fukuda, Y., Pecht, M. G., Fukuda, K., & Fukuda, S. (2003). Lead-free soldering in the Japanese electronics industry. *IEEE transactions on components and packaging technologies, 26*(3), 616-624.

Gaffard, V., Besson, J., & Gourgues-Lorenzon, A. F. (2005). Creep failure model of a tempered martensitic stainless steel integrating multiple deformation and damage mechanisms. *International journal of fracture*, *133*, 139-166.

Ganesan, S., & Pecht, M. G. (Eds.). (2006). *Lead-free electronics*. John Wiley & Sons.

Garofalo, F. (1963). An Empirical Relation Defining the Stress Dependence to Minimum Creep Rate in Metals. *Trans. Metall. Soc. AIME*, *227*, 351.

Garofalo, F., Richmond, O., Domis, W. F., & Von Gemmingen, F. (1963, June). Paper 30: Strain-Time, Rate-Stress and Rate-Temperature Relations during Large Deformations in Creep. In *Proceedings of the Institution of Mechanical Engineers, Conference Proceedings* (Vol. 178, No. 1, pp. 1-31). Sage UK: London, England: SAGE Publications.

Gebhardt, E., & Petzow, G. (1959). Über den Aufbau des Systems Silber-Kupfer-Zinn. *International Journal of Materials Research*, *50*(10), 597-605.

Glazer, J. (1994). Microstructure and mechanical properties of Pb-free solder alloys for low-cost electronic assembly: a review. *Journal of Electronic Materials*, *23*, 693-700.

Glazer, J. (1995). Metallurgy of low temperature Pb-free solders for electronic assembly. *International Materials Reviews, 40*(2), 65-93.

Gourlay, C., Nogita, K., Read, J., & Dahle, A. (2010). Intermetallic formation and fluidity in Sn- rich Sn-Cu-Ni alloys. *Journal of electronic materials, 39*(1), 56-69.

Greig, W. (2007). *Integrated circuit packaging, assembly and interconnections*. Springer Science & Business Media.

Gyenes, A., Benke, M., Teglas, N., Nagy, E., & Gacsi, Z. (2017). Investigation of Multicomponent Lead-Free Solders. *Archives of Metallurgy and Materials*, *62*(2B), 1071-1074.

Gyenes, A., Simon, A., Lanszki, P., & Gácsi, Z. (2015). Effects of nickel on the microstructure and the mechanical properties of Sn-0.7 Cu lead-free solders. *Archives of Metallurgy and Materials*, *60*(2B), 1449-1454.

Ha, S.-S., Jang, J.-K., Ha, S.-O., Yoon, J.-W., Lee, H.-J., Joo, J.-H., Kim, Y.-H., & Jung, S.-B. (2010). Effect of multiple reflows on interfacial reaction and shear strength of Sn–Ag electroplated solder bumps for flip chip package. *Microelectronic Engineering, 87*(3), 517- 521.

Hall, P. (1987). Creep and stress relaxation in solder joints of surface-mounted chip carriers. *IEEE Transactions on Components, Hybrids, and Manufacturing Technology*, *10*(4), 556-565.

Hammad, A. E. (2013). Evolution of microstructure, thermal and creep properties of Ni-doped Sn–0.5 Ag–0.7 Cu low-Ag solder alloys for electronic applications. *Materials & Design (1980-2015)*, *52*, 663-670.

Hammad, A. E. (2013). Investigation of microstructure and mechanical properties of novel Sn–0.5 Ag–0.7 Cu solders containing small amount of Ni. *Materials & Design*, *50*, 108-116.

Hammad, A. E. (2018). Enhancing the ductility and mechanical behavior of Sn-1.0 Ag-0.5 Cu lead-free solder by adding trace amount of elements Ni and Sb. *Microelectronics Reliability*, *87*, 133-141.

Han, J., Chen, H., Li, M., & Wang, C. (2013). Shear Deformation Behaviors of Sn3. 5Ag lead-free solder samples. *Journal of Materials Science & Technology*, *29*(5), 471-479.

Handwerker, C., Bath, J., Benedetto, E., Bradley, E., Gedney, R., Siewert, T., ... & Sohn, J. (2003, September). NEMI lead-free assembly project: comparison between PbSn and SnAgCu reliability and microstructures. In *Proceedings of SMTA International* (pp. 664-669).

Handwerker, C., Kattner, U., & Moon, K. W. (2007). Fundamental properties of Pb-free solder alloys. *Lead-Free Soldering*, 21-74.

Haq, M. A., Hoque, M. A., Suhling, J. C., & Lall, P. (2020, October). Determination of Anand Parameters from Creep Testing of SAC305 Solder Joints. In *International Electronic Packaging Technical Conference and Exhibition* (Vol. 84041, p. V001T01A016). American Society of Mechanical Engineers.

He, M., Ekpenuma, S. N., & Acoff, V. L. (2008). Microstructure and creep deformation of Sn-Ag- Cu-Bi/Cu solder joints. Journal of electronic materials, 37(3), 300-306.

Herrmann, K. (2011). The fundamentals of hardness testing. *Hardness Testing—Principles and Applications*, 1-23.

Hidaka, N., Watanabe, H., & Yoshiba, M. (2009). Creep behavior of lead-free Sn-Ag-Cu+ Ni-Ge solder alloys. *Journal of electronic materials*, *38*, 670-677.

Hirai, Y., Oomori, K., Morofushi, H., & Shohji, I. (2019). Effect of Bi Addition on Tensile Properties of Sn-Ag-Cu Solder at Low Temperature. *Materials Transactions*, *60*(6), 909-914.

Hodulova, E., Palcut, M., Lechovič, E., Šimeková, B., & Ulrich, K. (2011). Kinetics of intermetallic phase formation at the interface of Sn-Ag-Cu-X (X= Bi, In) solders with Cu substrate. *Journal of Alloys and Compounds*, *509*(25), 7052-7059.

Hosford, W. F. (2013). *Fundamentals of engineering plasticity*. Cambridge University Press.

Hu, T., Li, Y., Chan, Y. C., & Wu, F. (2015). Effect of nano Al2O3 particles doping on electromigration and mechanical properties of Sn–58Bi solder joints. *Microelectronics Reliability*, *55*(8), 1226-1233.

Hu, X., Chan, Y. C., Zhang, K., & Yung, K. C. (2013). Effect of graphene doping on microstructural and mechanical properties of Sn-8Zn-3Bi solder joints together with electromigration analysis. *Journal of Alloys and Compounds*, *580*, 162-171.

Hua, L., Hou, H. N., Zhang, H. Q., Wu, T., & Deng, Y. H. (2010, August). Effects of Zn, Ge doping on electrochemical migration, oxidation characteristics and corrosion behavior of lead-free Sn-3.0 Ag-0.5 Cu solder for electronic packaging. In *2010 11th International Conference on Electronic Packaging Technology & High Density Packaging* (pp. 1151-1157). IEEE.

Huang, M., & Wang, L. (2005). Effects of Cu, Bi, and In on microstructure and tensile properties of Sn-Ag-X (Cu, Bi, In) solders. *Metallurgical and Materials Transactions A, 36*(6), 1439- 1446.

Hull, D. (1999). *Fractography: observing, measuring and interpreting fracture surface topography*. Cambridge University Press.

Humpston, G., & Jacobson, D. M. (2004). Fluxless soldering processes: fluxless soldering is required for joints in high-performance and aerospace electronics where no contamination is permissible from flux residues or cleaning agents. *Advanced materials & processes, 162*(11), 35-38.

JESD22A121, J. S. (2005). Measuring whisker growth on tin and tin alloy surface finishes. *JEDEC Solid State Technology Association, Arlington, VA*.

Jiang, N., Zhang, L., Liu, Z. Q., Sun, L., Long, W. M., He, P., ... & Zhao, M. (2019). Reliability issues of lead-free solder joints in electronic devices. *Science and technology of advanced materials*, *20*(1), 876-901.

Kadesch, J. S., & Brusse, J. (2001). The continuing dangers of tin whiskers and attempts to control them with conformal coating. *NASA EEE Links Newsletter*.

Kanda, Y., Kariya, Y., & Oto, Y. (2012). Influence of cyclic strain-hardening exponent on fatigue ductility exponent for a Sn-Ag-Cu micro-solder joint. *Journal of electronic materials*, *41*, 580-587.

Kang, H., Rajendran, S. H., & Jung, J. P. (2021). Low melting temperature Sn-Bi solder: Effect of alloying and nanoparticle addition on the microstructural, thermal, interfacial bonding, and mechanical characteristics. *Metals*, *11*(2), 364.

Karakaya, I., & Thompson, W. T. (1987). The Ag-Sn (silver-tin) system. *Bulletin of Alloy Phase Diagrams*, *8*(4), 340-347.

Kattner, U. R., & Boettinger, W. J. (1994). On the Sn-Bi-Ag ternary phase diagram. *Journal of Electronic Materials*, *23*, 603-610.

Kawabata, T., & Izumi, O. (1976). The relationship between ductility and grain-boundary precipitates in an Al-6.0% Zn-2.6% Mg alloy. *Journal of Materials Science*, *11*, 892-902.

Kerr, M., & Chawla, N. (2004). Creep deformation behavior of Sn–3.5 Ag solder/Cu couple at small length scales. *Acta materialia*, *52*(15), 4527-4535.

Kim, H. K., Tu, K. N., & Totta, P. A. (1996). Ripening-assisted asymmetric spalling of Cu-Sn compound spheroids in solder joints on Si wafers. *Applied Physics Letters*, *68*(16), 2204-2206.

Kim, K., Huh, S., & Suganuma, K. (2003). Effects of intermetallic compounds on properties of Sn–Ag–Cu lead-free soldered joints. *Journal of Alloys and Compounds, 352*(1-2), 226- 236.

Kim, K. S., Huh, S. H., & Suganuma, K. (2003). Effects of fourth alloying additive on microstructures and tensile properties of Sn–Ag–Cu alloy and joints with Cu. *Microelectronics Reliability*, *43*(2), 259-267.

Kotadia, H. R., Howes, P. D., & Mannan, S. H. (2014). A review: On the development of low melting temperature Pb-free solders. *Microelectronics Reliability, 54*(6-7), 1253-1273.

Kroupa, A., Andersson, D., Hoo, N., Pearce, J., Watson, A., Dinsdale, A., & Mucklejohn, S. (2012). Current problems and possible solutions in high-temperature lead-free soldering. *Journal of Materials Engineering and Performance, 21*, 629-637.

KS, F. P., Boon, T. H., Sivalingam, K., Kuan, L. B., Sun, A. Y., & Bidin, R. (2004, July). Development of high power QFN package. In *IEEE/CPMT/SEMI 29th International Electronics Manufacturing Technology Symposium (IEEE Cat. No. 04CH37585)* (pp. 295-300). IEEE.

Ladou, J., & Lovegrove, S. (2008). Export of electronics equipment waste. *International journal of occupational and environmental health, 14*(1), 1-10.

Lall, P., Limaye, G., Shantaram, S., & Suhling, J. (2013, July). Effect of isothermal aging and high strain rate on material properties of innolot. In *International Electronic Packaging Technical Conference and Exhibition* (Vol. 55751, p. V001T05A012). American Society of Mechanical Engineers.

Lau, J., Harkins, G., Rice, D., & Kral, J. (1987, April). Thermal fatigue reliability of SMT packages and interconnections. In *25th International Reliability Physics Symposium* (pp. 250-259). IEEE.

Lau, J. H. (1987, December). Stiffness of PLCC J lead and its effect on solder joint reliability. In *ASME Winter Annual Meeting* (pp. 13-15).

Lau, J. H. (1989). Thermal stress analysis of SMT PQFP packages and interconnections.

Lau, J. H. (1990, May). Thermal stress analysis of plastic leaded chip carriers. In *InterSociety Conference on Thermal Phenomena in Electronic Systems* (pp. 57-66). IEEE.

Lau, J. H., & Harkins, C. G. (1988). Thermal-stress analysis of SOIC packages and interconnections. *IEEE Transactions on Components, Hybrids, and Manufacturing Technology*, *11*(4), 380-389.

Lau, J. H., & Harkins, C. G. (1990). Stiffness of 'gull-wing' leads and solder joints for a plastic quad flat pack. *IEEE Transactions on Components, Hybrids, and Manufacturing Technology*, *13*(1), 124-130.

Lau, J. H., Harkins, G., Rice, D., Kral, J., & Wells, B. (1988). Experimental and statistical analyses of surface-mount technology PLCC solder-joint reliability. *IEEE transactions on reliability*, *37*(5), 524-530.

Lau, J. H., & Pao, Y. H. (1997). *Solder joint reliability of BGA, CSP, flip chip, and fine pitch SMT assemblies*. McGraw-Hill Professional Publishing.

Lau, J. H., & Rice, D. W. (1990, May). Thermal stress/strain analysis of ceramic quad flat pack packages and interconnections. In *40th Conference Proceedings on Electronic Components and Technology* (pp. 824-834). IEEE.

Lau, J. H., Rice, D. W., & Harkins, C. G. (1990). Thermal stress analysis of tape automated bonding packages and interconnections. *IEEE Transactions on Components, Hybrids, and Manufacturing Technology*, *13*(1), 182-187.

Lau, J. H. S. (1973). *Elasto-plastic finite element analysis with special reference to reinforced concrete* (Doctoral dissertation, University of British Columbia).

Lau, J., Li, M., Yang, L., Li, M., Yong, Q. X., Cheng, Z., ... & Lee, R. (2018, May). Reliability of fan-out wafer-level packaging with large chips and multiple re-distributed layers. In *2018 IEEE 68th Electronic Components and Technology Conference (ECTC)* (pp. 1574-1582). IEEE.

Lau, J., Powers-Maloney, L. M., Baker, J. R., Rice, D., & Shaw, B. (1990). Solder joint reliability of fine pitch surface mount technology assemblies. *IEEE Transactions on Components, Hybrids, and Manufacturing Technology*, *13*(3), 534-544.

Laurila, T., Hurtig, J., Vuorinen, V., & Kivilahti, J. K. (2009). Effect of Ag, Fe, Au and Ni on the growth kinetics of Sn–Cu intermetallic compound layers. *Microelectronics Reliability, 49*(3), 242-247.

Lee, H. T., & Lee, Y. H. (2005). Effects of in situ nickel particle addition on the microstructure and microhardness of Sn–Ag solder. *Science and Technology of Welding and Joining, 10*(3), 353-360.

Lee, H. Y., Sharma, A., Kee, S. H., Lee, Y. W., Moon, J. T., & Jung, J. P. (2014). Effect of aluminium additions on wettability and intermetallic compound (IMC) growth of lead free Sn (2 wt.% Ag, 5 wt.% Bi) soldered joints. *Electronic Materials Letters*, *10*, 997-1004.

Li, F., Verdingovas, V., Dirscherl, K., Harsányi, G., Medgyes, B., & Ambat, R. (2020). Influence of Ni, Bi, and Sb additives on the microstructure and the corrosion behavior of Sn–Ag–Cu solder alloys. *Journal of Materials Science: Materials in Electronics*, *31*, 15308-15321.

Li, J., Qiu, Y. Y., Wang, H. D., & Wang, Z. X. (2019). Estimation of the strength coefficient and strain hardening exponent from monotonic tensile properties of steels. *International Journal of Steel Structures*, *19*, 1951-1968.

Li, L. F., Cheng, Y. K., Xu, G. L., Wang, E. Z., Zhang, Z. H., & Wang, H. (2014). Effects of indium addition on properties and wettability of Sn–0.7 Cu–0.2 Ni lead-free solders. *Materials & Design*, *64*, 15-20.

Li, G. Y., Chen, B. L., Shi, X. Q., Wong, S. C., & Wang, Z. F. (2006). Effects of Sb addition on tensile strength of Sn–3.5 Ag–0.7 Cu solder alloy and joint. *Thin Solid Films*, *504*(1-2), 421-425.

Li, Q., Ma, N., Lei, Y., Lin, J., Fu, H., & Gu, J. (2016). Characterization of low-melting-point Sn-Bi-In lead-free solders. *Journal of Electronic Materials*, *45*, 5800-5810.

Li, Y., & Wong, C. P. (2006). Recent advances of conductive adhesives as a lead-free alternative in electronic packaging: Materials, processing, reliability and applications. *Materials Science and Engineering: R: Reports, 51*(1-3), 1-35.

Libot, J. B., Alexis, J., Dalverny, O., Arnaud, L., Milesi, P., & Dulondel, F. (2018). Microstructural evolutions of Sn-3.0 Ag-0.5 Cu solder joints during thermal cycling. *Microelectronics Reliability*, *83*, 64-76.

Liu, Y., Sun, F., & Zou, P. (2011, October). Shear strength and interfacial microstructures of low-Ag SAC/Cu and SAC-Bi-Ni/Cu solder joints. In *2011 International Symposium on Advanced Packaging Materials (APM)* (pp. 186-189). IEEE.

Liyana, N. K., Fazal, M. A., Haseeb, A. S. M. A., & Rubaiee, S. (2019). Effect of Zn incorporation on the electrochemical corrosion properties of SAC105 solder alloys. *Journal of Materials Science: Materials in Electronics, 30,* 7415-7422.

London, J. (1986). ASHALL. D W. Compond growth and fracture at copper/tin-silver solder interfaces. *Brazing Soldering* (11), 49-55.

Long, X., Tang, W., Wang, S., He, X., & Yao, Y. (2018). Annealing effect to constitutive behavior of Sn–3.0 Ag–0.5 Cu solder. *Journal of Materials Science: Materials in Electronics*, *29*, 7177-7187.

Long, X., Wang, S., Feng, Y., Yao, Y., & Keer, L. M. (2017). Annealing effect on residual stress of Sn-3.0 Ag-0.5 Cu solder measured by nanoindentation and constitutive experiments. *Materials Science and Engineering: A*, *696*, 90-95.

Loomans, M., & Fine, M. (2000). Tin-silver-copper eutectic temperature and composition. *Metallurgical and Materials Transactions A, 31*(4), 1155-1162.

Loomans, M. E., & Fine, M. E. (2000). Tin-silver-copper eutectic temperature and composition. *Metallurgical and Materials Transactions A, 31*, 1155-1162.

Lopez, E. P., Vianco, P. T., & Rejent, J. A. (2005). Solderability testing of Sn-Ag-XCu Pb-free solders on copper and Au-Ni-plated Kovar substrates. *Journal of Electronic Materials, 34*(3), 299-310.

Lopez, E. P., Vianco, P. T., Rejent, J. A., George, C., & Kilgo, A. (2010). Compression stress–strain behavior of Sn-Ag-Cu solders. *Journal of electronic materials*, *39*, 97-104.

Lu, T., Yi, D., Wang, H., Tu, X., & Wang, B. (2019). Microstructure, mechanical properties, and interfacial reaction with Cu substrate of Zr-modified SAC305 solder alloy. *Journal of alloys and compounds*, *781*, 633-643.

Luciano, C. N. C., Udoh, K.-i., Nakagawa, M., Matsuya, S., & Ohta, M. (2002). AuCu–Sn pseudobinary phase diagram. *Journal of Alloys and Compounds, 337*(1-2), 289-295.

Luo, W., Ho, C., Tsai, J., Lin, Y., & Kao, C. (2005). Solid-state reactions between Ni and Sn–Ag– Cu solders with different Cu concentrations. *Materials Science and Engineering: A, 396*(1- 2), 385-391.

Ma, H. (2009). Constitutive models of creep for lead-free solders. *Journal of Materials Science, 44*(14), 3841-3851.

Ma, H., & Suhling, J. C. (2009). A review of mechanical properties of lead-free solders for electronic packaging. *Journal of materials science, 44*(5), 1141-1158.

Ma, H., Suhling, J. C., Lall, P., & Bozack, M. J. (2006, May). Reliability of the aging lead free solder joint. In *56th Electronic Components and Technology Conference 2006* (pp. 16-pp). IEEE.

Ma, H., Suhling, J. C., Zhang, Y., Lall, P., & Bozack, M. J. (2007, May). The influence of elevated temperature aging on reliability of lead free solder joints. In *2007 Proceedings 57th Electronic Components and Technology Conference* (pp. 653-668). IEEE.

Mahdavifard, M. H., Sabri, M. F. M., Shnawah, D. A., Said, S. M., Badruddin, I. A., & Rozali, S. (2015). The effect of iron and bismuth addition on the microstructural, mechanical, and thermal properties of Sn–1Ag–0.5 Cu solder alloy. *Microelectronics Reliability*, *55*(9-10), 1886-1890.

Manikam, V. R., & Cheong, K. Y. (2011). Die attach materials for high temperature applications: A review. *IEEE Transactions on Components, Packaging and Manufacturing Technology, 1*(4), 457-478.

Mattila, T. T., Marjamaki, P., & Kivilahti, J. K. (2006). Reliability of CSP interconnections under mechanical shock loading conditions. *IEEE Transactions on Components and Packaging Technologies*, *29*(4), 787-795.

Mattila, T. T., Vuorinen, V., & Kivilahti, J. K. (2004). Impact of printed wiring board coatings on the reliability of lead-free chip-scale package interconnections. *Journal of materials research, 19*(11), 3214-3223.

Mattila, T., & Kivilahti, J. (2006). Reliability of lead-free interconnections under consecutive thermal and mechanical loadings. *Journal of Electronic Materials, 35*(2), 250-256.

Mavoori, H., & Jin, S. (1998). New, creep-resistant, low melting point solders with ultrafine oxide dispersions. *Journal of electronic materials*, *27*, 1216-1222.

Mei, Z., & Morris, J. (1992). Superplastic creep of low melting point solder joints. *Journal of Electronic Materials, 21*(4), 401-407.

Michaelides, S., & Sitaraman, S. K. (1998, May). Effect of material and geometry parameters on the thermo-mechanical reliability of flip-chip assemblies. In *ITherm'98. Sixth Intersociety Conference on Thermal and Thermomechanical Phenomena in Electronic Systems (Cat. No. 98CH36208)* (pp. 193-200). IEEE.

Miller, C. M., Anderson, I. E., & Smith, J. F. (1994). A viable tin-lead solder substitute: Sn-Ag- Cu. *Journal of electronic materials, 23*(7), 595-601.

Minzari, D. (2010). Investigation of electronic corrosion mechanisms. *Technichal University of Denmark, Lyngby*.

Mishiro, K., Ishikawa, S., Abe, M., Kumai, T., Higashiguchi, Y., & Tsubone, K.-i. (2002). Effect of the drop impact on BGA/CSP package reliability. *Microelectronics Reliability, 42*(1), 77-82.

Mohammad Hossein, M. (2017). *Investigation on mechanical, microstructural and thermal properties of Sn-0.7 Cu and Sn-1Ag 0.5 Cu solder alloys bearing Fe and Bi/Mohammad Hossein Mahdavifard* (Doctoral dissertation, University of Malaya).

Mohd Nazeri, M. F., Yahaya, M. Z., Gursel, A., Cheani, F., Masri, M. N., & Mohamad, A. A. (2019). Corrosion characterization of Sn-Zn solder: a review. *Soldering & Surface Mount Technology, 31*(1), 52-67.

Moon, K.-W., Boettinger, W. J., Kattner, U. R., Biancaniello, F. S., & Handwerker, C. (2000). Experimental and thermodynamic assessment of Sn-Ag-Cu solder alloys. *Journal of Electronic Materials, 29*(10), 1122-1136.

Motalab, M., Basit, M., Suhling, J. C., Bozack, M. J., & Lall, P. (2014, May). Creep test method for determination of Anand parameters for lead free solders and their variation with aging. In *Fourteenth Intersociety Conference on Thermal and Thermomechanical Phenomena in Electronic Systems (ITherm)* (pp. 127-141). IEEE.

Motalab, M., Cai, Z., Suhling, J. C., Zhang, J., Evans, J. L., Bozack, M. J., & Lall, P. (2012, May). Improved predictions of lead free solder joint reliability that include aging effects. In *2012 IEEE 62nd Electronic Components and Technology Conference* (pp. 513-531). IEEE.

Motalab, M., Cai, Z., Suhling, J. C., Zhang, J., Evans, J. L., Bozack, M. J., & Lall, P. (2012, May). Improved predictions of lead free solder joint reliability that include aging effects. In *2012 IEEE 62nd Electronic Components and Technology Conference* (pp. 513-531). IEEE.

Motalab, M., Mustafa, M., Suhling, J. C., Zhang, J., Evans, J., Bozack, M. J., & Lall, P. (2013, May). Correlation of reliability models including aging effects with thermal cycling reliability data. In *2013 IEEE 63rd Electronic Components and Technology Conference* (pp. 986-1004). IEEE.

Mu, D., Huang, H., & Nogita, K. (2012). Anisotropic mechanical properties of Cu_6Sn_5 and (Cu, Ni) $_6Sn_5$. *Materials Letters, 86*, 46-49.

Mustafa, M., Cai, Z., Roberts, J. C., Suhling, J. C., & Lall, P. (2012, May). Evolution of the tension/compression and shear cyclic stress-strain behavior of lead-free solder subjected to isothermal aging. In *13th InterSociety Conference on Thermal and Thermomechanical Phenomena in Electronic Systems* (pp. 765-780). IEEE.

Mustafa, M., Cai, Z., Suhling, J. C., & Lall, P. (2011, May). The effects of aging on the cyclic stress-strain behavior and hysteresis loop evolution of lead free solders. In *2011 IEEE 61st Electronic Components and Technology Conference (ECTC)* (pp. 927-939). IEEE.

Negm, S. E., Mady, H., & Bahgat, A. A. (2010). Influence of the addition of indium on the mechanical creep of Sn–3.5% Ag alloy. *Journal of alloys and compounds*, *503*(1), 65-70.

Niranjani, V. L., Rao, B. C., Sarkar, R., & Kamat, S. V. (2012). The influence of addition of nanosized molybdenum and nickel particles on creep behavior of Sn–Ag lead free solder alloy. *Journal of alloys and compounds*, *542*, 136-141.

Noble, P. J. (2013). *Printed circuit board assembly: The complete works*. Springer Science & Business Media.

Oh, C. S., Shim, J. H., Lee, B. J., & Lee, D. N. (1996). A thermodynamic study on the Ag- Sb- Sn system. *Journal of Alloys and Compounds, 238*(1-2), 155-166.

Ohnuma, I., Miyashita, M., Anzai, K., Liu, X., Ohtani, H., Kainuma, R., & Ishida, K. (2000). Phase equilibria and the related properties of Sn-Ag-Cu based Pb-free solder alloys. *Journal of Electronic Materials, 29*(10), 1137-1144.

Okamoto, H. (2007). Ag-Sb (silver-antimony). *Journal of Phase Equilibria and Diffusion*, *28*, 403-403.

Okamoto, H. (2008). Ni-Sn (nickel-tin). *Journal of phase Equilibria and Diffusion*, *29*, 297-298.

Okamoto, H. (2010). Bi-Sn (bismuth-tin). *Journal of Phase Equilibria and Diffusion*, *31*, 205-205.

Okamoto, H. (2012). Sb-Sn (antimony-tin). *Journal of phase equilibria and diffusion*, *33*, 347-347.

Okamoto, H., & Massalski, T. B. (1990). Binary alloy phase diagrams. *ASM International, Materials Park, OH, USA*, *12*.

Osório, W. R., Leiva, D. R., Peixoto, L. C., Garcia, L. R., & Garcia, A. (2013). Mechanical properties of Sn–Ag lead-free solder alloys based on the dendritic array and Ag_3Sn morphology. *Journal of Alloys and Compounds, 562*, 194-204.

Öztürk, E., Aksöz, S., Keşlioğlu, K., & Maraşlı, N. (2013). The measurement of thermal conductivity variation with temperature for Sn-20 wt.% In based lead-free ternary solders. *Thermochimica Acta, 554*, 63-70.

Pan, J., Tonkay, G. L., Storer, R. H., Sallade, R. M., & Leandri, D. J. (2004). Critical variables of solder paste stencil printing for micro-BGA and fine-pitch QFP. *IEEE Transactions on Electronics Packaging Manufacturing*, *27*(2), 125-132.

Pan, T. Y. (1991). Thermal cycling induced plastic deformation in solder joints—Part I: Accumulated deformation in surface mount joints.

Pang, H. L. J., & Chong, Y. R. (2000). FEA modeling of FCOB assembly solder joint reliability. *Proc. MicroMat*, 159-166.

Pang, J. H., Tan, T. I., Chong, Y. R., Lim, G. Y., & Wong, C. L. (1998). Analysis of underfill encapsulation curing deformations on flip chip on board (FCOB) package reliability. *Journal of Electronics Manufacturing*, *8*(03n04), 181-191.

Pantazopoulos, G. A. (2019). A short review on fracture mechanisms of mechanical components operated under industrial process conditions: Fractographic analysis and selected prevention strategies. *Metals*, *9*(2), 148.

Pantazopoulos, G., Toulfatzis, A., Vazdirvanidis, A., & Rikos, A. (2016). Analysis of the degradation process of structural steel component subjected to prolonged thermal exposure. *Metallography, Microstructure, and Analysis*, *5*, 149-156.

Pecht, M., Shibutani, T., & Wu, L. (2016). A reliability assessment guide for the transition planning to lead-free electronics for companies whose products are RoHS exempted or excluded. *Microelectronics Reliability*, *62*, 113-123.

Plumbridge, W. J., Matela, R. J., & Westwater, A. (2007). *Structural integrity and reliability in electronics: enhancing performance in a lead-free environment*. Springer Science & Business Media.

Prakash, K. H., & Sritharan, T. (2004). Tensile fracture of tin–lead solder joints in copper. *Materials Science and Engineering: A*, *379*(1-2), 277-285.

Pulicandla, V., Dunford, S., & Kivilahti, J. (2004). Reliability Aspects of Lead-Free Solders in Electronic Assemblies. In *The Handbook of Lead (Pb)-Free Technology for Microelectronics Assemblies* (pp. 769-850). Marcel Dekker.

Puttlitz, K. J., & Stalter, K. A. (2004). *Handbook of lead-free solder technology for microelectronic assemblies*. CRC Press.

Qin, W., Li, J., Liu, Y., Kang, J., Zhu, L., Shu, D., Peng, P., She, D., Meng, D., & Li, Y. (2019). Effects of grain size on tensile property and fracture morphology of 316L stainless steel. *Materials Letters, 254*, 116-119.

Ramli, M. I. I., Salleh, M. A. A. M., Abdullah, M. M. A. B., Zaimi, N. S. M., Sandu, A. V., Vizureanu, P., ... & Amli, S. F. M. (2022). Formation and Growth of Intermetallic Compounds in Lead-Free Solder Joints: A Review. *Materials, 15*(4), 1451.

Roessle, M. L., & Fatemi, A. (2000). Strain-controlled fatigue properties of steels and some simple approximations. *International journal of fatigue*, *22*(6), 495-511.

Sanders, T. E. (2016). *Extreme environment reliability of components for computing with SAC305 and alternative high reliability solders* (Doctoral dissertation, Auburn University).

Sasikala, G., Mathew, M. D., Rao, K. B. S., & Mannan, S. L. (1999). Creep deformation and fracture behaviour of a nitrogen-bearing type 316 stainless steel weld metal. *Journal of nuclear Materials*, *273*(3), 257-264.

Sattiraju, S., Dang, B., Johnson, R. W., Li, Y., Smith, J. S., & Bozack, M. J. (2002). Wetting characteristics of Pb-free solder alloys and PWB finishes. *IEEE Transactions on Electronics Packaging Manufacturing, 25*(3), 168-184.

Satyanarayan, & Prabhu, K. N. (2013). Spreading behavior and evolution of IMCs during reactive wetting of SAC solders on smooth and rough copper substrates. *Journal of electronic materials*, *42*, 2696-2707.

Saunders, N., & Miodownik, A. (1990). The Cu-Sn (copper-tin) system. *Bulletin of Alloy Phase Diagrams, 11*(3), 278-287.

Sayyadi, R., & Naffakh-Moosavy, H. (2019). The role of intermetallic compounds in controlling the microstructural, physical and mechanical properties of Cu-[Sn-Ag-Cu-Bi]-Cu solder joints. *Scientific reports, 9*(1), 1-20.

Sayyadi, R., & Naffakh-Moosavy, H. (2019). The role of intermetallic compounds in controlling the microstructural, physical and mechanical properties of Cu-[Sn-Ag-Cu-Bi]-Cu solder joints. *Scientific Reports, 9*(1), 1-20.

Shah, M. K. (1990). Analysis of parameters influencing stresses in the solder joints of leadless chip capacitors.

Shalaby, R. M. (2009). Influence of indium addition on structure, mechanical, thermal and electrical properties of tin–antimony based metallic alloys quenched from melt. *Journal of Alloys and Compounds, 480*(2), 334-339.

Shangguan, D. (Ed.). (2005). *Lead-free solder interconnect reliability*. ASM international.

Sharif, A., Chan, Y., & Islam, R. A. (2004). Effect of volume in interfacial reaction between eutectic Sn–Pb solder and Cu metallization in microelectronic packaging. *Materials Science and Engineering: B, 106*(2), 120-125.

Sharma, A., Sohn, H. R., & Jung, J. P. (2016). Effect of graphene nanoplatelets on wetting, microstructure, and tensile characteristics of Sn-3.0 Ag-0.5 Cu (SAC) alloy. *Metallurgical and Materials Transactions A*, *47*, 494-503.

Shen, J., Pu, Y., Wu, D., Tang, Q., & Zhao, M. (2015). Effects of minor Bi, Ni on the wetting properties, microstructures, and shear properties of Sn–0.7 Cu lead-free solder joints. *Journal of Materials Science: Materials in Electronics*, *26*, 1572-1580.

Shen, Y. A., Hsieh, H. M., Chen, S. H., Li, J., Chen, S. W., & Nishikawa, H. (2021). Investigation of FeCoNiCu properties: thermal stability, corrosion behavior, wettability with Sn-3.0 Ag-0.5 Cu and interlayer formation of multi-element intermetallic compound. *Applied Surface Science, 546,* 148931.

Sherby, O. D., & Burke, P. M. (1968). Mechanical behavior of crystalline solids at elevated temperature. *Progress in materials science*, *13*, 323-390.

Shim, J.-H., Oh, C.-S., Lee, B.-J., & Lee, D. (1996). Thermodynamic assessment of the Cu-Sn system. *International Journal of Materials Research, 87*(3), 205-212.

Shimizu, K., Nakanishi, T., Karasawa, K., Hashimoto, K., & Niwa, K. (1995). Solder joint reliability of indium-alloy interconnection. *Journal of Electronic Materials, 24*(1), 39-45.

Shohji, I., Nakamura, T., Mori, F., & Fujiuchi, S. (2002). Interface reaction and mechanical properties of lead-free Sn-Zn alloy/Cu joints. *Materials transactions, 43*(8), 1797-1801.

Sommadossi, S., Gust, W., & Mittemeijer, E. (2003). Characterization of the reaction process in diffusion-soldered Cu/In–48 at.% Sn/Cu joints. *Materials Chemistry and Physics, 77*(3), 924-929.

Subramanian, K. N. (2007). *Lead-Free Electronic Solders: A Special Issue of the Journal of Materials Science: Materials in Electronics*. Springer Science+ Business Media, LLC.

Subramanian, K. N., & Frear, D. R. (2007). Issues related to the implementation of Pb-free electronic solders in consumer electronics. *Lead-Free Electronic Solders: A Special Issue of the Journal of Materials Science: Materials in Electronics*, 319-330.

Suganuma, K. (2003). *Lead-free soldering in electronics: Science, technology, and environmental impact*. CRC Press.

Sukhontapatipak, P., & Sungkhaphaitoon, P. (2023). Improvements in the properties of low-Ag SAC105 solder alloys with the addition of tellurium. *Journal of Materials Science: Materials in Electronics, 34*(17), 1327.

Takaku, Y., Liu, X. J., Ohnuma, I., Kainuma, R., & Ishida, K. (2004). Interfacial reaction and morphology between molten Sn base solders and Cu substrate. *Materials transactions, 45*(3), 646-651.

Tan, C. Y., Salleh, M. A. A. M., & Saud, N. (2020, October). The effect of germanium addition on the lead-free solder alloys: a short review. *In IOP Conference Series: Materials Science and Engineering* (Vol. 957, No. 1, p. 012060). IOP Publishing.

Tang, Y., Li, G. Y., & Pan, Y. C. (2014). Effects of TiO2 nanoparticles addition on microstructure, microhardness and tensile properties of Sn–3.0 Ag–0.5 Cu–xTiO2 composite solder. *Materials & Design*, *55*, 574-582.

Tang, Y., Luo, S. M., Huang, W. F., Pan, Y. C., & Li, G. Y. (2017). Effects of Mn nanoparticles on tensile properties of low-Ag Sn-0.3 Ag-0.7 Cu-xMn solder alloys and joints. *Journal of Alloys and Compounds*, *719*, 365-375.

Tateyama, K., Ubukata, H., Yamaoka, Y., Takahashi, K., Yamada, H., & Saito, M. (2000). Effects of Bi content on mechanical properties and bump interconnection reliability on Sn-Ag solder alloys. *International Journal of Microcircuits and Electronic Packaging*, *23*(1), 131-137.

Tao, Q. B., Benabou, L., Le, V. N., Nguyen, N. A. T., & Nguyen-Xuan, H. (2020). Temperature-dependent fatigue modelling of a novel Ni, Bi and Sb containing Sn-3.8 Ag-0.7 Cu lead-free solder alloy. *Fatigue & Fracture of Engineering Materials & Structures*, *43*(12), 2883-2891.

Tao, Q. B., Benabou, L., Tan, K. L., Morelle, J. M., & Ouezdou, F. B. (2015, December). Creep behavior of Innolot solder alloy using small lap-shear specimens. In *2015 IEEE 17th Electronics Packaging and Technology Conference (EPTC)* (pp. 1-6). IEEE.

Tao, Q. B., Benabou, L., Van, T. N., & Nguyen-Xuan, H. (2019). Isothermal aging and shear creep behavior of a novel lead-free solder joint with small additions of Bi, Sb and Ni. *Journal of Alloys and Compounds*, *789*, 183-192.

Tao, Q. B., Benabou, L., Vivet, L., Le, V. N., & Ouezdou, F. B. (2016). Effect of Ni and Sb additions and testing conditions on the mechanical properties and microstructures of lead-free solder joints. *Materials Science and Engineering: A*, *669*, 403-416.

Tao, Q.-B., Benabou, L., Vivet, L., Tan, K.-L., Morelle, J.-M., Le, V.-N., & Ben Ouezdou, F. (2017). A design of a new miniature device for solder joints' mechanical properties evaluation. *Proceedings of the Institution of Mechanical Engineers, Part C: Journal of Mechanical Engineering Science, 231*(20), 3818-3830.

Tao, W., Chen, C., Ho, C., Chen, W., & Kao, C. (2001). Selective interfacial reaction between Ni and eutectic BiSn lead-free solder. *Chemistry of materials, 13*(3), 1051-1056.

Tay, S. L., Haseeb, A. S. M. A., Johan, M. R., Munroe, P. R., & Quadir, M. Z. (2013). Influence of Ni nanoparticle on the morphology and growth of interfacial intermetallic compounds between Sn–3.8 Ag–0.7 Cu lead-free solder and copper substrate. *Intermetallics, 33,* 8-15.

Totani, M., Teshima, Y., Ito, N., Nagatake, M., & Otaguro, H. (1995). Design of 0.35-mm pitch QFP lead and its assembly technology. *IEEE Transactions on Components, Packaging, and Manufacturing Technology: Part B*, *18*(3), 456-462.

Tsao, L. C., Cheng, S. Y., Chen, C. W., & Chen, T. Y. (2016). Effect of nano-TiO2 particles and cooling rate on the thermal, microstructure and mechanical properties of novel low-ag Sn1. 5Sb1Ag solders. *Materials Science and Engineering: A*, *658*, 159-166.

Tsukamoto, H., Nishimura, T., Suenaga, S., & Nogita, K. (2010). Shear and tensile impact strength of lead-free solder ball grid arrays placed on Ni (P)/Au surface-finished substrates. *Materials Science and Engineering: B, 171*(1-3), 162-171.

Tummala, E. R. R., & Rymaszewski, E. J. (1997). Microelectronics Packaging Handbook.

Tummala, R. R. (2001). Fundamentals of microsystems packaging.

Vandevelde, B., Gonzalez, M., Limaye, P., Ratchev, P., & Beyne, E. (2004, May). Hermal cycling reliability of SnAgCu and SnPb solder joints: A comparison for several IC-packages. In *5th International Conference on Thermal and Mechanical Simulation and Experiments in Microelectronics and Microsystems, 2004. EuroSimE 2004. Proceedings of the* (pp. 565-570). IEEE.

Vasudevan, V., & Fan, X. (2008, May). An acceleration model for lead-free (SAC) solder joint reliability under thermal cycling. In *2008 58th Electronic components and technology conference* (pp. 139-145). IEEE.

Vaynman, S. (1989). Effect of strain rate on fatigue of low-tin lead-base solder. *IEEE transactions on components, hybrids, and manufacturing technology*, *12*(4), 469-472.

Vianco, P., Erickson, K., & Hopkins, P. (1994). Solid state intermetallic compound growth between copper and high temperature, tin-rich solders—part I: experimental analysis. *Journal of electronic materials, 23*(8), 721-727.

Vianco, P. T., & Rejent, J. A. (1999). Properties of ternary Sn-Ag-Bi solder alloys: Part I—Thermal properties and microstructural analysis. *Journal of electronic materials*, *28*, 1127-1137.

Villars, P. (1995). Handbook of ternary alloy phase diagrams. *ASM international*, *7*, 8754-8755.

Wang, C.-h., & Chen, S.-w. (2006). Sn–0.7 wt.% Cu/Ni interfacial reactions at 250 C. *Acta Materialia, 54*(1), 247-253.

Wang, F., Chen, H., Huang, Y., Liu, L., & Zhang, Z. (2019). Recent progress on the development of Sn–Bi based low-temperature Pb-free solders. *Journal of Materials Science: Materials in Electronics, 30,* 3222-3243.

Willis, B. (2003). Reflow soldering processes and troubleshooting SMT, BGA, CSP and Flip Chip Technologies. *Soldering & Surface Mount Technology*, *15*(1).

Witkin, D. (2012a). Creep behavior of Bi-containing lead-free solder alloys. *Journal of electronic materials, 41*(2), 190-203.

Witkin, D. B. (2012b). Influence of microstructure on quasi-static and dynamic mechanical properties of bismuth-containing lead-free solder alloys. *Materials Science and Engineering: A*, *532*, 212-220.

Witkin, D. B. (2013, February). Influence of Microstructure on Mechanical Behavior of Bi-Containing Pb-Free Solders. In *Proceedings of IPC APEX EXPO Conference and Exhibition* (Vol. 1, pp. 540-560). San Diego, CA.

Wu, C. M. L., Yu, D. Q., Law, C. M. T., & Wang, L. (2004). Properties of lead-free solder alloys with rare earth element additions. *Materials Science and Engineering: R: Reports*, *44*(1), 1-44.

Xiao, Q., Bailey, H. J., & Armstrong, W. D. (2004). Aging effects on microstructure and tensile property of Sn3. 9Ag0. 6Cu solder alloy. *J. Electron. Packag.*, *126*(2), 208-212.

Xiong, M. Y., & Zhang, L. (2019). Interface reaction and intermetallic compound growth behavior of Sn-Ag-Cu lead-free solder joints on different substrates in electronic packaging. *Journal of materials science*, *54*(2), 1741-1768.

Xu, L., & Pang, J. H. (2006, May). Intermetallic growth studies on SAC/ENIG and SAC/CU-OSP lead-free solder joints. In *Thermal and Thermomechanical Proceedings 10th Intersociety Conference on Phenomena in Electronics Systems, 2006. ITHERM 2006.* (pp. 6-pp). IEEE.

Yahaya, M. Z., & Mohamad, A. A. (2017). Hardness testing of lead-free solders: a review. *Soldering & Surface Mount Technology*, *29*(4), 203-224.

Yang, C., Le, F., & Lee, S. R. (2016). Experimental investigation of the failure mechanism of Cu–Sn intermetallic compounds in SAC solder joints. *Microelectronics Reliability*, *62*, 130-140.

Yang, C., & Pang, S. S. (1996). Stress-strain analysis of single-lap composite joints under tension.

Yang, L., Fenglian, S., & Miaosen, Y. (2013, August). Shear strength and brittle failure of low-Ag SAC-Bi-Ni solder joints during ball shear test. In *2013 14th International Conference on Electronic Packaging Technology* (pp. 750-753). IEEE.

Yasmin, T., Sadiq, M., & Khan, M. (2014). Effect of lanthanum doping on the microstructure evolution and intermetallic compound (IMC) growth during thermal aging of SAC305 solder alloy. *J. Mater. Sci. Eng*, *3*, 1000141.

Yen, Y. W., & Chen, S. W. (2004). Phase equilibria of the Ag–Sn–Cu ternary system. *Journal of materials research, 19*(8), 2298-2305.

Yen, Y. W., Tsai, P. H., Fang, Y. K., Lo, S. C., Hsieh, Y. P., & Lee, C. (2010). Interfacial reactions on Pb-free solders with Au/Pd/Ni/Cu multilayer substrates. *Journal of alloys and compounds*, *503*(1), 25-30.

Yiteng, L. (2014). Fe Impacts on Solder Joint Properties in Microelectronic Assembly. *National University of Singapore.*

Yoon, J.-W., Kim, S.-W., & Jung, S.-B. (2005). Interfacial reaction and mechanical properties of eutectic Sn–0.7 Cu/Ni BGA solder joints during isothermal long-term aging. *Journal of Alloys and Compounds, 391*(1-2), 82-89.

Yoon, J. W., Lee, Y. H., Kim, D. G., Kang, H. B., Suh, S. J., Yang, C. W., ... & Jung, S. B. (2004). Intermetallic compound layer growth at the interface between Sn–Cu–Ni solder and Cu substrate. *Journal of alloys and compounds*, *381*(1-2), 151-157.

Yu, D. Q., Jillek, W., & Schmitt, E. (2006). Electrochemical migration of lead free solder joints. *Journal of Materials Science: Materials in Electronics, 17*, 229-241.

Zeng, G., Xue, S., Zhang, L., Gao, L., Dai, W., & Luo, J. (2010). A review on the interfacial intermetallic compounds between Sn–Ag–Cu based solders and substrates. *Journal of Materials Science: Materials in Electronics*, *21*, 421-440.

Zeng, K., Vuorinen, V., & Kivilahti, J. K. (2001, May). Intermetallic reactions between lead-free SnAgCu solder and Ni (P)/Au surface finish on PWBs. In *2001 Proceedings. 51st Electronic Components and Technology Conference (Cat. No. 01CH37220)* (pp. 693-698). IEEE.

Zhang, L., Han, J. G., Guo, Y., & He, C. W. (2014). Anand model and FEM analysis of SnAgCuZn lead-free solder joints in wafer level chip scale packaging devices. *Microelectronics Reliability*, *54*(1), 281-286.

Zhang, L., Xue, S. B., Gao, L. L., Sheng, Z., Ye, H., Xiao, Z. X., ... & Yu, S. L. (2010). Development of Sn–Zn lead-free solders bearing alloying elements. *Journal of Materials Science: Materials in Electronics, 21,* 1-15.

Zhang, L., Xue, S. B., Zeng, G., Gao, L. L., & Ye, H. (2012). Interface reaction between SnAgCu/SnAgCuCe solders and Cu substrate subjected to thermal cycling and isothermal aging. *Journal of Alloys and Compounds*, *510*(1), 38-45.

Zhang, Q., Zhu, Q., Zou, H., & Zhang, Z. (2010). Fatigue fracture mechanisms of Cu/lead-free solders interfaces. *Materials Science and Engineering: A, 527*(6), 1367-1376.

Zhang, X., Liu, J., & Deng, Z. (2024). Bismuth-based liquid metals: advances, applications, and prospects. *Materials Horizons.*

Zhang, X. P., Yu, C. B., Shrestha, S., & Dorn, L. (2007). Creep and fatigue behaviors of the lead-free Sn–Ag–Cu–Bi and Sn60Pb40 solder interconnections at elevated temperatures. *Journal of materials science: materials in electronics*, *18*, 665-670.

Zhang, Y., Cai, Z., Suhling, J. C., Lall, P., & Bozack, M. J. (2008, May). The effects of aging temperature on SAC solder joint material behavior and reliability. In *2008 58th Electronic Components and Technology Conference* (pp. 99-112). IEEE.

Zhang, Y., Kurumaddali, K., Suhling, J. C., Lall, P., & Bozack, M. J. (2009, May). Analysis of the mechanical behavior, microstructure, and reliability of mixed formulation solder joints. In *2009 59th Electronic Components and Technology Conference* (pp. 759-770). IEEE.

Zhao, M., Zhang, L., Liu, Z. Q., Xiong, M. Y., & Sun, L. (2019). Structure and properties of Sn-Cu lead-free solders in electronics packaging. *Science and technology of advanced materials*, *20*(1), 421-444.

Zhao, N., Huang, M. L., & Wu, C. M. L. (2016). Tensile creep behavior of Sn–Ag–Cu–Ni multicomponent lead-free solder alloy. *Journal of Materials Science: Materials in Electronics*, *27*, 6630-6636.

Zhou, J., Sun, Y., & Xue, F. (2005). Properties of low melting point Sn–Zn–Bi solders. *Journal of alloys and compounds, 397*(1-2), 260-264.

Zhou, Y., Yang, P., Yuan, C., & Huo, Y. (2013). Electrochemical migration failure of the copper trace on printed circuit board driven by immersion silver finish. *Chemical Engineering Transactions*, *33*, 559-564.

Zhu, Z., Chan, Y. C., Chen, Z., Gan, C. L., & Wu, F. (2018). Effect of the size of carbon nanotubes (CNTs) on the microstructure and mechanical strength of CNTs-doped composite Sn0. 3Ag0. 7Cu-CNTs solder. *Materials Science and Engineering: A*, *727*, 160-169.

Zienkiewicz, O. C., & Morice, P. B. (1971). *The finite element method in engineering science* (Vol. 1977). London: McGraw-hill.

Zribi, A., Clark, A., Zavalij, L., Borgesen, P., & Cotts, E. (2001). The growth of intermetallic compounds at Sn-Ag-Cu solder/Cu and Sn-Ag-Cu solder/Ni interfaces and the associated evolution of the solder microstructure. *Journal of Electronic Materials, 30*(9), 1157-1164.